



The
University
Of
Sheffield.

Pattern Formation in the Axon: Self-Assembly of the Neuronal Membrane Periodic Skeleton

Helen Pringle

A thesis submitted in partial fulfilment of the requirements for the
degree of Doctor of Philosophy

The University of Sheffield
Faculty of Science
Department of Physics and Astronomy

October 2022

Abstract

Neuronal axons are crucial to the connectivity of the nervous system; however, they are vulnerable to damage through injury and neurodegenerative diseases, both of which can disrupt the internal cell cytoskeleton, resulting in cell death or loss of function.

Recent advances in super-resolution microscopy techniques have exposed a highly organised cytoskeletal structure within the axon, referred to as the membrane-associated periodic skeleton (MPS). This structure consists of rings of actin filaments, spaced periodically at approximately 190 nm intervals, and connected laterally by spectrin tetramers. The mechanism by which this structure forms, and the benefits derived from its organisation, are currently unknown.

We use *in silico* models to investigate the factors driving self-assembly of the MPS structure in axons. We model key cytoskeletal components, actin and spectrin, simulating their motion within an axon-like environment. We include stochastic protein-level events to model relevant biological processes, such as the formation and turnover of crosslinks, and polymerisation of actin filaments. We seek evidence of actin ring formation and periodic patterning through analysis of configurational data.

Through searching parameter space, we show that self-assembly of an MPS-like structure is possible under specific parameter values, with the polymerisation of actin within the cell environment, and its interactions with dense populations of membrane-associated spectrin, playing a key role in overall patterning.

Contents

List of Figures	v
List of Tables	viii
Preface	ix
Acknowledgements	xi
Nomenclature	xii
Declaration	xiv
1 The Membrane Periodic Skeleton	1
1.1 The Neuron: Structure and Function	1
1.1.1 Dendrites	3
1.1.2 The Soma	3
1.1.3 The Axon	3
1.1.4 Axon Terminals	4
1.2 The Cytoskeleton	4
1.2.1 Microtubules	5
1.2.2 Intermediate Filaments	5
1.2.3 Actin	5
1.2.4 Spectrin	7
1.2.5 Motor Proteins	8
1.3 The MPS: A Unique Neuronal Cytoskeleton	10
1.3.1 MPS is Present in Several Regions of the Neuron	12
1.3.2 MPS is Present in Many Types of Neuron	13
1.3.3 Actin Filaments Form Periodic Rings	13
1.3.4 Flexible Spectrin Links Adjacent Rings	16
1.3.5 Actin and Spectrin are Essential, and Interdependent	16
1.3.6 Many Accessory Proteins are Involved	17
1.3.7 The MPS Links with Microtubule Arrays	21

1.3.8	Myosin Motors Associate with the MPS	22
1.4	Why Do We Need the MPS?	24
1.4.1	The MPS in Cell Morphology and Plasticity	25
1.4.2	The MPS Improves Mechanical Properties	31
1.4.3	The MPS in Sensory Function	32
1.4.4	The MPS Assists Axonal Transport	32
1.4.5	The MPS connects with Ion Channels and Cell Adhesion Molecules	33
1.4.6	The MPS is the Catalyst of Degenerative Pathways	33
1.5	The Development Timeline	35
1.5.1	Axon Specification and the Growth Cone	35
1.5.2	Axon Specification is Independent of MPS Assembly	36
1.5.3	Spectrin Becomes Enriched in the Axon	36
1.5.4	MPS Assembles Early in Development	37
1.5.5	The Final Axonal Pattern is Conserved	39
1.5.6	Components Differ at the AIS and Nodes of Ranvier	41
1.5.7	Synaptic MPS is Less Regular and More Dynamic	42
1.5.8	The Soma contains a 2D Lattice	44
1.5.9	MPS May Appear in Stem Cells and Glia	45
1.6	How Does the Structure Self-Assemble?	48
1.6.1	Evidence of MPS Self-Assembly	49
1.6.2	Self-Assembly of Similar Structures	50
1.6.3	Modelling the Cytoskeleton	53
1.6.4	Open Questions on MPS Assembly	55
2	MPS Self-Assembly: Minimal Model	57
2.1	Introduction	57
2.2	Description of Physical Model	58
2.2.1	Axon-Like Geometry	58
2.2.2	Actin Rods	59
2.2.3	Spectrin Tetramers	61
2.2.4	Coordinate System	61
2.2.5	Boundary Conditions	61
2.2.6	Interactions	63
2.3	Numerical Implementation and Algorithm	63
2.3.1	Random Walks and Monte Carlo Scheme	63
2.3.2	Crosslinking Method	67
2.3.3	Translational Motion Method	68
2.3.4	Orientational Motion Method for Loosely Bound Rods	68
2.3.5	Orientational Motion Method for Unpartnered or Tightly Bound Rods	69
2.4	Data Analysis Methods	73
2.4.1	Qualitative Analysis	73
2.4.2	Angle of Orientation Method	74
2.4.3	Radial Positioning Methods	74

2.4.4	Axial Positioning Methods	75
2.5	Actin Filaments within a Cylindrical Axon	77
2.5.1	Simulation Images	77
2.5.2	Angle of Orientation	77
2.5.3	Radial Positioning	80
2.5.4	Axial Positioning	82
2.6	Actin Filaments within an Axon with Microtubule Array	83
2.6.1	Simulation Images	85
2.6.2	Angle of Orientation	85
2.6.3	Radial Positioning	86
2.6.4	Axial Positioning	89
2.7	Crosslinking Actin Filaments	91
2.7.1	Simulation Images	91
2.7.2	Angle of Orientation	93
2.7.3	Radial Positioning	95
2.7.4	Axial Positioning	95
2.8	Crosslinking Actin and Spectrin	97
2.8.1	Simulation Images	97
2.8.2	Angle of Orientation	100
2.8.3	Radial Positioning	100
2.8.4	Axial Positioning	102
2.9	Discussion	104
3	Self-Assembly of a Single Actin Filament Ring	106
3.1	Introduction	106
3.2	Methods	108
3.2.1	Cytosim software	109
3.2.2	Data Analysis Methods	110
3.2.3	Cell Environment and Boundary Conditions	114
3.2.4	Global Fibre Properties	117
3.2.5	Protein-Level Events	119
3.2.6	Timestep and Simulation Duration	121
3.2.7	Actin Filament Properties	122
3.2.8	Spectrin Tetramer Properties	123
3.3	Actin Filament Stiffness	123
3.4	Membrane-Bound Actin	125
3.5	Membrane-Bound Spectrin	127
3.6	Ordered Membrane Binding	132
3.7	In-Cell Actin Polymerisation	138
3.8	Discussion	150
4	Multiple Filament Self-Assembly	152
4.1	Introduction	152
4.2	Methods	153
4.3	Initial Investigations	154

4.3.1	Spectrin Stiffness	154
4.3.2	Cell Size and Boundaries	156
4.4	Membrane-Bound Spectrin	158
4.5	In-Cell Actin Polymerisation	163
4.5.1	Initial Investigation	163
4.5.2	Varying Actin Stiffness and Growth Rate	165
4.6	Actin-Spectrin Crosslinking	175
4.7	Spectrin Density	182
4.8	Actin Stiffness and Polymerisation Rate	188
4.9	Effect of Cell radius	193
4.10	Discussion	194
5	Conclusions	199
5.1	Discussion and Evaluation	200
5.2	Future Work	202
5.2.1	Parameter Optimisation	202
5.2.2	Exploration of Different Morphologies	202
5.2.3	Microtubule Interactions	203
5.3	Concluding Remarks	203
	Appendix A Timestep Dependency	205
	Bibliography	209

List of Figures

1.1	Neuron Structure	2
1.2	Microtubule	6
1.3	Actin Filament	7
1.4	Typical Actin Cortex	8
1.5	Spectrin Tetramers	9
1.6	Myosin	11
1.7	STORM Image of MPS	12
1.8	PREM Images of Actin and Spectrin	15
1.9	Main Components of MPS	18
1.10	PREM Images of pMLC	23
1.11	Axonal Beading	26
1.12	Axonal Twists	28
1.13	Growth Cone	36
1.14	Actin Perturbations	38
1.15	MPS Development	39
1.16	Spectrin and Adducin Periodic Patterns	40
1.17	Node of Ranvier	42
1.18	Spectrin at Nodes of Ranvier	43
1.19	Somatic Spectrin Lattice	46
1.20	MPS in Differentiating Oligodendrocytes	47
1.21	Axon-Axon Contact	48
2.1	Model Microtubule Array	60
2.2	Model Actin Filament	60
2.3	Model Coordinate System	62
2.4	Alpha Method	70
2.5	Actin Rods in Cylindrical Cell - Images	78
2.6	Actin Rods in Cylindrical Cell - Orientation	79
2.7	Actin Rods in a Cylindrical Cell - Individual Orientation Profiles	80
2.8	Actin Rods in a Cylindrical Cell - Radial Distribution	81
2.9	Actin Rods in a Cylindrical Cell - Axial Distribution	82
2.10	Actin Rods in a Cylindrical Cell - Periodicity	84
2.11	Actin Rods in Cylinder with Microtubule Array - Images	85

2.12	Actin Rods in Cylinder with Microtubule Array - Orientation . . .	86
2.13	Actin Rods in Cylinder with Microtubule Array - Individual Ori- entation Profiles.	87
2.14	Actin Rods in Cylinder with Microtubule Array - Radial Distri- bution	88
2.15	Actin Rods in Cylinder with Microtubule Array - Axial Distribution	89
2.16	Actin Rods in Cylinder with Microtubule Array - Periodicity . . .	90
2.17	Crosslinking Actin Rods - Images	92
2.18	Crosslinking Actin Rods - Orientation	93
2.19	Crosslinking Actin Rods - Individual Orientation Profiles	94
2.20	Crosslinking Actin Rods - Radial Distribution	95
2.21	Crosslinking Actin Rods - Axial Distribution	96
2.22	Crosslinking Actin Rods - Periodicity	98
2.23	Crosslinking Actin and Spectrin Rods - Images	99
2.24	Crosslinking Actin and Spectrin Rods - Orientation	100
2.25	Crosslinking Actin and Spectrin Rods - Individual Orientation Profiles	101
2.26	Crosslinking Actin and Spectrin Rods - Radial Distribution . . .	102
2.27	Crosslinking Actin and Spectrin Rods - Axial Distribution	103
2.28	Crosslinking Actin and Spectrin Rods - Periodicity	105
3.1	Test Circle Generation	112
3.2	Reference ORP Calculation	113
3.3	ORP Calculation	115
3.4	ORP Examples	116
3.5	Single Filament - Actin Stiffness	124
3.6	Single Filament - Membrane-Bound Actin	126
3.7	Mean ORP with Spectrin Density	128
3.8	Mean ORP with Actin Stiffness	130
3.9	Simulation Images for Single Filament with Spectrin	133
3.10	Aligned Actin Membrane Binding	134
3.11	Aligned Actin Membrane Binding Examples	135
3.12	ORP Measurement after Detachment of Membrane Binding Pro- teins	137
3.13	Filament Configuration after Detachment of Membrane Binding Proteins	139
3.14	Crosslinked Filament Configuration after Detachment	140
3.15	Mean ORP with Actin Stiffness	143
3.16	Mean ORP with Actin Polymerisation Rate	144
3.17	Mean ORP with Actin Stiffness in Presence of Spectrin Tetramers	146
3.18	Mean ORP with Actin Polymerisation Rate in Presence of Spec- trin Tetramers	147
3.19	Ring Formation for In-Cell Polymerisation	149
4.1	Mean ORP for Different Spectrin Stiffnesses	155
4.2	Effect of Boundaries and Cell Size	157

4.3	Mean ORP with Actin Stiffness	159
4.4	Mean ORP with Spectrin Number	160
4.5	Membrane-Bound Spectrin: Set Comparison	161
4.6	Multiple Filaments - Variation of ORP with Actin Stiffness and Growth Rate	164
4.7	In-Cell Actin Polymerisation Examples: $\kappa_{\text{actin}} = 0.0365 \text{ pN } \mu\text{m}^2$	166
4.8	In-Cell Actin Polymerisation Examples: $\kappa_{\text{actin}} = 0.00913 \text{ pN } \mu\text{m}^2$	167
4.9	In-Cell Actin Polymerisation Examples: $\kappa_{\text{actin}} = 0.00228 \text{ pN } \mu\text{m}^2$	168
4.10	Mean ORP with Actin Stiffness and Polymerisation Rate	170
4.11	ORP Classification with Actin Stiffness and Polymerisation Rate	171
4.12	ORP with Polymerisation Rate	172
4.13	ORP Classification with Polymerisation Rate	173
4.14	Actin Polymerisation: Set Comparison	174
4.15	In-Cell Polymerisation: Timelapse Images	176
4.16	Actin-Spectrin Crosslink Turnover	178
4.17	Actin-Spectrin Crosslinking: ORP for $r_{\text{bind}} = 1 \text{ s}^{-1}$ with Varying r_{unbind}	179
4.18	Actin-Spectrin Crosslinking: ORP Classification for $r_{\text{bind}} = 1$ s^{-1} with Varying r_{unbind}	180
4.19	ORP with Number of Actin-Spectrin Linking Proteins	181
4.20	ORP with Spectrin Density	183
4.21	ORP Classification with Spectrin Density	185
4.22	Periodicity of Actin with 0 Spectrin	186
4.23	Periodicity of Actin with 1500 Spectrin	187
4.24	Periodicity of Actin with 3000 Spectrin	189
4.25	Periodicity of Actin with 4500 Spectrin	190
4.26	Mean ORP with Polymerisation Rate and Actin Stiffness	191
4.27	Number of Rings with Polymerisation Rate and Actin Stiffness .	192
4.28	Low Stiffness/Slow Polymerisation Combination	193
4.29	Effect of Increasing Axon Radius	195
4.30	Effect of Increasing Axon Radius - Examples	196
5.1	Actin Polymerising within a Spherical Cell	204
A.1	Mean Bending Energy with Timestep	206
A.2	Plateau Bending Energy with Timestep	208

List of Tables

1.1	Common Cytoskeletal Drug Treatments	14
2.1	Actin Rods in a Cylindrical Cell - Autocorrelation Peak Data . .	83
2.2	Actin Rods in Cylindrical Cell with Microtubule Array - Auto- correlation Peak Data	91
2.3	Crosslinking Actin Rods - Autocorrelation Peak Data	96
2.4	Crosslinking Actin and Spectrin Rods - Autocorrelation Peak Data	103
3.1	Constants used in Single Filament Model	125
3.2	Spectrin Tetramers - Variation in Mean ORP	129
3.3	Spectrin Tetramers - ORP Results Below Threshold	131
3.4	Aligned Actin Membrane Binding - ORP Results Below Threshold	136
3.5	In-Cell Polymerisation - Variation in Mean ORP	142
3.6	In-Cell Polymerisation with Spectrin - Variation in Mean ORP .	148
4.1	Spectrin Tetramers - Variation in Mean ORP	162
4.2	In-Cell Polymerisation with Spectrin - Variation in Mean ORP .	165
A.1	Plateau Mean Bending Energy	207

Preface

Neurons are the cells of the nervous system responsible for receiving and transmitting signals throughout the body and brain. Each neuron has a challenging task; they may receive input from up to 150,000 connections (Kandel et al. (2000), Chapter 2), and can transmit information between spatially distant regions, spanning distances of up to a startling 30 metres (Smith (2009)). Neurons also respond dynamically to patterns of activity and it is possible for some rewiring to occur in the nervous system throughout life (Kandel et al. (2000), Chapter 63).

Neurons play a crucial role in cognitive, sensory, and motor function, however, being non-dividing cells they are limited in number (Datar et al. (2019)), and despite their remarkable properties, neurons are vulnerable to damage, possessing very limited regenerative capacity once damage has occurred (Kandel et al. (2000), Chapter 55). Due to these limitations, injuries, neurodegenerative diseases, and even normal ageing processes, can cause serious and irreparable loss of function, often severely affecting quality of life for those affected.

The axon - the region of the cell along which signals are transmitted, is particularly vulnerable to injury; it is generally long and thin, and subject to frequent motion-related stresses. Studies have demonstrated a high tolerance for stretching (Smith et al. (1999)), with the axonal cytoskeleton - a structure which provides shape and support to the cell, appearing to have an important role in strain resistance (Tofangchi et al. (2016)). Excessive or rapid strain resulting from an impact can cause axons to become damaged however, leading to traumatic axonal injury, a common form of traumatic brain injury. In traumatic axonal injury there may be axon breakage (primary axotomy), followed by formation of bulbs and axon retraction (Wallerian degredation) (Smith et al. (1999)), or secondary pathology in the form of swelling or beading in regions along the axon, and these processes have been linked to cytoskeletal disruption (Datar et al. (2019), Krieg et al. (2014), Krieg et al. (2017)). The pathology relating to such injuries can be long-lasting, and may be detected over many years following an injury (Adalbert and Coleman (2013)).

In addition to injury related changes, axon degeneration is a feature of many neurodegenerative diseases such as Parkinson's (Godena et al. (2014)), Alzheimer's, Amyotrophic Lateral Sclerosis (ALS), and glaucoma (Adalbert and Coleman (2013)). While the molecular mechanisms of each disease may vary, early cytoskeletal disruption, which later leads to swelling and retraction of axons, is a common hallmark (Eira et al. (2016), Datar et al. (2019)). Even without pathology, similar processes of axon loss occur in ageing, with populations of myelinated axons in humans diminishing to 45% of their initial numbers by 80 years of age (Adalbert and Coleman (2013)).

The neuron has a unique elongated morphology, however recent evidence has shown that neurons are distinct not only in outward appearance, but also in the organisation of their cytoskeleton. Imaging studies focussing on the axon have uncovered rings of the cytoskeletal protein, actin, spaced at regular intervals, in an arrangement referred to as the membrane-associated periodic skeleton (MPS)

(Xu et al. (2013), D’Este et al. (2015), He et al. (2016)). A variety of proteins have been found to associate with the rings, connecting them axially, controlling their shape, and influencing their position. While it is thought that this organised and tightly regulated structure of rings and associated proteins may offer mechanical support to this fragile region of the cell (Leite et al. (2016)) with possible contributions to the organisation and maintenance of other cytoskeletal components such as microtubules (Qu et al. (2017)), the factors driving its self-assembly, and the significance of this unique arrangement, remain a mystery.

In this study, we build *in silico* models of the axonal cytoskeleton to investigate how self-assembly of this well-ordered, crucial structure could occur. Chapter 1 provides an introduction to neurons and the cytoskeleton. We introduce the MPS, summarising evidence on its key properties, components, roles within the cell, and assembly processes. In Chapter 2, a simple model of linking rod particles is used to investigate whether systems of rods could arrange in a ring-like manner based on interactions with one another and the cell boundaries. Chapter 3 builds on this work to develop a more complex model, introducing further biological features to simulate self-assembly of a single actin filament ring. In Chapter 4 we adapt the model of Chapter 3 to include multiple actin filaments interacting within a larger axon-like cell space, seeking both ring formation and periodic patterning. Finally in Chapter 5, we summarise and discuss our results, concluding the research, and suggesting avenues for future investigations on this topic.

Acknowledgements

I would like to thank the Centre for Doctoral Training in Polymers, Soft Matter, and Colloids, at the University of Sheffield for giving me the opportunity to complete this PhD, and providing support, training, and opportunities throughout my years in Sheffield. I am especially grateful to Dr Joe Gaunt who went above and beyond to support me through the difficulties I encountered at the beginning of my studies. I gratefully acknowledge funding from EPSRC for this research.

Thanks to my CDT cohort, it was wonderful to work with such an inspiring group of PhD students. Special thanks to Dr Anna Mroz for so much kindness during a particularly troublesome time, and Dr Hasina Begum for being so positive and friendly, and organising cohort social activities.

I am deeply grateful to my supervisor, Dr Rhoda J. Hawkins, for being there at every step of this rollercoaster, for always having faith in me, and for showing the utmost compassion. I will be eternally grateful that you chose to supervise me despite the rather unexpected way in which I joined your group.

Thanks to Tash, James, Mon, and Lianne in the Biological Physics group - I am so grateful for the help and support you have given me throughout my time in the Department.

I could not have survived these difficult years without the unwavering support of my mother, Theresa, who picked me up more times than I can count, who pushed me on with her kind words, and who prayed for me relentlessly.

Lastly, I want to thank my children, Matilda Jean, and Maxwell James, who have been my most difficult challenge, my biggest source of distraction, and yet my greatest source of inspiration. Thank you.

Nomenclature and Abbreviations

A list of key terms and abbreviations is given here for ease of reference.

AFM - Atomic force microscopy

AIS - Axon initial segment

AnkB - Ankyrin-B

AnkG - Ankyrin-G

CNS - Central nervous system

DAAM - Dishevelled-associated activator of morphogenesis

DIV - Days *in vitro*

DRG - Dorsal root ganglion

ELC - Essential Light Chain

HIV - Hours *in vitro*

KD - Knockdown

KO - Knockout

MAP - Microtubule-associated protein

MD - Molecular dynamics

Microfilaments - A term for neuronal actin filaments

MLC - Myosin Light chain

MLCK - Myosin Light Chain Kinase

MPS - Membrane periodic skeleton

MTOC - Microtubule Organising Centre

Neurofilaments - A term for neuronal intermediate filaments

NGF - Nerve growth factor

NM II - Non-muscle myosin II

pMLC - phosphorylated myosin light chain

PNS - Peripheral nervous system

PREM - Platinum-replica electron microscopy

RGC - Retinal ganglion cells

RLC - Regulatory Light Chain

SIM - Structured illumination microscopy

SMLM - Single-molecule localisation microscopy

Soma - An equivalent term for the cell body

STED - Stimulated emission-depletion nanoscopy

STORM - Stochastic optical reconstruction microscopy

TD - Trophic degeneration

TFW - Trophic factor withdrawal

WD - Wallerian degeneration

WT - Wild type

Declaration

I, the author, confirm that the Thesis is my own work. I am aware of the University's Guidance on the Use of Unfair Means (www.sheffield.ac.uk/ssid/unfair-means). This work has not been previously been presented for an award at this, or any other, university.

Chapter 1

The Membrane Periodic Skeleton

In this chapter we introduce the neuron, briefly detailing its anatomical regions, functions, and the cytoskeleton which supports the cell internally. We introduce the specific form of cytoskeleton found mainly in the axons of neurons, explaining its discovery, components, and purpose. We then review evidence of the timeline of its development, finally reflecting on factors which may have involvement in driving assembly of cytoskeletal components into this highly ordered structure.

1.1 The Neuron: Structure and Function

The nervous system has 2 main parts; the central nervous system (CNS) which, in vertebrates, includes the brain and spinal cord (Kandel et al. (2000), Chapter 1), and the peripheral nervous system (PNS) which consists of neurons involved in sensation and motion.

Two cell types make up the nervous system; neurons and glial cells (glia). Neurons are highly polarised cells which are activated by electrical impulses and form signalling networks throughout the body and brain, while glia have a variety of roles such as supporting neurons, performing housekeeping tasks, and forming the myelin sheath which surrounds many neurons (Kandel et al. (2000), Chapter 2). The human brain has vast quantities of these cells, with neurons numbering on the order of 10^{11} and glial cell abundance at 10-50 times this number (Kandel et al. (2000), Chapter 2).

Neurons exist in 3 broad functional classes; sensory neurons transmit sensation from the periphery of the body to the CNS, motor neurons transmit CNS signals to muscles and glands, and interneurons transmit information within or between brain regions, allowing complex processing to take place (Kandel

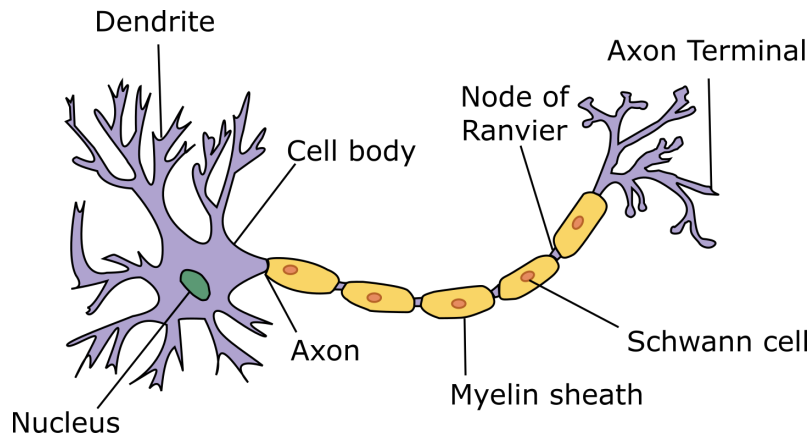


Figure 1.1: Structure of a Typical Neuron. *Branching dendrites extend from the cell body or soma which contains the nucleus. The axon extends away from the cell body, ending in a set of axon terminals. In most cells the axon is myelinated by glial cells such as the Schwann cells shown here, with gaps in the myelin, known as Nodes of Ranvier, at regular intervals.* Image source: <https://commons.wikimedia.org/w/index.php?curid=1474927>. Reprinted under Creative Commons Attribution License: <https://creativecommons.org/licenses/by-sa/3.0/>

et al. (2000), Chapter 2, p25)). With more than 50 distinguishable types, neurons come in many different shapes and sizes (Kandel et al. (2000), Chapter 4), however the majority share four common morphological features; branching dendrites, a cell body (soma) containing the nucleus, a long thin axon, and a set of braching axon terminals. A typical neuron morphology is shown in Figure 1.1.

In addition to sharing a common morphology, all neurons share similar functional mechanisms. A resting negative charge is maintained across the plasma membrane of each neuron, of around 65 mV in magnitude. This potential difference occurs through a combination of an ion pump, which removes Na^+ ions from the cell while pumping K^+ ions in, and non-gated ion channels which leak K^+ ions out, resulting in an overall negative potential difference (Kandel et al. (2000), Chapter 2). The signalling behaviour of neurons is a result of changes in the electrical potential of the cell, which can trigger electrical impulses.

The subsections that follow detail the main structural and functional properties of each of these regions.

1.1.1 Dendrites

Dendrites are long, branching protrusions (often referred to as processes), which receive signals. The number and length of dendrites correlates with the number of contacts they receive, with some cell types such as Purkinje cells in the cerebellum receiving around 150,000 input connections (Kandel et al. (2000), Chapter 2) and a typical cell receiving up to 10,000 (Kandel et al. (2000), Chapter 10).

Signals are received through receptors on dendrites which accept charges, and these charges alter the resting potential, with each receptor contributing either a depolarising/excitatory increase or hyperpolarising/inhibitory decrease in charge. Excitatory receptors are commonly located on the small spike or mushroom shaped protrusions extending from dendrites known as dendritic spines (Bär et al. (2016)). Incoming charges may be mechanical or chemical in origin; in sensory neurons an influx of ions can flow through mechanically gated ion channels which are operated by changes in tension such as the stretch of a muscle, and this creates a receptor potential (Kandel et al. (2000), Chapter 2). In other neuron types, charge is generated by chemical energy as neurotransmitters are received and bind to ligand-gated ion channels (Kandel et al. (2000), Chapter 6) creating a synaptic potential (Kandel et al. (2000), Chapter 2).

Local currents generated by individual ion channels flows passively, decaying in magnitude due to the axial resistance of the dendrite, which depends upon its radius and length (see Magee (2000) for a review).

1.1.2 The Soma

The soma is the body of the cell, and contains the nucleus. Like dendrites, this region can receive signals in the form of incoming charges, however the proximity of the soma to the axon minimises spatial signal decay, hence somatic signals are powerful. Somatic inputs are commonly inhibitory, providing a strong shunting inhibition that can quickly dampen excitation of the neuron (Kandel et al. (2000), Chapter 12).

1.1.3 The Axon

Axons are long and thin with typical lengths of between 0.1 mm and 3 m (Kandel et al. (2000), Chapter 2), extending up to 30 m in the spine of the blue whale (Smith (2009)), and diameters ranging from 0.1 - 10 μm (Perge et al. (2012)) to a maximum of around 1mm in the giant axon of a squid (Kandel et al. (2000), Chapter 8). Proximal to the soma is the axon initial segment (AIS) which generally occupies the first 20-60 μm of the axon (Leterrier et al. (2017)).

Charges received by dendrites and the soma accumulate over time and space, and these charges integrate at the AIS causing an overall change in resting potential of the cell membrane. Should the change in potential exceed a trigger threshold, an action potential is generated. This occurs due to the presence of voltage gated sodium ion channels in this region, which open if the neuron is

sufficiently depolarised, allowing a flood of positively charged sodium ions to cross the membrane into the cell (Kandel et al. (2000), Chapter 2) at a rate of up to 500 volts per second (Kandel et al. (2000), Chapter 6).

The action potential itself is a signal of around 100 mV in amplitude and 1 s duration, which propagates down the axon at speeds of up to 100 m s^{-1} (Kandel et al. (2000), Chapter 2). An action potential has a fixed magnitude, but the number of pulses and the delay between them is used to convey information on the strength of the input signal (Kandel et al. (2000), Chapter 2). The velocity of conduction is increased for large diameter axons, and can be increased further by myelination - the wrapping of glial cells such as the Schwann cells shown in Figure 1.1 around the axon. Myelinated axons propagate action potentials actively, regenerating the signal periodically through activation of voltage-gated sodium ion channels located at the Nodes of Ranvier - gaps in myelin sheath of around $2 \mu\text{m}$ occurring every 1-2 mm along the length of the axon (Kandel et al. (2000), Chapter 8).

1.1.4 Axon Terminals

Once the action potential has traversed the axon it stimulates an output. The output may be physical, such as a muscle contraction, however it frequently involves the transfer of signals to other neurons with which it is connected via synapses (Kandel et al. (2000), Chapter 2).

A typical neuron forms around 1000 synapses (Kandel et al. (2000), Chapter 10). The synapse is a link between the axon terminals of the pre-synaptic neuron, and the dendrites or soma of the post-synaptic neuron. In some cases there is a physical connection, and ions flow directly between the cells via a gap-junction channel forming an electrical synapse, however the majority of synapses are chemical, with axon terminals arranged proximate to dendrites with a small gap or cleft between them. The action potential triggers opening of calcium ion channels in a duration-dependent manner (Kandel et al. (2000), Chapter 12), causing the pre-synaptic cell to release neurotransmitters - chemical signals which fuse with the membrane, crossing the synaptic cleft to bind to receivers on the post-synaptic cell, stimulating the opening or closing of ion channels (Kandel et al. (2000), Chapter 10).

1.2 The Cytoskeleton

Internally, each cell is supported by a cytoskeleton; a framework made up of filaments and connecting proteins. The cytoskeleton has many functions; it determines cell shape, provides mechanical support, assists in cell division and growth, enables crawling and motile behaviours, and also provides tracks and docking areas for cargo to allow intracellular transport (Alberts et al. (2002), Chapter 16). The main component filaments in eukaryotic cells are microtubules, intermediate filaments, and actin, and these components are discussed

further in the following sections, along with a protein called spectrin and a number of motor proteins that associate with cytoskeletal filaments.

1.2.1 Microtubules

Microtubules are made of protofilaments composed of alternating α and β tubulin monomers as shown in Figure 1.2. Around 13 of these protofilaments associate laterally to form a hollow cylinder with an outer diameter of 25 nm (Alberts et al. (2002), Chapter 2) and a thickness of around 5 nm (Kasas et al. (2004)). Microtubules are dynamic; their plus ends grow through addition of GTP-bound $\alpha\beta$ -tubulin dimers. This GTP is hydrolysed to GDP once incorporated into the microtubule, which reduces stability, and the GDP-bound tubulin monomers are then likely to detach at the minus end of the microtubule (Kandel et al. (2000), Chapter 4).

Microtubules are usually nucleated from γ -tubulin which forms a microtubule organising centre or MTOC, nucleating microtubules from their minus ends so the plus ends grow out into an aster shape (Alberts et al. (2002), Chapter 16). In the axon of neurons, however, microtubules of a few μm in length each orient into parallel bundles with their plus end directed towards the axon terminal region (Alberts et al. (2002), Chapter 16). These microtubule arrays are used as tracks by the molecular motors, kinesin, and dynein, which step towards the plus end, and minus end, respectively. This allows transport of proteins along the axon. Axonal microtubules also tend to maintain a stable length without dynamic growth and shrinkage (Yogev et al. (2016)).

1.2.2 Intermediate Filaments

Intermediate filaments, often referred to as neurofilaments in neurons, are around 10 nm in diameter and form a rope-like structure where sets of 8 staggered tetramers associate and twist (Alberts et al. (2002), Chapter 16). Intermediate filaments are generally stable, being polymerised to a high degree (Kandel et al. (2000), Chapter 4) and also exhibit strain-stiffening mechanical properties which helps to give shape and mechanical support to the cell (Lowery et al. (2015)). There are many types of proteins which can form intermediate filaments, however in neurons, the proteins NF-L, NF-M, and NF-H are most common (Alberts et al. (2002), Chapter 16). Neurofilaments have been shown to increase axon diameter through crosslinking (see Costa et al. (2018) for a review).

1.2.3 Actin

Actin filaments, referred to as microfilaments in neurons, are made up of monomers of the globular protein, G-Actin. These monomers assemble into a pair of protofilaments which wind around one another, forming a helix with a pitch of around 37 nm (Alberts et al. (2002), Chapter 16). The resulting actin filaments have a diameter of between 5 and 9 nm (Alberts et al. (2002), Chapter 4).

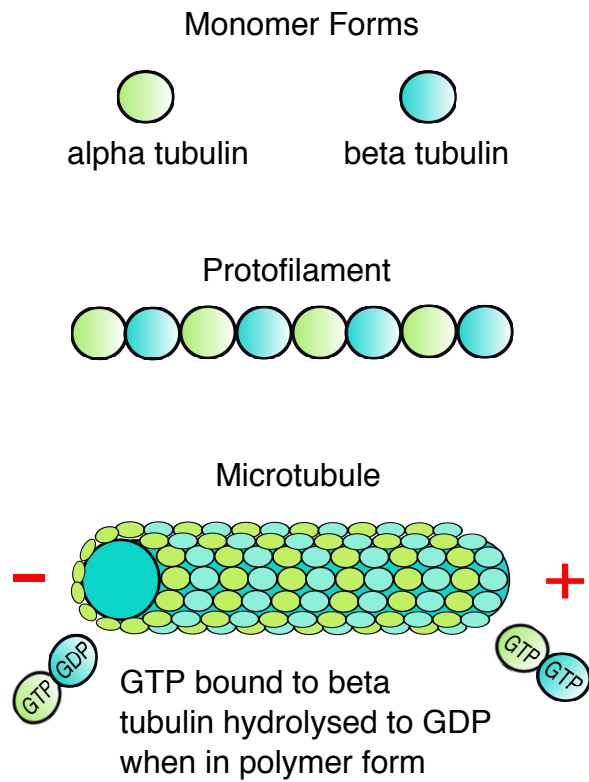


Figure 1.2: Microtubules. *Tubulin monomers form protofilaments of alternating α and β monomers. Protofilaments laterally associate into hollow cylinders which can grow through addition of GTP-bound tubulin dimers, and shrink as hydrolysis to GDP occurs, causing dimers to dissociate.*

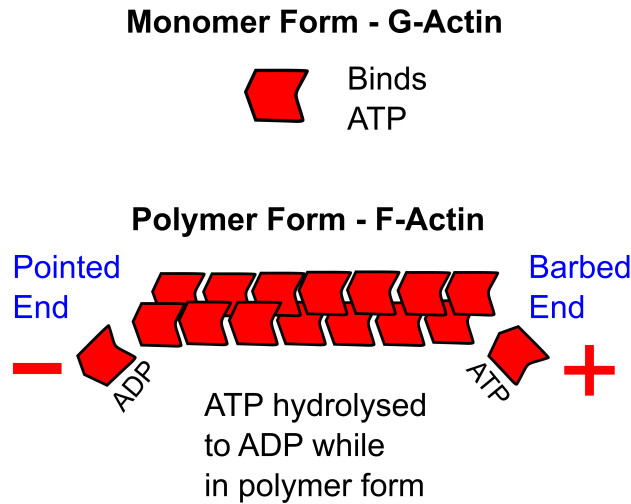


Figure 1.3: Actin. *The upper pane shows the monomeric form of actin, known as Globular or G-Actin, while below, Filamentous or F-Actin is shown as 2 protofilaments forming a helix. Monomers join the barbed end, dissociating at the pointed end once ATP hydrolysis has occurred.*

As with microtubules, actin filaments are dynamic; as illustrated in Figure 1.3, ATP-bound monomers of G-Actin join the plus or barbed end of the filament, causing fast growth. This ATP is then hydrolysed to ADP which reduces the stability of these monomers, causing them to detach at the minus or pointed end of the filament (Dominguez and Holmes (2011)).

Actin filaments tend to be nucleated close to the plasma membrane of the cell, forming a cell cortex which is a gel-like network (Alberts et al. (2002), Chapter 16). This network, shown in Figure 1.4, can become contractile through interaction of myosin molecular motors with actin filaments.

1.2.4 Spectrin

Spectrin is made up of a string of repeat units, with each unit composed of 3 helices (referred to as A, B, and C) and a linker region as shown in Figure 1.5 (upper). There are 2 monomeric forms; α which has around 20-21 full repeat units and a partial repeat of a 'C' helix (Brown et al. (2015), Baines (2014)), and β which has 16 full repeats and a partial repeat with A and B helices (Baines (2014)). The monomers join laterally to form $\alpha\beta$ -spectrin heterodimers. They then associate head to head to form a tetramer by linking their partial repeats to make a full set of helices as shown in Figure 1.5 (lower). Tetrameric spectrin has a contour length of 200 nm (Bloch and Pumplun (1992)) and diameter of 4 - 6 nm (Shotton et al. (1979)).

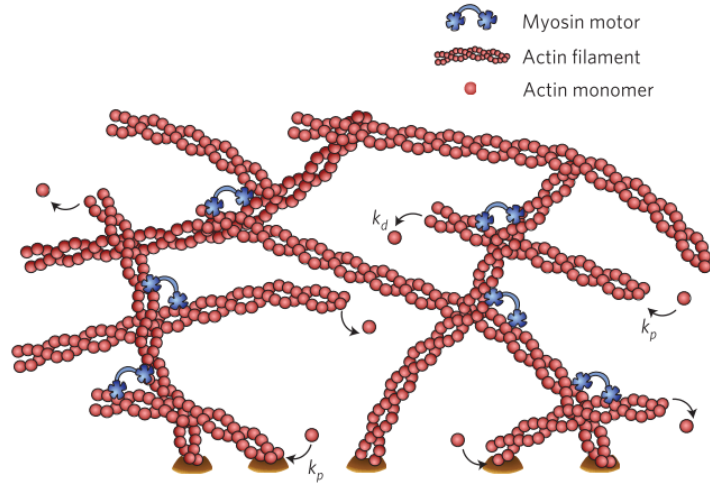


Figure 1.4: Typical Actin Cortex. *Actin filaments (red), polymerising and depolymerising at rates k_p and k_d respectively, are arranged into a thin mesh and linked by myosin motors (blue).* Image Source: Prost et al. (2015). Reprinted with permission from Nature Publishing.

The most studied form of spectrin is that found in the erythrocyte, where tetramers form an organised 2D polygonal lattice along with actin. It appears to be a flexible protein able to fold and extend in a concertina-like manner (Bloch and Pumplin (1992)), occupying the erythrocyte skeleton at a short end-to-end distance of 55-65 nm (Brown et al. (2015)). Spectrin tetramers have the capacity to bind a single actin filament at each end (Brown et al. (2015)) and link to the cell membrane through a connecting protein, ankyrin (Bloch and Pumplin (1992)).

1.2.5 Motor Proteins

A range of molecular motor proteins associate with cytoskeletal filaments. These motor proteins can bind to filaments and step along them with a directionality dependent on the polarity of the filament and motor type, using ATP hydrolysis to power each step (Alberts et al. (2002), Chapter 16). Motor proteins may move cargo throughout the cell, using cytoskeletal filaments as tracks, and can also exert forces on the filaments themselves, enabling dynamic rearrangement of the cytoskeleton. The most common motor proteins are described briefly below:

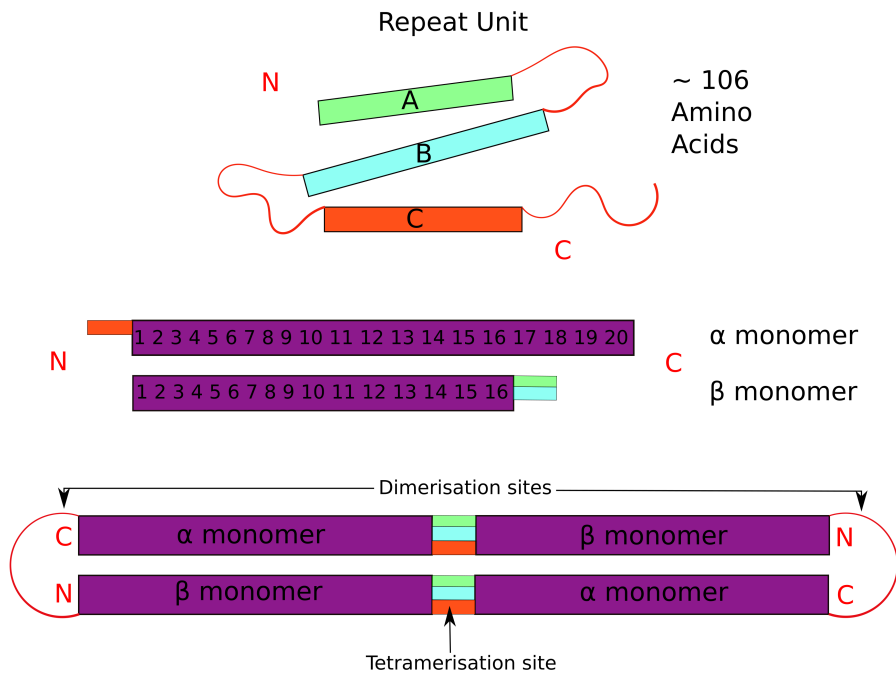


Figure 1.5: Spectrin Tetramer Formation Stages. *Upper pane shows a single repeat unit composed of 3 helices and a linker region. These units combine in series to form the alpha and beta spectrins shown in the central pane. $\alpha\beta$ monomers associate laterally to form heterodimers, then join head to head, forming heterotetramers as shown in the lower pane.*

Myosin

Myosin-II is a common actin-associated motor protein found in neurons as well as many other cell types. As shown in Figure 1.6, it is a hexameric complex composed of a pair of heavy chains and 2 pairs of myosin light chains (MLCs) of which 2 are essential (ELC) and 2 are regulatory (RLC) (Brito and Sousa (2020)). The heavy chains form a long coiled-coil tail, while the light chains occupy head regions which bind to and step towards the plus or barbed ends of actin filaments, propelled by cycles of ATP hydrolysis driven conformational changes (Alberts et al. (2002), Chapter 16).

In non-muscle cells myosin-II can exist in an inactive state, with the tail region tucked behind the head. To activate the molecule, the RLCs are phosphorylated by myosin light-chain kinase (MLCK), which releases the tail and allows actin binding activity (Alberts et al. (2002), Chapter 16). When activated, non-myosin-II (NM-II) tails can aggregate in anti-parallel configurations, assembling into small contractile filaments of about 30 molecules and length-scales around 300 nm (Dasbiswas et al. (2018)) as shown in Figure 1.6.

Kinesin and Dynein

Kinesin and dynein are microtubule-associated motor proteins. Kinesin has 2 stepping head domains, 2 heavy chains, and 2 light chains (Alberts et al. (2002), Chapter 16) and steps towards microtubule plus ends. In neurons, kinesins are involved in anterograde transport, with their heavy chains creating a fan-like tail that can bind to organelles (Kandel et al. (2000), Chapter 5). Dynein is a large motor protein with many light chains and 2-3 heavy chains, and can have 2 or more head domains (Alberts et al. (2002), Chapter 16). Dynein steps towards the minus ends of microtubules, and in neurons is used for retrograde transport (Moughamian and Holzbaaur (2012)).

1.3 The MPS: A Unique Neuronal Cytoskeleton

Based on early imaging studies it appeared that neurons had a homogeneous, gel-like actin cortex (Papandréou and Leterrier (2018), references within), as found in most cell types and shown in Figure 1.4, however these studies utilised conventional fluorescence microscopy, which is limited by diffraction to a resolution greater than 250 nm (Bär et al. (2016)).

Recent developments in super-resolution microscopy have allowed imaging of cytoskeletal proteins at the sub-diffraction scale with resolutions as low as 10 nm (Bär et al. (2016), references within). In 2013 an *in vitro* study using a form of super-resolution imaging called stochastic optical reconstruction microscopy (STORM) detected a highly organised structure consisting of regularly spaced rings of actin filaments arranged along the axons of cultured rat hippocampal neurons, further confirming this result *in vivo* in hippocampal tissue slices (Xu et al. (2013)). In this structure, referred to as the membrane periodic skele-

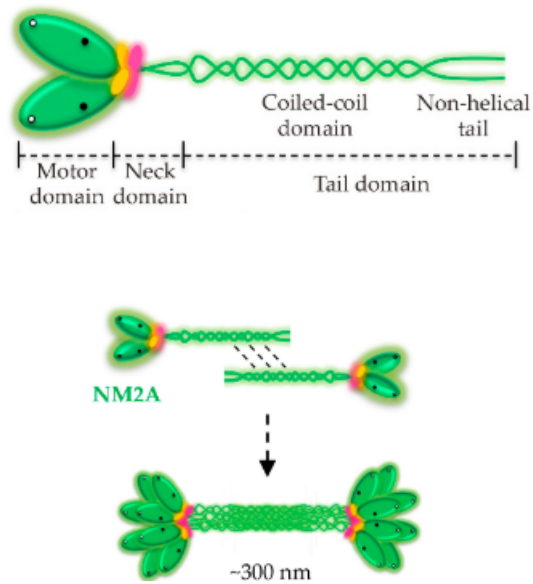


Figure 1.6: Myosin. *A single myosin molecule is shown in the upper pane. The heavy chain is shown in green, with a stepping motor domain 'head' and coiled-coil tail region. Essential light chains (ELCs) are shown in yellow, while regulatory light chains (RLCs) are shown in pink within the neck domain. The lower pane shows myosin molecules forming anti-parallel mini-filaments of around 300 nm in length. Image source: Brito and Sousa (2020). Adapted and reprinted under Creative Commons Attribution Licence: <https://creativecommons.org/licenses/by/4.0/>*

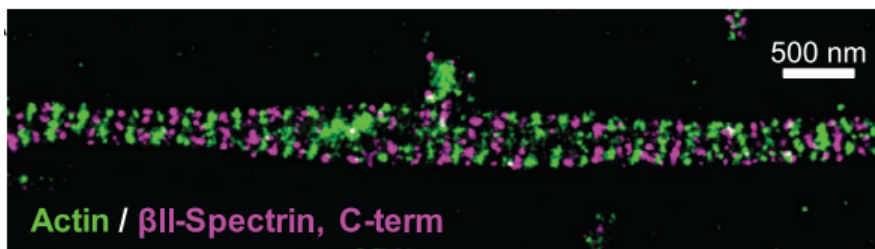


Figure 1.7: STORM image of MPS in rat hippocampal cell. *Actin is shown stained in green, while the centrally located β II spectrin C-terminal is shown in magenta. Actin and spectrin show an alternating, periodic pattern.* Image source: Xu et al. (2013). Reprinted with permission from AAAS.

ton or MPS, actin filaments have a 1D ladderlike appearance, and adjacent rings were found to be spaced periodically at 180-190 nm and connected by the tetrameric form of spectrin, with STORM images showing alternating stripes of fluorescence for these 2 components as shown in Figure 1.7.

Developments in membrane-permeable fluorogenic probes combined with super-resolution imaging confirmed the presence of the MPS in living cells; Lukinavičius et al. (2014) detected actin periodicity of 181 nm in live cultured rat hippocampal neurons using the super-resolution imaging technique, stimulated emission-depletion nanoscopy (STED).

1.3.1 MPS is Present in Several Regions of the Neuron

Subsequent studies have found the axonal MPS to be robust and highly regular, covering the entire axon from proximal to distal regions (Zhong et al. (2014)). It is present in the AIS (Xu et al. (2013)), and Nodes of Ranvier (D’Este et al. (2015)), and while it is difficult to image underneath the myelin sheath that coats most cells *in vivo*, it has been successfully detected in myelinated mouse sciatic nerve fibres (D’Este et al. (2016)).

It is not just a feature of the axon however, and can be found to a lesser extent in other areas of the neuron; although not detected in the original study, the MPS has since been imaged at postsynaptic sites, being present in both dendrites (D’Este et al. (2015), Han et al. (2017)) and dendritic spine necks (Bär et al. (2016)). Small regions of MPS can also be found pre-synaptically at axon terminal boutons (He et al. (2016)).

The MPS appears to be largely a feature of thin, tubular processes (Lavoie-Cardinal et al. (2020)), although 1D ladderlike strips have been recently detected in other neuronal geometries (Han et al. (2017), Hauser et al. (2018)).

1.3.2 MPS is Present in Many Types of Neuron

While the MPS was originally imaged in rat hippocampal tissues, it appears to be highly evolutionarily conserved, being found in a wide range of cell types and species. The pattern has been observed in a range of vertebrate and invertebrate species, including humans, rats, chickens, *Caenorhabditis elegans*, and *Drosophila* (He et al. (2016)).

The MPS is present throughout both central and peripheral nervous systems. In addition to the hippocampus, a study on cultured mouse cells found the pattern to be present in the cortex and midbrain CNS regions (He et al. (2016)), while in the peripheral nervous system, it has been found in sciatic motor neurons (D’Este et al. (2015)) and in sensory dorsal root ganglion (DRG) cells (He et al. (2016), D’Este et al. (2016), Leite et al. (2016)). It is a feature of both excitatory and inhibitory neurons (He et al. (2016), D’Este et al. (2016)), and is present in many cell types, including granule, Golgi, and Purkinje neurons, as well as cells of the retina, including the highly specialised retinal bipolar cells (D’Este et al. (2016)) and retinal ganglion cells (Leite et al. (2016)).

While there is substantial evidence that the MPS is ubiquitous in neurons, it has not been consistently found in imaging studies on glia (D’Este et al. (2016), He et al. (2016), Hauser et al. (2018)).

1.3.3 Actin Filaments Form Periodic Rings

The key feature of the MPS is the presence of rings composed of actin filaments, however the length and number of filaments that make up each ring, and the means by which they are nucleated remains unclear.

Initial observations were suggestive of a large number of short actin filaments per ring; in the original STORM images, Xu et al. (2013) found spots of adducin, an actin capping protein, colocalised with the actin rings, suggestive of short, stable filaments, capped to prevent further polymerisation. The MPS bears many similarities with the erythrocyte cortex (Unsain et al. (2018b)) in which actin filaments are short, ranging between 26-41 nm in length (Mische et al. (1987)). Qu et al. (2017) gave further support to the presence of large numbers of short filaments; using structured illumination microscopy (SIM) they imaged several hundred axons, measuring MPS abundance (defined as the number of axonal image segments exhibiting a periodic pattern relative to control) in *Drosophila* Primary neurons. MPS in mature cells (cultured for a period of 10 days *in vitro* (DIV)) appeared to rely upon nucleation, but not elongation; MPS abundance in mutants null for the actin elongation factor, profilin, was similar to wild type (WT), however abundance was strongly reduced in mutants null for nucleation factors, Arp2/3, and Dishevelled-associated activator of morphogenesis (DAAM). In addition, Cytochalasin D (CytoD) reduced abundance to 32% of WT, while Latrunculin A (LatA) did not have a significant effect. As detailed in Table 1.1, both drugs suppress or slow polymerisation by sequestering monomers, however CytoD additionally destabilises the barbed ends of actin filaments (Peterson and Mitchison (2002)). Overall these results appear

Table 1.1: Common Cytoskeletal Drug Treatments

Drug	Target and Action	Reference
Colchicine	Microtubules - binds to tubulin monomers preventing polymerisation	Peterson and Mitchison (2002)
Cucurbitacin E	Actin - binds to actin filaments preventing depolymerisation	Sørensen et al. (2012)
Cytochalasin D (CytoD)	Actin - destabilises filament barbed ends and sequesters monomers	Peterson and Mitchison (2002)
Latrunculin A (LatA)	Actin - sequesters monomers	Peterson and Mitchison (2002)
Nocodazole	Microtubules - binds to tubulin monomers preventing polymerisation	Peterson and Mitchison (2002)
Taxol	Microtubules - stabilises filaments and stimulates polymerisation	Peterson and Mitchison (2002)

to show nucleation of new filaments being of greater importance in mature cells than further polymerisation of existing filaments, suggestive of the presence of many short filaments.

While the studies described above give compelling evidence of short actin

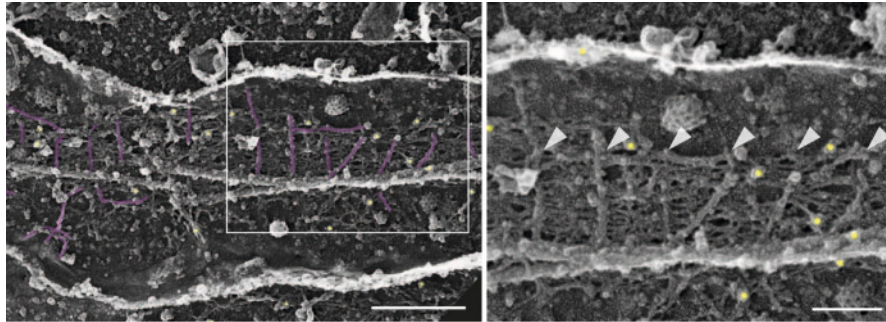


Figure 1.8: PREM Images of an Unroofed Axon. *Actin filaments labelled in purple on left image and with arrowheads on right image. Gold dots show immunogold labelling of all present spectrin isoforms.* Image source: Vassilopoulos et al. (2019). Reprinted under Creative Commons Attribution License: <http://creativecommons.org/licenses/by/4.0/>

filaments, in each case length was inferred from other factors, and not directly visualised. A recent study challenged these conclusions, obtaining images of actin rings with a combination of single-molecule localisation (SMLM) techniques and platinum-replica electron microscopy (PREM) as shown in Figure 1.8, finding each ring to be composed of 2 intertwined filaments with average lengthscales per filament of $1.13 \mu\text{m}$ (Vassilopoulos et al. (2019)). This study noted that adducin may also associate with the side of an actin filament and is not necessarily performing a capping function, although previous *in vitro* assays have shown that capping functions are preferential (Li et al. (1998)). We await further investigations to support this result.

Several proteins nucleate actin filaments, however due to the linear nature of the rings it seems most likely that they are created by formins, nucleating unbranched actin (Pruyne et al. (2002)), as opposed to branched actin network nucleators such as Arp2/3 (Coles and Bradke (2015)). While Qu et al. (2017) found that disruption of both Arp2/3 and the formin, DAAM, had an effect on MPS abundance, DAAM disruption had the greatest effect, reducing MPS abundance to 60%. MPS abundance was observed to be similar to WT in null mutants for profilin, an elongation factor that helps to build long actin filaments, however null mutants for nucleation factors, Arp2/3, and DAAM had reduced MPS abundance, at 80% and 60% that of WT respectively. The results of this study are difficult to interpret as both of these nucleators play key roles in the growth cone, with Arp2/3 creating lamellipodia, and DAAM creating filopodia (Coles and Bradke (2015)), and its disruption may affect the growth cone, influencing the MPS indirectly. The formin, DAAM, may also be performing roles other than nucleation, as it is known to stabilise microtubules and link them to actin (Szikora et al. (2017)), the disruption of which may also cause indirect disorganisation of the MPS or axonal retraction.

1.3.4 Flexible Spectrin Links Adjacent Rings

Through observation of spacing between actin rings, and comparison to the erythrocyte cortex composition, Xu et al. (2013) postulated the presence of spectrin tetramers connecting adjacent rings, confirming this hypothesis using STORM imaging. The spectrin tetramers form a dense mesh between rings as observed by Vassilopoulos et al. (2019) and shown in Figure 1.8.

The end to end distance of spectrin tetramers appears to be close to their 200 nm contour length in both the MPS and also in the 2D polygonal cytoskeleton decorating the soma of neurons (Han et al. (2017)). This lengthscale is substantially longer than the 55-65 nm found in erythrocytes (Brown et al. (2015)). Coarse-grained molecular dynamics (MD) simulations of erythrocyte spectrin predicted an equilibrium end-to-end distance between 160-180 nm, finding that elastic properties were non-linear, allowing spectrin tetramers to be compressed to short lengths with minimal force, however in contrast to this finding, further MD simulations obtained an end-to-end distance of 74.3 nm after equilibration (Zhang et al. (2017)).

Differences between erythrocyte and brain spectrin, or the presence of tensile or compressive forces, may explain the elongated configuration of spectrin tetramers in neurons, and it appears that both factors may contribute; Mehboob et al. (2010) confirmed a higher stiffness of brain spectrin, which is due to increased formation of hydrogen bonds, and the presence of a helical linker region which is unstructured in erythrocytes, while Krieg et al. (2014) investigated forces in *C. elegans* touch receptor neurons using a molecular force sensor genetically encoded into β spectrin, finding each axonal spectrin to be subjected to 1.5 pN of tension.

1.3.5 Actin and Spectrin are Essential, and Interdependent

The periodic organisation of actin and spectrin may be destroyed through manipulations to either one of these components.

In rat hippocampal cells Xu et al. (2013) observed that treatment of actin filaments with LatA not only destroyed the periodic patterns of actin, but also disturbed the periodic organisation of β II spectrin. Zhong et al. (2014) confirmed the loss of β II spectrin periodicity in hippocampal cells treated with LatA at 10 DIV, further finding that the spectrin pattern can be disrupted more rapidly when LatA or CytoD are used on immature cells at 3 DIV. Vassilopoulos et al. (2019) used Swinholide A, which both inhibits polymerisation and severs existing filaments, and found that while this caused loss of periodicity of both actin and spectrin in the distal axon, some periodic spectrin organisation persisted in the AIS, likely as a result of superior membrane binding in this region. In *Drosophila* primary neurons, results differed, with CytoD reducing MPS abundance to 32% of WT at 10 DIV, while abundance after LatA treatment remained high at 94% (Qu et al. (2017)). This study did however

confirm that the structure was less stable in young cells, with MPS abundance in cells grown for 8 hours *in vitro* (HIV) dropping to 38% after CytoD, and 48% after LatA treatment. While it is not clear why LatA disrupts MPS in mature mammalian cells more readily than in *Drosophila*, it has subsequently been shown by Lavoie-Cardinal et al. (2020) that the use of SiR-Actin, a silicone rhodamine based fluorescent probe used to label actin, can alter the dynamics of actin filaments. This probe may have stabilised actin filaments in the study by Qu et al. (2017), preventing disruption by LatA. Interestingly, Vassilopoulos et al. (2019) found that stabilising actin using Cucurbitacin E (see Table 1.1) had a positive effect on β II spectrin, which appeared dense and more regular after this treatment.

While there are limitations on manipulations available for spectrin tetramers, with β II spectrin knockout in mammalian cells proving lethal (Leterrier (2019)), the use of shRNA knockdown (KD) of β II spectrin was shown to destroy the periodic pattern of actin in rat hippocampal cells (Zhong et al. (2014)). In *Drosophila*, Qu et al. (2017) found MPS abundance was reduced in spectrin null mutants, with abundance at 89% of WT for those lacking the α monomer, and 58% for β null mutants, proving the greater importance of the β monomer. Lorenzo et al. (2019) found that β II spectrin mutant mice with very low levels of the protein had minimal periodicity of actin and adducin, although there was some recovery of periodicity after further days *in vitro*, suggesting an alternate mechanism could partially compensate.

The results show that actin and spectrin are both required to maintain an MPS, but are also connected in a manner that renders them inter-dependent.

It appears that as well as disrupting the periodic arrangement, manipulations of either actin or spectrin can alter properties of both the MPS and the axon; a study on *Drosophila* motor neurons detected an increase in axon diameter when actin was disrupted with CytoD, suggesting a role for actin rings in maintaining the narrow tubular shape of the axon (Fan et al. (2017)), while *Drosophila* null mutants for spectrin β monomers showed increased spacing between rings, rising from 183 nm to 197 nm on average (Qu et al. (2017)).

1.3.6 Many Accessory Proteins are Involved

In addition to actin and spectrin, several accessory proteins have been identified which are consistently associated with the MPS, and many more are believed to be involved. A schematic diagram in Figure 1.9 shows some of these components.

Adducin

Adducin is a heterodimer made up of α and β monomers which has been shown to bundle actin filaments through crosslinking activities, forming bridges at 35.2 nm intervals (equivalent to one actin helix) and promoting binding of spectrin to actin, possibly through creation of a new spectrin binding site on actin filaments (Mische et al. (1987)). *In vitro* assays show that while adducin can associate

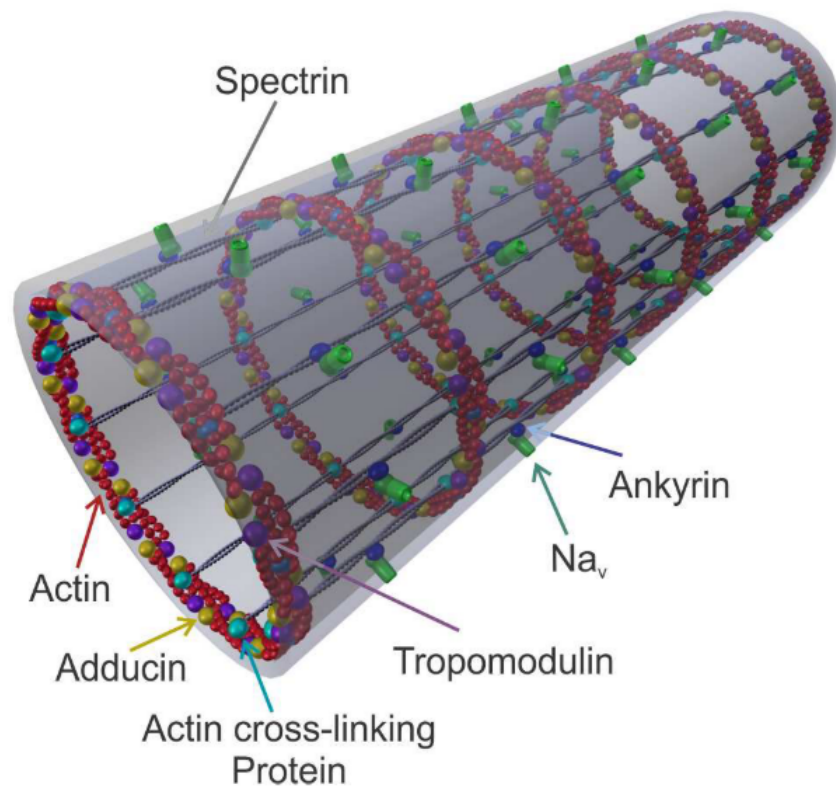


Figure 1.9: Main Components of the MPS. *This image shows actin rings with capping proteins adducin and tropomodulin. Also shown are spectrin tetramers, secured to the membrane with Ankyrin, which also attaches sodium ion channels.* Image source: Zhang et al. (2017). Reprinted under Creative Commons Attribution License: <https://creativecommons.org/licenses/by/4.0/>

with the sides of actin filaments, it has a high affinity for the barbed ends of actin filaments, where it prevents turnover of monomers and recruits spectrin (Li et al. (1998)). STORM imaging found adducin colocalised with actin rings, showing a very similar and regular periodicity, suggestive of a role as an actin capping protein, similar to its role in erythrocytes (Xu et al. (2013)). Adducin does not, however, appear to be required during early development of the MPS, only beginning to show periodic distribution from 6 DIV when actin and spectrin periodicity is already well established throughout the axon (Zhong et al. (2014)).

While not required for MPS assembly, adducin may be required for its maintenance; Leite et al. (2016) discovered a role for adducin in controlling the diameter of both actin rings and the axon. In vivo, α -adducin knockout (KO) mice showed progressive axon enlargement and loss throughout the optic nerve, spinal cord, and sciatic nerves, with tissue slices from the optic nerve showing a decrease to just 40% of WT axon numbers between 20 and 100 days postnatal. Furthermore, Leite et al. (2016) showed that this increase in axon diameter was directly related to actin rings; using STED microscopy to image cultured hippocampal and retinal ganglion cells (RGC), they found that actin ring diameters were 1.3 fold larger than WT, a degree of enlargement similar to that observed in optic nerve axons in vivo. While all hippocampal axons were found to progressively narrow between 8 and 30 DIV, the diameter difference between KO and WT cells was maintained at each observed stage. This shows that while lack of adducin causes an overall enlargement of axons, actin rings are dynamic and can alter their diameter in an adducin-independent manner. Periodicity of actin rings was longer than WT initially, at 8 DIV, but this had normalised by 16 DIV. Kymographs on hippocampal and DRG cells showed some slowing of transport of mitochondria and lysosomes, however synaptic vesicles were not affected.

In *Drosophila*, Qu et al. (2017) found that periodicity of rings was unaffected by adducin KO, in agreement with the results of Leite et al. (2016), however they additionally found that adducin KO had an overall destructive effect on the MPS, with abundance diminishing to 43.5% of its WT levels in the null mutant, and 69.2% in a mutant with loss of adducin function. This effect was also observed by Zhou et al. (2020), with KD or KO of α -adducin causing partial disruption of the MPS in mouse neurons.

Together, these results show that while adducin is not involved in the initial assembly of the MPS, it contributes to both stabilising the actin within rings, perhaps by capping or linking activity, and helping to prevent enlargement of the axon.

Tropomyosin

Xu et al. (2013) predicted the association of Tropomyosins with the MPS, given that they are a component of the erythrocyte cortex with which many parallels are drawn. Tropomyosins are dimers which bind to actin filaments; some isoforms are involved in recruiting and activating myosin motor proteins, while other isoforms increase actin stability by giving protection from the severing and

destabilising activities of ADF and cofilin (Gateva et al. (2017)). Tropomyosins have not yet been imaged in the distal axon, however the isoform Tpm3.1 has shown some degree of colocalisation with actin rings in the AIS, affecting their spacing, regularity, and tilt if inhibited (Abouelezz et al. (2020)). Zhou et al. (2020) found that MPS formation was affected by KD/KO of the isoform Tropomyosin 1. It is not clear, however, what role these proteins play and why they are required for assembly.

Tropomodulin

Tropomodulins are a family of 4 proteins which cap the pointed or minus ends of actin filaments, increasing filament stability by reducing monomer turnover (Fath et al. (2011)). The capping activity of tropomodulins is greatly enhanced through binding of tropomyosin proteins (Yamashiro et al. (2012)). As the actin filaments forming rings in the MPS appear stable, capping of the pointed end seems likely, with tropomodulins suggested to be involved (Zhang et al. (2017)).

Tropomodulin 1 and 2 were identified in a large scale protein analysis study by Zhou et al. (2020), with both of these components showing a periodic arrangement. KO of Tropomodulin 1 caused some disruption to the MPS, while Tropomodulin 2 had little effect.

Ankyrin

Given its presence in the erythrocyte membrane skeleton where it anchors spectrin tetramers to the membrane, Xu et al. (2013) predicted that ankyrin-B (AnkB) could adopt a similar role in the MPS. Their imaging studies confirmed some periodic organisation of AnkB in the distal axon, with a wavelength matching that of actin and spectrin periodicity, however AnkB appeared less regular, possibly due to the presence of multiple ankB binding sites on each spectrin tetramer. A further isoform, ankyrin-G (AnkG) was found to be arranged periodically at the AIS (Zhong et al. (2014)), and at Nodes of Ranvier (D'Este et al. (2016)).

The importance of ankyrin is unclear; in *Drosophila*, ankyrin null mutants showed a small reduction of MPS abundance to 92% of WT, suggesting that it is not required for MPS formation or maintenance. Interestingly, while Zhong et al. (2014) found no change to β II spectrin periodicity in AnkB KO mice at 10 DIV, STORM imaging showed that these cells had developed highly regular periodic organisation of β II spectrin and adducin throughout dendrites as well as in the axon. Overexpression of β II spectrin gave similar results, suggesting that while AnkB may not be required for MPS formation directly, it could have an important role in controlling the distribution of spectrin, ensuring the β II isoform is enriched in the axon.

Miscellaneous Proteins

Recent experiments have identified a further two MPS component proteins; Zhou et al. (2020) detected periodic organisation of coronin2b and dematin in the axon, with dematin KO causing disruption to the MPS structure. Dematin (also known as band 4.9 in erythrocytes) is a trimeric protein which attaches to the membrane and interacts with actin, forming bundles of actin filaments, and slowing the rate of actin polymerisation (Siegel and Branton (1985)). It has also been found to facilitate interaction between actin and spectrin; co-sedimentation assays show that the weak binding observed between spectrin and actin filaments is substantially enhanced in the presence of dematin (Koshino et al. (2012)). Coronin2b is enriched throughout the nervous system, particularly the CNS, where it associates with actin filaments and slows the speed of polymerisation (Chen et al. (2020)).

While all of the proteins mentioned in this section have been confirmed to show periodic organisation in neurons, there are likely to be many more; Zhou et al. (2020) identified 515 proteins consistently associated with MPS components, 162 of which were significantly up or down regulated upon β II spectrin KD. We await further experimental results.

1.3.7 The MPS Links with Microtubule Arrays

There is evidence that actin and microtubules are connected within axons; early evidence of this is a study conducted prior to the detection of the MPS which found that microtubule depolymerisation using Nocodazole, a drug which binds to tubulin monomers preventing their polymerisation (see Table 1.1), caused dramatic axon retraction, however this retraction could be prevented entirely by destabilising actin, with either LatA or CytoD (Ahmad et al. (2000)). This implies that actin is contractile longitudinally in the axon, and that this contraction is resisted by intact microtubules, indicative of a physical connection between actin and microtubule arrays.

Several more recent studies have supported this connection, furthermore showing that it is the actin within the MPS that interacts with microtubules; Zhong et al. (2014) found that the periodic arrangement of actin and spectrin was destroyed when microtubules were treated with Nocodazole, while Qu et al. (2017) disrupted actin using CytoD, observing that this caused gaps to appear in the microtubule array in a dose dependent manner, reversible under washout. A prolonged, high strength treatment of CytoD led to axon retraction and degeneration, with 45% of neurons losing their axon under these conditions.

It is not clear how microtubules and the MPS are connected, but it is possible that ankyrin proteins provide a link; in the AIS, AnkG was observed connecting directly to microtubules in PREM images (Vassilopoulos et al. (2019)). In the distal axon, AnkB can interact with the protein complex, dynactin (Lorenzo et al. (2014)); dynactin forms connections with the microtubule associated motor protein, dynein (Elshenawy et al. (2019)), and these dynein-dynactin complexes enable minus end directed axonal transport (Moughamian and Holzbaur

(2012)). It is possible that this protein complex could mediate connections between microtubules and spectrin within the MPS. Interestingly, inhibition of dynein has been demonstrated to cause axonal retraction, even when microtubules are fully intact (Ahmad et al. (2000)). As mentioned earlier, the formin DAAM, which has been shown to play a role in the MPS (Qu et al. (2017)), may also provide a link between microtubules and actin, and there are many other proteins which are able to connect these components in neurons (see Gordon-Weeks and Fournier (2014) and Coles and Bradke (2015) for reviews). Further research is required to establish which components provide links between the MPS and microtubules, and to isolate the mechanisms through which they are connected.

Microtubule arrays appear to expand the axon radially and lengthen axially (Costa et al. (2018)), with disruption using Nocodazole or a drug with a similar mode of action, Colchicine (see Table 1.1), resulting in decreased axon diameter (Fan et al. (2017)). Actin rings may play a role in maintaining these arrays, helping to consolidate the axon as it matures during development behind the growth cone and preventing branching (Gallo (2013)), and also regulating arrays in mature cells to prevent disorganisation which could affect transport and cause axon enlargement (Costa et al. (2018)), leading to neurodegeneration.

It has previously been found that use of the microtubule-stabilising drug, Taxol (see Table 1.1), causes multiple neurites to extend into axons (Witte et al. (2008)). Interestingly, Zhong et al. (2014) found that MPS was present in multiple axons generated by Taxol stabilisation, with β II spectrin appearing periodic. It is not clear whether the stabilisation of microtubules could directly enable the MPS to assemble, or if it triggers a signalling cascade associated with axonal growth which may include factors to drive MPS assembly.

1.3.8 Myosin Motors Associate with the MPS

Given that in other cell types myosin interacts with the actin cortex, influencing cell shape with its contractile properties, it is natural to speculate whether myosin could interact with the neuronal MPS in a similar manner. This raises questions as to the orientation and arrangement of actin filaments within rings and whether the rings themselves could become contractile through myosin association (Gallo (2013)).

Axons have been shown to maintain a longitudinal steady state tension (Bernal et al. (2007)), with myosin providing a contractile force acting axially to shorten the axon (Costa et al. (2018)). Ahmad et al. (2000) observed that axonal retraction caused by microtubule depolymerising treatments could be prevented by inhibition of myosin or depolymerisation of the actin upon which it acts. This observation has been supported by experimental results based on other means of axonal retraction; Mutalik et al. (2018) grew axons in curved configurations on substrates from which they were later detached, observing detached axons to shorten and straighten over time, while Tofangchi et al. (2016) observed the same behaviour in axons where tension had been reduced through

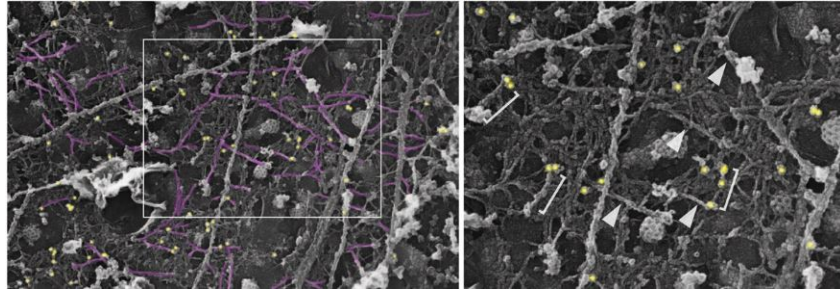


Figure 1.10: PREM Images of pMLC. *Actin filaments are labelled in purple, while gold dots show immunogold labelling for pMLC. Brackets on the right image show longitudinal filaments decorated with pMLC.* Image source: Vassilopoulos et al. (2019). Reprinted under Creative Commons Attribution License: <http://creativecommons.org/licenses/by/4.0/>

mechanical slackening. Both studies found that inhibition of myosin or disruption of actin either lessened the extent of the retraction, or prevented it entirely. These studies provide clear evidence of a contractile acto-myosin based force which acts to shorten the axon, however it is unclear whether this force is constant, resisted under normal conditions by stiff microtubules, or whether myosin activity is modulated in response to certain events. The loss of tension itself could trigger activation of myosin; myosin phosphorylation has been linked to both microtubule depolymerisation (Ahmad et al. (2000)) and loss of spectrin tension (Deng et al. (2015)).

As well as its involvement in axial contractility, myosin activity also appears to contract the axon circumferentially (Costa et al. (2018)). Fan et al. (2017) found that disruption of myosin activity resulted in increased axon diameter of *Drosophila* motor neurons - a similar result to that found in α -adducin KO cells (Leite et al. (2016)). It is not clear how both adducin and myosin contribute to maintenance of axon/actin ring diameter, however both effects can be modulated by Ca^{2+} , which could allow dynamic diameter changes in a calcium concentration dependent manner (Costa et al. (2018)).

While the above results confirm that myosin provides both axial and circumferential contraction in the axon, it is not clear precisely how myosin interacts with the MPS. Imaging studies have attempted to visualise the location of myosin and its interactions with the MPS, finding it to interact with actin rings to some degree; Berger et al. (2018) detected phosphorylated myosin light chain (pMLC) at the AIS and Nodes of Ranvier coinciding with actin rings, although associated non-muscle myosin II (NM-II) mini-filaments were not imaged in this study. Using SMLM imaging, Vassilopoulos et al. (2019) also found pMLC to be periodic at the AIS, and using correlative SMLM/PREM, visualised pairs of pMLC dots associated with filaments assumed to be NM-II mini-filaments. These filaments were oriented perpendicular to actin rings, sug-

gesting that myosin could form links between rings. Costa et al. (2020) also imaged pMLC with SMLM, confirming its presence in both the AIS and distal axon. While the pattern did not appear as regular as that of actin or spectrin, pMLC molecules were generally observed at roughly 200 nm intervals, in circular patterns coinciding with phalloidin-stained actin. Imaging of the heavy chains which form the myosin mini-filaments was less conclusive; some sites showed co-localisation of the centre of a myosin mini-filament with actin, while others showed alignment between centres of both myosin and spectrin tetramers, with other filaments being observed in a range of orientations. From these results it is unclear whether myosin is bound within a single ring, linking neighbouring rings, or acting upon other sources of actin such as longitudinal filaments. It is possible that all of these modes of operation occur.

Neither Wang et al. (2020), nor Costa et al. (2020) found short-term inhibition of myosin to affect periodicity of actin rings, however these studies did not agree on whether inhibition caused rings to tilt, with Wang et al. (2020) observing some degree of tilting, while Costa et al. (2020) did not see any changes to ring orientation. Prolonged inhibition of myosin was found to cause disruption to both actin rings and microtubule arrays however, suggesting that myosin contractility is essential for maintenance of the MPS (Wang et al. (2020)).

1.4 Why Do We Need the MPS?

The MPS is unique, being distinct from both the homogeneous actin cortex found in most cells, and also from the 2D polygonal membrane skeleton of the erythrocyte. The high level of organisation demonstrated, along with its ubiquity throughout regions of the nervous system, and between different organisms, is highly suggestive of a specific purpose or benefit derived from this specific cytoskeletal arrangement.

Neurons are non-dividing and limited in number (Datar et al. (2019)), with these cells, particularly their axons, being vulnerable to damage through disease, injury, or ageing processes (Kandel et al. (2000), Chapter 55). A devastating array of symptoms can occur due to this irreparable loss of function, severely impacting quality of life. Cytoskeletal disruption is a common hallmark of degeneration (Eira et al. (2016), Datar et al. (2019)), therefore a thorough understanding of cytoskeletal structures found within the axon could deeply enhance our understanding of degeneration mechanisms, inspiring avenues of research which could lead to improved treatments of neurological disease and injury.

On discovering the MPS, researchers speculated that the structure could give superior mechanical support to the long, slender axon (Xu et al. (2013)). In this section we summarise research which confirms that while this is indeed one benefit of the MPS, the structure is key to a number of functional processes, with relevance to both the healthy functioning of the cell and pathways of degeneration.

1.4.1 The MPS in Cell Morphology and Plasticity

Axon dimensions span a wide range, with diameters from 0.1 μm (Perge et al. (2012)) up to 1 mm (Kandel et al. (2000), Chapter 8), and lengths from around 0.1 mm (Kandel et al. (2000), Chapter 2) up to a striking 30 m (Smith (2009)). While there is usually a single axon, in some cell types axons branch into multiple processes (Kandel et al. (2000), Chapter 4). Size is strongly influenced by a requirement for efficient wiring of the nervous system; neuron firing rates increase approximately linearly with diameter, however these information transfer benefits come at a cost in terms of space and energy, and this drives a preference towards small caliber axons (Perge et al. (2012)). Axon shape and size is dynamic, changing throughout the life of the cell from initial extension of a young neurite (Kandel et al. (2000), Chapter 54), rapid expansion of synapsed neurons as organisms grow (Pfister et al. (2004)), retraction to allow neuronal plasticity (Datar et al. (2019)), transient changes to boost function (see Costa et al. (2018) for a review), and finally, morphological changes related to injury, disease, or ageing (Adalbert and Coleman (2013)). The cytoskeletal arrangement within the cell provides a framework, determining its shape (Kandel et al. (2000), Chapter 4) and recent evidence shows the MPS arrangement to influence and dynamically control both length and diameter of the axon.

Axon Length and Axial Tension

Axons are known to maintain a longitudinal steady state tension, and this is an important factor in establishing their length, with axons changing their dimensions to maintain the preferred level of tension. Stretched axons contract, shortening and straightening to re-establish tension once the stretch is released in PC12 neurites (Bernal et al. (2007)), and *Drosophila* motor neurons (J. Rajagopalan et al. (2010)). Similar results occur when axons are detached from substrate on which they were grown in curved configurations (Mutalik et al. (2018)), or when tension is relaxed through mechanical slackening (Tofangchi et al. (2016)), while a sudden release of tension through transection with laser ablation results in a rapid 'snapping' - a sudden shortening of the axon on a time-frame of under 1 second, followed by slower retraction thereafter (Datar et al. (2019)). Extrapolation of force-displacement curves obtained using *Drosophila* suggest a longitudinal steady state tension of between 1-13 nN (J. Rajagopalan et al. (2010)), or 0.1-3.5 nN (Fan et al. (2019)).

Most studies show that actin disruption is not linked to axon length changes, however it does appear to lower longitudinal tension; in chick DRG cells, Ahmad et al. (2000) noted many axons showing a wavy appearance at the edges when disrupted with either LatA or CytoD, indicative of tension loss or imbalance, while LatA was found to reduce axonal tension at a rapid rate, from 13 nN in control to 1.8 nN after a 30 minute treatment (Dubey et al. (2020)). Use of CytoD, on *Drosophila* motor neurons caused a complete loss of the observed 0.1-3.5 nN steady state tension and a slack appearance even when the drug was targeted to a small, local area via a narrow microfluidics channel (Fan et al.

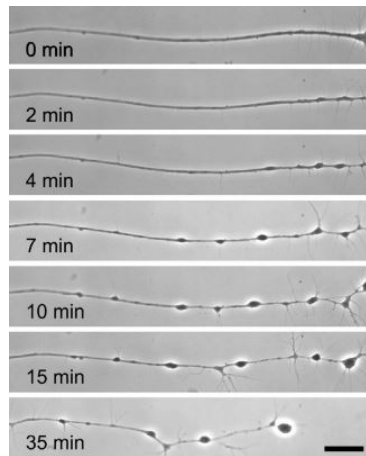


Figure 1.11: Axonal Beading and Retraction over Time. *Axonal beading progression after addition of Nocodazole. Scale bar shows 20 μm .* Image source: Datar et al. (2019). Reprinted with permission from Elsevier.

(2019)). In contrast, Datar et al. (2019) found LatA collapsed the growth cone of chick DRG cells, creating a retracting 'front' of cytoskeletal components which rapidly retracted to the soma leaving a trail of membrane behind. They were able to prevent this retraction by use of taxol to stabilise microtubules, however Dubey et al. (2020) found that tension loss could not be prevented with Taxol.

Disruption of myosin appears equivalent to actin disruption, with length being maintained but evidence of tension loss with wavy edges (Ahmad et al. (2000)) and slack appearance (Fan et al. (2019)). Datar et al. (2019) similarly found no change of axon length when myosin was inhibited with Blebbistatin, however when combined with LatA-induced growth cone collapse, the speed of retraction appeared to be enhanced.

Microtubules appear to have a key role in maintaining the length of the axon, likely counteracting contractile acto-myosin forces. Disruption of microtubules using nocodazole causes morphological changes in the form of beading, followed by retraction of the axon (Ahmad et al. (2000), Datar et al. (2019)). Beads are dynamic, moving back and forth with a net drift towards the soma, leaving a thin trail of empty membrane behind as shown in Figure 1.11. Retraction was observed only when the drug was able to infiltrate the growth cone, accessing microtubules in states of low stability, and the axon was unaffected by local applications to proximal or mid-sections (Datar et al. (2019)). While retraction may not occur in cases of local application at a distance from the growth cone, tension does still appear to be affected, with Fan et al. (2019) finding a decrease in stiffness of treated regions when applying noco through a microfluidics channel, with these local areas having increased curvature. While Dubey et al. (2020) also observed beading and loss of tension on use of Nocodazole, they

noted that actin rings were lost on use of the drug, while microtubule stabilisation with Taxol lead to increased formation of actin rings. This is supportive of previous findings showing interconnectedness between the actin-spectrin MPS and microtubule arrays (Qu et al. (2017)). The effects of microtubule disruption are less clear where retraction is induced; when mechanically slackened, axons contracted quicker if microtubules were disrupted with Nocodazole or Colchicine (Tofangchi et al. (2016)), however axons grown on curved substrates were slower to contract and straighten if Nocodazole was used (Mutalik et al. (2018)). Where retraction was induced through laser ablation, Taxol stabilisation had a positive effect, halting the retraction earlier than in untreated cells (Datar et al. (2019)), demonstrating that intact/stabilised microtubules resist contractility. Interestingly, the microtubule associated motor protein, dynein, also appears to have a role equivalent to that of microtubules in a way that parallels the actin/myosin connection; Ahmad et al. (2000) found that disruption of dynein activity through use of Dynamin, a drug which dissociates the dynein/dynactin complex, lead to retraction of the axon, however without the occurrence of beading prior.

While there is some disagreement in the literature, the results mentioned largely support ideas of actin and myosin providing contractile forces to shorten and straighten the axon, with this force being resisted by microtubules, with assistance from dynein. As expected for such a balance of forces, the use of both LatA and Nocodazole was not found to induce any retraction, while disruption of myosin also prevented Nocodazole-induced retraction, although some beading was apparent in this case (Ahmad et al. (2000)), while in induced retraction, use of LatA/CytoD or inhibition of myosin was found to lessen (Tofangchi et al. (2016)), or prevent (Mutalik et al. (2018)) the contractile shortening and straightening of the axon. Similar impairment was observed after release of stretched axons when treated with CytoD (Fan et al. (2017)). As well as preventing Nocodazole-induced retraction, LatA treatment was similarly able to prevent retraction caused by dynein disruption, with no beading observed in this case (Ahmad et al. (2000)). Unusually, Datar et al. (2019) found that treatment with LatA or Blebbistatin and Nocodazole together caused the rate of beading to be enhanced compared to use of Nocodazole alone, citing culture conditions and exposure time as possible reasons for the disparity with other studies.

As well as acto-myosin, spectrin is also implicated in the generation and maintenance of longitudinal tension; Krieg et al. (2014) calculated each β spectrin as being held under 1.5 pN of tension in axons, a result bolstered by observations of β spectrin null mutants retracting at slower paces and to a lesser extent, after laser axotomy, than WT, consistent with an overall reduction in tension. Krieg et al. (2017) found that mutants lacking the β spectrin monomer (but with α component still present) had axonal tension that was 5% lower than WT, and a shorter periodicity. Dubey et al. (2020) noted a large drop in axonal tension when spectrin was knocked down by a specific morpholino, estimating that the series of parallel spectrin tetramers within the MPS contributes 6-10 nN to axonal tension. Datar et al. (2019) found that if β II spectrin was

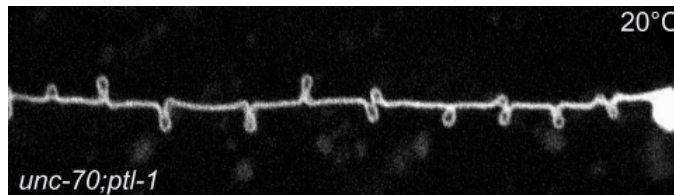


Figure 1.12: Axonal Twisting in Touch Receptor Neurons. *Double mutants for β spectrin and tau protein show large loops along their axons.* Image source: Krieg et al. (2017). Reprinted under Creative Commons Attribution License: <https://creativecommons.org/licenses/by/4.0/>

knocked down prior to use of nocodazole, then beading increased in a manner dependent on the extent of the knockdown, while knockdown followed by use of LatA resulted in a reduced speed of retraction. Krieg et al. (2017) showed that both double mutant *C. elegans* lacking β spectrin (via *unc-70* gene) and the microtubule stabilising tau protein (via *plt-1* gene) have axons that form large bends, kinks, helices, and loops, which reorganise after laser axotomy *in vivo* indicative of being held twisted and under tension, as shown in Figure 1.12. They note that microtubules may form twisted bundles if not stabilised by tau, however given that these shape defects are apparent only in mutants which are also lacking spectrin, it appears that the spectrin is able to stabilise the axon against twisting. Lorenzo et al. (2019) found that mice lacking β II spectrin had axons with considerably shorter lengths and a lack of the long axonal projections usually observed.

Axon Diameter and Circumferential Tension

In addition to involvement in length and axial tension, there is evidence of a role for the MPS in setting axon diameter through circumferential tension. Disruption of adducin (Leite et al. (2016)), or actin/myosin (Fan et al. (2017), Wang et al. (2020)) leads to increased axon diameter, while disruption of microtubules decreases diameter in an actin-dependent manner (Fan et al. (2017)). Leite et al. (2016) confirmed that this increase in diameter was directly connected to actin ring expansion through comparison of STED images of actin rings *in vitro* and axons observed *in vivo*, while Wang et al. (2020) observed dilation of both plasma membrane and actin rings. While myosin inhibition led to expansion of the axon, attempts to increase the level of myosin activation had little effect, indicating that myosin exists in a highly activated state in the axon, maintaining tension on the plasma membrane (Wang et al. (2020)). These results suggest that actin and myosin are contractile circumferentially with adducin possibly helping to secure the rings, with this force being resisted by intact microtubules. In support of this, Qu et al. (2017) found that disruption of MPS-based actin lead to gaps in microtubule arrays and eventual

axon loss, suggesting that circumferential tension from actin rings could prevent microtubule arrays from becoming disordered. In mice, Lorenzo et al. (2019) observed that β II spectrin depletion led to enlarged myelinated axons and signs of degeneration and neuroinflammation.

The MPS in regulation of Geometry

The results discussed above demonstrate that MPS components regulate axonal tension in both circumferential and axial directions, affecting length and diameter of the axon, as well as its curvature. We observe acto-myosin contracting the axon, reducing radius in tandem with adducin, and shortening the length, likely with some help from spectrin which is held under tension. Microtubules have an opposing role, seeking to expand the axon radially, and maintaining length, along with dynein. The MPS and microtubule arrays are interdependent (Zhong et al. (2014), Qu et al. (2017)), with possible connections between microtubules and spectrin via ankyrin (Vassilopoulos et al. (2019)), or with actin rings via formins or similar proteins (Qu et al. (2017), Coles and Bradke (2015), Gordon-Weeks and Fournier (2014)). The precise nature of the interactions of myosin with the MPS is unclear; it may connect neighbouring rings, or sit within individual rings as previously discussed.

Tension may play a role in establishing axon length in developing neurons. Young cells have a growth cone in which cell membrane is propelled forward by actin polymerisation, leaving space for microtubules to invade the region (Kandel et al. (2000), Chapter 54). The presence of stable microtubule bundles appears to trigger formation of actin rings (Zhong et al. (2014)), meaning MPS could begin to assemble around bundles of mature microtubules stabilised by microtubule-associated proteins (MAPs). The axial and circumferential tension provided by the MPS could be an additional means of stabilising microtubule arrays, preventing any further growth and keeping the bundle organised by compression (Gallo (2013)). Interestingly, if axial tension on microtubule bundles is reduced by an external force, growth can be triggered; young axons with a growth cone can be 'towed' in this manner, extending up to 1 mm per day (see Smith (2009) for a review), while integrated axons without a growth cone show remarkable ability to elongate, tolerating increasing rates of stretching up to around 8mm per day, and extension of 10 cm was possible over a 28 day stretching period (Pfister et al. (2004)). In both cases the diameter of the axon remained constant or increased, while new regions of axon appeared to be fully functional with a normal cytoskeleton and transport. A recent study implicates microtubule-based transport of spectrin via kinesins in the formation of new regions of MPS at regularly spaced 'hotspots' along the axon during integrated axon growth (Glomb et al. (2022)). In addition to a role for axial tension in setting length of individual axons, it has been proposed that this tension could contribute to CNS morphogenesis, causing the cortical sheet to fold in a manner which minimises distance between heavily connected regions and helping to shape brain tissue on a macroscopic scale (Van Essen (1997)).

Throughout the life of a neuron, the MPS can be altered to enhance function.

Diameter can be controlled transiently, with Wang et al. (2020) showing local myosin-dependent radial expansion of the axon to allow cargo to pass. Certain axons shorten and swell temporarily when stimulated by action potentials to allow faster conduction through decrease in internal electrical resistance, and while this has not been investigated, it seems highly likely that this reversible alteration in shape is generated by alterations to the MPS (see Costa et al. (2018) for a review).

The MPS can be disrupted or disassembled when plasticity is required; Lavoie-Cardinal et al. (2020) imaged actin rings in dendrites at low activity levels, surprisingly observing a transition from rings to longitudinal actin fibres when stimulation was increased, while Sidenstein et al. (2016) noted disruption of MPS at pre and post-synaptic sites which favour plasticity over stability. Axonal retraction can be triggered as connections are pruned either during development or in mature cells to aid plasticity, altering connections to cater to patterns of use (Datar et al. (2019)). Fan et al. (2019) found that local disruption of either actin or myosin led to a global loss of tension, and this local control over global properties could enable rapid changes in cell shape to be triggered by local signals.

Axonal shape changes are common after injury or as a result of disease processes. Recent evidence has found that many of these changes can occur as a result of an imbalance of tension maintained by the MPS. For example, diffuse axonal injury is a common subtype of traumatic brain injury, where trauma caused by a rapid stretch of the axon is followed by widespread degeneration (Hill et al. (2016)). It is likely that these forces could cause spectrin tetramers to become disconnected. As spectrin is held under tension (Krieg et al. (2014)) this disconnection is likely to be irreversible, and this was confirmed in a model by Zhang et al. (2017) (although this model may have underestimated the persistence length of brain spectrin), with the results of Fan et al. (2019) suggesting that such a local perturbation could cause global tension loss. Neurons have little to no ability to regenerate and repair after injury (Kandel et al. (2000), Chapter 55), and this permanent and widespread loss of tension could partly explain the reason for this fragility to injury.

In neurodegenerative diseases, axonal beading such as that shown in Figure 1.11 is common. This beading has previously been understood to be caused by microtubule breakage and dysfunction leading to improperly transported organelles pooling at regular intervals, however Datar et al. (2019) showed using kymographs that even after bead formation, organelles were still able to traverse the axon on a core of remaining microtubule tracks, instead arguing that beading is a result of a pearling instability - a propagating instability arising when surface tension in tubular membranes exceeds a certain threshold and with a wavelength related to tube circumference (Bar-Ziv and Moses (1994)). Datar et al. (2019) found that the membrane surface tension threshold is lowered substantially when the elastic resistance to surface tension is reduced by microtubule disruption. If tension imbalance is the primary cause of such shape changes in degenerating cells then understanding how the MPS and microtubules are connected and establish tension could give insight into cytoskeletal disruption

in disease processes.

1.4.2 The MPS Improves Mechanical Properties

Axons are relatively stiff, with mature rat hippocampal cells having an axonal Young’s modulus of 4.6 kPa, while dendrites and soma were softer at 2.5 and 0.7 kPa respectively (Zhang et al. (2017)). Microtubules are generally considered to be the component that confers stiffness to the axon and studies confirm this influence; Fan et al. (2019) noted a decrease in stiffness on use of Nocodazole, which was partly reversible after washout of the drug, while Dubey et al. (2020) found that Taxol stabilisation increased Young’s modulus. Microtubule stabilising proteins are also important; mutants null for tau protein and those with compromised binding of MAPs demonstrate a reduction in stiffness, with Young’s moduli of 4.6 and 4.3 kPa respectively, compared to 6.3 kPa for WT (Krieg et al. (2017)).

A new role for the actin and spectrin of the MPS in axonal stiffness is emerging. In a study using atomic force microscopy (AFM) on *C. elegans* touch receptor neurons, Krieg et al. (2017) found that LatA disruption of actin reduced the Young’s modulus from 6.3 to 4.9 kPa, while spectrin disruption had an even greater effect, with mutants with missense alleles leaving them unable to form tetramers having a Young’s modulus of just 3 kPa. This supports previous results in β spectrin mutants where membrane tension was found to be 10 pN per micron lower than in WT (Krieg et al. (2014)), with no cumulative effect from actin disruption to these cells. Dubey et al. (2020) found that while taxol increased the Young’s modulus, use of jasplakinolide to stabilise actin gave an even greater boost to axonal stiffness, while LatA also had a greater effect at reducing axonal tension than Nocodazole, even where microtubules were stabilised with Taxol. KD of spectrin with the β II specific morpholino also caused a big reduction in tension. Zhang et al. (2017) considers the MPS to be the main contributor to the 4.6 kPa Young’s modulus measured as the AFM indentation depth is relatively shallow at 200 nm and is unlikely to make significant contact with microtubules or intermediate filaments, further finding that LatB, a drug which inhibits actin polymerisation, reduces the axonal Young’s modulus to 2.2 kPa. In a coarse-grained MD model of the actin and spectrin structure of the MPS they were able to obtain estimates of contributions to stiffness, with actin rings (assumed to be 1 filament thick) having Young’s modulus of 8.3 kPa and the spectrin-rich regions between at 1.13 kPa. Through radial expansion they obtained an average Young’s modulus of 4.23 kPa for the axon, fitting well with experimental results. While LatA/LatB appear to reduce stiffness, Fan et al. (2019) did not detect any loss of stiffness when using the similar drug, CytoD.

Axons are subject to stresses and strains through motion, with those axons closer to the periphery being subject to the greatest strains of up to 50% (Krieg et al. (2017)). Evidence suggests that the MPS has a role in protecting slender neuronal processes from the motion-induced strains that they endure. An important result supporting this was found prior to detection of the MPS, with

a study on β spectrin null mutant *C. elegans* demonstrating the importance of this key MPS component, and therefore of the MPS itself. Hammarlund et al. (2007) compared mutants with WT, and while they found axons and dendrites grew normally, mutants quickly began to accumulate axonal defects, with 24% of neurons showing defects on hatching, quickly rising to 60% after 24 hours. Visual inspection showed axonal breakage and unusual branching, while longitudinal observations detected repeated axon breakage, with new growth cones and branches appearing as cells attempted to regenerate. Further, paralysis of mutants was shown to prevent these axonal defects, clearly linking axonal damage to motion. These results shed light on the possible processes occurring in diseases involving β spectrin, noting that conditions such as spinocerebellar ataxia involve a gradual onset of symptoms, which are likely to result from strain-induced axonal damages. Krieg et al. (2014) showed that spectrin tetramers played an important role in axial tension; through observation of touch receptor neurons of *C. elegans* β spectrin null mutants, they noted buckling when axons were compressed through motion, whereas WT axons moved with the body. They also showed that tetramer formation is needed, as missense alleles where spectrin is present but tetramer formation is prevented showed similar buckling to null mutants. Dubey et al. (2020) noted strain-softening behaviour of axons, with models showing that this could occur through reversible folding and unfolding of spectrin tetramers, and this feature could explain spectrin's role in tolerating cycles of compression and extension due to motion. It has been suggested that axonal tension, balanced with internal hydrostatic pressure, could convey elastic properties to brain tissue as a whole, allowing deformation without damage (Van Essen (1997)), while the actin-spectrin MPS has also been shown to combat torque which could give protection from twisting and bending as well as tensile stresses (Krieg et al. (2017)).

1.4.3 The MPS in Sensory Function

MPS-based axial tension appears to play a role in sensory cell function; in *C. elegans*, Krieg et al. (2014) noted that as well as exhibiting a loss of axial tension in their touch receptor neurons, β spectrin null mutants had significantly impaired responses to touch sensation when stimulated through stroking with an eyebrow hair. This demonstrates a role for the MPS in detection or relaying of sensory signals.

1.4.4 The MPS Assists Axonal Transport

The MPS has been found to have a positive, regulatory effect on axonal transport. Wang et al. (2020) found transport of large cargo to be facilitated by a short-lived radial fluctuation with myosin-dependent actin ring expansion and corresponding expansion of the plasma membrane followed by contraction once the cargo has moved through the region. Radial expansion increased speed of transport overall, however if expansion was prolonged, cargo accumulated and

the axon ultimately degenerated. This suggests that radial contractility of the axon mediated through the MPS is necessary to regulate the flow of cargo along the axon. A recent study found that KO of JIP3, a protein that couples lysosomes to dynein, resulted in axonal swellings with looped microtubules, but also widespread disruption to the MPS, extending well beyond the local swellings (Rafiq et al. (2022)), further implicating the MPS in axonal transport.

1.4.5 The MPS connects with Ion Channels and Cell Adhesion Molecules

The MPS appears to have a role in connecting and arranging several types of proteins.

Xu et al. (2013) found that sodium ion channels (Na_v) were periodic at the AIS, coinciding roughly with the tetrameric centre of the βIV spectrin isoform found in this region (Xu et al. (2013)), although the pattern was less regular than that of spectrin, likely due to multiple binding sites.

Hauser et al. (2018) found periodic strips of MPS in neural stem cells, particularly in regions that made contact with adjacent cells. As these cells developed, these strips of MPS lined up at the periphery of the cell, with rings even tilting to ensure contact was maintained, while cell adhesion molecules, Neurofascin and L1CAM, were near periodic and coincident with the MPS. LatA treatment destroyed periodicity of these molecules, confirming their association with the MPS.

Zhou et al. (2019) found that the MPS attaches cell surface receptors that transmit extracellular signals to the cell, altering patterns of gene expression. This shows that the MPS acts as a platform for signalling and cell-cell interactions, connecting the axon with the extracellular environment.

1.4.6 The MPS is the Catalyst of Degenerative Pathways

Neurons possess an apoptosis pathway of programmed cell death, which is suspended through supply of neurotrophic factors such as nerve growth factor (NGF) provided by the cells to which the neuron is connected (Kandel et al. (2000), Chapter 53). If neurotrophic factors are withdrawn, trophic degeneration (TD) is triggered involving the activation of caspase and calpain enzymes which cleave other proteins within the cell, causing a breakdown of cellular components (Wang et al. (2019)).

Studies on mouse sensory DRG cells have found that the MPS is broken down during these TD pathways. Unsain et al. (2018a) withdrew supplies of NGF at 3 DIV, observing a rapid collapse of the growth cone occurring within 30 minutes of withdrawal but also a global reduction in actin indicating that dismantling of the cytoskeleton is triggered throughout the axon. By 24 hours post trophic factor withdrawal (TFW), the axon had broken down into fragments forming beads containing microtubules. The group then used STED imaging and a custom image analysis tool, *Gollum* (Barabas et al. (2017)); they first determined

a correlation coefficient corresponding to a visibly periodic pattern, and used the tool to quantify MPS abundance (proportion of regions showing periodic patterns above correlation coefficient), and MPS correlation (mean correlation coefficient of regions meeting the minimum threshold). Analysis of STED images of β II spectrin and phalloidin-stained actin showed a decrease of 50% in both abundance and correlation within 3 hours of TFW, with these measures then plateauing until fragmentation begins at around 18 hours post TFW. This shows that the actin and spectrin of the MPS is rapidly dismantled during TD. Wang et al. (2019) similarly observed a breakdown of the MPS, however surprisingly they found MPS disruption occurred prior to activation of caspase enzymes and could not be prevented by inhibition of the apoptosis pathway. They further observe that while the periodicity of components decreased substantially, overall levels of α II and β II spectrin, and actin were unchanged at 9 hours post TD. These results show that the MPS is not broken down as a result of protein cleavage associated with the apoptosis pathway. Wang et al. (2019) noted widespread phosphorylation of spectrin and adducin occurring on TD - a process which may reduce affinity of components for one another, assisting dissociation.

Stabilisation of the MPS appears to have a beneficial effect in preventing degeneration. Unsain et al. (2018a) found treatment with Cucurbitacin E enhanced MPS abundance in cells subjected to TFW; when treated for 3 hours after 24 hours of TFW conditions, MPS abundance reverted to similar levels as in control cells supplied with NGF, while axon fragmentation levels were improved, with 40% of cells having intact axons compared to 20% of untreated cells. This demonstrates that even late stage stabilisation treatments can significantly reduce degeneration and fragmentation. Similarly, Wang et al. (2019) found that TD was prevented when actin was stabilised by jasplakinolide. Interestingly, the removal of β II spectrin using shRNA knockdown in *in vitro* cultures and genetic deletion in live mice had a similar protective effect, appearing to inhibit some enzymatic activity that forms part of the apoptotic pathway.

The above results show that MPS disassembly is a key part of TD, however it occurs prior to the activation of enzymes involved in protein cleavage, and proceeds even when the apoptosis path is blocked. Disruption of the actin of the MPS using LatA was actually observed to stimulate kinases which activate the pro-degenerative pathway, leading to activation of capsases, however this MPS-based signalling occurred only if the axon was intact, and was prevented in the case of axotomy (Wang et al. (2019)). This degeneration was prevented in cells lacking β II spectrin, demonstrating that it is the actin based within the MPS structure which triggers the degenerative pathway on its disruption. It appears from these results that the MPS is a signalling platform, with its disruption triggering a signalling cascade to the soma, commencing the apoptosis pathway. Research into the MPS structure could therefore greatly aid our understanding of neurodegeneration, potentially leading to breakthroughs in understanding and treatment of diseases and injuries affecting the nervous system.

1.5 The Development Timeline

The MPS begins to assemble in early stages of cell development, appearing more widespread and regular as the cell matures. In this section we first explain briefly how neurons grow and develop, and the cytoskeletal mechanisms that facilitate this. We then focus on the MPS, reviewing evidence of how the structure develops over time, finally summarising some basic properties of the mature structure.

1.5.1 Axon Specification and the Growth Cone

Newly differentiated neurons begin to grow neurites - multiple protrusions of similar length extending from the cell body. In one of these neurites, microtubules become stabilised through acetylation, and this neurite then breaks symmetry, becoming longer than the others (Witte et al. (2008)). Breaking of symmetry triggers axon specification; feedback loops are triggered which reinforce growth of this neurite, while suppressing growth of the others. This extended neurite will continue to grow, becoming an axon, while remaining neurites become dendrites (Schelski and Bradke (2017)). In the cultured hippocampal cells commonly used in imaging studies, the axon is specified at the end of developmental stage 2, corresponding to around 1.5 DIV (D'Este et al. (2015)). The axon then undergoes a period of rapid extension up to around 4 DIV, growing at rates of between 1-100 μm per hour (Leterrier et al. (2017)).

The growing axon extends towards targets, spanning distances up to several meters, and following a range of guidance cues. Each developing axon has at its end a growth cone - a dynamic fan-shaped cytoskeletal structure which reads attractive or repellant cues from the environment, and is able to stop, start, or turn, in response to these cues (Kandel et al. (2000), Chapter 54).

The growth cone consists of 3 domains as shown in Figure 1.13; at the periphery, actin filaments make up both filopodia and the mesh-like lamellipodia, while the central domain contains stable microtubule bundles moving into the growth cone from the axon shaft, with a transitional domain separating these regions (Schelski and Bradke (2017)). Filopodia connect to receptors, reading signals from the environment, and advance by actin polymerisation. This drives the membrane forward, allowing microtubule bundles to invade the new space, and leaving a region of new axon behind (Kandel et al. (2000), Chapter 54).

The growth cone cytoskeleton is controlled by motor proteins; while most microtubules are kept in the central domain, cytoplasmic dynein generates a force which pushes some microtubules into the peripheral domain. Most microtubules remain in the central domain due to retrograde actin flow and the action of kinesins, however the growth cone can be turned in response to local kinesin concentration gradients, allowing microtubules to invade the peripheral domain on the side of lowest kinesin concentration (Kahn and Baas (2016)).

At stage 4 (4-7 DIV for cultured hippocampal cells), the AIS assembles, and the neuron begins to form synapses, connecting with other cells (Leterrier et al. (2017)).

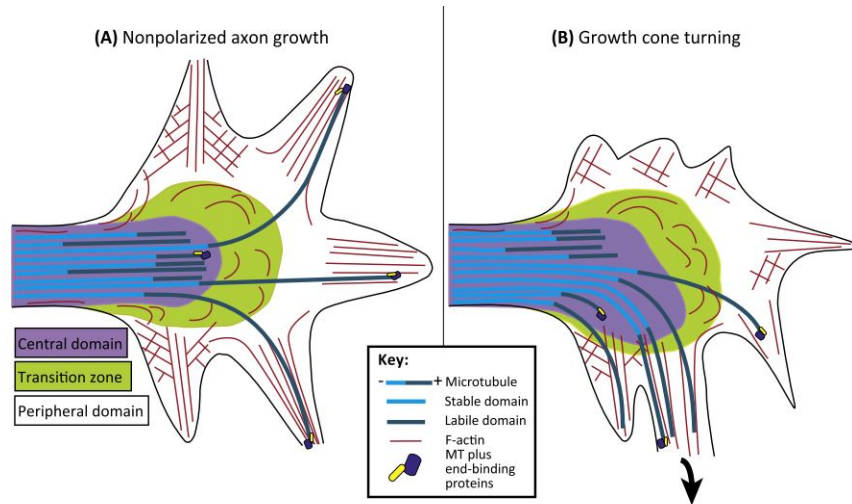


Figure 1.13: Neuronal Growth Cone. *Growing axons terminate in a fan-shaped growth cone which can be driven forwards or turned by actin and microtubules.* Image source: Kahn and Baas (2016). Reprinted with permission from Elsevier.

1.5.2 Axon Specification is Independent of MPS Assembly

Given the role of the MPS in shaping the axon through a combination of axial and circumferential tension, it is natural to consider whether the MPS is responsible for the tubular morphology of axons. This does not appear to be the case; axon specification and both axonal and dendritic outgrowth progress normally in β spectrin null mutant *C. elegans* with early growth processes appearing indistinguishable from WT (Hammarlund et al. (2007)). In mice, however, low levels of β II spectrin is associated with limited axonal outgrowth, with mutant axons appearing shorter than in WT (Lorenzo et al. (2019)).

1.5.3 Spectrin Becomes Enriched in the Axon

In cultured hippocampal cells, AnkB and β II spectrin were found to be enriched at the tips of growing axons from the point of axon specification onwards (stage 3), and these proteins backfill the axon (Galiano et al. (2012)), forcing other isoforms such as those associated with the AIS towards the cell body (Liu and Rasband (2019)). As the microtubule-associated kinesin motor proteins, KAP3/KIF3, were found to colocalise with AnkB, forming a complex as confirmed by immunoprecipitation experiments (Galiano et al. (2012)), it is likely that microtubule-based transport is a key factor in transporting MPS proteins into the axon. Overexpression of α II or β II spectrin promotes trafficking of AnkB towards the distal end of the axon, leaving a larger space available for

AIS assembly at the proximal segment, while the AIS is smaller on overexpression of AnkB (Galiano et al. (2012)).

Axonal MPS formation appears to require a high local concentration of β II spectrin; He et al. (2016) notes that glia, which express lower levels of β II spectrin than neurons, are generally lacking in MPS. AnkB itself is not a requirement for MPS formation, as the MPS is fully formed in both AnkB knockout mice (Zhong et al. (2014)), and null mutant *Drosophila* (Qu et al. (2017)), however when absent the MPS pattern becomes more prevalent in dendrites in addition to the axon. This is suggestive of a role for AnkB in controlling the concentration of β II spectrin and facilitating its enrichment in axons, indirectly enabling robust MPS formation within this region (Zhong et al. (2014)). Overexpression of β II spectrin similarly enhanced MPS formation in dendrites (Zhong et al. (2014)).

1.5.4 MPS Assembles Early in Development

MPS can be detected at early stages of development. In fixed hippocampal cells, Xu et al. (2013) detected actin periodicity from 5 DIV, becoming clearly visible by 7 DIV and remaining present at 28 DIV. In the same cell type, Zhong et al. (2014) imaged β II spectrin and identified periodicity occurring earlier, at just 2 DIV (stage 3), although actin periodicity was not detected at this stage. This early organisation of spectrin was confirmed by Barabas et al. (2017) who similarly detected β II spectrin periodicity in a small proportion of regions imaged at 2 DIV. Using the membrane permeable actin label, SiR-Actin, along with STED nanoscopy D’Este et al. (2015) confirmed presence of some periodicity within the neurite from 2 DIV in 35.7% of live cultured rat hippocampal cells, rising to 62.5% at 3 DIV. These early results could not be replicated on fixed cells, and phalloidin labelling was only able to detect a pattern from 5 DIV, however in a later study on DRG cells, both live cells stained with SiR-Actin and phalloidin-stained fixed cells showed periodicity of actin from 2 DIV (D’Este et al. (2016)). Given the regularity of β II spectrin apparent from 2 DIV, and the ability to perturb this pattern by actin manipulations (Zhong et al. (2014)), it is likely that the failure of some studies to detect actin periodicity at this stage is due to issues with imaging of actin, particularly when stained with phalloidin, rather than an absence of periodic actin. Qu et al. (2017) used *Drosophila* primary neurons stained with SiR-Actin and imaged with structured illumination microscopy (SIM), finding that 20% of axon segments showed some actin periodicity from as early as 6 DIV. Mean spacing at this stage was 197 nm but there was substantial variability, with some actin peaks reaching up to 300 nm spacing. By 10 DIV, 82% of axon segments had periodic distributions of actin.

In early growth stages the MPS can be easily disrupted; Zhong et al. (2014) found that CytoD and LatA both destroyed periodic patterns of β II spectrin in hippocampal cells at 3 DIV as shown in Figure 1.14, while the effect of LatA was less pronounced at 10 DIV. This shows that immature MPS is unstable to perturbation, but that it becomes more resilient over time, perhaps by adding

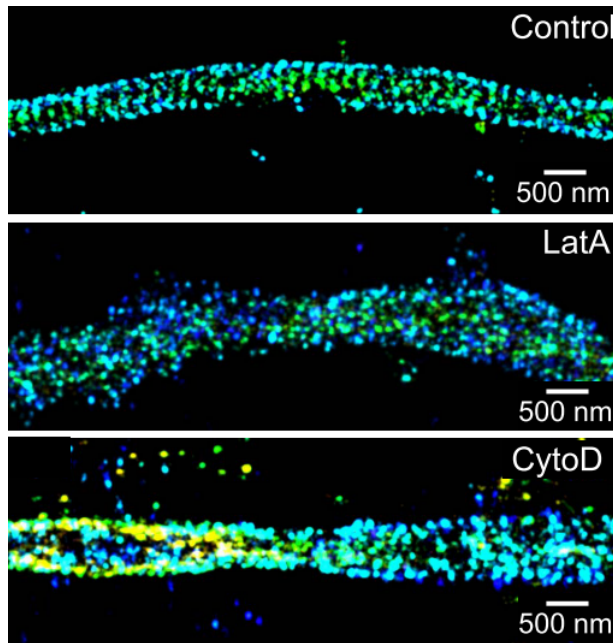


Figure 1.14: Actin Perturbations Destroy Spectrin Periodicity. *Effect of actin perturbations, LatA and CytoD, on β II spectrin periodicity shown for a hippocampal cell 3 DIV.* Image source: Zhong et al. (2014). Reprinted under Creative Commons Attribution License: <https://creativecommons.org/licenses/by/4.0/>

stabilising proteins. For example, adducin periodicity emerges from around 6 DIV (Zhong et al. (2014)), and the addition of this protein may help to stabilise the structure as it matures. Similarly, Qu et al. (2017) found that while periodic patterns of actin in *Drosophila* primary neurons were not significantly affected by LatA treatment at 10 DIV, however this treatment reduced the number of axon segments showing MPS to 48% of control levels when a prolonged treatment was carried out at 8 DIV.

Results show that periodicity is established in the proximal axon initially, extending throughout the distal axon as the cell matures (Zhong et al. (2014)). As shown in Figure 1.15, at 2 DIV there is strong periodicity in the proximal region, with much lower levels of organisation in middle to distal sections. At 6 DIV, all regions are showing clear periodicity, however the distal curve has lower autocorrelation amplitude on average than the proximal and mid-sections. This could represent the structure assembling from proximal to distal. Alternatively, there may be the appearance of isolated sections with short-range order which could travel towards the soma, perhaps through molecular motor activity, building long-range order in a proximal to distal manner.

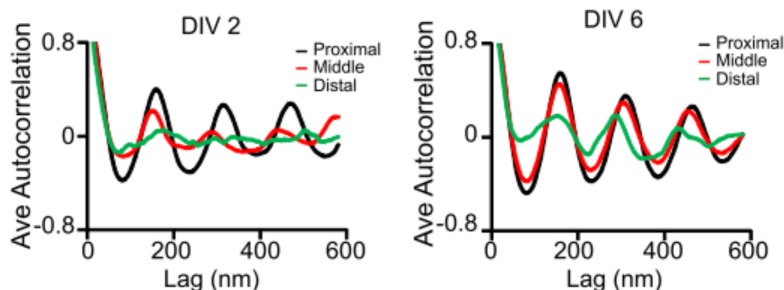


Figure 1.15: Periodicity in axon regions with growth stage. *The image on the left shows periodicity in 3 axonal regions at 2 DIV, as calculated by an autocorrelation function. The image on the right shows the same regions at 6 DIV.* Image source: Zhong et al. (2014). Reprinted under Creative Commons Attribution License: <https://creativecommons.org/licenses/by/4.0/>

1.5.5 The Final Axonal Pattern is Conserved

The MPS pattern is highly conserved in the axon, with a pattern of actin, spectrin, or related components exhibiting periodicity of between 180 and 200 nm (Xu et al. (2013), Lukinavičius et al. (2014), Zhong et al. (2014), D’Este et al. (2015), D’Este et al. (2016), Leite et al. (2016), Han et al. (2017), Qu et al. (2017), Krieg et al. (2017), Unsain et al. (2018a)). The periodicity was found to be outside of this range in the case of mouse retinal bipolar cells only, with a shorter periodicity of 169 nm for actin and β II spectrin (D’Este et al. (2016)). While MPS is not present in every axon, it is identifiable in the majority of axons imaged; Xu et al. (2013) found a periodic pattern in over 80% of axons in their sample, while D’Este et al. (2016) identified axonal MPS in 95.8% of cortical neurons, 88% of striatal neurons, 90.6% of rat cerebellar granule cells, and 77.5% of mouse retinal bipolar cells. Barabas et al. (2017) identified MPS in around 50% of image segments analysed, however these images were a mix of axons and dendrites.

We believe the rings to be discrete, unconnected rings, separated by spectrin, rather than helices. Xu et al. (2013) obtained 3D STORM images of β II spectrin staining, and as shown in Figure 1.16 (upper pane, inset) the axonal cross-section shows a clear ring-like shape.

Rings may change diameter over time (Leite et al. (2016)), however the mature MPS appears to be static, with no axial motion; Zhong et al. (2014) imaged β II spectrin fluorescence in live rat hippocampal cells for several minutes, finding no fluctuations in period or phase shift in time.

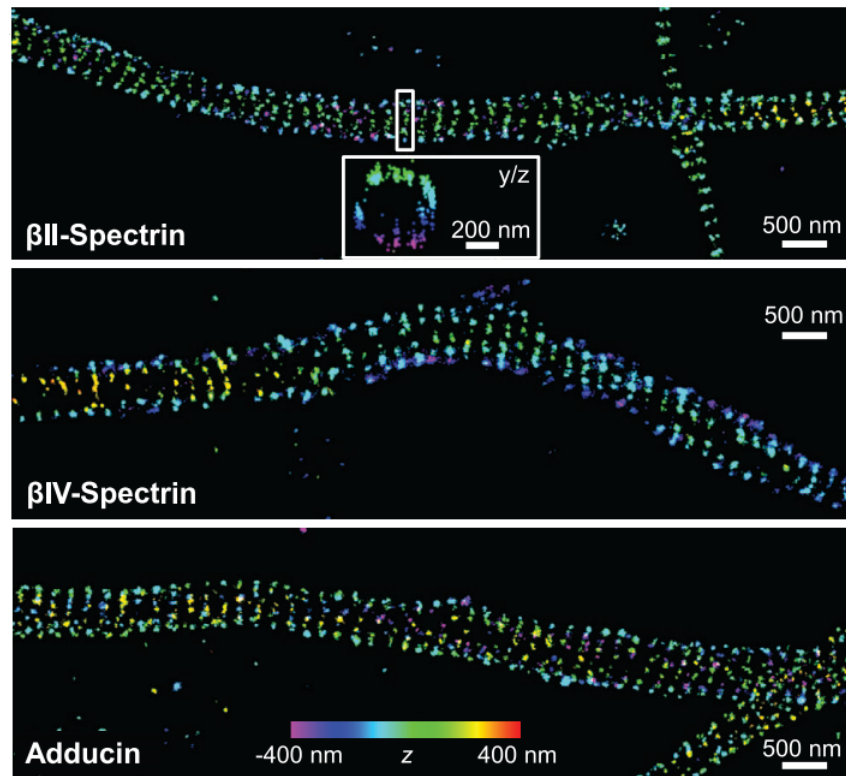


Figure 1.16: Spectrin and Adducin Periodic Patterns. *STORM images show periodic 1D ladderlike organisation of spectrin and adducin, with a cross-section showing a ring-like organisation of spectrin.* Image source: Xu et al. (2013). Reprinted with permission from AAAS.

1.5.6 Components Differ at the AIS and Nodes of Ranvier

Axons have an AIS - a specialised section proximal to the soma, and protein isoforms within this region may differ to those found in the more distal axon. AnkG is essential for AIS assembly; *in vivo*, AnkG is seen populating a region around 10 μm from the cell body in 1 day postnatal mice, proceeding to backfill this section towards the soma, with a dense 10 μm section of AnkG being present at the proximal axon by 5 days postnatal (Galiano et al. (2012)). In cultured hippocampal cells, AnkG appears some time after AnkB enrichment in the axon, however once AnkG is present, both AnkB and the βII spectrin isoform are excluded from the AIS region (Galiano et al. (2012)). This study found the length of the AIS could be extended by overexpression of AnkG, while overexpression of AnkB shortened the AIS. ShRNA silencing of AnkB or $\alpha\text{II}/\beta\text{II}$ spectrin seems to disrupt this polarisation, allowing AnkG to diffuse throughout the cell.

Periodic distribution of cytoskeletal components has been detected within the AIS as well as in the distal axon; in both cultured rat hippocampal cells, and in brain slices, Xu et al. (2013) found 194 nm periodicity of actin and spectrin, with the βIV isoform replacing βII in this region. Zhong et al. (2014) found that while AnkG and βIV spectrin levels are low initially, they become enhanced at the proximal axon from 8 DIV, showing periodicity at 12 DIV. Interestingly, βII spectrin was found to be periodic at the AIS region initially, however its periodicity and overall levels dropped as βIV isoform became periodic, indicating that this isoform is replacing βII on an existing lattice. shRNA knockdown of βII spectrin reduced enrichment of the βIV isoform and affected its periodicity, suggesting that βII is needed to establish the initial lattice. Zhong et al. (2014) observed that both βIV spectrin and AnkG showed periodicity for their N termini only, while the C termini were less regular and were thought to be hanging off the lattice. This was similarly observed by Vassilopoulos et al. (2019) who found AnkG C termini attaching to microtubules at the AIS.

In vivo, most cells are myelinated and possess Nodes of Ranvier denoted by gaps in the myelin coating. These specialist compartments are around 2 μm in length, spaced at 1-2 mm intervals throughout the distal axon, and are active in regeneration of action potentials through the triggering of voltage-gated ion channels (Kandel et al. (2000), Chapter 8). Nodes of Ranvier appear to assemble in a similar way to the AIS; the node itself contains ankG and βIV spectrin as well as sodium ion channels, and connects to extracellular matrix (ECM) through the neuronal cell adhesion protein, neurofascin (NF186), as shown in Figure 1.17. The node is flanked by paranodes; these areas are connected to glia by the glial form of neurofascin (NF155) and contain a cytoskeleton of αII and βII spectrin. Glia direct NF186 to the nodes, and both NF186 and paranodal βII spectrin are required to form the nodes, ensuring clustering of nodal components βIV spectrin and AnkG, to these areas (Amor et al. (2017)), while a further study showed that αII spectrin is also essential for node formation (Huang et al. (2017)).

Detection of periodic cytoskeletal organisation is challenging at nodes and

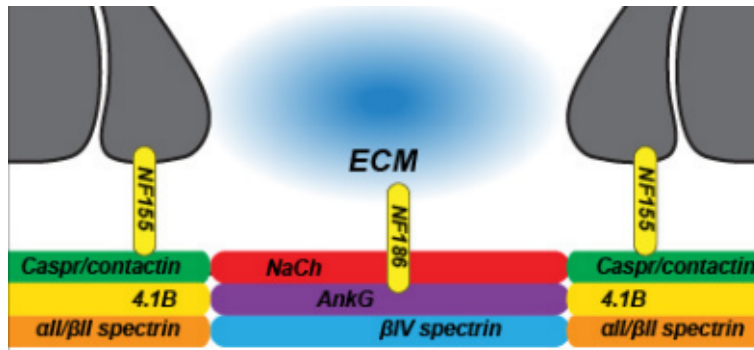


Figure 1.17: Nodal and Paranodal Cytoskeletal Components. *The Node of Ranvier is shown in the centre of the image, connected to extracellular matrix by cell adhesion molecules. The paranodes to either side have different components, and connect to glial cells.* Image source: Amor et al. (2017). Reprinted under Creative Commons Attribution License: <https://creativecommons.org/licenses/by/4.0/>

paranodes as the myelin sheath causes imaging aberrations, however at Nodes of Ranvier in sliced mouse sciatic nerves D'Este et al. (2015) detected β IV spectrin organisation at a regular spacing of around 180 nm. Figure 1.18 shows this organisation in a Node of Ranvier; Caspr is stained to highlight the paranodes which flank the node itself, while periodic green dots of spectrin are shown at the top and bottom of the axon slice, suggestive of rings encompassing the axon. Huang et al. (2017) found periodic organisations of α II and β IV spectrin at roughly 190 nm intervals throughout the nodes of mouse DRG cells. Mouse sciatic nerve slices were also shown to have periodic organisation of AnkG, which is likely to connect with spectrin as in the rest of the axon (D'Este et al. (2016)). At paranodal regions in mouse DRG cells, α II and β II spectrin were found to show the 190 nm periodicity (Huang et al. (2017)), with α II spectrin being essential for periodic organisation of both β II spectrin at paranodes, and β IV spectrin at the nodes themselves. It was not possible to detect organisation of actin due to its enrichment at nodes and paranodes (D'Este et al. (2016)), and fragility to fixation procedures (D'Este et al. (2015)).

1.5.7 Synaptic MPS is Less Regular and More Dynamic

While the MPS develops with high regularity early in development in the neuronal axon, its presence at synapses has not been so widely detected.

Pre-synaptically the MPS is largely absent, with a study finding the periodic pattern of β II spectrin to be disrupted at 70% of axonal synaptic boutons (He et al. (2016)). Sidenstein et al. (2016) also confirms the absence of β II spectrin at

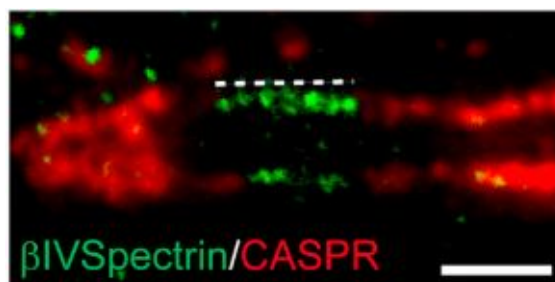


Figure 1.18: β IV Spectrin is Periodic at Nodes of Ranvier. *The image shows a slice lengthways through the axon, showing regular spacing of spectrin tetramer centres across the nodal region. Scale bar shows 1 μ m. Image source: D’Este et al. (2015). Reprinted with permission from Elsevier.*

pre-synaptic sites, while an earlier study by Pielage et al. (2008) found ankyrin disruption at synaptic boutons in *Drosophila* motor neurons.

Post-synaptically, in dendrites and their spines, many studies have detected some level of periodic organisation, however results between studies are highly variable. Studies labelling the β II spectrin isoform showed limited success in dendrites; Xu et al. (2013) did not detect any periodicity of this isoform, while in other studies, both β II (Zhong et al. (2014), He et al. (2016)), and β III (Zhong et al. (2014)) spectrin isoforms were found in small fraction of dendrite images analysed, mainly being present at later developmental stages, and as short, isolated sections, with little long-range order. A study on hippocampal cells at 17-30 DIV was more successful, detecting periodic β II spectrin in all dendrites in the sample (Sidenstein et al. (2016)). Actin labelling appears to be more successful in these regions; Xu et al. (2013) did not detect periodic rings of actin in dendrites, instead observing organisation of phalloidin-stained actin into longitudinal bundles, however in live rat hippocampal cells labelled with SiR-Actin, D’Este et al. (2015) detected periodic actin organisation in 21 of 90 cells imaged at different stages from 5-17 DIV, although imaging was obscured at 16 DIV as actin became enriched at dendritic spines. Bär et al. (2016) also found actin periodicity in each of 18 dendrite images, with 190 nm spacing on average. Lavoie-Cardinal et al. (2020) found that while actin showed rings in dendritic shafts, β II spectrin appeared mostly disorganised, suggesting that other isoforms may connect actin rings in these regions. Finally, a large-scale quantitative study analysed 400 STORM images of 3 μ m dendritic segments taken from 28 DIV cultured mouse hippocampal cells (Han et al. (2017)). In this study, periodic organisation of actin, adducin, and both β II and β III spectrin were identified. 50-60% of dendritic images in their sample were classified as displaying MPS, compared to 95% of axonal images, with an average autocorrelation amplitude for dendrites being 40% that of axons. This shows that MPS is less common in dendrites, with a lower level of long-range organisation, however analysis

of image segments from individual dendrites showed over 80% had at least 1 periodic section, with continuous periodic stretches reaching up to 30 μm . While both βII and βIII spectrin showed the same degree of periodicity, KD of βII spectrin causes disruption of the MPS, indicating that this isoform is required for assembly, despite the presence and incorporation of other isoforms.

As well as in the shaft of the dendrite, MPS is also present in the spines with which synapses are formed, particularly in the neck regions. He et al. (2016) noted βII spectrin periodicity in over 25% of dendritic spine necks in a sample of 18 DIV hippocampal neurons, while Bär et al. (2016) found periodic actin in every spine neck from a sample of 60 dendritic spines at 21 DIV, with average spacing of 186 nm. Only 50% of spines in this sample showed periodicity for βII spectrin. Sidenstein et al. (2016) found periodic βII spectrin in only the thicker spine necks, and this organisation was disrupted at the post-synaptic densities beyond the neck region.

Levels of MPS within dendrites have been found to differ with developmental stage. Han et al. (2017) carried out a large scale imaging analysis on hippocampal cells from 7 to 50 DIV. At 7 DIV, over 80% of axons displayed MPS, compared to around 10% for dendrites. The prevalence of MPS rose over time in both axons and dendrites, however the levels in dendrites plateau at just over 50%, showing little change from 28 DIV onwards, despite almost all axons having MPS at these time points. Dendritic MPS has also been found to depend on activity level in the neuron; a study by Lavoie-Cardinal et al. (2020) found actin rings were present in dendrites when synaptic activity was low, however these rings were dismantled and longitudinal fibres were seen at higher activity levels, suggesting the MPS may be more dynamic in dendrites, which could account for some of the differences between studies. As dendrites tend to have larger diameters than axons, the lower levels of MPS in dendrites could indicate that the MPS is diameter-dependent, forming only in narrow processes, however Han et al. (2017) found no dependence on diameter with autocorrelation amplitude of spectrin or adducin in their sample of hippocampal neurons with average axonal and dendritic diameters of 0.52 and 1.1 μm respectively.

In a subset of dendrites, Han et al. (2017) detected a 2D polygonal lattice, similar to that found in erythrocytes. The distance between adjacent nodes in this lattice was roughly 190 nm, matching the distances found between actin rings, and close to the 200 nm contour length of spectrin. This is significantly longer than the 55-65nm distances found in erythrocytes (Brown et al. (2015)). Roughly 10% of dendrites without detectable MPS possessed a 2D polygonal lattice organisation.

1.5.8 The Soma contains a 2D Lattice

While the pattern of periodic rings is common throughout axons, and to a lesser extent dendrites, cytoskeletal organisation of the soma resembles the polygonal lattice found in erythrocytes. Erythrocytes exhibit a characteristic biconcave shape which is believed to enhance gas and ion exchange functions by maximis-

ing surface area (Smith et al. (2018), references within), while assisting in flow by minimising rotation (Uzoigwe (2006)). The erythrocyte possesses a polygonal cytoskeletal lattice composed of short actin filaments, connected by spectrin tetramers which occupy lengthscales of 55-65 nm (Brown et al. (2015)). The lattice influences erythrocyte shape through interactions with myosin; myosin appears to be required to maintain biconcavity, with myosin inhibition relaxing membrane tension, resulting in an alteration in shape to one of reduced biconcavity and increased elongation (Smith et al. (2018)).

A study by Han et al. (2017) used STORM to image mouse neurons at 28 DIV, using a Voronoi tessellation algorithm to estimate that 40% of somatic regions imaged were covered by a polygonal lattice, however nodes were further apart, occurring at intervals of approximately 190 nm as shown in Figure 1.19. This indicates that the spectrin tetramers which form the edges of this network are in expanded configurations relative to those found in erythrocytes. This polygonal lattice was also observed on the somatic regions of rat hippocampal cells (Lavoie-Cardinal et al. (2020)).

Strikingly, while a 2D polygonal lattice was more common at the soma, Han et al. (2017) observed some small, isolated patches of a 1D, ladderlike arrangement, with stripes of alternating adducin and β III spectrin fluorescence echoing the MPS pattern on a relatively flat membrane.

1.5.9 MPS May Appear in Stem Cells and Glia

A recent study discovered the presence of MPS-like organisation in undifferentiated neural stem cells. Hauser et al. (2018) found these cells exhibited μm scale periodic strips of actin occurring at 180-190 nm intervals within their cell bodies and processes extending from them. Imaging of adducin and the β II spectrin C terminal (central to the tetramer) revealed alternating patterns, confirming that these structures have composition equivalent to axonal MPS. As these neural stem cells differentiated into either neurons or glia, the level of long-range order of these patches increased; strips of 1D ladderlike arrangements of β II spectrin could be seen at various orientations, joining up as the cell developed to form strips with order reaching up to 4 μm .

Results observing MPS arrangements in glia give conflicting results; He et al. (2016) imaged 4 types of glial cells (astrocytes, Schwann cells, microglia, and NG2 cells), finding some patches of periodic spectrin with short-range order in a small proportion of glia imaged. D'Este et al. (2016) did not detect periodic actin or spectrin arrangements in microglia or astrocytes, however Hauser et al. (2018) observed periodic actin and spectrin in multiple astrocyte processes, both in cells derived from neural stem cells, and in primary astrocytes obtained from hippocampal tissue. In live 5 DIV differentiating oligodendrocytes, D'Este et al. (2016) observed some short-range 190 nm periodicity of actin, confirming periodic patterns of both actin and β II spectrin in cells fixed at 6 DIV. Hauser et al. (2018) found 180 nm alternating adducin and β II spectrin in mature oligodendrocytes, in some cases spanning the processes of over 1 μm in width

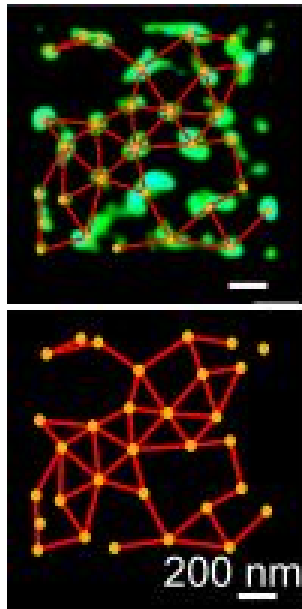
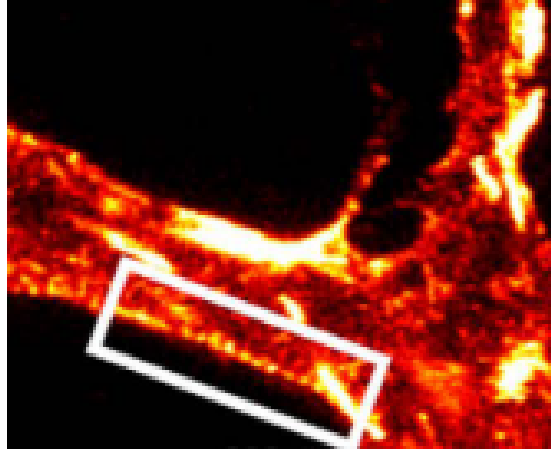
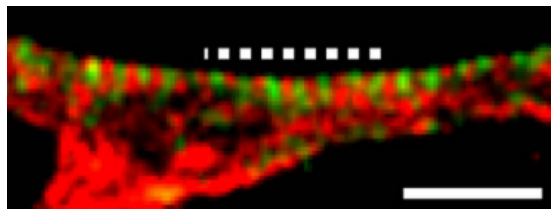


Figure 1.19: Somatic β III Spectrin Lattice. *The image shows organisation of β III spectrin on the neuronal soma captured by STORM imaging, with spectrin terminals marked by green fluorescence. A lattice generated using Voronoi tessellation shows the expected structure, with actin filament positions approximated by the nodes of the network as shown in yellow, and spectrin tetramer locations illustrated by the red network edges. Scale bar shows 200 nm. Image source: Han et al. (2017). Reprinted with permission from National Academy of Sciences.*



(a) Actin stained with SiR-Actin and imaged in a live cell at 5 DIV.



(b) Phalloidin-stained actin (red) and β II spectrin (green) imaged in a fixed cell at 6 DIV. Scale bar 1 μ m.

Figure 1.20: Periodic distributions of actin and spectrin in differentiating mouse oligodendrocytes. *These STED images show the presence of MPS features in glial cells with fine processes.* Image source: D'Este et al. (2016). Reprinted under Creative Commons License: <https://creativecommons.org/licenses/by/4.0/>

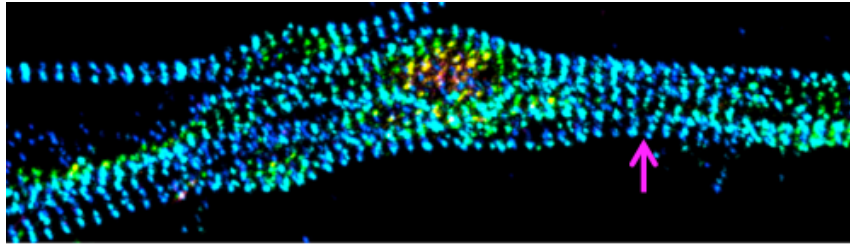


Figure 1.21: Axon-Axon Contact. *This image shows 2 axons making contact, with β II spectrin labelled. The colouring indicates the depth, with green closest, cyan in middle distance, and dark blue at the deepest point in the plane. We can see regions of agreement where spectrin strips make contact, while the magenta arrow marks a region where rings are tilted in order to maintain contact.* Image source: Hauser et al. (2018). Reprinted under Creative Commons Attribution License: <https://creativecommons.org/licenses/by/4.0/>

extending from these cells, suggestive of ring formation encompassing these wide processes.

In both axons and glia, MPS appears to be particularly enhanced at regions of cell-cell contact; Hauser et al. (2018) found that spatial correlation was high when comparing MPS localisation between axons which contact other axons, or glia, although axon-glia contacts showing lower correlation amplitude. Figure 1.21 shows high levels of alignment of spectrin tetramers between 2 contacting axons, with the magenta arrow showing some local tilting of rings in order to maintain alignment between cells. The cell adhesion molecules, Neurofascin and L1CAM, were shown to have some short-range periodicity as discussed previously, with possible involvement of other cell-adhesion molecules.

1.6 How Does the Structure Self-Assemble?

In Sections 1.3 - 1.5, we introduced the highly ordered cytoskeletal arrangement found mainly in the axons of neurons known as the MPS, reviewing evidence on its composition and structure, its purpose, and how the structure develops over time. While research has given great insight into these aspects of the MPS, the underlying factors which drive its self-assembly remain poorly understood.

Neurodegenerative disease processes and injuries to the nervous system are irreversible (Kandel et al. (2000), Chapter 55) and progressive (Adalbert and Coleman (2013)). In Section 1.4.6, we discussed evidence that the MPS is not only affected by these processes, but appears to control signalling processes which cause this downward spiral of degeneration (Unsain et al. (2018a), Wang et al. (2019)). An understanding of the factors and conditions which cause the MPS to assemble in developing cells could provide critical information on

the reasons for the limited regenerative capacity of neuronal cells, potentially inspiring treatments to prevent, stall, or even reverse degenerative processes affecting the nervous system.

In Section 1.6.1 we summarise key MPS features that may be relevant to self-assembly processes followed by a short review of self-assembly in similar biological contexts in Section 1.6.2. Finally, in Section 1.6.4, we discuss open questions relating to MPS self-assembly which we aim to investigate in this research and in future studies.

1.6.1 Evidence of MPS Self-Assembly

The following briefly summarises several key features of the MPS as described in Sections 1.3 - 1.5 which may give some insight into the conditions necessary for MPS self-assembly:

- **Geometric Factors** - The pattern is most common in narrow protrusions such as axons, but this is not exclusive; Han et al. (2017) and Hauser et al. (2018) observed 1D ladder-like patterns exhibited in small regions of soma where the membrane has little curvature, while D’Este et al. (2016) detected MPS in relatively wide glial processes. Han et al. (2017) found no correlation between the width of the axon or dendrite, and the level of MPS present. These results suggest that a tubular geometry is not essential (although on flatter surfaces the MPS pattern exists as a series of periodic stripes rather than rings). It could be that the pattern favours tubular environments, but is influenced by further factors which enable assembly in regions of minimal curvature.
- **Spectrin Tetramer Presence** - Spectrin is essential and its disruption destroys the periodic pattern (Zhong et al. (2014), Qu et al. (2017), Lorenzo et al. (2019)). Disruption of the β monomer appears to have a greater destructive impact (Qu et al. (2017)), which could be explained by the presence of an ankyrin binding domain on this monomer which enables membrane linking (see Rasband (2010) for a review). Interestingly, Krieg et al. (2017) noted that a missense allele - a genetic mutation preventing tetramer formation - does not prevent periodic organisation of α spectrin, though the periodicity reduces from 197 to 188 nm. The α monomer has also been found to be essential in organising β II and β IV isoforms at paranodes and Nodes of Ranvier respectively, as well as being required for the Nodes themselves to form (Huang et al. (2017)). It also appears to provide a scaffold at the AIS, allowing isoforms of β monomer to be exchanged on an existing lattice (Zhong et al. (2014)). As the lattice is disrupted when β monomers are depleted, but is present when monomers are present at normal concentrations but are unable to form tetramers, it is possible that spectrin can still organise to some degree in its monomeric or dimeric form. This may be achieved through a tendency to form parallel bundles,

as noted by Hauser et al. (2018), with bundle formation possibly being more likely on membranes with high curvature.

- **Extracellular Signalling** - Hauser et al. (2018) showed that regions of MPS align in contacting cells. This suggests that patterning could be directed from an extracellular source, possibly with influence from trans-membrane proteins. While plausible that an existing periodic organisation could be transmitted between cells in close contact with one another this does not explain how the initial cell would develop the pattern.
- **Microtubule Connections** - Actin rings and microtubule arrays are understood to be connected, with actin or microtubule stabilisation both leading to more robust appearance of rings (Dubey et al. (2020)), and disruption of either component leading to destruction of the MPS (Zhong et al. (2014), Qu et al. (2017)). Stabilising microtubules can lead to multiple axons (Witte et al. (2008)), each exhibiting an MPS pattern (Zhong et al. (2014)). An exciting recent study by Glomb et al. (2022) could potentially shed light on this dependency; α spectrin hotspots of $\sim 0.5 \mu\text{m}$ in width and spaced at intervals of $\sim 1.1 \mu\text{m}$ were observed in *C. elegans* motor neurons. These hotspots were found to supply newly synthesised spectrin, which was incorporated into the MPS at these locations, with sites becoming wider and further apart during rapid growth of integrated axons. A complex of proteins connecting spectrin to kinesin molecular motors was detected, implicating microtubule-based transport in the delivery of spectrin to sites of MPS construction. It's likely that such hotspots could provide an explanation for the mysterious βII spectrin peak detected at $1.71 \mu\text{m}$ intervals by Costa et al. (2020) alongside the expected 190 nm periodicity. Similar hotspots of actin have been identified at $3\text{-}4 \mu\text{m}$ intervals along the axon (see Papandréou and Leterrier (2018) for a review), and it would be illuminating to determine whether actin synthesised by these sites is incorporated into the MPS.

1.6.2 Self-Assembly of Similar Structures

While the MPS is currently understood to be unique to neurons, rings of actin are present in other biological contexts, in some cases exhibiting periodic arrangements. We briefly review examples of ring formation and discuss whether similar mechanisms of self-assembly could be applicable to the MPS.

The Cytokinetic Ring

The majority of eukaryotic cells divide through the action of a contractile actomyosin based cytokinetic ring. This ring is located at the site of division, which is generally the cell equator, but may be elsewhere such as the mother-bud neck in the case of the budding yeast, *Saccharomyces cerevisiae* (Faty et al. (2002)). The components of the cytokinetic ring are well studied; in fission

yeast, *Schizosaccharomyces pombe*, Pelham and Chang (2002) found that ring formation required a supply of both formins and profilin at the site of ring formation. Vavylonis et al. (2008) observed the ring originating from a broad band of nodes which decorate the membrane at the cell equator. Formins and myosin motor proteins were recruited to these nodes, with myosin forming transient connections between pairs of actin filaments polymerising from nearby nodes. Over time these attractive connections draw nodes together into a single, aligned ring, as replicated in Monte Carlo simulations. The formation of actin bundles is required for rings assembly (Vavylonis et al. (2008)), and a balanced degree of actin cross-linking was found to be essential to prevent ring collapse under myosin contraction (Laporte et al. (2012)).

While the cytokinetic ring assembly arises from proteins recruited to the division site, this site must first be determined, and mechanisms for establishing this site are diverse. In animal cells and *Drosophila*, microtubule mitotic spindles set the position; Gregory et al. (2008) found evidence in *Drosophila* of a relationship between RacGAP, a protein which associates with microtubules of the mitotic spindle, and Anillin, a protein which locates at the cell cortex and recruits components to the cytokinetic ring. In *S. pombe* the ring site is independent of spindles, instead being linked to position of the nucleus; the protein Mid1 was found to migrate between the nucleus and cell cortex where it recruits actin and other ring components (Paoletti and Chang (2000)). In budding yeast, GTPase proteins known as septins are involved in creating a scaffold at the budding site with which other proteins can interact (Faty et al. (2002)). Septins are able to self-assemble into a range of structures including rings (see Mostowy and Cossart (2012) for a review), and are abundant in neurons (Faty et al. (2002)), but have not yet been implicated in assembly of the MPS.

While the results discussed here show a requirement of appropriately placed scaffolding proteins in assembly of the cytokinetic ring, *in vitro* experiments using spherical droplets contained within a phospholipid monolayer and suspended in oil found that when actin is polymerised within the cell alongside a buffer containing methylcellulose (which aids bundle formation by boosting attractive interactions between actin filaments), a ring is formed around the cell equator without a requirement for scaffolding proteins. The ring stemmed from a single filament or small bundle, occurring in cases where the radius of the droplet was equal to or less than the persistence length of actin (Miyazaki et al. (2015)).

Periodic Rings in Epithelial Cells

Epithelial cells develop rings of actin during wound healing and apical cell extrusion processes (see Schwayer et al. (2016) for a review). In addition to these single rings, periodic rings of actin have also been observed in populations of epithelial cells where they provide a submembranous framework, creating a series of invaginations in the membrane which shape the cuticular tissue that lines these cells at later stages of development (Leite and Sousa (2016)). In *C. elegans* hypodermal cells which form the surface epithelial layer, Costa et al. (1997) detected actin filament bundles organised circumferentially around the embryo,

occurring at regular spacings of between 0.36-0.69 μm , coincident with the furrows on the cuticle. Similarly, epithelial tracheal tubes in *Drosophila* exhibit periodic rings which form across multiple cells, with around 15-20 rings per cell, spaced at around 0.5 μm (Hannezo et al. (2015)). Hannezo et al. (2015) was able to reproduce periodic ring formation using a hydrodynamic model of an active, contractile actomyosin gel in contact with a rigid substrate representing the extracellular matrix. Myosin contractility-induced flows caused a transition from a uniform actomyosin cortex to a series of 2D periodic stripes. This pattern required high contractility and low turnover time of actin, and was friction dependent, with anisotropy of friction aiding pattern formation, and increased magnitude of friction decreasing ring spacing.

These studies give compelling evidence of the formation of periodic rings in biological contexts, however there are several distinctions between the rings of epithelial cells and those within the MPS; spectrin, which is a necessary component of the MPS and likely to determine ring spacing, does not feature in the periodic rings in epithelial cells (though spectrin spaced periodically at 190-200 nm has recently been detected in *C. elegans* epithelial stem cells (Jia et al. (2019))). Additionally, the extracellular matrix connections and myosin contractility which is essential for pattern formation in the model by Hannezo et al. (2015) are not essential for formation of the MPS pattern (Leite and Sousa (2016)), while timelapse imaging showed tracheal actin rings to be dynamic (Hannezo et al. (2015)), and therefore distinct from the static rings of the MPS (Zhong et al. (2014)).

IQGAP Actin Rings

The recent results of Vassilopoulos et al. (2019) suggest that the MPS is composed of long actin filaments, raising questions as to how these filaments could adopt tightly curved configurations. An exciting new study may give insight into how this could be achieved; Palani et al. (2020) found that the protein, Rng2, decorates the cell membrane in *S. pombe*, and is able to bend actin filaments well below their persistence length through the action of a region known as 'curly', consisting of an actin binding domain and an unstructured domain, leading to a range of rings and spirals. The protein, which has a human homolog of IQGAP1, requires mobility on the plane of the membrane, and is facilitated by interactions with tropomyosin and myosin. It is believed to reduce actin stiffness, allowing it to bend without damaging the filament structure.

IQGAP1 is known to be expressed in dendritic spines, where it links to microtubules through CLIP-170, a protein which binds to microtubule plus ends (see Gordon-Weeks and Fournier (2014) for a review). While not required for assembly of the cytokinetic ring (Pelham and Chang (2002)), we await results to show whether IQGAP proteins are involved in MPS assembly.

1.6.3 Modelling the Cytoskeleton

Cytoskeletal modelling is a thriving and highly active field, encompassing a wide range of theoretical and computational techniques applied at various temporal and spatial scales. A full review of this topic is beyond the scope of the Chapter, and so we focus instead on giving a brief introduction, summarising common techniques and giving examples of their application. We begin at the scale of individual cytoskeletal component proteins, moving on to coarse-grained representations of biopolymer networks, and arriving at the larger-scale continuum models. Finally we turn our attention to models specific to the MPS structure.

Molecular Models

Modelling of individual component proteins or small aggregates can give microstructural information on cytoskeletal properties. Molecular dynamics (MD), a simulation method based on Newton's Equations of Motion, is frequently used to simulate components at the angstrom scale, with femtosecond resolution (Yamaoka et al. (2012)).

Studies utilising MD have investigated conformation changes of individual actin monomers due to nucleotide binding, while a variant on MD, steered molecular dynamics, has been employed to determine the force required to release bound phosphate from ATP-bound actin monomers. At the larger scale, MD has been applied at the filament level to determine tensile and torsional stiffness (Yamaoka et al. (2012), references within). MD has similarly been applied to individual tubulin monomers which are the building blocks of microtubules, with Zeiger and Layton (2008) using this method to determine axial and circumferential elastic moduli of these subunits.

MD can similarly give insight into the properties of spectrin; through MD simulations Mehboob et al. (2010) highlighted the importance of the spectrin tetramerisation domain in the flexibility and conformation of the junction region. Force-extension behaviour of single spectrin repeat units has been demonstrated using MD variants, illustrating the force-buffering effect as helices unwind under tension (Takahashi et al. (2018), Paramore et al. (2006)).

Coarse-Grained Molecular Models

A larger scale can be modelled through coarse-graining in which structural details and interactions are simplified; a single molecule or group of molecules is represented as a bead. Beads can be connected to represent polymeric proteins, and a range of potentials can be employed to approximate interactions (Gartner and Jayaraman (2019)). Simulation techniques for coarse-grained models include MD or Brownian Dynamics (BD) - a technique in which solvent is modelled implicitly as a random friction and the Langevin Equation is solved (Yamaoka et al. (2012)).

BD has been applied to actin in many studies, investigating polymerisation, depolymerisation, and severing, and thermal fluctuations of single actin fila-

ments (Yamaoka et al. (2012), references within). Kim et al. (2009) used BD to investigate properties of cross-linked polymerising actin networks, observing transitions from a homogeneous gel-like network to a bundled network akin to stress fibres, dependent on model parameters. Letort et al. (2015) adopted the BD-based cytoskeletal simulation package, Cytosim (Nedelec and Foethke (2007)) to model organisation of polymerising actin networks under geometrical constraints, observing a wide range of actin structures emerging under varying levels of confinement.

Coarse-grained MD has been utilised to explore force-extension behaviour of a spectrin tetramer model (Mirijanian and Voth (2008)), while Li et al. (2005) used this technique to model the spectrin-based erythrocyte membrane skeleton, reproducing conformational changes observed experimentally.

Coarse-graining has also proved useful in microtubule-based studies; Lazarus et al. (2015) demonstrated a protective role for the microtubule-associated tau protein when applying stretch and torsion to microtubule bundles, while Ahmadzadeh et al. (2015) identified how loading rate and microtubule length affects stress-resistance in microtubule bundles, with relevance to traumatic brain injury.

These models provide a useful bridge between the microscopic and continuum properties of cytoskeletal networks, and is suitable for studying events that occur on relatively large time and spatial scales, such as polymerisation.

Continuum Models

Continuum models are useful for exploring cell-scale phenomena related to the cytoskeleton. These methods are commonly applied to the acto-myosin cortex which lies beneath the plasma membrane, modelling the network of crosslinked actin filaments as a linear elastic, fluid, or viscoelastic material, or using poro-elastic solid or soft glassy material models. Finite element techniques can be employed to model properties such as mechanical behaviour of migrating or adherent cells, or the coupling of the cytoskeleton to the membrane (see Banerjee and Park (2015) for a review).

The acto-myosin cortex is a non-equilibrium system due to the presence of chemical processes which contribute to force generation via molecular motors or dynamic filament behaviour. Active gel theory is an emerging field in which the cortex and other actin structures can be modelled as a viscoelastic material of polar filaments, with motion described by modified hydrodynamic equations, where an active term representing these non-equilibrium processes is included (see Prost et al. (2015) for a review). This method can capture behaviour such as spontaneous cortical flows and wave propagation (see Jülicher et al. (2007) for a review), and can account for cell motility (Whitfield and Hawkins (2016)). The active gel model is able to reproduce and explain patterns of self-organisation observed in vivo; Hannezo et al. (2015) used the model to investigate patterning of acto-myosin when in frictional contact with a surface, observing periodic ring formation occurring as a result of a hydrodynamic instability, matching the self-organisation observed in the epithelial cells of *Drosophila* tracheal tubules.

Elastic continuum models can similarly be adapted through the introduction of an active stress term, with the model being able to reproduce cell shapes and deformations through modulation of active tensions and moments (Berthoumieux et al. (2014)).

Modelling of the MPS

Modelling of the MPS is a relatively unexplored area however a small number of studies have focused on this structure. A coarse-grained MD method was applied by Zhang et al. (2017) to explore mechanical properties of a model MPS, with bead-spring representation of actin filaments, spectrin tetramers, and the membrane-binding protein, ankyrin. By combining simulation with experimental results, the study was able to estimate the degree to which actin rings and spectrin tetramers contribute to the overall stiffness of the neuronal axon, matching the combined effect with results obtained through atomic force microscopy (AFM). Zhang et al. (2019) used coarse-grained MD to explore the effect of the model MPS on diffusion of transmembrane and monotopic proteins, observing an anisotropic diffusion barrier effect as actin rings provide a 'fence' which reduces longitudinal transport on the membrane. Dubey et al. (2020) used a theoretical model, representing spectrin tetramers as worm-like chains - strain-stiffening polymers, and finding a viscoelastic response to stretching due to domain unfolding in the spectrin repeat units.

1.6.4 Open Questions on MPS Assembly

The conditions required for MPS self-assembly are poorly understood; as the structure appears most common in thin protrusions such as axons, it has been suggested that the components may naturally adopt this configuration when contained within a tubular geometry (Qu et al. (2017)), and to our knowledge this has not yet been investigated.

The method by which actin filaments form the rings of the MPS appears distinct from assembly of rings in dividing or epithelial cells as discussed in Section 1.6.2. Polymerisation of actin within the tubular geometry may influence its arrangement, causing it to curve around the membrane surface as found in spherical cells (Miyazaki et al. (2015)). Alternatively, actin nucleators and other scaffolding proteins may be placed on the membrane as in the contractile ring (Pelham and Chang (2002)), perhaps as a result of external signalling such as that generated by cell-cell contact (Hauser et al. (2018)). IQGAP proteins may also be present on the cell membrane, shaping actin into rings (Palani et al. (2020)). A range of proteins have roles in altering the structure and properties of actin, such as stiffness (Isambert et al. (1995), McCullough et al. (2008)), or polymerisation rate (Siegel and Branton (1985), Chen et al. (2020)), with several proteins which modify actin filament properties being detected within the MPS (Zhou et al. (2020)). Could actin modifications be required for MPS assembly?

In addition to the self-assembly of individual rings, the means by which they form larger scale periodic structures is similarly perplexing, and while the periodicity of actin rings is linked to the contour length of spectrin, it is not clear precisely how the arrangement forms. It is currently unknown whether spectrin connects existing rings, assembled independently, or if ring assembly is spectrin-dependent. Studies have indicated a propagation of periodicity from proximal to distal in developing axons (Zhong et al. (2014)). This may indicate an assembly process beginning at the cell body, or the collaging together of smaller regions of local periodicity as observed in differentiating neural stem cells (Hauser et al. (2018)). Spectrin hotspots found during rapid growth phases (Glomb et al. (2022)) may also be present in early development, supplying spectrin for MPS assembly at a number of sites which may aggregate to give long range order.

While much progress has been made in unravelling the mysteries of the cytoskeleton, and in investigating key properties on the MPS, as briefly described in Section 1.6.3, to our knowledge the self-assembly of the MPS has not yet been studied computationally, leaving a clear gap in the literature.

Chapter 2

MPS Self-Assembly: Minimal Model

2.1 Introduction

In Chapter 1 we introduced the MPS cytoskeletal structure found mainly within neuronal axons, highlighting its key features and properties, and discussing the roles that it plays within the cell. As explained in Section 1.6.4, the mode of assembly of this highly organised structure is currently unknown, however one theory is that the system of filaments and proteins which form the MPS may spontaneously assemble into such a configuration based on their interactions with the tubular morphology of the axon in which they are contained (Qu et al. (2017)). The following evidence may offer some support to this hypothesis:

1. While MPS-like sections are able to form to a lesser degree in several regions of neurons or glia (Han et al. (2017), Hauser et al. (2018), D'Este et al. (2016)), the pattern is most common and robust within the narrow, tubular neuronal axons (Xu et al. (2013), D'Este et al. (2016)), with components tending to adopt hexagonal configurations similar to those observed in erythrocytes in regions of lower membrane curvature such as the soma (Han et al. (2017)). This is suggestive of a favourable influence of the specific axonal morphology on assembly of the MPS pattern.
2. Axon specification occurs prior to the formation of the MPS (Zhong et al. (2014)). Additionally, axon specification and growth proceeds in the absence of the essential MPS component, spectrin (Hammarlund et al. (2007)). While the MPS is understood to influence shape and size of the axon as described in Section 1.4.1, these results demonstrate that MPS assembly occurs within a pre-existing tubular environment.

3. When polymerised within a spherical cell, actin has been found to spontaneously form rings, which are contractile in the presence of myosin (Miyazaki et al. (2015)). This suggests an ability of actin to conform to the environment in which it is polymerised - a result which may also apply to assembly of larger structures through crosslinking of short actin filaments.

In this Chapter, we create a highly simplified *in silico* model, exploring the configurations adopted by actin filaments and spectrin tetramers when contained within a narrow cylindrical cell. Our model incorporates crosslinking between actin filaments, and connections between actin and spectrin, as well as the introduction of a microtubule array. We use a random walk method to simulate stochastic motion of actin filaments and spectrin tetramers within the bounds of the cylindrical cell, adopting Monte Carlo techniques to sample example configurations from large numbers of simulations.

Section 2.2 describes the model which we use to represent the axon and MPS components, Section 2.3 details the numerical techniques used to simulate this model system, and Section 2.4 contains information on the methods used to analyse our results. We begin our investigations in Section 2.5 by simulating a number of short, non-interacting actin filaments within a cylindrical space representing an axonal segment, increasing the level of confinement by introducing a microtubule array which occupies the central core of the cylinder in Section 2.6. In Section 2.7, we continue to explore the highly confined environment of Section 2.6, while introducing crosslinking interactions between actin filaments, allowing larger scale actin structures to assemble. Section 2.8 extends the results of Section 2.7 by introducing spectrin tetramers which are able to link actin filaments. Finally we discuss the results of this Chapter in Section 2.9.

2.2 Description of Physical Model

In order to test whether MPS components are able to spontaneously assemble into an organised structure within an axon-like environment we created a model of an axonal segment, introducing actin filaments and spectrin tetramers as rigid rod-like particles. Here we describe the model used to represent this simplified system, detailing the axonal environment, the methods by which actin and spectrin were represented, the coordinate system and boundary conditions used, and the details of interactions between particles in the system.

2.2.1 Axon-Like Geometry

The axon was modelled as a 3 dimensional cylinder with dimensions chosen to provide suitable confinement effects while minimising computation time. The radius was chosen to be $R_{\text{axon}} = 0.2 \mu\text{m}$ which is within the accepted range of radii for neurons of $0.1 - 10 \mu\text{m}$ and corresponds approximately to the $0.41 \mu\text{m}$ mean diameter of rod neurons found in the eye Perge et al. (2012). A short

length of $L_{\text{axon}} = 2 \mu\text{m}$ was used. Axons typically range in length from 0.1 mm up to 3 m (Kandel et al. (2000), Chapter 2), with an axon initial segment (AIS) occupying between 20 – 60 μm (Letierrier et al. (2017)). The model therefore represents 1/40th of the length of an axon, assuming the minimum axon and AIS lengthscales. This length is however, sufficient to allow up to 10 actin rings to form at the observed 180-200 nm spacing, and corresponds to a typical segment length used for imaging of actin rings (Leite et al. (2016)). In addition, the level of radial confinement far exceeds that of axial confinement, and with these considerations in mind this axon length was deemed adequate for the model.

In some cases a microtubule array was included in the model. In an array, microtubules of 25 nm outer diameter assemble hexagonally with a centre to centre spacing of 45 nm (Shahinnejad et al. (2013), Soheilypour et al. (2015)). There are between 10 and 100 microtubules in the array (Shahinnejad et al. (2013)). We assume an array of 37 microtubules, in the region of the ~ 35 microtubules typically found within a rod neuron (Perge et al. (2012)). We model the microtubule array in a simplified form, approximating the hexagonal array as a cylinder by drawing a curve through the outermost microtubule centres as shown in Figure 2.1. The radius of the cylinder is $R_{\text{mt}} = 135$ nm based on an array of microtubules with the dimensions and spacing given above.

2.2.2 Actin Rods

Note - the results in this Chapter were carried out prior to the study by Vasilopoulos et al. (2019) which detected long, intertwined pairs of actin filaments in MPS rings. We therefore represented actin as short filaments with properties as suggested by the experimental results available at the time of creating the model.

Actin filaments were modelled as inflexible cylindrical rods with hemispherical ends. The rods were assigned a fixed radius of $r_{\text{actin}} = 4$ nm, giving an 8 nm diameter within the 5-9 nm range (Alberts et al. (2002), Chapter 4), and a length of $l_{\text{actin}} = 40$ nm, within the 26-41 nm length range of erythrocyte actin filaments (Mische et al. (1987)) with which they were expected to share similarities (Xu et al. (2013), Qu et al. (2017)). The choice to model these filaments as rigid rods without twisting or bending was made to simplify the calculation and speed up computation time, and was deemed to be reasonable for this model as the 40 nm filament length is well below the persistence length of actin, $L_p = 9 \mu\text{m}$ (Isambert et al. (1995)).

Because the actin filaments which form rings in the MPS are believed to be stable with very little turnover of components (Zhong et al. (2014)) we maintained a constant actin length, implicitly modelling the presence of the expected end capping proteins, adducin (Xu et al. (2013)) and tropomodulin (Zhou et al. (2020)). Figure 2.2 illustrates the model rod with associated capping proteins. While actin filaments are polar, their specific orientation within actin rings is currently unknown (Gallo (2013)), therefore their ends were considered indistinguishable for the purposes of our model.

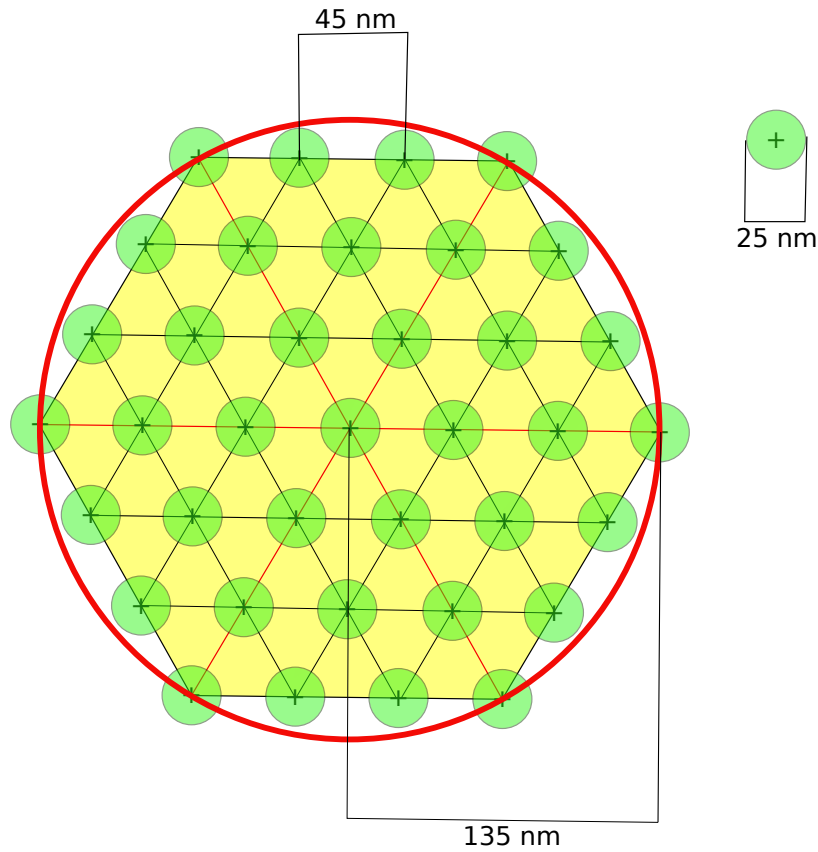


Figure 2.1: Model Microtubule Array. *37 hollow microtubules of 25 nm outer diameter form a hexagonal array with a centre to centre spacing of 45 nm. For the purposes of our model we take an approximate radius of this array and create a cylindrical section which we place at the centre of our axonal cell.*



Figure 2.2: Model Actin Filament. *This figure shows an example actin rod with capping proteins present at each end. Tropomodulin caps the pointed or minus end, while Adducin caps the barbed or plus end.*

Given the wide variety of roles and forms of actin within cells, changing concentration at different stages of development, and experimental limitations, the density of actin within neurons or other cell types is currently unknown. We include a number of actin filaments sufficient to build several rings, without being so densely packed as to restrict movement.

2.2.3 Spectrin Tetramers

We chose to represent spectrin as an inflexible rod of length $l_{\text{spectrin}} = 184$ nm, approximating the characteristic ~ 190 nm periodicity of spectrin found within both the MPS and the polygonal arrangements present in neurons (Han et al. (2017)), while allowing for a small junction region at each end where connections with actin rings are made. Radius was fixed at $r_{\text{spectrin}} = 2$ nm within the 4-6 nm diameter range observed (Shotton et al. (1979)). While modelling a complex protein such as spectrin as a rigid rod greatly simplifies its properties, for the purposes of this model we wished to consider its role in spacing groups of connected actin filaments only, and we therefore felt this representation was justified.

2.2.4 Coordinate System

We adopt a right-handed cylindrical coordinate system with z -axis corresponding to the longitudinal axis of the cylinder as shown in Figure 2.3 (left). Rod position was determined from the coordinates of the centrepoint, in addition to a set of 2 angles of orientation as illustrated in Figure 2.3 (right). α describes alignment with the z -axis, while β indicates orientation within the circular, xy plane of the cylinder.

The angles of orientation, α and β , were able to vary within the range $[-\pi, \pi]$. This range of positive and negative angles ensures consistent rotation behaviour, however, as rods are considered non-polar in this model, angles were converted to their positive equivalent for analysis purposes.

2.2.5 Boundary Conditions

Fixed boundary conditions were used for all cell surfaces, including the cylinder ends. These conditions dictate that the rod must remain within the finite boundaries of the cylinder at all times. Given the short length of the model axon this restriction may introduce some artificial effects by preventing free and continuous diffusion of particles in the axial direction, however given that the length of the cylinder is an order of magnitude greater than the width, the geometric restriction imposed is much greater radially than axially, and we therefore considered any effects due to axial confinement to be minimal. Results were monitored carefully to ensure rods did not accumulate excessively in these regions.

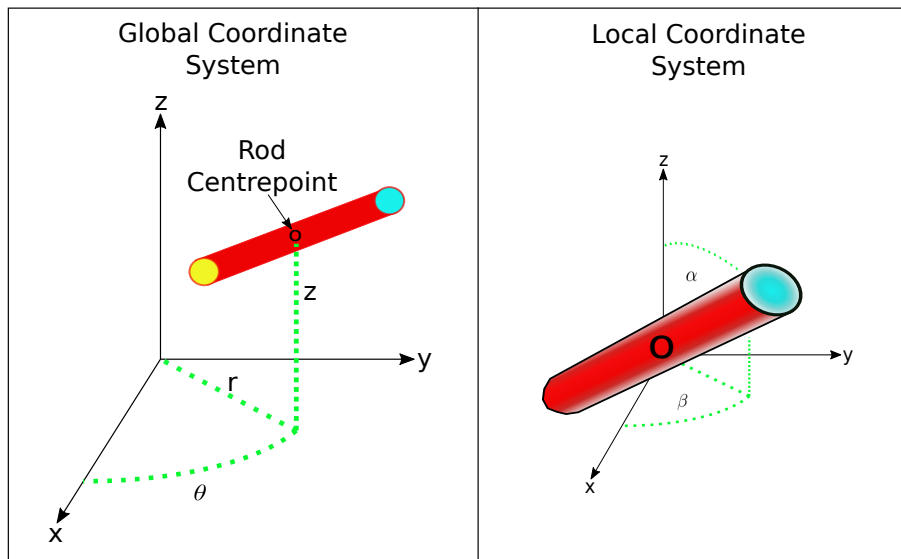


Figure 2.3: Model Coordinate System. *The left pane shows the global coordinate system governing positioning of rod within the cylinder. We use a cylindrical coordinate system with an origin based at the centre of the cylindrical cell and track the position of the centrepoint of each rod. The right pane shows the local coordinate system which describes the orientation of the rod. The α angle describes alignment with the z axis, while the second angle, β describes orientation within the xy plane of the cylindrical cell.*

2.2.6 Interactions

The model included two simple interactions; excluded volume interactions prevent rods from overlapping with one another, while crosslinking enables connections to be formed with nearby rods via specific binding sites. We describe these interactions below:

Excluded Volume Interactions

All rods, regardless of type, interacted with one another via excluded volume interactions. This was implemented as a hard-core repulsion, with a radius of interaction set as the combined radius of the pair of rods. Under these conditions, rods are able to move freely at any distance without bias, but are prevented from overlapping to any extent. The method used to implement this is described in Section 2.3.1.

Crosslinking

In some simulations rods were able to crosslink with one another. Actin rods were able to link with other actin, or with spectrin tetramers, and were considered to have sites of potential binding at 1 nm intervals along their length exclusive of the hemispherical regions at each end of the filament, giving a total of 33 binding sites per actin rod. Spectrin tetramers were assigned a single binding site for actin at each end, consistent with experimental observations (Brown et al. (2015)). As the turnover of components within the mature MPS structure appears to be slow (Zhong et al. (2014)), we chose not to include any unbinding events, and crosslinks were maintained for the duration of the simulation once formed.

2.3 Numerical Implementation and Algorithm

We used Python Version 3.7 to write custom software in order to build and simulate our model system. Here we give an overview of the Monte Carlo scheme used, detailing the algorithms employed to carry out translational, rotational, and crosslinking steps.

2.3.1 Random Walks and Monte Carlo Scheme

The rods were free to move around all areas of the cylinder without restriction, however they were required to remain entirely within the bounds of the cylinder, and were not able to overlap with other rods.

At the beginning of the simulation all rods were placed randomly. Python's built-in uniform distribution was used to select an initial position and orientation from the possible ranges. Checks were then carried out to ensure that the rod remained entirely within the confines of the cell, and that excluded volume

conditions were met. If the selected placement would cause any part of the rod to leave the cylinder or overlap another rod, the placement was rejected and another set of coordinates drawn at random. This procedure was carried out iteratively until all rods were suitably placed.

Once an initial random configuration was chosen for the rods, their motion via a random walk was simulated using the following algorithm:

- At each step, a rod, p_{mover} , was selected at random using Python’s built-in ‘choice’ function from the set of actin and spectrin rods.
- A custom function was used to generate a trial move for p_{mover} to take. This was achieved by labelling each potential move with a number, and using Python’s built-in ‘random integer’ function to select one of the available moves. For non-crosslinking simulations there were 10 possible moves, while for crosslinking simulations there were 11, with each move equally likely. The possible moves were as follows:
 1. Translational move by 1 nm in positive or negative x,y or z directions.
 2. Orientational α move by ± 1 degree.
 3. Orientational β move by ± 1 degree.
 4. (optional) Crosslinking move.

The rod, p_{mover} was repositioned according to the translational or orientational step taken. Where p_{mover} was connected to other rods through crosslinks, either directly or indirectly, translational moves were also applied to the connected rods as described in Section 2.3.3. Orientational moves were carried out via a rotation about the rod centrepoin in the case of unconnected rods and those with multiple crosslinks, with the rotation being applied to all connected rods as described in Section 2.3.4. If rods were connected via a single crosslink, the rotation was applied to p_{mover} only and carried out about the crosslink coordinates, allowing a small amount of orientational freedom as described in Section 2.3.5. If a crosslinking operation was chosen, the crosslink function was called to determine whether a link can be formed as detailed in Section 2.3.2.

- If a translational/orientational move was carried out, a Metropolis Monte Carlo scheme was then used to determine whether the trial move was accepted or rejected, as detailed below. This was carried out recursively for all connected rods. Acceptance of a trial move was conditional on all connected rods meeting the acceptance criteria.
- Where a trial move was rejected, the selected rod and all connections were returned to their previous positions and orientations.
- Once all of the above steps were completed, we proceeded to the next step in the random walk.

Random walks were carried out for 2.5×10^5 steps, and the position and orientation of all actin filaments was sampled at the final step. The chosen number of steps was deemed to allow an adequate period to equilibrate the system; this was tested by carrying out a comparison of orientational and positional outputs generated at increasing numbers of steps, with outputs showing little variation between 2.5×10^5 steps and 1×10^6 steps. For each set of simulation parameters used in this Chapter, 1000 simulations were carried out in parallel on an HPC cluster in order to gather large scale statistics on the stochastic properties under investigation.

Metropolis Monte Carlo Scheme

The Metropolis Monte Carlo scheme (Metropolis et al. (1953)) used to determine whether a translational/orientational step was accepted or rejected, is detailed below. In this scheme, the likelihood of a step is determined by calculating the Boltzmann factor for the change in configuration as follows:

$$P_{\text{initial} \rightarrow \text{final}} = e^{-\beta[\Delta E]} \quad (2.1)$$

Where $\Delta E = E_{\text{final}} - E_{\text{initial}}$ representing the change in energy of the system, and $\beta = \frac{1}{k_B T}$ where k_B is Boltzmann's constant with a value $k_B = 1.380649 \times 10^{-23} \text{ J K}^{-1}$.

This probability is then used in a further step during which we determine whether the trial move is accepted or rejected on this occasion as follows (Frenkel and Smit (2002)):

$$x = \text{Rand}[0, 1] \quad (2.2)$$

$$\begin{cases} x < e^{-\beta[\Delta E]} & \text{Accept Trial Move} \\ x \geq e^{-\beta[\Delta E]} & \text{Reject Trial Move} \end{cases} \quad (2.3)$$

The model in this Chapter has a simplistic energy landscape, influenced only by the requirements to remain within the environment and avoid overlapping neighbouring rods, and therefore the Boltzmann factors for this system reduce to the following:

Case 1: In the case that the rod moves to a location within the limits of the cylindrical cell and does not overlap other rods:

$$P_{\text{initial} \rightarrow \text{final}} = e^{-\beta[0]} = 1 \quad (2.4)$$

Case 2: In the case that the rod moves to a location beyond the cell limits and/or overlaps another rod:

$$P_{\text{initial} \rightarrow \text{final}} = e^{-\beta[\infty]} = 0 \quad (2.5)$$

Boundary Test

In order to test whether the position and orientation of a rod met the boundary conditions, the acceptable radial and axial limits were calculated as follows:

$$z_{\min} = (0 + r_{\text{rod}}) \quad (2.6)$$

$$z_{\max} = (L_{\text{axon}} - r_{\text{rod}}) \quad (2.7)$$

$$\begin{cases} r_{\min} = 0 & \text{(if no microtubule array)} \\ r_{\min} = (R_{\text{mt}} + r_{\text{rod}}) & \text{(if microtubule array)} \end{cases} \quad (2.8)$$

$$r_{\max} = (R_{\text{axon}} - r_{\text{rod}}) \quad (2.9)$$

Where r_{rod} is the radius of the rod being tested, R_{mt} is the radius of the microtubule array if present, and R_{axon} and L_{axon} are the radius and length of the simulation cell respectively.

The longitudinal axis of the rod was parametrised into a series of coordinate points at 1 nm intervals, and each point was tested to ensure it satisfied the boundary conditions. Hemispherical endcaps of rods were neglected in this calculation as they are accounted for in the limits above.

Overlap Test

Neighbouring rods with the potential to overlap were identified by calculating the centrepoint to centrepoint distance and testing under the following criteria:

$$d_{\text{centre}} < \left(\frac{l_a + l_b}{2} \right) \quad (2.10)$$

Where d_{centre} is the centre to centre distance between the 2 rods, l_a is the length of the rod for which we are trying to identify neighbours, and l_b is the length of the potential neighbour rod. In all cases rod length is inclusive of the radii of its hemispherical ends.

Any pair of rods meeting the above criteria could potentially overlap depending on their respective orientation. Once a list of neighbouring rods was generated, each rod was parametrised into a series of points at 1 nm intervals. The point to point distance is then calculated iteratively to test for overlapping regions using the following criteria:

$$d_{\text{points}} < (r_a + r_b) \quad (2.11)$$

Where d_{points} is the distance between the current point on the rod in question, and the current point on the neighbour rod for which we are testing for overlap, r_a is the radius of the rod for which we are calling the function, and r_b is the radius of the potential neighbour rod. To improve performance, this

function was created using the Cython package (Behnel et al. (2011), available at <https://cython.org/>) and loaded as an extension module.

If the criteria stated in Equation 2.11 is met, this indicates that the trial move would violate the excluded volume requirements described in Section 2.2.6, and the move is therefore rejected.

Angle Corrections

At each step involving a change in rod orientation, a series of tests were carried out to ensure that the angle of orientation remained within acceptable parameters. Both α and β angles were restricted to remain within the range $[-\pi, \pi]$ and angle corrections were carried out should the angle exceed the limits of this range. In addition, should a move result in a change of sign of the α angle, the β angle is incremented by 180 degrees. This step ensures that the rod rotates fully in 3 dimensions. The conditions and corrections applied are listed below:

$$\begin{cases} \alpha = \alpha - 2\pi & \text{if } \alpha > \pi \\ \alpha = \alpha + 2\pi & \text{if } \alpha < -\pi \\ \beta = \beta - \pi & \text{if } (\alpha_{\text{previous}}\alpha_{\text{current}}) < 0 \\ \beta = \beta - 2\pi & \text{if } \beta > \pi \\ \beta = \beta + 2\pi & \text{if } \beta < -\pi \end{cases} \quad (2.12)$$

Where α_{initial} and α_{final} are the α angles of orientation before and after an orientational change respectively.

This series of angle corrections were carried out as a subroutine after each orientational trial move.

2.3.2 Crosslinking Method

If a crosslinking trial move was chosen, the crosslinking subfunction was called and linking was attempted. Binding sites were placed as described in Section 2.2.6. The crosslinking function uses binding site data to carry out the following process:

1. A class method is called to determine whether one or more unoccupied binding sites are present on the selected rod, p_{mover} . Indices of any free sites are stored.
2. A second class method is called which generates a list of neighbouring rods, using the criteria given in Equation 2.10. Each neighbour is tested to determine whether it has any unoccupied binding sites and the initial list of neighbours is filtered to include only those neighbours which have at least one unoccupied binding site.
3. For each unoccupied binding site on p_{mover} , we iterate over each site on each neighbour and test proximity of the pairs of sites to determine

whether binding can occur. The condition for binding is a distance of $d_{\text{bind}} < 15$ nm. This distance was selected to be slightly larger than the combined radius of 2 actin rods, ensuring only those rods in close proximity can bind.

4. If the criteria for binding are met, class methods are called to change the status of the relevant binding sites to occupied. This method also updates the lists of partners for each of the connecting rods.
5. The function terminates when either a single binding operation has been carried out, or when all possible binding combinations have been exhausted.

As unoccupied binding sites are identified by iterating over sites in order, crosslinks form at binding sites located at the end of a rod with a higher probability than at those sites which are more centrally located. As the rods are short in length, the effect of this is likely to be small, however if longer rods were to be modelled this bias could be removed by selecting available binding sites at random.

2.3.3 Translational Motion Method

If a translational step was selected, the Cartesian form of the position coordinates of the central point on the rod were updated to include the coordinate increment chosen, and the rod was repositioned. If the rod selected to take a step, p_{mover} , had any partners, this process was repeated for all connected rods, ensuring that they moved as a rigid body. NumPy (Harris et al. (2020)) was used to create arrays of coordinates during trial moves. Once all rods were repositioned, boundary and overlap checks were carried out. Should the trial move be denied for any of the connected rods in this cluster, all rods were reset to their original positions.

2.3.4 Orientational Motion Method for Loosely Bound Rods

This special case allowed for rods which were loosely bound (i.e. have only a single connection) to have some degree of orientational freedom independent of the rod to which they were connected. If an orientational trial move was chosen and p_{mover} was connected to a single partner rod by 1 crosslink only, then a function was called to attempt a rotation as follows:

1. The index of the occupied binding site on p_{mover} is identified and used to find the coordinates of this point.
2. The centrepoint of p_{mover} is translated to the coordinates of the binding site found in the previous step.

3. The angles of orientation of p_{mover} are updated with the increment determined by the trial move. A class method is then used to update the position and orientation of this rod.
4. The new coordinates of the binding site are determined.
5. A translation vector is defined extending from the new binding site coordinates to the rod centrepoint (i.e. the initial binding site coordinates).
6. The translation vector is then added to the current centrepoint coordinates. This replaces the binding site at its original coordinates, and while translating the rod centrepoint to a new location based on rotation about the binding point.
7. Boundary and overlap checks are carried out. If the new location does not meet these conditions then the rod is returned to its original location.

2.3.5 Orientational Motion Method for Unpartnered or Tightly Bound Rods

This section applies to any rod which does not have any partners, and also to any rod which has multiple partners and/or crosslinks. Rods with multiple crosslinks are considered to be tightly bound and as such, all attached rods (both direct and indirect connections) rotate as a rigid body, with distance between all points being conserved. The point about which the cluster rotates is defined in relation to the p_{mover} via the following algorithm:

1. A list of all rods in the cluster is generated. This includes any rod connected either directly or indirectly to p_{mover} .
2. Current positions and orientations are stored in a Numpy array (Harris et al. (2020)) for all rods in this cluster.
3. Angles of orientation are updated for p_{mover} , as per the angle increment determined in the trial move. Angle corrections are carried out as detailed in Equation 2.12. A class method is called to reposition the rod.
4. If the chosen rod has partners, a process is carried out to determine the new locations and angles of any connected rods based on rigid body motion. The methods for changes in both α and β angles are detailed below. All partner rods are repositioned with the relevant class method, according to the coordinates and angles calculated using these methods.
5. Once every rod in the cluster has been repositioned, overlap and boundary checks are carried out. If the new location is unacceptable for any rod in the cluster, then the trial move is denied and all rods are reset to their original positions and orientations.

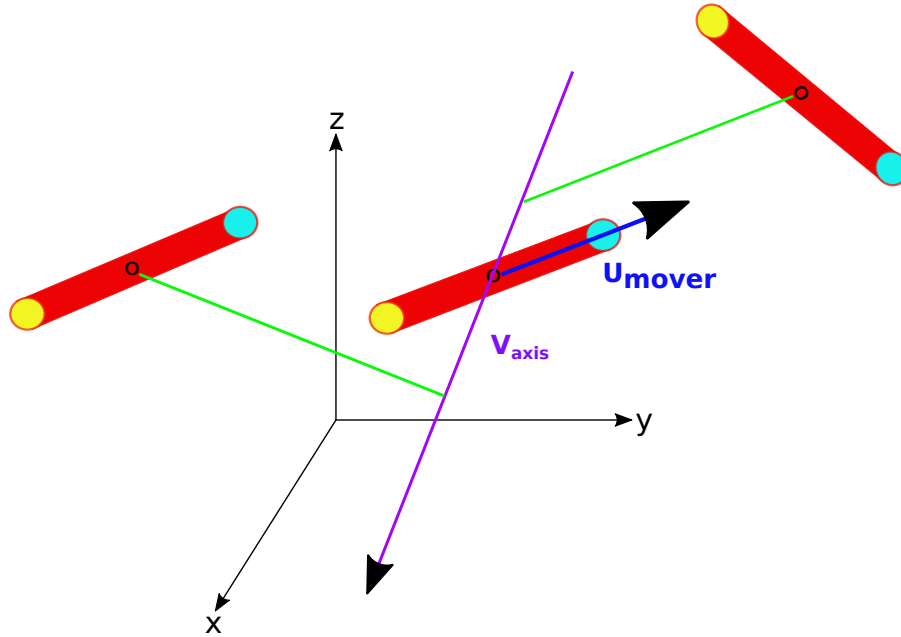


Figure 2.4: Alpha Method. When a rod which is part of a pair or cluster rotates in the α directed, we represent this rod as vector, U_{mover} , and define an axis perpendicular to this vector at constant z , V_{axis} . We create further vectors as shown in green, running perpendicular to V_{axis} and connecting the partner rod centrepoint to a point of intersection on V_{axis} . This gives us a point about which to rotate the partner rods to ensure rotation as a rigid body.

alpha method

When the α angle changes, this involves not only a change in the z coordinate, but also alters the projection of the rod in the xy plane. All rods within the cluster must be rotated about an axis of rotation centred on the centrepoint of p_{mover} .

As illustrated in Figure 2.4, we first represent p_{mover} as a vector, \mathbf{U}_{mover} , beginning at the rod's centrepoint and pointing towards its endpoint:

$$\mathbf{U}_{mover} = u_1\mathbf{x} + u_2\mathbf{y} + u_3\mathbf{z} \quad (2.13)$$

Next we define a second vector, \mathbf{V}_{axis} representing the axis about which all rods in the cluster are to be rotated:

$$\mathbf{V}_{axis} = v_1\mathbf{x} + v_2\mathbf{y} + v_3\mathbf{z} \quad (2.14)$$

We require \mathbf{V}_{axis} to be perpendicular to the 2D, xy projection of vector

$\mathbf{U}_{\text{mover}}$, and constant in z . We therefore set the dot product of the vectors to zero:

$$\begin{aligned}\mathbf{V}_{\text{axis}} \cdot \mathbf{U}_{\text{mover}} &= v_1 u_1 + v_2 u_2 + v_3 u_3 \\ &= 0\end{aligned}\tag{2.15}$$

Setting the z component of \mathbf{V}_{axis} to zero and choosing an arbitrary value for v_1 gives the following solution for v_2 :

$$v_3 = 0\tag{2.16}$$

$$v_1 = 1\tag{2.17}$$

$$\begin{aligned}v_2 &= -\frac{u_1}{u_2} v_1 \\ &= -\frac{u_1}{u_2}\end{aligned}\tag{2.18}$$

In order to determine the point on the vector \mathbf{V}_{axis} about which a partner rod should be rotated, we use the vectors to generate 2 parametrised equations. The first equation describes a line, U_{partner} , beginning at the point of rotation on the partner rod and proceeding in a direction parallel to the xy projection of p_{mover} with a constant z component:

$$U_{\text{partner}} = [x_p, y_p, z_m] + s[u_1, u_2, 0]\tag{2.19}$$

Where x_p and y_p are the x and y coordinates of the point that we wish to rotate on the partner rod, and z_m is the z component of the centrepoint coordinates of p_{mover} .

The second equation is the axis vector \mathbf{V} as defined in Equations 2.14 - 2.18, beginning from the centrepoint of p_{mover} :

$$V_{\text{axis}} = [x_m, y_m, z_m] + t[v_1, v_2, 0]\tag{2.20}$$

Where x_m and y_m are the x and y coordinates of the centrepoint of p_{mover} , and other terms are as defined previously.

The coordinates of the point about which we need to rotate the partner rod in question can be found at the intersection of the lines given in Equations 2.19 and 2.20. The intersection can be found by setting the equations as equal and rearranging as follows:

$$[x_p, y_p, z_m] + s[u_1, u_2, 0] = [x_m, y_m, z_m] + t[v_1, v_2, 0]\tag{2.21}$$

$$t[v_1, v_2, 0] - s[u_1, u_2, 0] = [x_p, y_p, z_m] - [x_m, y_m, z_m]\tag{2.22}$$

This gives 2 simultaneous equations as follows:

$$\begin{cases} tv_1 - su_1 = x_p - x_m \\ tv_2 - su_2 = y_p - y_m \end{cases} \quad (2.23)$$

These equations can be represented in matrix form as follows:

$$\begin{pmatrix} v_1 & -u_1 \\ v_2 & -u_2 \end{pmatrix} \begin{bmatrix} t \\ s \end{bmatrix} = \begin{bmatrix} x_p - x_m \\ y_p - y_m \end{bmatrix} \quad (2.24)$$

The NumPy linear algebra solver (Harris et al. (2020)) was then used to solve for t and s . These values were then substituted back into the equations to determine the point of intersection.

A rotation vector was defined, beginning at this point of intersection and extending to the point on the partner rod to be rotated. The α angle of this rotation vector was calculated to determine whether the partner rod was parallel or anti-parallel to the selected rod. If the rods were parallel, the sign of α was set to match that of the selected rod, and if anti-parallel the sign was reversed. This ensured rotation in the correct sense.

The trial orientational move was then applied to the partner rod by incrementing the α angle of the rotation vector. Angle checks were carried out and the translated coordinates of the point on the partner rod were calculated.

This process was carried out to determine translated coordinates for both the centrepoint and an endpoint of the partner rod, and the new coordinates were then used to determine updated angles. The partner rod was then placed in the new configuration.

beta method

Changes of the beta angle change neither the z component nor the alpha angle, and so the method of rotation in this direction is more straightforward than for the alpha angle. In this case, partner rods undergo an orientational change as well as a translation as they move as a rigid body with p_{mover} .

A rotation vector was defined travelling from the centrepoint of p_{mover} to the centrepoint of the partner rod. The α and β angles of this rotation vector were determined and set within acceptable limits using the angle corrections described in Section 2.3.1. The β angle of this vector was then updated with the angle increment, and the updated coordinates of the vector endpoint were calculated, giving the new coordinates for the partner rod centrepoint. We translate the partner rod to these updated coordinates, and apply the orientational change by incrementing its β angle.

2.4 Data Analysis Methods

For each model system that we investigate, we carry out a series of 4 analyses on the configuration of rods, sampling results at the final step of our random walk. For analyses where results are averaged, we carry out parallel random walks, averaging over these configurations at the final step. This method was used as an alternative to carrying out a single simulation and averaging results over time, at different step intervals. This choice was made due to the inclusion of crosslinks in some model systems; the crosslinks did not detach and therefore accumulate as the number of steps elapsed increases. Configurational averaging ensures that systems from which average properties are generated possess similar degrees of crosslinking.

In the MPS, actin filaments are positioned adjacent to the membrane, forming rings around the membrane circumference, and adopting a periodic spacing of 180 and 200 nm (Xu et al. (2013), Lukinavičius et al. (2014), Zhong et al. (2014), D’Este et al. (2015), D’Este et al. (2016), Leite et al. (2016), Han et al. (2017), Qu et al. (2017), Krieg et al. (2017), Unsain et al. (2018a)). We wish to establish whether this configuration could occur within our highly simplified model, and seek evidence of an arrangement with these properties by observing the configuration of actin rods in terms of their overall appearance, their orientation, their radial positioning, and their arrangement with respect to the longitudinal axis of the axon-like cell in which we simulate. We describe here the methods used for each analysis.

2.4.1 Qualitative Analysis

To observe an example configuration of our actin rods, we run a single simulation, sampling the configuration of rods at the final step, and outputting the coordinates of rod endpoints, or those of a subset of rods, to a text file. The sampling procedure used is detailed within the relevant results sections.

We load coordinates into Mathematica Version 12.0 (Wolfram Research (2019)) and plot the rod configuration. Actin rods are plotted as a red cylinder of radius $r_{\text{actin}} = 4$ nm. As rods in our model have hemispherical endcaps, we add a sphere to each end of our actin rod images; these are coloured cyan and yellow to represent the implied presence of capping proteins, adducin and tropomodulin, as illustrated in Figure 2.2. Other components are added as detailed in the related results section.

We show 3 viewpoints of our rod configuration; an orthographic view taken from the upper corner, a front view, and a view from above, looking down the longitudinal axis of the cylinder. These views help us to see how rods are arranged and oriented within the cell space.

2.4.2 Angle of Orientation Method

For each actin rod within the simulation, we calculate and record the angle of orientation at the final step of the random walk. The angle is taken with respect to the longitudinal axis of the axon-like cell, with an angle of 0° indicating alignment with this axis, and 90° being perpendicular to this axis, fully aligned within the circular plane of the cell. As the rods are considered to have indistinguishable ends, we normalise rod angles to this range by adding π to the angle if it is negative, and subtracting the angle from π if the angle is greater than $\frac{\pi}{2}$. This ensures we measure the angle of the end of the rod pointing in the positive z direction.

We produce a composite distribution, combining data from 1000 parallel simulations, each containing 500 actin rods, giving a total of 500,000 angles of orientation. We plot results in R using the `ggplot2` package Version 3.3.3 (Wickham (2009)) to create a bar chart for our histogram data.

In addition to our composite distribution, we plot a series of 4 distributions from individual simulations. We select the first 4 sets of simulation results and plot a bar chart for each simulation, each containing angles of orientation for 500 actin rods.

With this analysis, we seek to establish whether our actin rods orient themselves within or close to the circular plane of the cylindrical cell space, which is the expected orientation of actin within rings.

Note - we present angle distributions in terms of the raw data only, for the purpose of detecting rods perpendicular to the circular plane. A true assessment of the distribution of rod orientation would require use of spherical statistical methods.

2.4.3 Radial Positioning Methods

To observe the radial positioning of actin rods, we output the coordinates of all points or vertices on each of our actin rods to a text file, sampling this configuration at the final step of our random walk. To obtain coordinates we use a class function which parametrises the longitudinal axis of a rod into a series of points at 1 nm intervals (excluding hemispherical endpoints). This gives a total of 33 points per actin rod.

We form a composite distribution, combining results from 1000 simulations, each containing 500 actin rods. We calculate the number of points within each 5 nm radial range, from r_a to r_b , giving a set of 40 histogram bins. Due to the increase in volume of cell space as the radial range moves to larger values, we correct for volume the volume, dividing the number of points within each range by the volume of the cylindrical shell with an inner radius of r_a and outer radius of r_b . This gives a density of actin points per cubic μm . We plot results as a histogram in R using the `ggplot2` package Version 3.3.3 (Wickham (2009)).

In the MPS, actin filaments form rings around the membrane circumference. We therefore seek a pattern in which the density of actin points is skewed

towards the largest radii which are membrane-adjacent.

2.4.4 Axial Positioning Methods

We use a range of methods to examine axial positioning of our rods; we create a composite distribution of axial coordinates, we perform autocorrelation analysis, and we carry out a Fourier Transform and calculate power across spatial frequencies.

We output the coordinates of all points on our actin rods as previously, using a class method to parametrise each rod into a series of points at 1 nm spacing. The configuration is sampled at the final step in our random walk. Results for each of the 1000 parallel simulations are output to a text file, with 16500 actin point coordinates being recorded per simulation.

The methods used are detailed below:

Composite Distribution

We combine results from our set of 1000 parallel simulations. We calculate the number of actin points within each 50 nm axial section of the cell, and plot as a histogram using ggplot2 package Version 3.3.3 (Wickham (2009)).

Autocorrelation Analysis

We perform autocorrelation analysis, comparing our input data with a copy of itself shifted by various lags. The autocorrelation function returns a value which indicates how alike the data is with a copy of itself at each offset, with a maximum value of 1 indicating perfect correlation. This analysis identifies any periodic organisation within spatial data; we expect to obtain at least one peak of over 0.2 in magnitude in the case of periodic data, while multiple peaks of similar spacings are indicative of periodicity over longer ranges.

We first clean the data by extracting axial coordinates from simulation output files using Python Version 3.8 and the NumPy package (Harris et al. (2020)), writing these coordinates to a separate text file per simulation. To perform autocorrelation analysis on axial data from each simulation, we created a custom script in Matlab Version R2020b (The Mathworks (2020)) to carry out the following procedure:

1. The histogram function is used to bin axial coordinates into 20 nm intervals.
2. We calculate the mean number of points per bin, and normalise the histogram data by subtracting the mean from the value of each bin.
3. We apply the 'xcorr' function, from the Signal Processing Toolbox, to the normalised histogram data. This function returns the autocorrelation value at each lag, at increments of 20 nm.

4. As the data at negative lags is symmetrical to that of positive lags, we subset the data to include only positive, non-zero lags.
5. We use the 'findpeaks' function to locate any local maxima within the autocorrelation data, and their locations. We use the 'max' function to determine the maximum autocorrelation amplitude for this simulation.
6. We apply 'findpeaks' with specified minimum amplitude, to detect peaks of specific heights, from > 0.1 to > 0.9 .

We use a loop to apply this analysis iteratively on each of the 1000 simulation results, outputting the maximum autocorrelation amplitude, and the number of peaks within each amplitude range to a text file. For the analysis tables produced in this Chapter, these text files of autocorrelation results were loaded into R and summary statistics were produced.

Fourier Transform and Power Analysis

While autocorrelation analysis gives us details of the individual peaks within the data, it is also useful to use Fourier Transforms to determine dominant spatial frequencies within the data. To perform this analysis, we created a custom script in Matlab Version R2020b (The Mathworks (2020)) which carries out the following steps:

1. The histogram function is used to bin axial coordinates into $\Delta x = 20$ nm intervals.
2. We calculate the spatial sampling frequency, $f_x = \left(\frac{1}{\Delta x}\right)$.
3. We apply the Fast Fourier Transform function, 'fft', from the Signal Processing Toolbox to our axial coordinate data. This returns a vector y , of length L_{FFT} .
4. As the input function is real valued, we convert the 2 sided Fourier Transform data to a single sided spectrum, subsetting to retain the first half of the data.
5. We calculate the power spectrum, P_x , where $P_x = \left(\frac{|y|^2}{L_{\text{FFT}}}\right)$. As we have removed one half of the spectrum, we multiply each of the peaks that feature twice in the original spectrum by 2. The phase information of the Fourier Transform is lost in converting to a power spectrum, however this conversion makes it easier to identify dominant spatial frequencies amid a noisy signal as the signal magnitude is squared.
6. To generate a power magnitude between 0 and 1, relative to the peak at 0 frequencies, we normalise by dividing by the size of the 0 frequency peak.
7. We create a vector of the relevant spatial frequencies.

8. We use the 'FindPeaks' function to identify any local maxima within the Power data. We use the 'max' function to determine the magnitude of the largest peak in the simulation.

In this Chapter, we carry out a loop, iterating over each of the 1000 simulation results, and outputting the magnitude of the largest peak in Power to a text file. This data was then analysed by loading the text file into R and producing summary statistics.

For the simulation which produced the largest peak, we plotted the Power data against positive spatial frequencies in Matlab. To see the data clearly, we neglect the large peak at 0 frequency, and use a y axis scaling of 0 to 0.2, extending further if any peaks exceeded this range.

2.5 Actin Filaments within a Cylindrical Axon

To begin, we place 500 short actin rods of $l_{\text{actin}} = 40$ nm into our cylindrical axon-like cell. We carry out a random walk of 2.5×10^5 steps, repeating 1000 times to generate a large volume of example configurations, with the configuration being sampled at the final step in each case. We carry out the analyses detailed in Section 2.4, observing an example configuration qualitatively initially, before analysing quantitative information on angle of orientation, and spatial positioning within the cell. These results help to inform us on how systems of short, rod-like particles could arrange themselves within a cylindrical space of axon-like dimensions.

2.5.1 Simulation Images

The actin configuration corresponding to the final step of an example simulation is shown in Figure 2.5. The images show the set of 500 rods in a variety of positions and orientations, while the view from above appears to show a higher density of rods occupying the centre of the cylinder, with fewer rods around the edges.

2.5.2 Angle of Orientation

We recorded the angle of orientation of each of the 500 actin rods with respect to the longitudinal axis of the cylindrical axon-like cell. The angle was sampled at the final simulation step (step 2.5×10^5) and results from 1000 simulations were combined and analysed together. The results are shown in Figure 2.6. The graph shows a fairly even distribution across the range of possible angles, with angles between $0 - 30^\circ$ having slightly higher frequencies.

The dataset containing results from all simulations indicates that angles of orientation are largely isotropic when data is combined, however it is also useful view distributions from individual simulations. We show a set of 4 example distributions in Figure 2.7. Figures 2.7a and 2.7c show the largest angles of

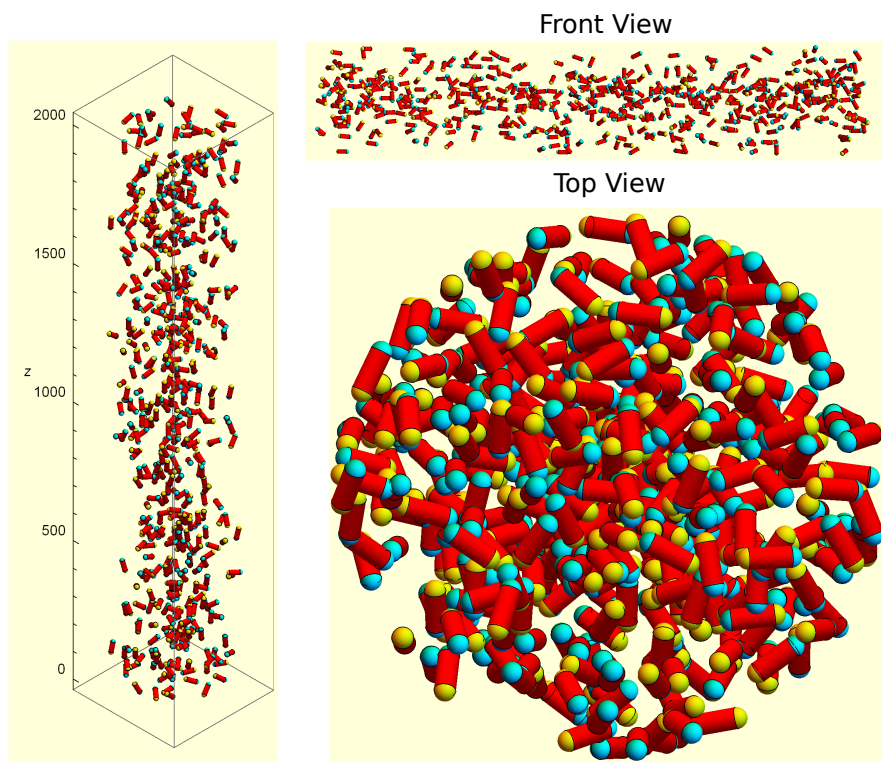


Figure 2.5: Actin Rods within a Cylindrical Cell. *This simulation contains 500 non-crosslinking actin rods which can move freely within a cylinder provided they do not overlap with one another or exceed the cell limits. We see an orthographic view from above on the left, and front and upper views on the right.*

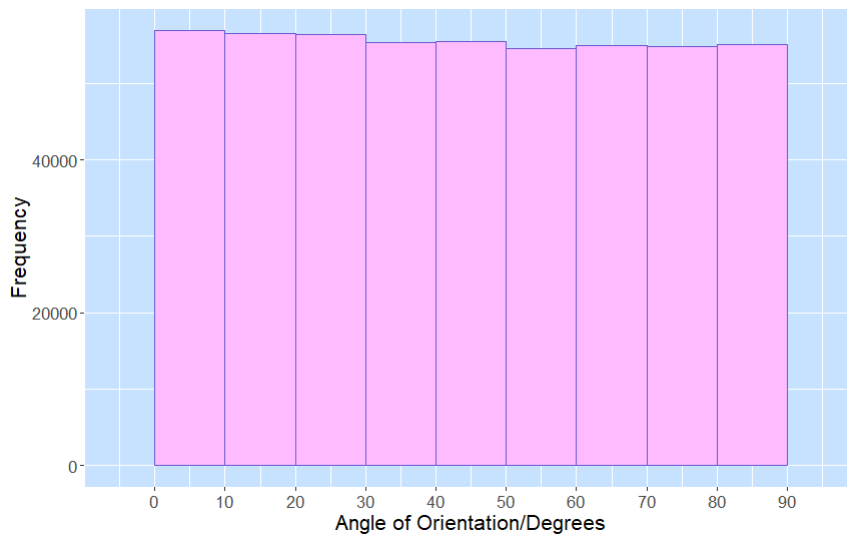


Figure 2.6: Orientation of Actin Rods in a Cylindrical Cell. *This simulation contains 500 non-crosslinking actin rods which can move freely within a cylinder provided they do not overlap with one another or exceed the cell limits. Data is combined from 1000 repeat simulations and the distribution of angles of orientation is displayed in the graph. A zero angle indicates an actin rod aligned with the longitudinal axis of the cylinder, while a 90 degree angle indicates a rod aligned perpendicular to this axis, and parallel to the circular plane of the cylindrical cell space. The distribution appears fairly even across the range of orientations.*

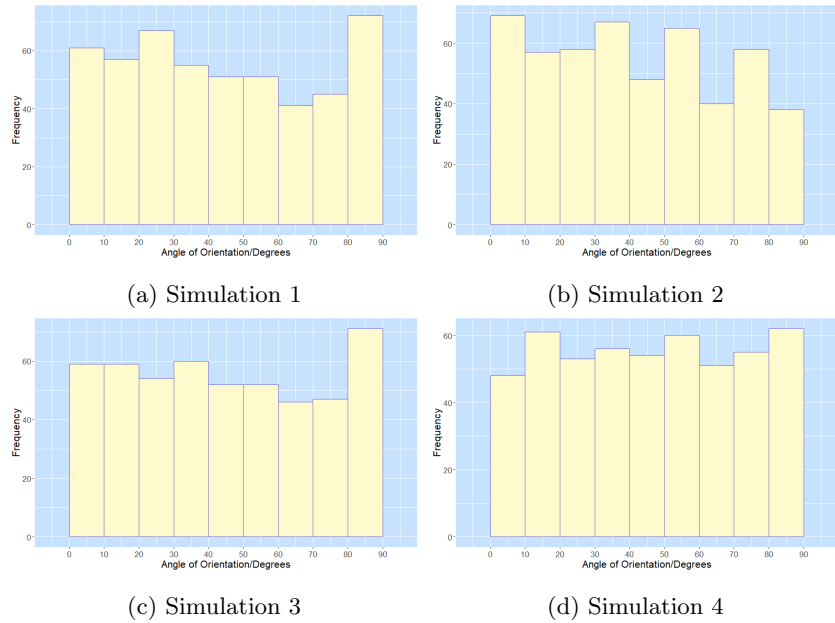


Figure 2.7: Orientation of Actin Rods in a Cylindrical Cell - Individual Simulations. *Here we show the distribution of angle of orientation for 4 individual simulations, each containing 500 actin rods. These single simulation results show more variability than the combined data used in Figure 2.6.*

80 – 90° occurring with the highest frequency, while Figure 2.7b peaks at the smallest angles of 0 – 10°. Figure 2.7d displays peaks of similar sizes at 3 points across the angle range.

Overall these results show that there is some variability in the distribution of angle of orientation across different simulation runs with the same parameters, however there is no clear pattern, and this results in an overall isotropic distribution.

2.5.3 Radial Positioning

Next we observe the radial positioning of our actin rods. As before, we combine data from 1000 simulations, each containing 500 actin rods, with the point coordinates being sampled at the final, $2.5 \times 10^{5\text{th}}$, step in our random walk.

In Figure 2.8 we show the radial positioning of actin points, represented as a density of points per cubic μm of cell space, which takes into account the different volumes of the cylindrical shell spaces available at each of our radial coordinates ranges. This graph shows a clear pattern, with a greater density of actin points per unit volume occupying the centre of the cell, reducing steeply

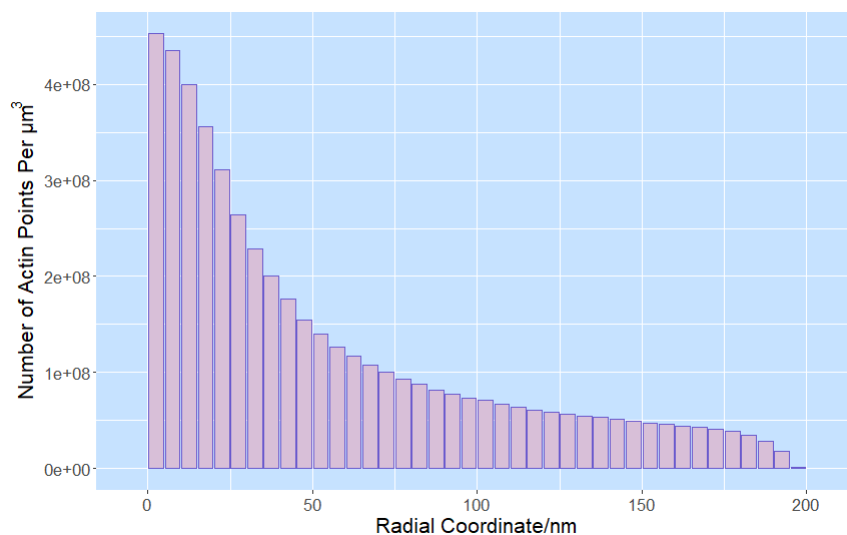


Figure 2.8: Radial Distribution of Actin Rods in a Cylindrical Cell. *Data is combined from 1000 repeat simulations, each containing 500 actin rods, and the number of actin points is displayed as a density per cubic μm within each 5 nm radial range. The distribution of actin points appears heavily skewed towards the lower coordinates, indicating a high density of actin occupying the central regions of the cylinder.*

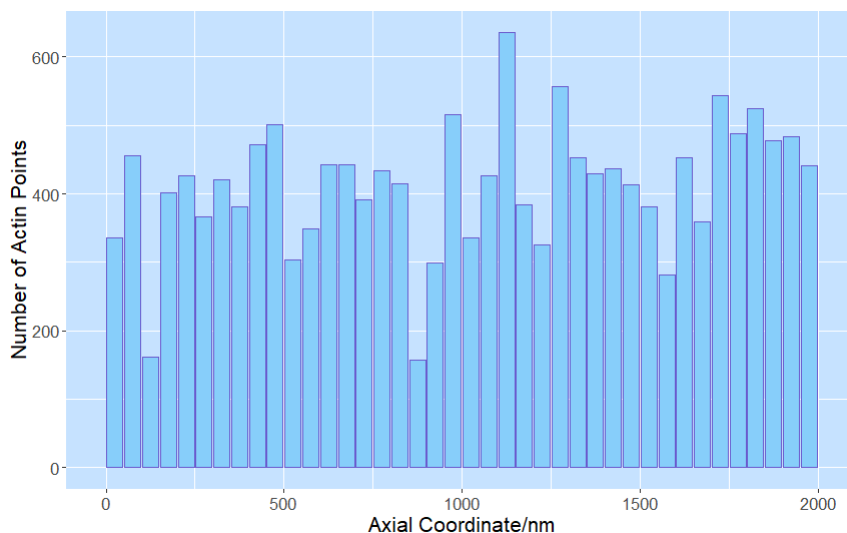


Figure 2.9: Axial Distribution of Actin Rods Within a Cylindrical Cell. *The number of actin points within 50 nm axial regions are displayed with data combined from 1000 repeat simulations of 500 actin rods each.*

as volume increases. This indicates that the centre of the cell is most densely populated, with actin rods unlikely to aggregate at the edges of the cylinder. This is in line with the qualitative observations of Section 2.5.1

2.5.4 Axial Positioning

We continue our positional analysis, using actin point coordinates to display an axial distribution. We combine results from 1000 simulations as previously and plot a histogram showing the number of actin points within each 50 nm section. Results are shown in Figure 2.9. There is substantial variability in this distribution with several large peaks and troughs, making it difficult to interpret whether there is any underlying pattern in the data.

We next calculate the autocorrelation function for each of the 1000 simulations, using the methods described in Section 2.4.4. The maximum autocorrelation amplitude found within this sample was 0.362, with a minimum of 0.102, and a mean of 0.185 to 3 significant figures. Details of specific peaks are shown in Table 2.1. There were large numbers of small peaks with autocorrelation amplitudes exceeding 0.1 and reaching up to 0.2, with individual simulations showing 0 – 12 peaks of this magnitude, and a mean number of 4.42. Larger peaks in the range $0.2 < a \leq 0.3$ were far less common, with 356 in total, and a maximum of 3 peaks in individual simulations. Just 5 simulations showed peaks greater than 0.3, with a maximum number of 1 occurring within a single

Table 2.1: Autocorrelation of Actin Rods in a Cylindrical Cell. *This table details the total number of peaks within stated ranges of autocorrelation amplitude, as well as the minimum, maximum, and mean numbers of peaks occurring within individual simulations.*

Autocorrelation Amplitude, a	Number of Peaks			
	Total	Min	Mean	Max
$0.1 < a \leq 0.2$	4422	0	4.42	12
$0.2 < a \leq 0.3$	356	0	0.356	3
$0.3 < a \leq 0.4$	5	0	0.005	1

simulation. No peaks exceeded 0.4 in magnitude.

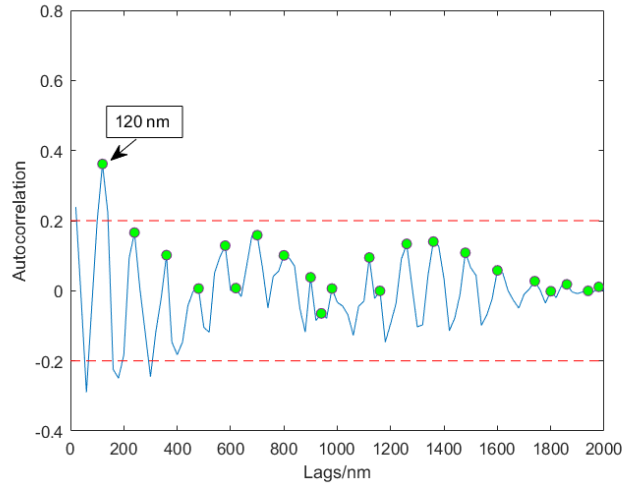
To complement the autocorrelation analysis, we calculated the power of each simulation, using the methods described in Section 2.4.4. The maximum of the normalised power function was 0.0377 to 3 significant figures, with a mean of 0.0128.

To visualise these results, we plot autocorrelation and power for the individual simulations which corresponded to the largest magnitudes of these measures, displaying results in Figure 2.10. In Figure 2.10a, we see a peak in autocorrelation of 0.362 amplitude, occurring at a lag of 120 nm. There are several further peaks as lag increases, however these peaks are small at magnitudes of less than 0.2. Figure 2.10b shows a peak in power of 0.0377 at a frequency of 0.002 nm^{-1} . This corresponds to a wavelength of 500 nm which is quarter of the cell size.

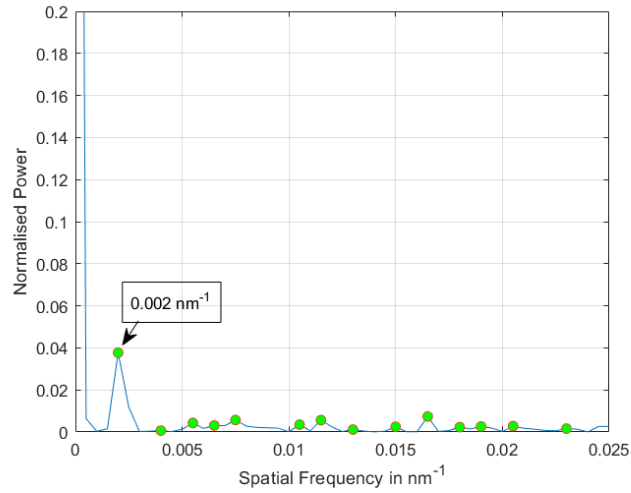
Taken together, these results do not show significant levels of periodic organisation of actin, with the majority of simulations showing low autocorrelation and power amplitudes.

2.6 Actin Filaments within an Axon with Microtubule Array

Simulations were carried out as in Section 2.5, however, the axon-like cell space was modified to include a microtubule array of radius $R_{\text{mt}} = 135 \text{ nm}$, as described in Section 2.2.1. This array is located within the central core of the axon, and is modelled implicitly by preventing rods from entering the region that it occupies. The array was introduced to more closely replicate the conditions of the axon; as described in Section 1.2.1, axons possess a central microtubule array which acts as a track for axonal transport. As the microtubules pack closely together, actin is restricted to the outer regions of the cylindrical axon.



(a) Autocorrelation - Simulation 711. A peak of 0.362 is shown at 120 nm, with a series of smaller peaks at larger lags.



(b) Power with Spatial Frequency - Simulation 545. A peak in normalised power of 0.0377 is shown at 0.002 nm⁻¹, corresponding to a period of 500 nm.

Figure 2.10: Periodicity of Actin Rods in a Cylindrical Cell. Results are shown for simulations with peaks of greatest magnitude in autocorrelation and power. These results are low in magnitude, indicating a lack of significant periodicity.

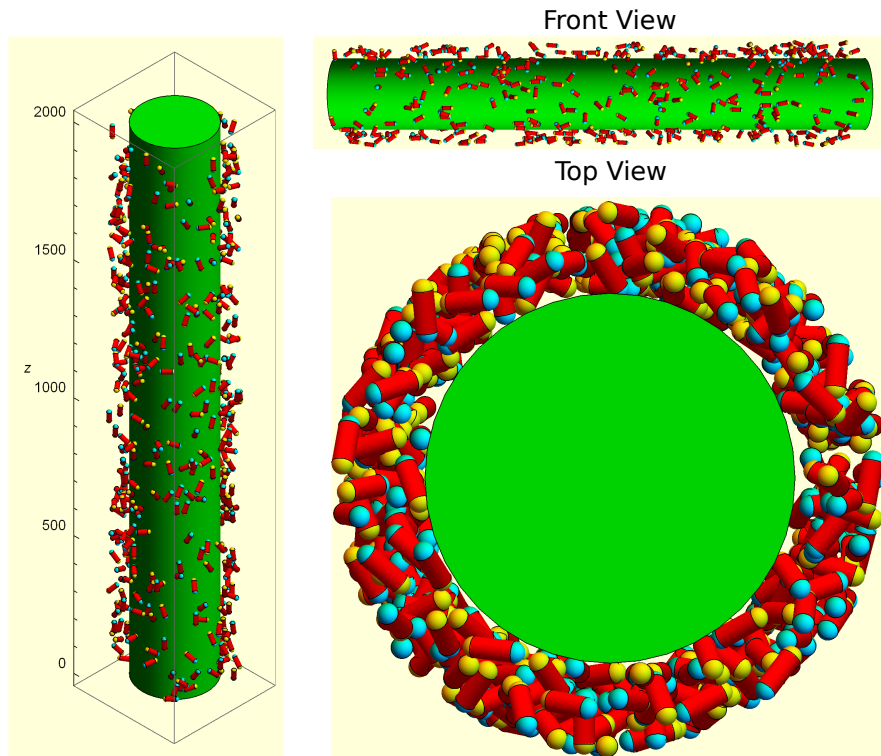


Figure 2.11: Actin Rods within a Cylinder with Microtubule Array. *This simulation contains non-linking actin rods which can move freely within a cylindrical shell space subject to restrictions to prevent overlapping or leaving the cell. A microtubule array blocks out the centre of the cylinder as shown in green, and rods are not able to access this region.*

2.6.1 Simulation Images

Figure 2.11 shows the 500 rods in the configuration adopted at step 2.5×10^{-5} of an example simulation. The microtubule array is illustrated as a green cylinder, occupying a radius of $R_{\text{mt}} = 135$ nm, centred on the longitudinal axis of the cell. Despite the increase in concentration caused by the presence of a microtubule array, rods continue to appear isotropic, with no observable pattern of position or orientation.

2.6.2 Angle of Orientation

As previously, we display the distribution of angles of orientation in Figure 2.12. Unlike the results of Figure 2.6, rod orientation here appears skewed towards

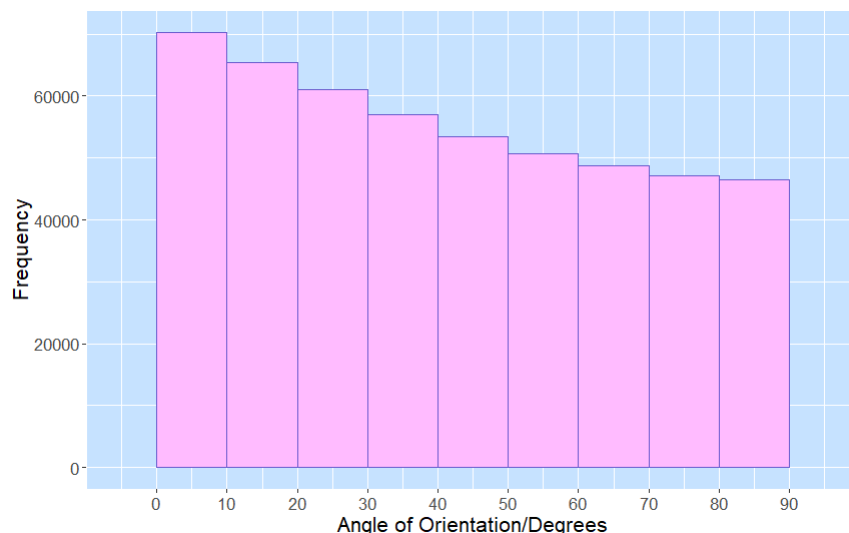


Figure 2.12: Orientation of Actin Rods in a Cylinder Containing a Microtubule Array. *This simulation contains 500 non-crosslinking actin rods which can move freely within a cylindrical shell region surrounding a microtubule array. The graph shows the distribution of angles of orientation with a zero angle relating to an actin rod aligned with the longitudinal axis of the cylindrical space, and 90 degrees being perpendicular to this axis.*

smaller angles, with the frequency of each orientation declining as angle increases towards its maximum value of 90° .

When viewing the set of 4 example distributions shown in Figure 2.13, we observe higher occurrences at small angles of $0 - 20^\circ$ fairly consistently across each of the simulations, despite some variations at larger angles.

As we have substantially restricted the radial space available to our rods, it is logical that we see a greater level of alignment with the longitudinal axis as opposed to the isotropic orientations observed in a cylindrical cell without a microtubule array.

2.6.3 Radial Positioning

We analyse the radial position of our rods as previously. Results are shown in Figure 2.14; we plot a histogram displaying the number of actin points within each 5 nm radial range from 135 – 200 nm as a density per cubic μm of cell volume. The highest densities of actin points occur between around 160 – 170 nm, with very low numbers in the regions close to the outer boundary, or adjacent to the microtubule array surface.

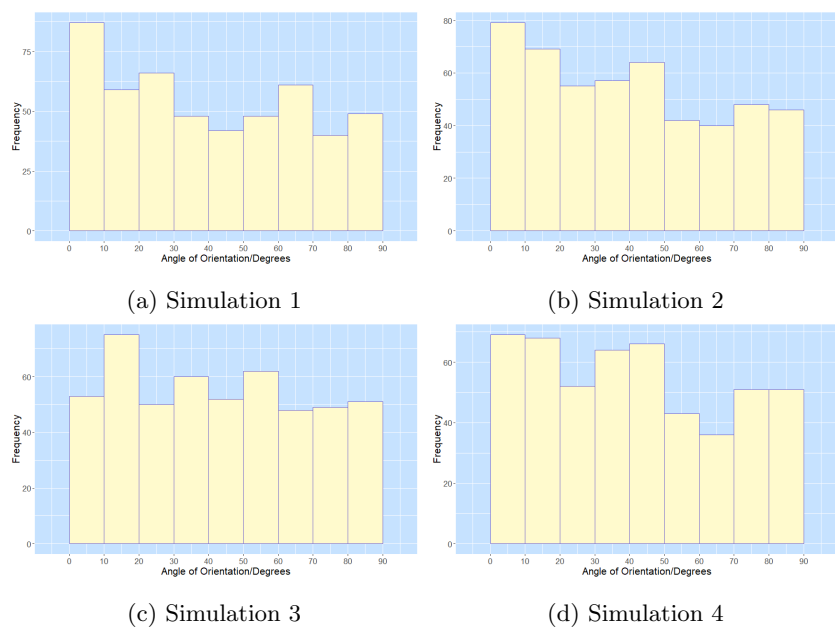


Figure 2.13: Orientation of Actin Rods in a Cylinder Containing a Microtubule Array. Each of the 4 individual simulations shows a higher frequency at small angles with respect to the longitudinal axis.

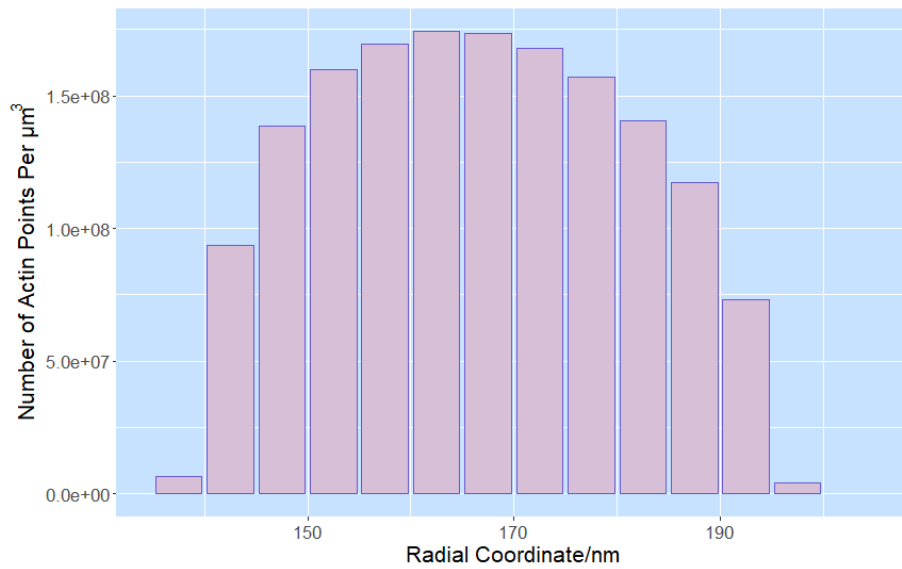


Figure 2.14: Radial Distribution of Actin Rods in a Cylindrical Cell Containing a Microtubule Array. *Actin points are shown as a density per cubic μm of cell space for each 5 nm radial range, however a microtubule array occupies a radius of 135 nm, reducing the available space substantially. Graphs show a higher density of actin points close to the centre of available space, with the cylindrical shell between radii of 160 - 170 nm being most densely populated.*

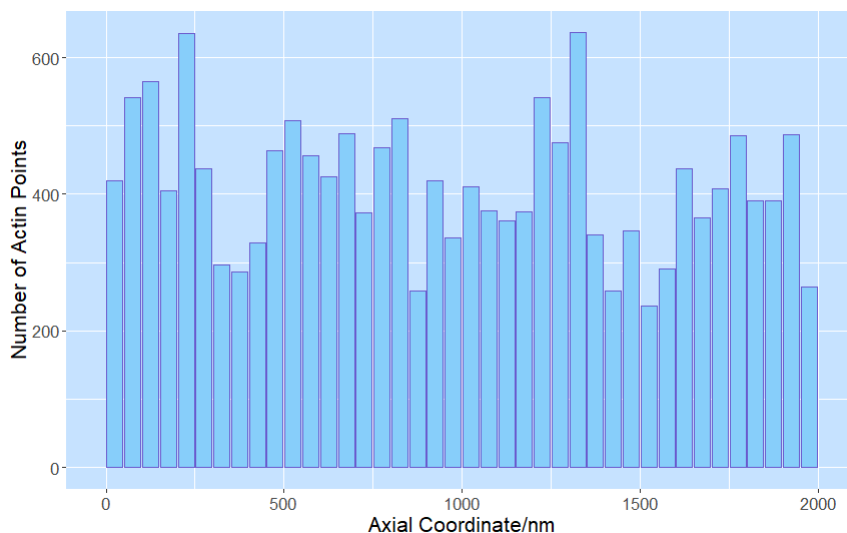


Figure 2.15: Axial Distribution of Actin Rods Within a Cylinder Containing a Microtubule Array. *The number of actin points within 50 nm axial regions are displayed with data combined from 1000 repeat simulations of 500 actin rods each.*

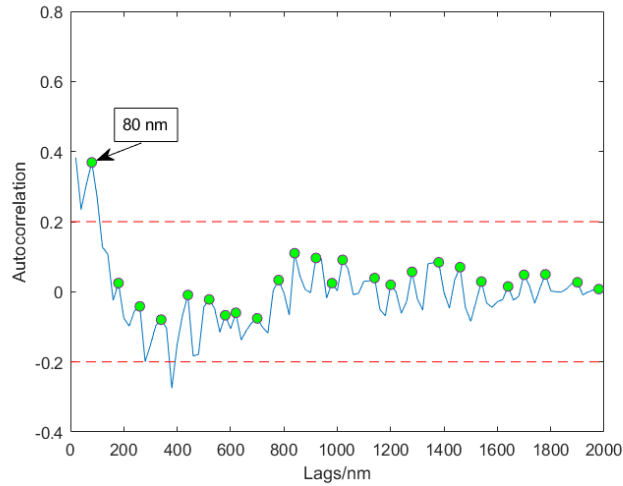
2.6.4 Axial Positioning

We display the axial position of actin rod points in Figure 2.15. As previously, this graph shows large peaks and troughs at certain locations, with variations of over 400 points between different coordinate ranges, although no clear pattern is visible.

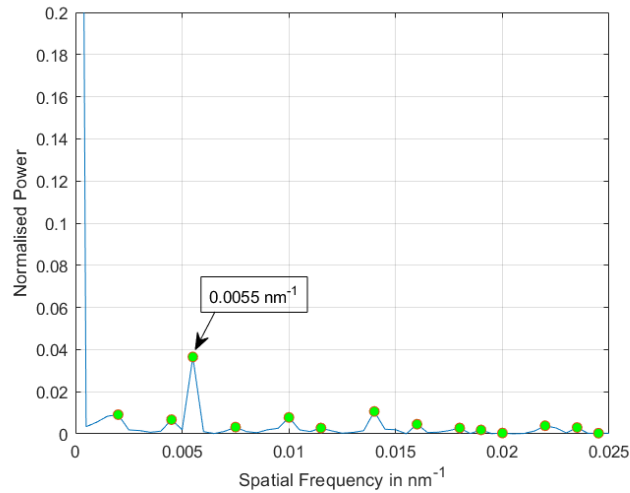
To investigate the distribution further, we carry out autocorrelation analysis as previously. The maximum autocorrelation amplitude found in this sample was 0.369, with a minimum of 0.0953 and mean of 0.187 to 3 significant figures. Details of specific peaks are shown in Table 2.2. The numbers of small peaks exceeding 0.1 in magnitude, and reaching up to 0.2, were similar to the results of Section 2.5.4, while larger peaks were slightly more common when a microtubule array was present.

We calculate the power as previously, finding a maximum power amplitude of 0.0365 to 3 significant figures, and a mean of 0.00128. These results are very close to the values found in simulations without a microtubule array.

To visualise these results, we plot autocorrelation and power for the individual simulations corresponding to the largest magnitudes of these measures, displaying results in Figure 2.16. In Figure 2.16a, we see a peak in the autocorrelation amplitude of 0.369, corresponding to a lag of 80 nm. Figure 2.16b shows power with a peak of 0.0365 in magnitude at a frequency of 0.0055 nm^{-1} , with a corresponding wavelength of 182 nm.



(a) Autocorrelation - Simulation 796. A peak of 0.369 is shown at a lag of 80 nm.



(b) Power with Spatial Frequency - Simulation 124. A peak in normalised power of 0.0365 is shown at a low frequency, corresponding to wavelength of 182 nm.

Figure 2.16: Periodicity of Actin Rods in a Cylindrical Cell Containing a Microtubule Array. We show results for autocorrelation and power for the simulations which contained peaks of the greatest magnitude in each case. These results are low in magnitude, indicating a lack of significant periodicity.

Table 2.2: Autocorrelation of Actin Rods in a Cylindrical Cell Containing a Microtubule Array. *This table details the total number of peaks at within stated ranges of autocorrelation amplitude, as well as the minimum, maximum, and mean numbers of peaks within individual simulations.*

Autocorrelation Amplitude, a	Number of Peaks			
	Total	Min	Mean	Max
$0.1 < a \leq 0.2$	4425	0	4.43	10
$0.2 < a \leq 0.3$	406	0	0.406	4
$0.3 < a \leq 0.4$	15	0	0.015	2

While the inclusion of a microtubule array does increase the number of autocorrelation peaks slightly, there are still very few significant peaks within our data, and the power result also remains very small. Again, we find no evidence of periodic organisation.

2.7 Crosslinking Actin Filaments

Here we adopt the environment of Section 2.6, containing a microtubule array, but enable more complex interactions by allowing actin rods to crosslink with one another. As previously we run for 2.5×10^5 steps with 1000 parallel simulations.

As described in Sections 2.3.1 and 2.3.2, crosslink formation is a probabilistic event which can occur in place of a positional or orientational move with a probability of $\left(\frac{1}{11}\right)$ at each step in the random walk. The number of links formed therefore varies between repeat simulations. For this set of 1000 simulations, the mean number of crosslinks formed between the 500 actin rods was 1144, with a range of 872 – 1545.

2.7.1 Simulation Images

The example images relating to crosslinking actin filaments are shown in Figure 2.17. For clarity, only rods which have formed links with others are shown in these images, with 294 of the 500 rods meeting this criteria. Linked bundles appear to consist mainly of pairs of rods, with few larger structures visible. Again, there is no clear pattern, and linked rods continue to maintain a range of orientations, often perpendicular to the rod with which they are linked.

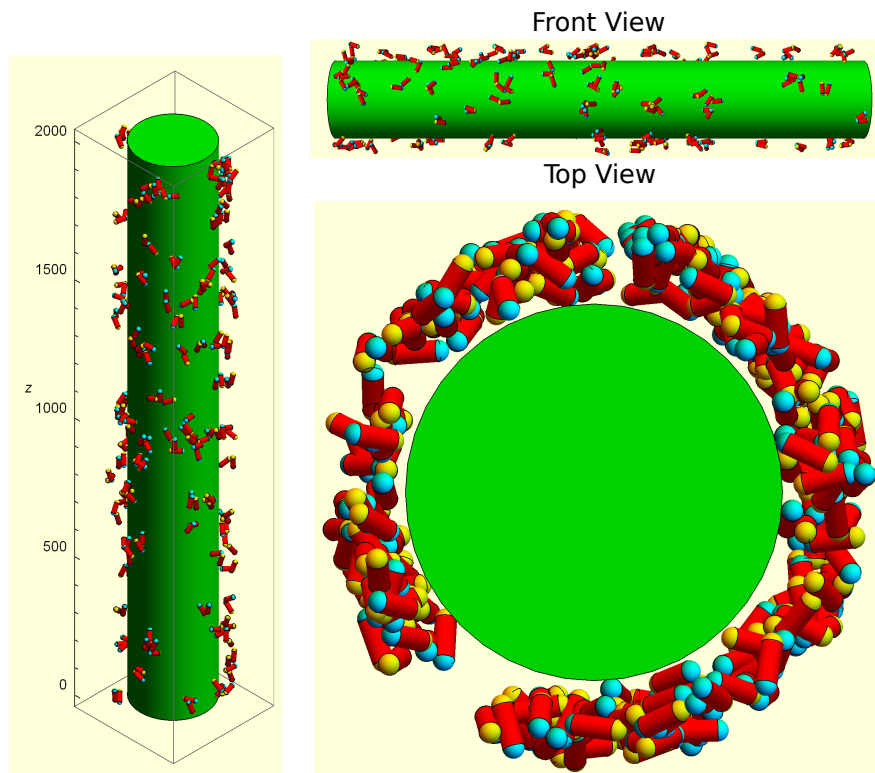


Figure 2.17: Actin Rods within a Cylindrical Shell with Crosslinking Interactions. *This simulation contains crosslinking actin rods which can move freely within a cylindrical shell space. A microtubule array blocks out the centre of the cylinder as shown in green, and rods are not able to access this region. Only the 294 linked rods are shown in these images.*

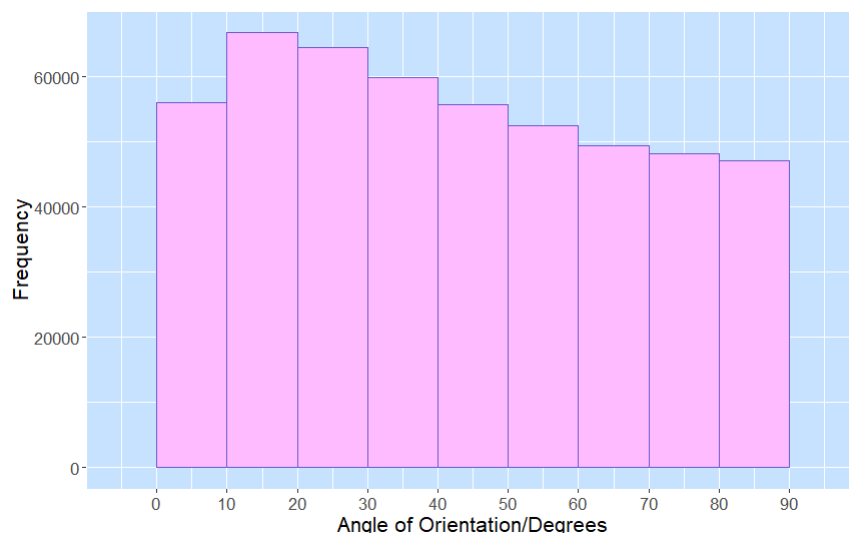


Figure 2.18: Orientation of Crosslinking Actin Rods in a Cylindrical Cell Containing a Microtubule Array. *This simulation contains 500 crosslinking actin rods which can move freely within a cylindrical shell region surrounding a microtubule array. The graph shows the distribution of angles of orientation with a zero angle relating to an actin rod aligned with the longitudinal axis of the cylindrical space, and 90 degrees being perpendicular to this axis.*

2.7.2 Angle of Orientation

We display the distribution of angles of orientation in Figure 2.18. Here we see a maximum frequency at angles of $10 - 20^\circ$, with a reduction in frequency with increased angle beyond this point. This is slightly different to the non-crosslinked actin rods of Section 2.6. It is difficult to interpret the reason for the reduced frequency at angles of $0 - 10^\circ$ in this case, however it is likely to be connected to the formation of larger actin structures; while free rods show a tendency to move towards configurations in which they align with the longitudinal axis of the cell, connected rods may be unable to do so if they become fixed at a large angle to their partners. For all connected rods, including those which align in parallel, the increased size and altered shape of their combined structure may also alter their preferred orientational alignment.

Distributions from individual simulations are shown in Figure 2.19. Figures 2.19b - 2.19d each have a maximum frequency in the $10 - 30^\circ$ range which corresponds well with the combined data of Figure 2.18.

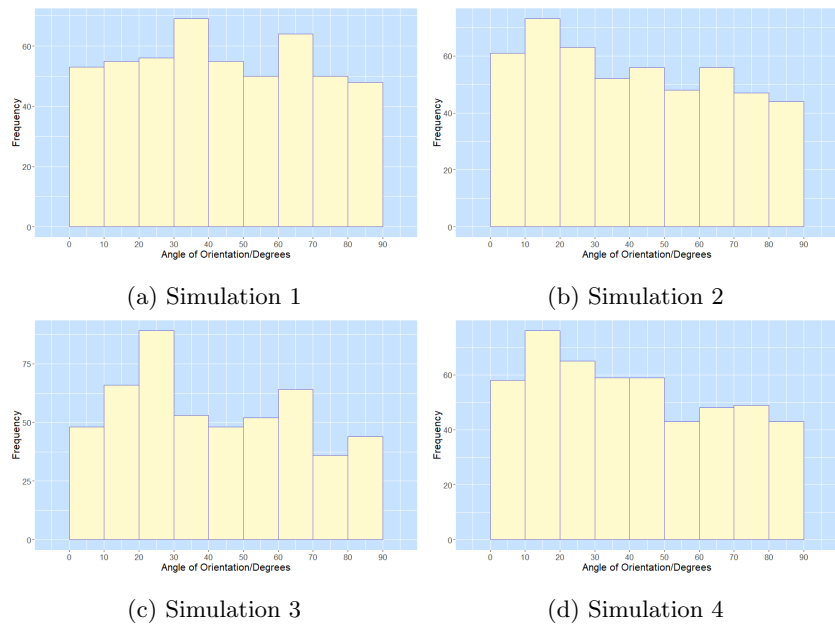


Figure 2.19: Orientation of Crosslinking Actin Rods in a Cylindrical Cell Containing a Microtubule Array - Individual Simulations. *Here we show the distribution of the angle of orientation for 4 individual simulations, each containing 500 actin rods.*

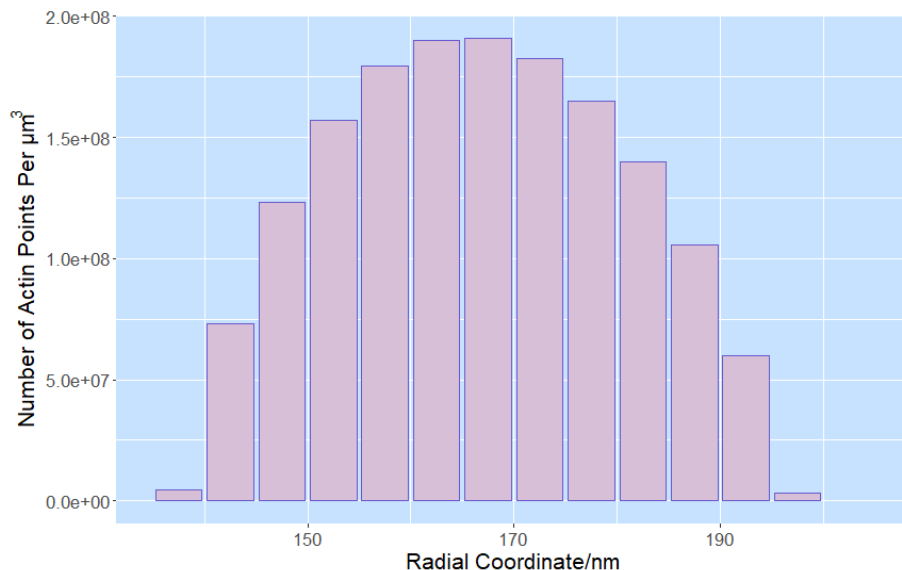


Figure 2.20: Radial Distribution of Crosslinking Actin Rods in a Cylindrical Cell Containing a Microtubule Array. *Actin points are shown as a density per cubic μm of cell space within each 5 nm radial range. The rods appear most dense within the radial range of 160 - 170 nm, close to the centre of available space.*

2.7.3 Radial Positioning

The radial position distribution is shown as a density per cubic μm in Figure 2.20. These distributions appear similar to those of non-crosslinking rods in a cell with a microtubule array. These results would suggest that crosslinking does not significantly influence the radial position of actin rods.

2.7.4 Axial Positioning

We display the axial position of actin rod points in Figure 2.21. This graph shows a large dip at 500 – 600 nm, and peaks of over 600 actin points at 4 locations of 250 – 300 nm, 700 – 750 nm, 1250 – 1300 nm, and 1850 – 1900 nm.

Autocorrelation analysis on this set of simulations yielded a maximum amplitude of 0.383, with minimum of 0.106 and mean of 0.190. These values are slightly larger than those obtained in simulations without crosslinking. Details of specific peaks are shown in Table 2.3. The numbers of the smallest peaks is reduced in comparison to the results of Sections 2.5.4 and 2.6.4, with a small increase in larger peaks.

We calculate the power as previously, finding a maximum power amplitude

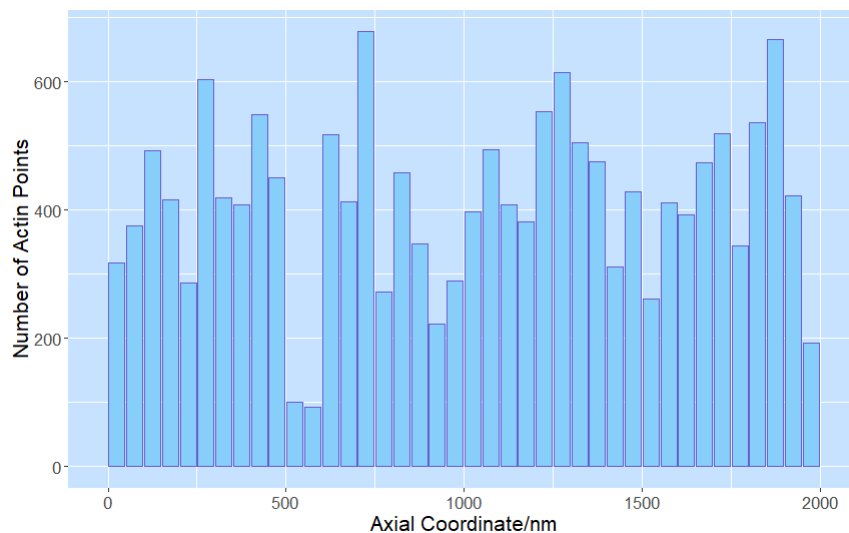


Figure 2.21: Axial Distribution of Crosslinking Actin Rods Within a Cylinder Containing a Microtubule Array. *The number of actin points within 50 nm axial regions are displayed with data combined from 1000 repeat simulations of 500 actin rods each.*

Table 2.3: Autocorrelation of Crosslinking Actin Rods in a Cylindrical Cell with Microtubule Array. *This table details the total number of peaks at within stated ranges of autocorrelation amplitude, as well as the minimum, maximum, and mean numbers of peaks within individual simulations.*

Autocorrelation Amplitude, a	Number of Peaks			
	Total	Min	Mean	Max
$0.1 < a \leq 0.2$	4269	0	4.27	10
$0.2 < a \leq 0.3$	426	0	0.426	3
$0.3 < a \leq 0.4$	22	0	0.022	1

of 0.0530 to 3 significant figures, and a mean of 0.0159. These values are slightly increased when compared to non-crosslinking results.

We plot autocorrelation and power for the individual simulations corresponding to the largest magnitudes of these measures, displaying results in Figure 2.22. In Figure 2.22a, we see a peak in the autocorrelation amplitude of 0.383, corresponding to a lag of 140 nm, followed by a further 3 consecutive peaks of over 0.2 in magnitude, occurring at 280, 440, and 580 nm. This simulation result does appear to show some long range periodicity with an average wavelength of 145 nm. To look into this further, we plot the power of this simulation (results not shown), however, while the plot does indicate a peak at 143 nm, it is of a small magnitude at 0.0142. Figure 2.22b shows power for the simulation with the maximum magnitude from this set, with a peak of 0.0530 at 0.004 nm^{-1} , which corresponds to a wavelength of 250 nm.

These results for crosslinked actin did show some interesting properties, with small increases in the numbers of larger peaks, and at least one simulation showing some long-range periodicity, however, the vast majority of simulations did not show any evidence of significant periodicity.

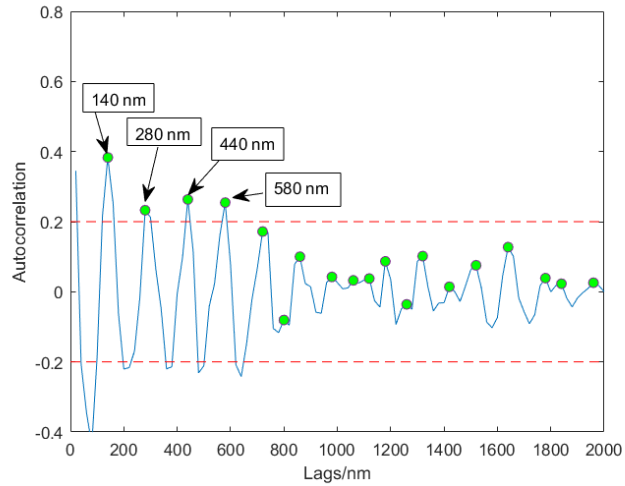
2.8 Crosslinking Actin and Spectrin

In these simulations, we allow actin to link to both other actin rods, and also to spectrin tetramers which have properties as defined in Section 2.2.3. Simulations included 500 actin rods, and 500 spectrin tetramers. We run for 2.5×10^5 steps, with 1000 repeat simulations.

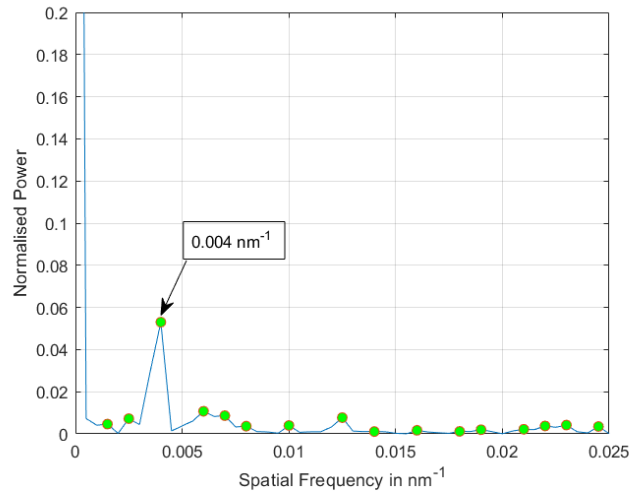
Crosslinks between actin and other actin or spectrin are attempted as described in Sections 2.3.1 and 2.3.2 and the number of links therefore varies between repeat simulations. At the final step of our simulation, the mean number of actin-spectrin crosslinks was 273.1, with a range of 226 – 236, while actin-actin crosslinks had a mean number of 773.5, and a range of 568 – 1056. The number of actin-actin crosslinks is reduced compared to Section 2.7 due to competition with spectrin for binding sites.

2.8.1 Simulation Images

In Figure 2.23 we see an example simulation with links between both actin and spectrin. We represent spectrin tetramers as purple cylinders in these images, and plot only those spectrin tetramers and actin rods which are connected, either directly or indirectly. Many spectrin rods appear to be aligned with the longitudinal axis of the cell, likely due to space constraints within the cylindrical shell region available. No clear positional patterning is observable in these images.



(a) Example Autocorrelation. A peak of 0.383 is shown at a lag of nm, followed by 3 smaller peaks.



(b) Example Power with Spatial Frequency. A peak in normalised power of 0.0530 is shown at low frequencies, corresponding to wavelength of 250 nm.

Figure 2.22: Periodicity of Crosslinking Actin Rods in a Cylindrical Cell Containing a Microtubule Array. We show results for autocorrelation and power for the simulations which contained peaks of the greatest magnitude in each case. Some degree of periodicity is observable within these simulations.

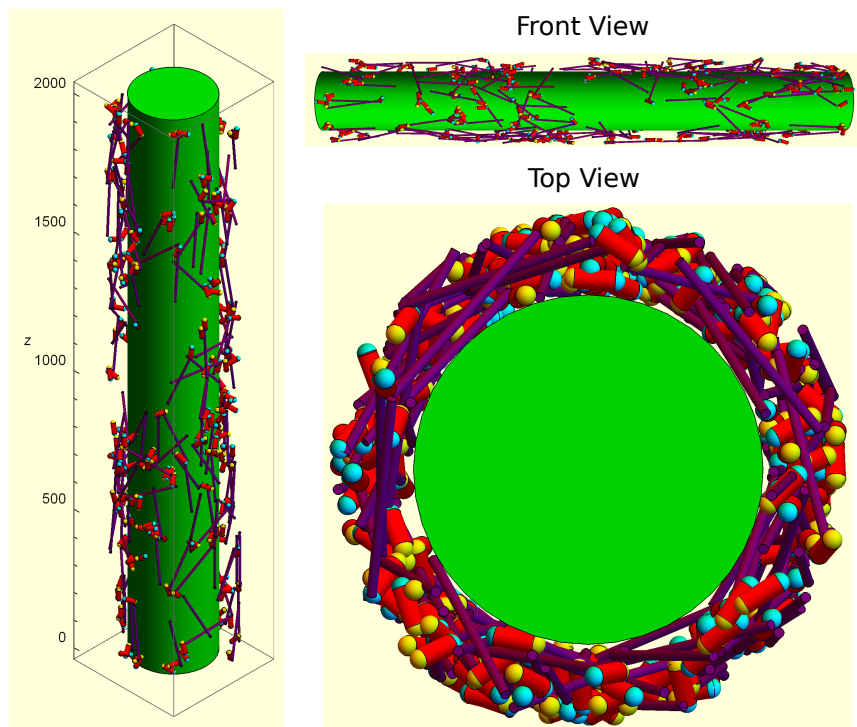


Figure 2.23: Actin Rods within a Cylindrical Shell with Actin-Actin and Actin-Spectrin Interactions. *Spectrin rods are shown in purple. For clarity, only those actin rods and spectrin tetramers which have formed direct/indirect links are shown in these images. There are 300 actin filaments, and 172 spectrin tetramers shown.*

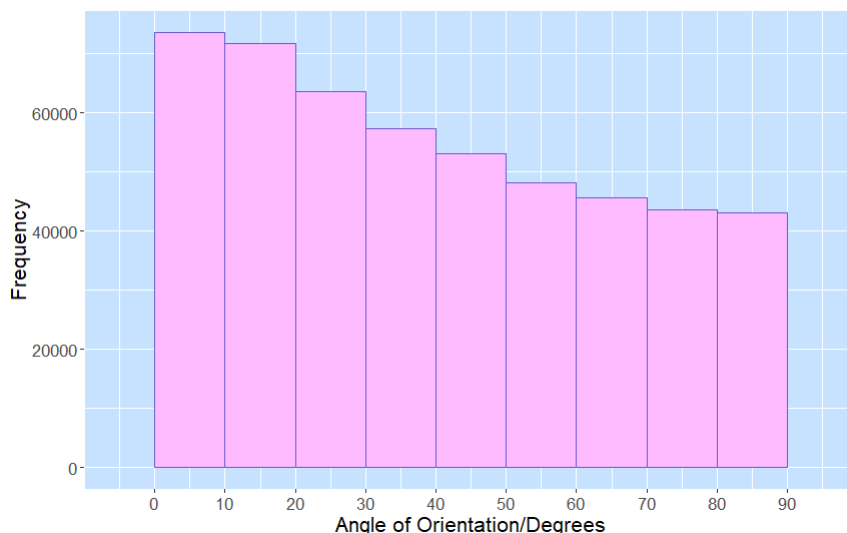


Figure 2.24: Orientation of Crosslinking Actin Rods Interacting with Spectrin in a Cylindrical Cell Containing a Microtubule Array. *This simulation contains 500 crosslinking actin rods which can move freely within a cylindrical shell region surrounding a microtubule array, while also crosslinking to spectrin tetramers. The graph shows the distribution of angles of orientation with a zero angle relating to an actin rod aligned with the longitudinal axis of the cylindrical space, and 90 degrees being perpendicular to this axis.*

2.8.2 Angle of Orientation

As in previous sections, we assess the angle of orientation of all actin rods within our simulations. These rods may be linked to actin, to spectrin, or to both, either directly or indirectly. We show results in Figure 2.24; the highest frequency occurs at angles of between $0-10^\circ$, falling with each subsequent angle range, and reaching a minimum at $80-90^\circ$.

Individual profiles are shown in Figure 2.25; in all cases the angles of $0-20^\circ$ are most common, indicating a high level of alignment with the longitudinal axis of the cylindrical cell space, as observed in the composite data of Figure 2.24.

2.8.3 Radial Positioning

The radial position distribution is shown as a density per cubic μm in Figure 2.26. These distributions appear similar to those of both non-crosslinking, and cross-linking actin rods in a cell with a microtubule array. The presence of spectrin tetramers to which actin can bind does not appear to influence the

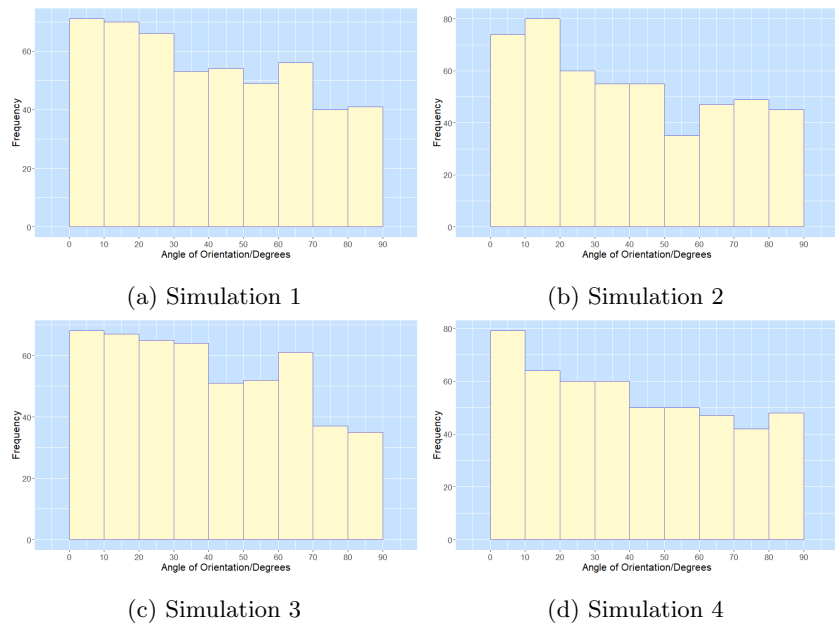


Figure 2.25: Orientation of Crosslinking Actin Rods Interacting with Spectrin in a Cylindrical Cell Containing a Microtubule Array - Individual Simulations. Here we show the distribution of angle of orientation for 4 individual simulations, each containing 500 actin rods.

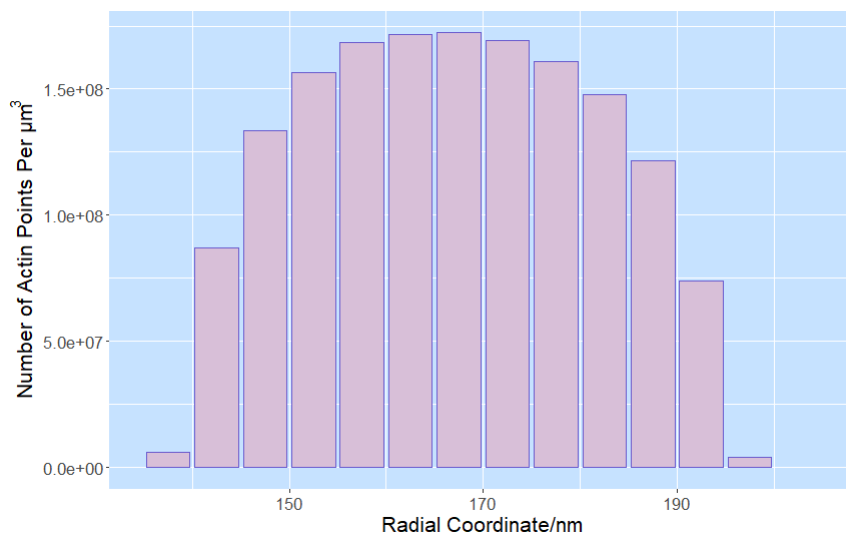


Figure 2.26: Radial Distribution of Crosslinking Actin Rods Interacting with Spectrin in a Cylindrical Cell Containing a Microtubule Array. *Actin points are shown as a density per cubic μm of cell space within each 5 nm radial range. As in the case of crosslinking rods without spectrin, rods appear most dense within the radial range of 160 - 170 nm, close to the centre of available space.*

radial distribution of actin.

2.8.4 Axial Positioning

We display the axial position of actin rod points in Figure 2.27. This graph shows large peaks at 700 – 750 nm and of 1150 – 1200 nm.

We perform autocorrelation analysis, finding a maximum amplitude of 0.345, with minimum of 0.0853 and a mean of 0.186. These values are slightly lower than those found for crosslinking actin without spectrin in Section 2.7.4. Details of specific peaks are shown in Table 2.4. Relative to crosslinking actin without spectrin, the smallest peaks have increased in number, while the numbers of larger peaks has diminished.

We found that the power had decreased slightly relative to the results in Section 2.7.4, for crosslinked actin without spectrin, with a maximum power of 0.0426, and mean of 0.0138.

We plot autocorrelation and power for the individual simulations corresponding to the largest magnitudes of these measures, displaying results in Figure 2.28. In Figure 2.28a, we see a peak in the autocorrelation amplitude of 0.345, corresponding to a lag of 400 nm. Figure 2.28b shows power for the simulation with the maximum magnitude from this set, with a peak of 0.0426 at 0.0065 nm^{-1} ,

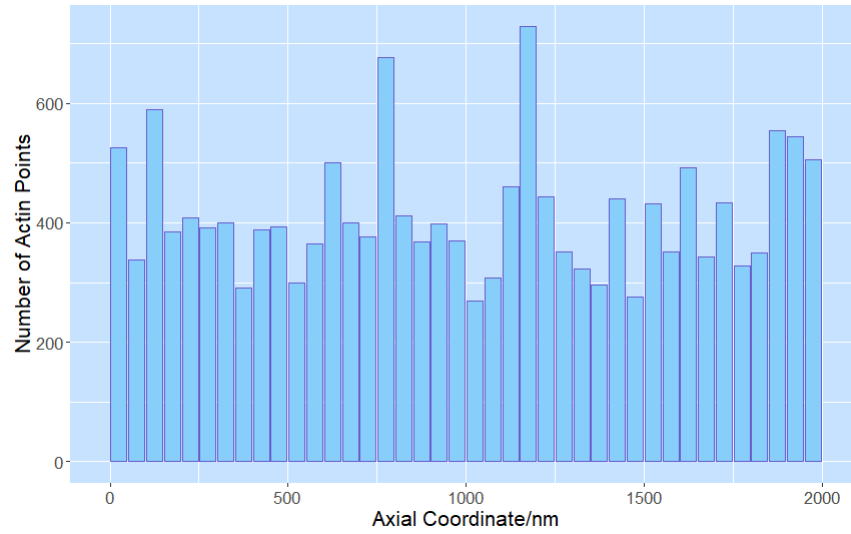


Figure 2.27: Axial Distribution of Crosslinking Actin Rods Interacting with Spectrin Within a Cylinder Containing a Microtubule Array. *The number of actin points within 50 nm axial regions are displayed with data combined from 1000 repeat simulations of 500 actin rods each.*

Table 2.4: Autocorrelation of Crosslinking Actin Rods Interacting with Spectrin in a Cylindrical Cell Containing a Microtubule Array. *This table details the total number of peaks at within stated ranges of autocorrelation amplitude, as well as the minimum, maximum, and mean numbers of peaks within individual simulations.*

Autocorrelation Amplitude, a	Number of Peaks			
	Total	Min	Mean	Max
$0.1 < a \leq 0.2$	4540	0	4.54	11
$0.2 < a \leq 0.3$	372	0	0.372	3
$0.3 < a \leq 0.4$	14	0	0.014	1

which corresponds to a wavelength of 154 nm.

As in previous sections, we do not find evidence of significant levels of periodicity, with some degree of periodic organisation present in few simulations.

2.9 Discussion

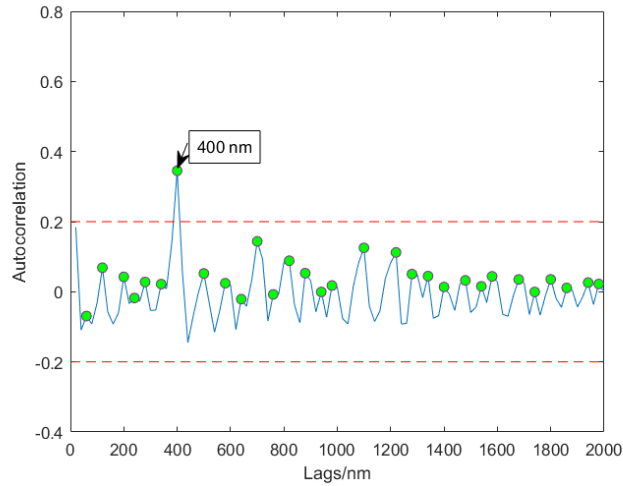
In this Section, we investigated 4 simple model systems. We included several features of the axonal cytoskeleton; short actin rods of fixed length were introduced to a cylindrical cell, a microtubule array was placed into the core of the cell, actin rods were able to crosslink into larger structures, and finally, spectrin tetramers were introduced in the form of long, thin, rigid rods to which actin could crosslink.

In each scenario we performed a random walk of 2.5×10^5 steps, running 1000 parallel simulations, and seeking an MPS-like configuration in terms of radial positioning, axial periodicity, and orientation within the circular plane of the cell.

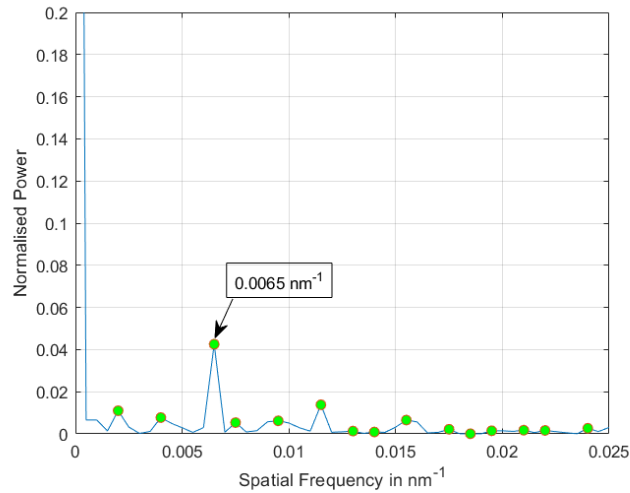
In the results of this Section, we did not find any evidence of MPS self-assembly within our simple model; actin rods tended to show high levels of alignment with the longitudinal axis of our cell, and were positioned within the centre of available radial space, far from inner and outer boundaries. We also did not detect significant periodicity except in isolated cases.

While this model was greatly simplified, the results indicate that it is highly unlikely that the MPS structure would assemble purely based on the cylindrical morphology of the axon as has been previously considered (Qu et al. (2017)). This suggests that the structure is assembled through a more complex path of active development, perhaps relying on a series of specific protein interactions which are signalled and modulated to generate such a structure in developing neurons. When considering evidence of the many roles of the MPS discussed in Section 1.4, it may be that the structure is specifically created in this ordered arrangement to serve a purpose, conveying benefits to the cell such as superior mechanical properties.

In the Chapters that follow, we continue to investigate MPS self-assembly. Creating a more complex model, we attempt to detect properties and parameters which could influence both ring formation and periodic organisation.



(a) Autocorrelation - Simulation 642. A peak of 0.345 is shown at a lag of 400 nm.



(b) Power with Spatial Frequency - Simulation 499. A peak in normalised power of 0.0426 is shown at low frequencies, corresponding to wavelength of 154 nm.

Figure 2.28: Periodicity of Crosslinking Actin Rods Interacting with Spectrin in a Cylindrical Cell Containing a Microtubule Array. We show results for autocorrelation and power for the simulations which contained peaks of the greatest magnitude in each case.

Chapter 3

Self-Assembly of a Single Actin Filament Ring

3.1 Introduction

In Chapter 2 we found that actin filaments did not spontaneously assemble into ordered structures based on their interaction with spectrin and the cylindrical geometry. In fact, even these short actin filaments had a strong tendency to align with the longitudinal axis of the cylinder and occupy the central regions of available space. This is in stark contrast to the membrane-adjacent ordered rings oriented within the circular plane that are observed in the MPS. How could this type of arrangement occur?

The previous model was simplistic, and while useful to show how systems of filaments could interact with the geometry of the axon, it lacked several biologically realistic details which may influence self-assembly, for example:

- While limited flexibility was possible through rotation of crosslinked actin filaments, the previous model considered both actin and spectrin in the rigid rod limit. This assumption was beneficial to the speed of calculation, however flexibility may play a role in conforming to tubular geometry; a recent imaging study found MPS-based actin lengthscales of $\sim 1\mu\text{m}$ (Vassilopoulos et al. (2019)) - longer than the few tens of nm previously inferred. Actin persistence lengths are measured experimentally at $\sim 2 - 18\mu\text{m}$ (Gittes et al. (1993), Isambert et al. (1995), McCullough et al. (2008)), with persistence length possibly reduced further via protein modification, suggesting flexibility may become a factor. Flexibility is less important for spectrin as our estimated stiffness detailed in Section 3.2.8 corresponds to a persistence length far greater than the length of a spectrin tetramer.

- Crosslinks were represented by the conservation of distance between connected points alone, with this inflexible connection leading to rigid body motion of connected fibres. This is likely to underestimate the flexibility of links between cytoskeletal filaments.
- Actin filaments were assumed to be of fixed length due to the presence of capping proteins which were modelled implicitly, however in early growth stages filaments are dynamic, and initial polymerisation stages within the cell environment may be important in influencing final configuration.
- Membrane interactions were passive, modelled simply as a restriction preventing fibres from leaving the cell space, however actin and spectrin are understood to bind to the membrane, and this attachment may help to shape the MPS.

In this chapter, we aim to extend the results of Chapter 2, developing a more detailed model which includes biologically realistic features such as flexibility of fibres and crosslinks, growth dynamics, and membrane binding. For speed of calculation and simplicity of interpretation, we initially neglect the periodic organisation of multiple filaments, instead focusing on the self-assembly of a single actin ring. We simulate an individual actin filament within a cylindrical axon-like environment, aiming to investigate the following questions:

1. What is the natural configuration of an actin filament within a cylindrical geometry? Is there a qualitative difference between a single, long filament, and the systems of connected short filaments used in Chapter 2?
2. Given that stiffness can be modified by various actin binding proteins, how does filament stiffness influence configuration?
3. How does this configuration differ if actin is able to bind to the membrane?
4. How does the presence of membrane-bound spectrin tetramers influence actin filament configuration? Does this change significantly if the density of spectrin is altered?
5. Is it possible to form actin rings if there are additional aligning factors? These may influence actin directly by aligning actin binding proteins, or indirectly through alignment of spectrin.
6. What impact, if any, does in cell nucleation and polymerisation have on the final configuration of actin?

We begin in Section 3.2 with a description of the methods used for simulation and data analysis. In Section 3.3 we investigate single actin filaments of a fixed length, observing how configuration within a short axon segment changes as their stiffness is varied. In Section 3.4 we introduce a large number of randomly placed proteins which can link actin to the membrane and investigate whether membrane tethering is sufficient to create rings of actin. We introduce spectrin

tetramers in Section 3.5, varying both actin stiffness and the density of spectrin present, observing the range of configurations generated by these interactions. In Section 3.6 we try a different approach, placing actin binding proteins in a ring around the membrane to determine whether ring formation is likely when interacting with ideally placed proteins. Finally in Section 3.7, we repeat the investigations of Section 3.5, however we make our actin filament dynamic, nucleating the filament within the cell and allowing it to polymerise at several rates. We discuss the results of this Chapter in Section 3.8.

3.2 Methods

In silico modelling of complex biological systems is challenging and it is difficult to balance the requirements for speed of calculation with the desire to include as many details as possible. Our requirements of a software package include flexible fibres, probabilistic nucleation, dynamic filament length, ability to add proteins which can connect and interact with specific fibres and also with surfaces such as the membrane, and capacity to introduce motor proteins which can step from site to site along a filament. While the system explored in this chapter is relatively simple, large-scale simulations are carried out in the chapter that follows, and it was essential that the software package used was able to calculate rapidly to cope with the quantities of filaments and other proteins which must be considered at each time step.

In Chapter 2, we wrote custom software to model our system. At the time of beginning this work our requirements were not clear due to the complexity and rapid development of the field, we therefore developed our own software to allow maximum flexibility to adapt as necessary as we developed our ideas on which components and properties to include. After revisiting our requirements at the beginning of the work of this Chapter, we chose to alter our approach, using the open source software package, Cytosim (Nedelec and Foethke (2007)). Three main factors influenced this decision:

- We had identified several biological processes which we wished to include in the model, including nucleation and polymerisation of filaments, and the ability to link filaments to the membrane.
- Our assumption of short actin filaments and subsequent neglect of their flexibility was challenged by new imaging results of (Vassilopoulos et al. (2019)), as explained in Section 1.3.3.
- Performance of our custom software was poor despite incorporations of techniques to increase speed of calculation.

Our software would require a substantial amount of further development to address the factors listed above, however Cytosim provided a good fit with many of our requirements, incorporating a range of biological processes such as filament nucleation and polymerisation, allowing fibre flexibility, and providing

rapid calculation speeds. Use of existing software imposed some limitations on our models as certain features were not implemented in the optimum way for our particular system, however this was not a major disadvantage. We give a short overview of the software in this section, explaining the advantages and limitations of this approach. We also discuss data analysis methods developed for this section.

3.2.1 Cytosim software

Cytosim (Nedelec and Foethke (2007)) is an open source software package specifically developed for simulation of the cell cytoskeleton (available at <https://gitlab.com/f-nedelec/cytosim>). In Cytosim, cytoskeletal filaments are represented as fibres which are incompressible and inextensible, but have bending elasticity. These fibres are modelled by a set of vertices, and the distance between points is maintained at each time step. The motion of fibres is described using a first-order Langevin equation, which is a stochastic equation approximating Brownian motion of systems of particles on a scale where viscous forces dominate while inertia is negligible:

$$d\mathbf{x} = \mu F(\mathbf{x}, t)dt + dB(t) \quad (3.1)$$

Here $F(\mathbf{x}, t)$ is a matrix describing the force acting on each fibre coordinate point \mathbf{x} at time t , while $B(t)$ is a stochastic matrix of random forces representing the molecular collisions that lead to Brownian motion. μ is a matrix containing the mobility factor for each fibre coordinate point. This is an approximated mobility based on an average of mobility factors of a straight rod, neglecting anisotropy, and is related to the fibre length and diameter as well as viscosity of the surrounding medium. The equations of motion are discretised using a finite-difference scheme; an implicit integration scheme is employed where equations are solved based on $x_{t+\tau}$ as opposed to x_t as used in explicit integration schemes. The equations are linearised and solved iteratively using a biconjugate gradient stabilised method. This approach is computationally intensive, however offers an improvement in numerical stability over explicit schemes, allowing larger timesteps to be used. A reshaping method is applied to re-establish constraints affected by the linearisation process. A more detailed explanation of the procedure is available in Nedelec and Foethke (2007).

In addition to Brownian motion of cytoskeletal filaments, Cytosim offers a range of stochastic events to represent realistic biological processes. Fibres can be nucleated, or can grow or shrink with a probability dependent upon rates set by the user. Fibres can also be acted upon by associated proteins, which can connect one or more fibres in a static or dynamic manner, representing crosslinking or motor proteins found in cellular systems. Proteins connecting to fibres are modelled as Hookean springs, imposing forces on the vertices to which they are connected. These events are evaluated separately to the main equations of motion, performed as a subroutine at each time step.

Cytosim is an established software package, and the modularity and customisability of this software allows it to be tailored to a wide range of cellular systems. It is a high performance software, able to complete simulations of large multiple filament systems in a relatively short timeframe due to the speed of the implicit integration scheme which allows use of a larger time step than explicit schemes. Cytosim also includes useful visualisation and data reporting tools. The methods used have limitations, as they greatly simplify the properties of cytoskeletal filaments and connecting proteins, neglecting the molecular structure which is likely to influence their properties and dynamics. To mitigate the effect of this limitation, biologically realistic parameters have been assigned to the filaments, proteins, and processes used in the simulations wherever possible.

3.2.2 Data Analysis Methods

The most reliable method of detecting an MPS-like structure is by visual inspection, however this has pitfalls; it can be difficult to see individual filaments in large, multi-component simulations and it is time-consuming and impractical where large quantities of results are generated through varying parameter sets or carrying out multiple repeat simulations. It is also less useful when it comes to comparing simulations that are similar, and so cannot determine small benefits from changing parameter sets.

It is therefore very useful to have quantitative measures of how 'MPS-like' each simulation result is. With this in mind, we define an oriented ring parameter (ORP), which compares each actin filament to an ideal configuration - a filament of equal length, oriented in a circle around the membrane. The method used to do this is described in detail below:

- **Preparing the Data** - Coordinates of the vertices of each filament in the system are output to a text file. The data is imported into Python Version 3.8 and parsed with NumPy (Harris et al. (2020)) to generate an array containing coordinates of actin filament vertices only, numbered to identify those belonging to each fibre. This method is also used to store spectrin coordinates where required.
- **Calculating Values** - Axon radius, R_{axon} , and actin filament length, L_{actin} are input manually, while the number of actin filaments in the system, $n_{\text{filaments}}$, and number of vertices per filament, n_{points} , are obtained from the data. From this information, we calculate the number of segments per fibre ($n_{\text{segments}} = n_{\text{points}} - 1$) and the length of each segment ($L_{\text{segment}} = L_{\text{actin}}/n_{\text{segments}}$). This is then used to calculate the angle in radians subtended by a chord of length L_{segment} as illustrated in Figure 3.1 (upper image) and calculated with the following expression:

$$\Delta\theta = 2 \arcsin \left(\frac{L_{\text{segment}}}{2R_{\text{axon}}} \right) \quad (3.2)$$

- **Reference ORP Calculation** - A set of coordinates is generated, representing a straight filament, α , of length L_{actin} with n_{segments} , each of length L_{segment} , aligned with the longitudinal axis of a cylinder. A target circle, β , is generated representing the straight filament rotated by 90 degrees about its centrepoint and curved around the boundary of the membrane to make a circle perpendicular to the longitudinal axis. Coordinates for this target circle were generated by iterating over the angle increment, $\Delta\theta$ as shown in Figure 3.1 (lower image). In this case only a single test circle is required as both circles give equivalent results. Figure 3.2 shows example α and β filaments with length slightly greater than the circumference of the axon. A measure was then generated representing the magnitude of distance between corresponding pairs of points on these 2 filaments as follows:

$$ORP_{\text{reference}} = \sum_{i=0}^{n_{\text{points}}} \sum_{j \in \{0, n_{\text{points}}\}}^{j=i} \mathbf{x}_i^\beta - \mathbf{x}_j^\alpha \quad (3.3)$$

Where \mathbf{x}_j^α is the coordinates of point j on the straight filament, and \mathbf{x}_i^β is the coordinates of point i on the target circle.

Equation 3.3 gives a reference value of the minimum ORP possible for a straight filament of length L_{actin} .

- **Calculating Possible ORP Values** - for each actin filament, j , in our simulation, we carry out a subroutine, iterating over each point, i , on the actin filament to generate a set of possible ORP values as follows:
 1. **Translating the Actin Filament** - We begin with point i , with coordinates $\mathbf{x}_i = (y, z, x)$ (see Figure 3.2 axes for an illustration of the coordinate system used). We take a line from the central axis of the axon, at coordinates $(0, 0, x)$, passing through this point, and determine its point of intersection with the surface of the membrane, $\mathbf{x}_{\text{intersection}} = (y_{\text{surface}}, x_{\text{surface}}, x)$. We assign starting coordinates for our ORP analysis as $\mathbf{x}_{\text{start}} = (y_{\text{surface}}, x_{\text{surface}}, 0)$ and perform a translation to our actin filament in which we project the i^{th} point to $\mathbf{x}_{\text{start}}$ while preserving the orientation of the filament. This is illustrated in Figure 3.3 (upper) with $i = 0$.
 2. **Test Circle Creation** - A target circle of radius R_{axon} is generated with its i^{th} point coinciding with the coordinates to which the i^{th} point on the actin filament was translated, $\mathbf{x}_{\text{start}}$. The test circle is generated by iterating over the angle, $\Delta\theta$, as shown in Figure 3.2. Each actin filament has a directionality due to the numbering of points, however the directionality is unimportant to our analysis, and is initially unknown. We therefore draw 2 test circles as shown in Figures 3.1 (lower) and 3.3, with Test Circle A proceeding clockwise, and B anticlockwise.

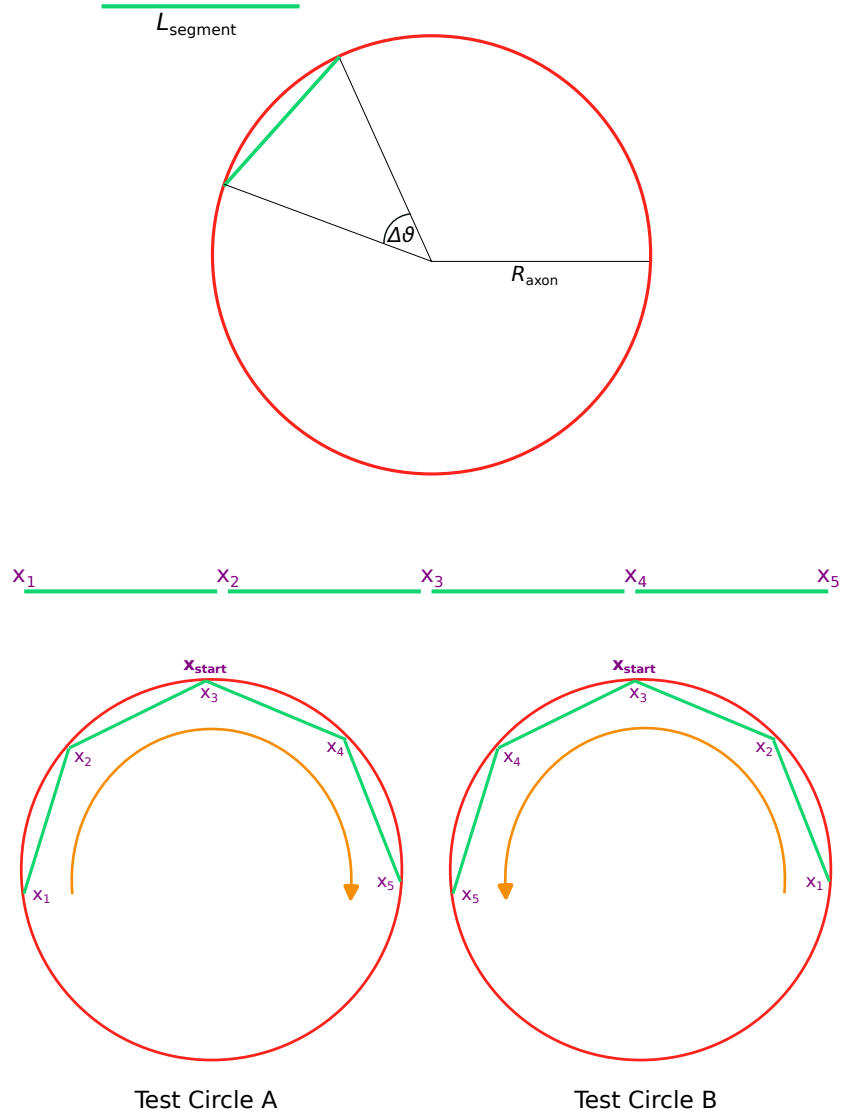


Figure 3.1: Test Circle Generation. *Test circles are created using an angle increment, $\Delta\theta$, as shown in the upper image. In the lower image we create a pair of test circles in opposite senses for a filament with 5 vertices. In this case we begin from the centrepoint of the filament, x_3 and calculate coordinates of the remaining points by iterating over $\Delta\theta$.*

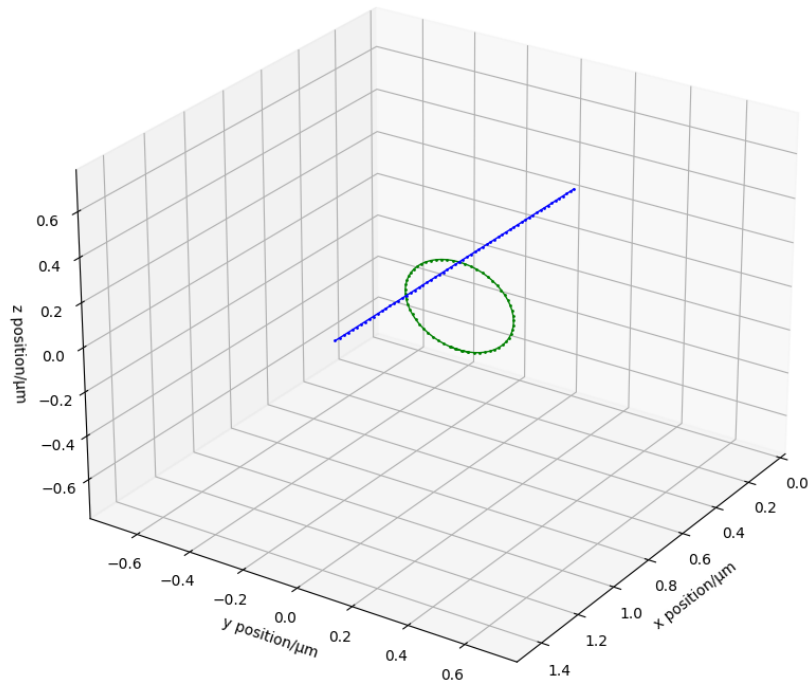


Figure 3.2: Reference ORP Calculation. A straight filament of length L_{actin} is generated and a circular filament of equal length is drawn with centrepoints of both filaments coinciding. Magnitude of distance between corresponding pairs of points is calculated and summed over all points.

3. **ORP Calculation** - For each point on the translated actin filament, the magnitude of distance is calculated between the corresponding point on Test Circle A and these values are summed. This is repeated for Test Circle B and the minimum value is stored in a Numpy array corresponding to actin filament, j , with a starting position of i .

This subroutine is carried out for each point $\in \{0, n_{\text{points}}\}$.

- **Determining the Optimum ORP Value for the Actin Filament** - An optimum ORP value is calculated by finding the minimum ORP measurement based on the data generated in the previous step, which corresponds to the best fit of our actin filament to an ideal oriented ring shape. We normalise this value by dividing by $ORP_{\text{reference}}$, giving a comparison relative to a straight filament oriented with the longitudinal axis of the axon.

Through these steps we obtain an ORP value for each actin filament which quantifies how closely it resembles a circle of R_{axon} oriented perpendicular to the longitudinal axis of the cylindrical cell. The ORP value is fairly intuitive, being approximately 1 for a straight filament, and close to 0 for filaments forming circles around the membrane. Example filament configurations corresponding to a range of ORP values are shown in Figure 3.4. In general, ORP values of < 0.3 are considered of interest. This value was chosen as a threshold after comparison of calculated ORP value and visual inspection of filament configuration for many example simulations. Configurations with ORP values of < 0.3 consistently show moderate to high levels of alignment with the target configuration throughout at least parts of their length. This value was therefore deemed to be a suitable threshold at which to identify cases for which further investigation was warranted.

Visualisation of individual fibres was carried out using Pyplot and Axes3D from Matplotlib Version 3.3.3 and its associated toolkits (Hunter (2007), version available at <https://doi.org/10.5281/zenodo.4268928>). This allowed coordinates of the fibre and its optimised test circle to be plotted, giving a straightforward visual interpretation of the ORP value as per the examples in Figure 3.4.

3.2.3 Cell Environment and Boundary Conditions

A 3-dimensional cylindrical cell was created to represent the axonal environment. R_{axon} was chosen to be $0.2 \mu\text{m}$. This dimension was selected for ease of visualisation and to minimise computation time while remaining within the biological diameter range of $0.1 - 10 \mu\text{m}$ (Perge et al. (2012)). Axons are difficult to simulate due to their high levels of elongation, with even the shortest axons extending $\sim 100 \mu\text{m}$ (Kandel et al. (2000), Chapter 2), so we instead chose to simulate a short segment of a larger axon, using periodic boundary conditions to mimic a larger space. The axon length was set at $L_{\text{axon}} = 2 \mu\text{m}$,

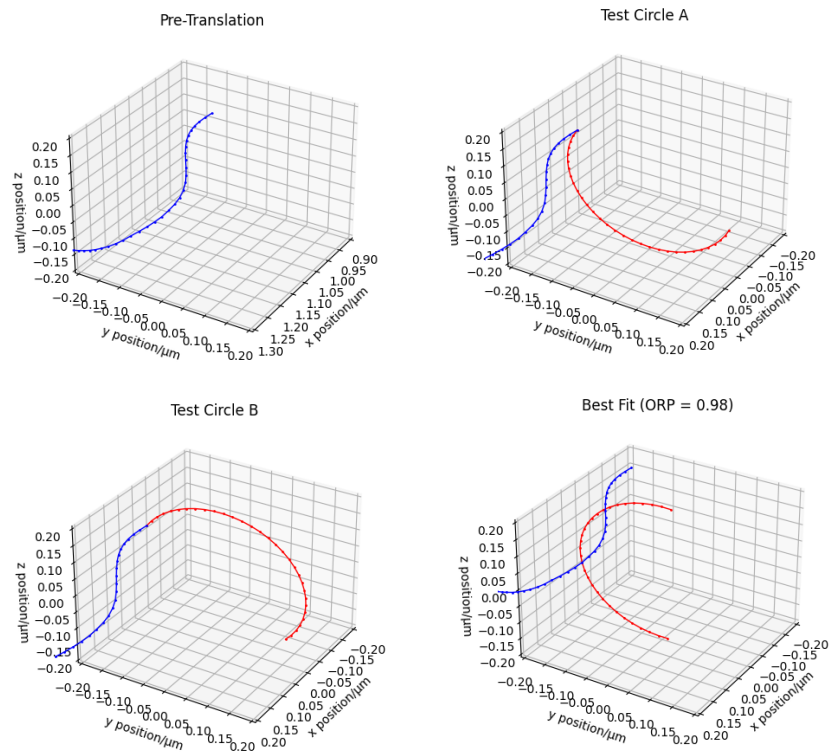


Figure 3.3: ORP Calculation. *The upper left image shows the filament's original positioning within the simulation cell. In the upper right and lower left images, the transformed filament is shown with example test circles in both senses beginning from its endpoint. The lower right image shows the test circle positioned at the point on the filament that gives the minimum value of the ORP calculation.*

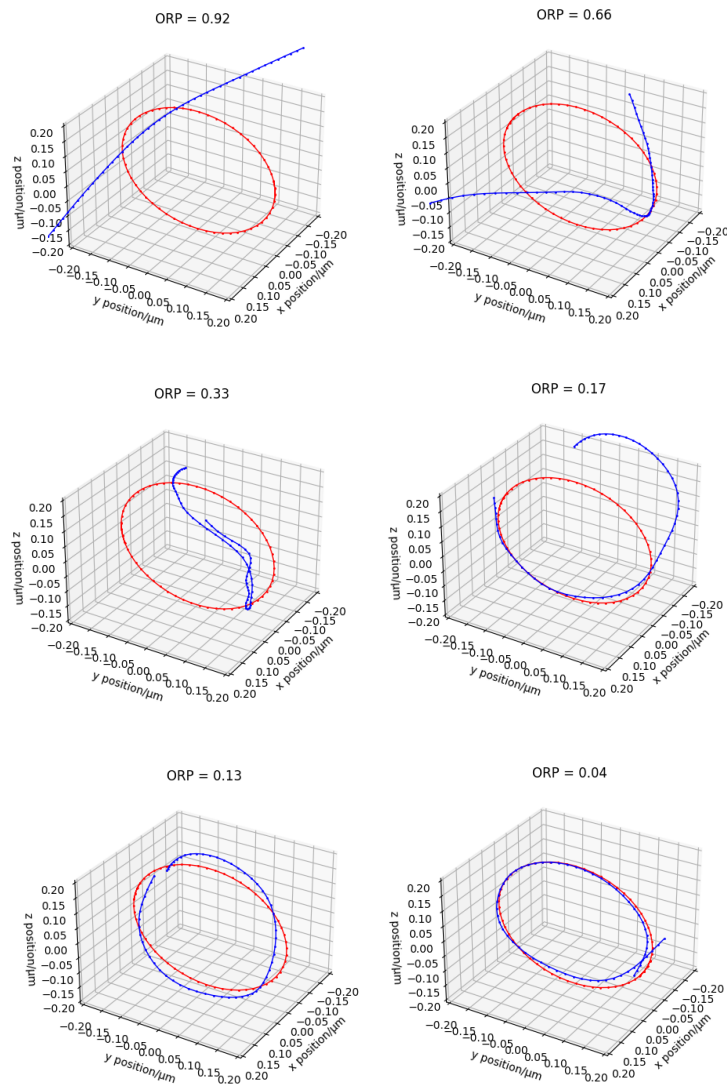


Figure 3.4: ORP Example Values and Corresponding Configurations. *Example actin filament configurations are shown corresponding to a range of ORP values from high (upper images) to low (lower images).*

which is slightly longer than the actin filaments used in this chapter, avoiding any self-interaction across the boundary.

The internal cell environment was set up with a viscosity of $\nu_{\text{axon}} = 1 \text{ pN s } \mu\text{m}^{-2}$ which approximates the internal cell cytoplasm (Kole et al. (2004)).

Temperature in Cytosim is set via a $k_{\text{B}}T$ value in units of $\text{pN } \mu\text{m}$. We use a typical mammalian cell temperature of 37°C (310.15 K) and Boltzmann’s Constant $k_{\text{B}} = 1.380649 \times 10^{-23} \text{ J K}^{-1}$ to arrive at a value of $k_{\text{B}}T = 0.00428 \text{ pN } \mu\text{m}$. This value was used for all simulations.

3.2.4 Global Fibre Properties

In this section we briefly explain key properties of fibres in the simulation generally. Parameters for each fibre type are discussed in the sections that follow.

Forces

Fibres in Cytosim are on μm lengthscales, corresponding to a low Reynolds number, and as such, inertia can be neglected and random molecular collisions leading to Brownian motion are considered only. This is implemented through the random forcing term in the Langevin equation as follows:

$$\delta B_t = \beta \theta \tag{3.4}$$

Where $\beta = \sqrt{2D\tau}$ and θ is a random number generated at each timestep from the normal distribution $N(0, 1)$. The value of D is found through Einstein’s relation:

$$D = \mu_p k_{\text{B}}T \tag{3.5}$$

Here μ_p is the approximated mobility for the fibre to which the point, p belongs as described in Section 3.2.1. Overall, this means a random force is applied to each point on a fibre, and the sum of all these random forces leads to diffusion of the fibre as a whole as per Einstein’s relation.

Fibres may be contained within the cell, or on its surface. A restoring force returns fibre vertices to the space to which they are confined through the following expression:

$$f_{\text{confine}} = k(\mathbf{x}_{\text{projection}} - \mathbf{x}_{\text{a}}) \tag{3.6}$$

Here k is a spring constant that we specify for the interaction, \mathbf{x}_{a} is the coordinates of the fibre vertex, and $\mathbf{x}_{\text{projection}}$ is the coordinates of the vertex when projected onto the boundary or surface of confinement.

When confining inside a cell space, $f_{\text{confine}} = 0$ when the fibre vertex is within the space, with the expression applying only when a vertex leaves the cell. For surface confinement this expression is always applied, providing a positive or negatively directed restoring force as required.

In addition to external forces relating to Brownian motion and confinement, fibres are also subject to internal torque and steric interactions, and these forces are discussed further in the sections that follow.

Fibre Flexibility

While incompressible and inextensible, fibres in cytosim are able to bend, and for each fibre type defined in the simulation, we must specify a rigidity or stiffness, κ , which is the bending elastic modulus or flexural rigidity of the filament being represented and is related to the Young’s modulus and persistence length of the filament as follows:

$$\kappa = EI = L_p k_B T \quad (3.7)$$

Here E is the Young’s modulus, L_p is the persistence length, and I is the moment of inertia of the fibre cross-section. As cytoskeletal filaments such as actin are not isotropic, EI is determined from experiment and the terms E and I can not be calculated independently (Gittes et al. (1993)).

This stiffness is used to calculate an internal bending elasticity force, applying a torque to each pair of segments which sums to zero over the length of the filament. The bending force is calculated by distributing forces relating to the bending modulus across each triplet of vertices to create a stiffness matrix as described in Section 5.1 of Nedelec and Foethke (2007). These forces represent an elastic response to external forces, resulting in changes in fibre curvature, but not causing any translational motion of the fibre as a whole.

Segmentation

Cytosim requires the specification of a segmentation parameter, S , which is used to break each fibre into a series of segments and vertices. The number of segments required is calculated through evaluation of the following expression:

$$N_{\text{segments}} \min \left| \frac{L}{N_{\text{segments}}} - S \right| \quad (3.8)$$

S should be sufficiently low that angles between consecutive segments are small (less than 45 degrees), with no kinks visible in simulated filaments. Filaments with high rigidity may be modelled with a higher segmentation to reduce the number of vertices to be evaluated at each time step, speeding up runtime. While S was set based on the details of each filament type, simulations were frequently monitored to ensure angles remained low and no kinks were visible.

Steric Interactions

Cytosim can include steric interactions. Stiffness constants for attractive and repulsive steric interactions, k_{pull} and k_{push} , are set globally and applied to all filaments. Steric radii are set for each filament type; d_0 is the effective

diameter of our fibre and d_1 is the distance up to which we would like attractive interactions to extend.

The following equation is used to calculate the force on a filament vertex arising from steric interactions with a nearby filament:

$$f(d) = k(d - d_0) \quad (3.9)$$

Force is calculated vertex by vertex. A line is drawn from each vertex, orthogonal to the filament for which this is being calculated. When this line intersects another fibre, the distance, d , is determined. A force is then applied using Equation 3.9, selecting the correct spring constant from the distance-based choices given in Equation 3.10:

$$k = \begin{cases} k_{\text{push}} & \text{if } d < d_0 \\ k_{\text{pull}} & \text{if } d_0 < d < d_0 + d_1 \\ 0 & \text{if } d_0 + d_1 < d \end{cases} \quad (3.10)$$

In all simulations, repulsive interactions were set with $k_{\text{push}} = 7.5 \text{ pN } \mu\text{m}^{-1}$ as found for actin filaments *in vitro* (Letort et al. (2015)). Attractive interactions observed for actin filaments *in vitro* are believed to originate from the presence of counterions and depletion effects of other polymers within the solution and result in bundling of actin filaments with an approximate value of $k_{\text{pull}} = 0.5 \mu\text{m}^{-1}$ (Letort et al. (2015)). Attractive interactions are, however, dependent on the chemical properties of the environment such as local polymer concentration and ionic strength, and given the complexity of these interactions and the presence of multiple filament types within our system, we chose not to include attractive steric interactions, instead using a physical linking protein to reproduce bundling where necessary.

3.2.5 Protein-Level Events

In addition to the mechanical calculation for fibre motion, Cytosim can perform events which alter the fibres, either directly, or through association of accessory proteins. The set of protein-level events is evaluated at each time step after the mechanical calculation using a modified Gillespie algorithm, adapted to allow time-dependence of reaction rates where needed.

For events that occur at a rate, r , that is not dependent on time, events are carried out at their expected time of occurrence, t , calculated through the following expression:

$$t = -\log\left(\frac{\text{random}()}{r}\right) \quad (3.11)$$

Where $\text{random}()$ utilises a Mersenne Twister algorithm to select a random number in the interval $(0,1]$.

Some protein-level events are force-dependent, e.g. detachment of linking proteins, and this results in the event occurring at a time-dependent rate. The rate is given by Kramer’s Reaction Rate theory:

$$r(f(t)) = r_{\text{unbind}} \left(\exp \left(\frac{f(t)}{f_{\text{unbind}}} \right) \right) \quad (3.12)$$

Here $r(f(t))$ is the reaction rate, and $f(t)$ is the force experienced by the linking protein at that timestep, while r_{unbind} and f_{unbind} are the unbinding rate and force respectively, which are constants that we specify.

An expected time of occurrence is then calculated; a time is initially selected at random in the interval $[0, 1]$:

$$t = -\log(\text{random}()) \quad (3.13)$$

At each timestep, the value of t is modified by subtraction of an increment with magnitude dependent on the rate calculated at that timestep according to Equation 3.12, $r(f(t))$, as follows:

$$t = t - \Delta t (r(f(t))) \quad (3.14)$$

The event is performed when the time to event occurrence crosses from future to past as indicated by a positive value of t . Further details of this procedure are detailed in Prados et al. (1997).

In this section, we describe in brief the key protein-level events that are implemented in our model.

Fibre Events

Fibres may be of fixed length, but can also alter their length during the course of the simulation, more accurately representing the biological events of polymerisation or depolymerisation which affect cytoskeletal filaments such as actin or microtubules. Actin fibres within the simulations carried out were either set with a fixed length, or were able to grow, polymerising at a rate r_{growth} up to a maximum length of L_{max} .

Fibres may be initiated directly or through the use of nucleating proteins, which create a fibre stochastically at a rate r_{nuc} that we specify.

Accessory Proteins

A range of proteins can be modelled in Cytosim. Proteins are represented by ‘hands’ which are able to attach, detach, and operate on filaments. These hands are used to create ‘singles’ in which a single hand can bind to a filament, or ‘couples’ which can link multiple points on a filament, or link a pair of filaments together, imitating a crosslinking protein.

For each hand that we define, we are able to specify values for several parameters; hands can bind at a given rate per second, r_{bind} , and can attach to fibres that are within a binding range in μm , d_{bind} . If we require a turnover

of proteins, we can specify an unbinding rate per second r_{unbind} and unbinding force in pN, f_{unbind} . These values are used to calculate a rate of detachment per second as follows:

$$r_{\text{detach}} = r_{\text{unbind}} \exp\left(\frac{|f_{\text{link}}|}{f_{\text{unbind}}}\right) \quad (3.15)$$

Hands may remain in place, or they may step between fibre lattice sites at a given rate to represent motor proteins. They may also be assigned other properties, such as the ability to nucleate a filament as mentioned previously.

Singles and couples are modelled as Hookean springs, with a spring constant k that we specify when defining them. A single which is fixed in a position with coordinates $\mathbf{x}_{\text{fixed}}$, exerts a force, f_a on a fibre to which it attaches as follows:

$$f_a = k(\mathbf{x}_{\text{fixed}} - \mathbf{x}_a) \quad (3.16)$$

Couples which connect two fibres, a and b exert the following forces, f_a and f_b upon the fibre points, \mathbf{x} , to which they are attached:

$$f_a = -f_b = k(\mathbf{x}_b - \mathbf{x}_a) \quad (3.17)$$

3.2.6 Timestep and Simulation Duration

An appropriate timestep and simulation duration was determined using a representative multiple filament system containing nucleated actin, spectrin, and crosslinkers within a 6 μm cylindrical cell. The representative system was simulated for up to 1 hour with a range of timesteps from 1-64 ms and 5 repeat runs for each timestep. While it was not practical to carry out the analysis required to determine the ORP measure from this large volume of simulations, a closely related measure, the mean bending energy of actin filaments, could be monitored easily, and was chosen as the output upon which to determine a suitable timestep.

While carrying out these simulations we noted a small dependency of bending energy on timestep. The discrepancy is detailed further in Appendix A. While this issue was reported to the developers of the software, a resolution could not be found during the course of this research project. A timestep of $\tau = 16\text{ms}$ was used as this was found to reduce any favourable influence this dependency may have.

Simulation duration was chosen by monitoring the output of the representative system over an extended period of time; we chose a duration of 800 seconds as this was observed to be a point at which the energy of the representative system had remained stable for some time. 50,000 steps were used, outputting results at 5 second intervals in most cases. Simulation time was increased in cases where slow, stochastic processes were included to ensure adequate time for interactions to take place. In simulations where spectrin tetramers were present, an initial period of 20 seconds (1250 timesteps) was simulated with spectrin and actin-spectrin linking proteins present, prior to the introduction of actin. This

ensured that actin was able to bind to spectrin immediately on its introduction to the cell. Additionally, in cases where actin filaments were polymerised within the cell, a period of extra simulation time was added to allow the filament to reach full length. This was calculated using the polymerisation rate, r_{growth} . For example, for $r_{\text{growth}} = 0.33 \mu\text{m s}^{-1}$, an actin filament of $L_{\text{actin}} = 1.32 \mu\text{m}$ is expected to take 4 seconds to reach full length once nucleated, and so 250 steps were added to the total simulation time in this case. No additional time was included for nucleation as these processes were expected to take 1 s or less.

As results show stochastic variability, we must run multiple simulations and obtain average results. We chose to carry out 10 simulations for each parameter set.

3.2.7 Actin Filament Properties

While previously accepted that actin filaments within the rings of the MPS were short in length, analogous to those of erythrocytes, during the course of our research, a paper was published which imaged these filaments directly, finding lengths of $\sim 1 \mu\text{m}$ (Vassilopoulos et al. (2019)) as discussed in Section 1.3.3. With this discovery in mind, we chose to model actin as long filaments, choosing a length of $1.32 \mu\text{m}$ which is slightly larger than the circumference of the axonal space used in the model. This allows a short region of overlap which is useful where crosslinking is desirable. While further confirmation is needed of the precise length and arrangement of actin filaments within rings, the use of longer filaments in this case could give similar results to a string of crosslinked short filaments, while simplifying dynamics and analysis.

Steric interactions were repulsive only, with the range of steric interactions corresponding to the effective diameter of actin filaments, $D_{\text{actin}}^{\text{eff}} = 15 \text{ nm}$ (Oda et al. (1998)).

The monomer-monomer distance of actin filaments is 5.5 nm (Kandel et al. (2000), Chapter 4). The binding lattice was set to allow one binding site per monomer, with a lattice size of $0.0055 \mu\text{m}$, while segmentation was set at $S = 0.022 \mu\text{m}$ which corresponds to roughly 4 actin monomers based on the monomer distance stated.

The stiffness or bending elasticity modulus for actin can be affected by modifications, including dynamic changes triggered by calcium ions (Isambert et al. (1995)), and was varied throughout the simulations to reflect this. As a guide, phalloidin-stabilised actin filaments have a stiffness of $\kappa_{\text{actin}} = 0.073 \text{ pN } \mu\text{m}^2$ relating to persistence lengths between $17.7\text{-}18 \mu\text{m}$ measured at room temperature ($20 - 26^\circ\text{C}$) (Gittes et al. (1993), Isambert et al. (1995)). Non-stabilised actin was found to have $L_p = 9 \mu\text{m}$ at 20°C , which corresponds to $\kappa_{\text{actin}} = 0.036 \text{ pN } \mu\text{m}^2$ (Isambert et al. (1995)). Actin bound to cofilin, a severing protein, had a lower persistence length of $L_p = 2.2 \mu\text{m}$, corresponding to $\kappa_{\text{actin}} = 0.0091 \text{ pN } \mu\text{m}^2$ (McCullough et al. (2008)).

Actin filaments were confined within the simulation cell with a potential of $k_{\text{cell}} = 100 \text{ pN } \mu\text{m}^{-1}$. The choice of this value was guided by the Cytosim docu-

mentation and examples, and tested to ensure filaments are suitably contained within the cell.

3.2.8 Spectrin Tetramer Properties

A spectrin tetramer was defined of length $L_{\text{spectrin}} = 0.2\mu\text{m}$, which is the contour length of spectrin (Bloch and Pumplun (1992)).

As with actin, steric interactions were repulsive only, and the effective diameter was set to $D_{\text{spectrin}}^{\text{eff}} = 6\text{ nm}$ which is approximately equal to the diameter found in low-angle shadowing experiments (Shotton et al. (1979)).

A spectrin repeat unit is approximately 5 nm in length inclusive of the linker region (Brown et al. (2015)) and so spectrin segmentation was set at $S = 0.02\mu\text{m}$, corresponding to 4 repeat units, while the binding lattice was set at $0.005\mu\text{m}$, allowing one binding site per repeat unit.

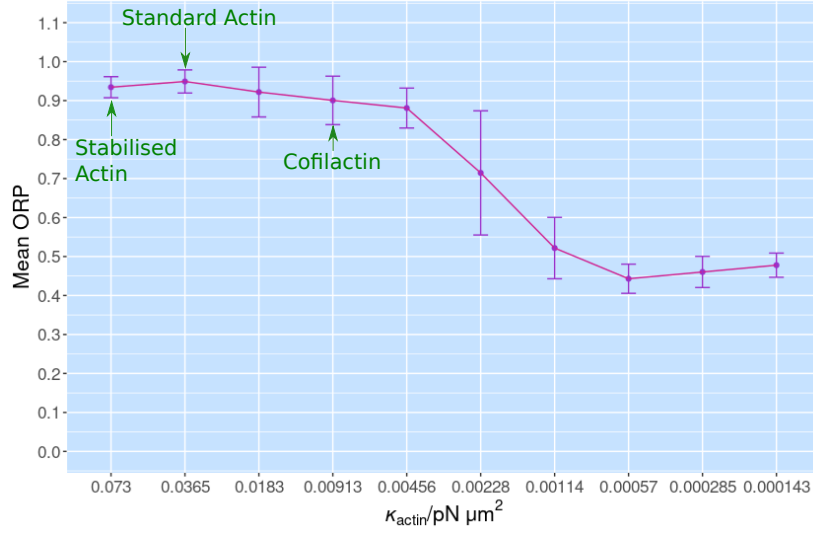
An experimental value for the stiffness or bending elasticity modulus of brain spectrin could not be found in the literature. For the more flexible erythrocyte spectrin, intrinsic viscosity experiments combined with theory produced a persistence length $L_p = 0.0164\mu\text{m}$ at 38°C , which gives a stiffness of $\kappa_{\text{spectrin}} = 7.02 \times 10^{-5}\text{ pN}\mu\text{m}^2$ (Stokke et al. (1985)). As neuronal spectrin is expected to be stiffer than the erythrocyte analogue (Mehboob et al. (2010)), this value was multiplied by a factor of 10^3 giving a guide stiffness of $\kappa_{\text{spectrin}} = 0.07\text{ pN}\mu\text{m}^2$. As the precise value was unknown, this stiffness was varied in Section 4.3 to determine the impact of this variable on overall results.

Spectrin tetramers were confined within the plane of the membrane simulation cell with a potential of $k_{\text{cell}} = 100\text{ pN}\mu\text{m}^{-1}$. This is a simplification of the biological process which involves connection of spectrin centres to the membrane via ankyrin, however we considered this justifiable given the high ankyrin concentration observed in early development (Galiano et al. (2012)), which is likely to result in high levels of recruitment to the membrane. This is discussed further in Section 4.3.

3.3 Actin Filament Stiffness

To begin our investigations, we placed a single fixed length actin filament within the centre of the periodic cylindrical space and simulated for 800 seconds. Stiffness was initially set at $\kappa_{\text{actin}} = 0.073\text{ pN}\mu\text{m}^2$ which corresponds to phalloidin-stabilised actin. We then varied κ_{actin} by a factor of 0.5 with each of the subsequent parameter set, to a minimum value of $0.000143\text{ pN}\mu\text{m}^2$. This allowed us to observe 10 different stiffnesses including approximate values of stabilised, standard, and cofilin-modified actin (cofilactin), as well as a range of lower stiffnesses. For each parameter set, 10 repeat simulations were carried out, and the mean and standard deviation of the ORP measure was recorded.

The mean ORP results for each value of κ_{actin} were plotted in ggplot2 Version 3.3.3 (Wickham (2009)) and are shown in Figure 3.5a. Three key stiffnesses are



(a) Mean ORP with Decreasing Actin Stiffness.



(b) Example Filament Configurations.

Figure 3.5: Single Filament - Actin Stiffness. *Single actin filaments diffuse freely around the cell space. In Figure 3.5a we vary the stiffness across the range $\kappa_{actin} \in [0.073, 0.000143] \text{ pN } \mu\text{m}^2$, observing a decrease in mean ORP from around 1 to 0.5 as actin stiffness is reduced. Example final configurations are shown in Figure 3.5b for actin stiffnesses of $\kappa_{actin} \in \{0.073, 0.00114, 0.000285\} \text{ pN } \mu\text{m}^2$. These images show a transition from straight filaments at the higher stiffness, to tightly coiled configurations at $\kappa_{actin} = 0.000285 \text{ pN } \mu\text{m}^2$.*

Table 3.1: Constants used in Single Filament Model

Constant	Value
R_{axon}	$0.2 \mu\text{m}$
L_{axon}	$2 \mu\text{m}$
ν_{axon}	$1 \text{ pN s } \mu\text{m}^{-2}$
$k_{\text{B}}T$	$0.00428 \text{ pN } \mu\text{m}$
k_{cell}	$100 \text{ pN } \mu\text{m}^{-1}$
k_{push}	$7.5 \text{ pN } \mu\text{m}^{-1}$
L_{actin}	$1.32 \mu\text{m}$
S_{actin}	$0.022 \mu\text{m}$
$D_{\text{actin}}^{\text{eff}}$	$0.015 \mu\text{m}$
L_{spectrin}	$0.2 \mu\text{m}$
S_{spectrin}	$0.02 \mu\text{m}$
$D_{\text{spectrin}}^{\text{eff}}$	$0.006 \mu\text{m}$

labelled approximating the phalloidin-stabilised, standard non-stabilised, and cofilin-modified actin values discussed in Section 3.2.7. We note from the ORP value close to 1 and the example configuration shown in Figure 3.5b (left) that stabilised actin filaments appear almost straight, aligned to a high degree with the longitudinal axis of the cylindrical space. There is little change in configuration across the range of $0.0730 \geq \kappa_{\text{actin}} \geq 0.00456 \text{ pN } \mu\text{m}^2$, however below this range, ORP begins to fall. The minimum average ORP value of $\sim 0.44 - 0.48$ is reached within the range $0.000570 \geq \kappa_{\text{actin}} \geq 0.000143 \text{ pN } \mu\text{m}^2$, with filaments adopting tightly coiled configurations as shown in Figure 3.5b (right). Results at stiffnesses of 0.00228 and $0.00114 \text{ pN } \mu\text{m}^2$ are more varied, with filaments showing a variety of curved configurations similar to the example in Figure 3.5b (centre). The minimum ORP value achieved in an individual simulation was 0.3808 , corresponding to an actin filament of $\kappa_{\text{actin}} = 0.000570 \text{ pN } \mu\text{m}^2$. As no result met the threshold of < 0.3 , we conclude that ring formation is unlikely for a μm scale actin filament, regardless of flexibility.

3.4 Membrane-Bound Actin

A number of proteins are thought to have the ability to link actin filaments to the membrane (e.g. dematin (Siegel and Branton (1985))), and in the pre-existing cylindrical axon environment, such linking may contour actin filaments to the curved membrane, allowing rings to form. We continue our investigations,

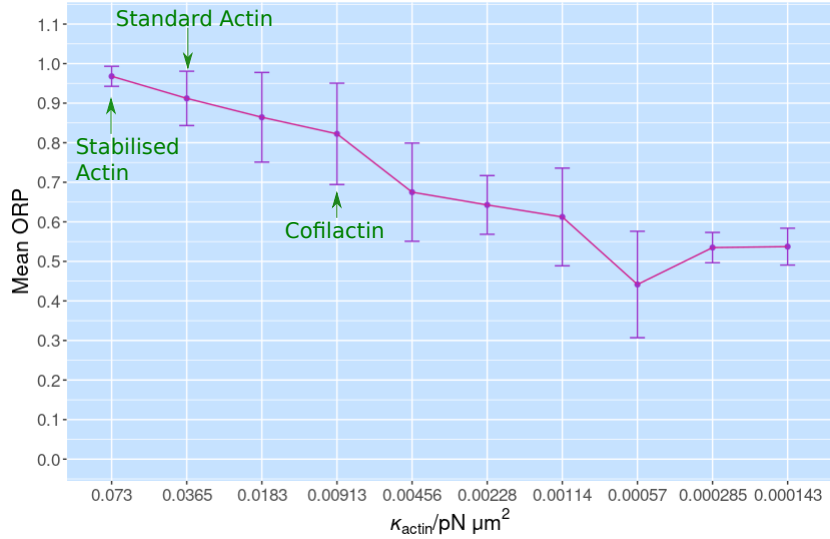


Figure 3.6: Single Filament - Membrane-Bound Actin. *Actin filaments can bind to a large number of membrane-associated linking proteins which are fixed in place at random locations on the cell membrane. Results show mean ORP decreasing as stiffness is reduced. The decrease is slightly greater than that observed in Figure 3.5a for unbound actin.*

considering a single actin filament with κ_{actin} varying across the range given in Section 3.3, however we define an additional protein which is able to link actin to the membrane.

As specific proteins involved in linking of MPS actin to the membrane are not currently known, a generic membrane linker was created. Cytosim documentation and examples were used as a guide to identify suitable values. The linker had a binding range of $0.01 \mu\text{m}$, and binding rate of 10 s^{-1} . The unbinding rate was chosen to be 0.1 s^{-1} , with an unbinding force of $f_{\text{unbind}} = 2.5 \text{ pN}$. The linker was confined to the membrane surface and fixed in place, and had a spring constant of $k_{\text{link}} = 25 \text{ pN } \mu\text{m}^{-1}$. 1000 linkers were scattered randomly upon the membrane at the beginning of each simulation.

Mean ORP values are shown in Figure 3.6. Compared to the freely diffusing actin filament results shown in Figure 3.5a, ORP for the membrane binding filament decreases more rapidly with decreasing stiffness. A minimum mean value of 0.4416 is reached for $\kappa_{\text{actin}} = 0.000570 \text{ pN } \mu\text{m}^2$, with 2 simulations from this set of 10 reaching ORP values below the threshold at 0.1219 and 0.2966, however the error bars for this datapoint are large and the drop in mean may be connected to the presence of these outliers, and therefore of limited significance. Stiffnesses below $\kappa_{\text{actin}} = 0.000570 \text{ pN } \mu\text{m}^2$ had slightly higher ORP on av-

erage than for a freely diffusing filament, at 0.5349 and 0.5373 for 0.000285 and 0.000143 pN μm^2 respectively, and appeared visually similar. Overall, membrane-attachment was not generally sufficient to cause actin filaments to form rings except in occasional cases with low stiffness actin.

3.5 Membrane-Bound Spectrin

In the previous sections we investigated a single freely diffusing actin filament, and the same filament linked to the membrane by a membrane-binding protein. We now introduce spectrin tetramers into the model. These tetramers are able to bind to actin via an accessory protein, and are fixed to the membrane with a confinement potential as described in Section 3.2.8. Binding to spectrin provides a link to the membrane, but with the added effect of a linked filament. This effect is most relevant when considering multiple actin filaments, as it has the potential to space adjacent filaments in a periodic manner, however it may prove relevant even in the case of single actin filament simulations as spectrin tetramers may stack, bundle, or orient themselves in way which alters the configurations adopted by the actin filaments with which they interact. To investigate these effects, we observed actin filaments across the range of 10 stiffnesses in line with previous sections, while introducing spectrin tetramers at different densities.

While adducin is generally considered to link actin and spectrin in the MPS, the periodic arrangement of actin and spectrin precedes that of adducin (Zhong et al. (2014)), leaving the precise mode of connection unknown. We therefore create a generic linking protein with properties within common ranges as guided by the Cytosim documentation and examples. Two binding hands were defined with specific binding to actin and spectrin respectively. Both hands had a binding range of $d_{\text{bind}} = 0.02 \mu\text{m}$, binding rates of $r_{\text{bind}} = 10 \text{s}^{-1}$, and unbinding of rate $r_{\text{unbind}} = 0.001 \text{s}^{-1}$ and force $f_{\text{unbind}} = 3 \text{pN}$. The actin binding hand was able to bind at any lattice site on the fibre, assuming one binding site per actin monomer, while the spectrin hand was restricted to the end lattice sites of the fibre consistent with the presence of a single actin binding site at each end of the spectrin tetramer (Brown et al. (2015)). These hands were then combined in a couple of stiffness $k_{\text{link}} = 25 \text{pN } \mu\text{m}^{-1}$.

The number of spectrin in the simulation, N_{spectrin} was varied with $N_{\text{spectrin}} \in \{0, 50, 100, 500, 1000, 1500\}$ and the number of actin-spectrin linking proteins was set at $5N_{\text{spectrin}}$ to ensure adequate availability. Spectrin tetramers were placed randomly on the membrane surface at the beginning of each simulation, while actin-spectrin linking proteins were able to diffuse around the cell.

Figure 3.7 shows the variation of mean ORP across the range of 10 actin stiffnesses tested, for varying numbers of spectrin. We include the case where $N_{\text{spectrin}} = 0$ as shown in red. For all values of N_{spectrin} we see a similar pattern; ORP values are close to 1 for the stiffest filaments of $\kappa_{\text{actin}} \geq 0.0183 \text{pN } \mu\text{m}^2$, then begin to reduce at lower stiffnesses, exhibiting substantial variations between repeat sets as indicated by large error bars. At the lowest stiffnesses, the mean ORP measurement is around 0.5 for $N_{\text{spectrin}} = 0$.

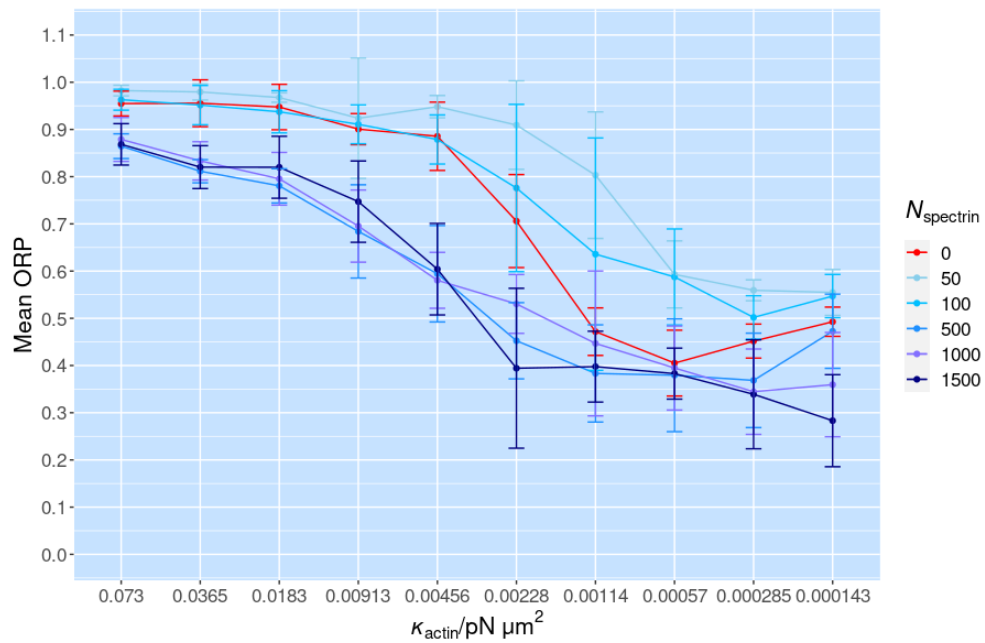


Figure 3.7: Mean ORP with Spectrin Density for Varying Actin Stiffnesses. Actin is able to connect with spectrin tetramers which are confined to the plane of the membrane. Results are shown for a range of spectrin numbers with the case of $N_{\text{spectrin}} = 0$ shown in red for reference. At many actin stiffnesses, mean ORP increases when spectrin is present at low levels of up to 100 tetramers, however at $N_{\text{spectrin}} = 500$ and above, there is a decrease in mean ORP at each of the 10 actin stiffnesses tested.

Table 3.2: Spectrin Tetramers: Mean ORP Variation Relative to $N_{\text{spectrin}} = 0$. We show the change in mean ORP to 3 significant figures for each value of N_{spectrin} , relative to the mean ORP value for $N_{\text{spectrin}} = 0$ given in column 2. Increases and decreases are shown in red and blue text respectively.

$\kappa_{\text{actin}}/\text{pN}$ μm^2	Mean ORP for $N_{\text{spectrin}} = 0$	Δ Mean ORP for N_{spectrin}				
		50	100	500	1000	1500
0.0730	0.9548	+0.0275	+0.0081	-0.0903	-0.0760	-0.0864
0.0365	0.9555	+0.0239	-0.004	-0.144	-0.122	-0.135
0.0183	0.9475	+0.02	-0.0101	-0.167	-0.152	-0.128
0.00913	0.9006	+0.0231	+0.0102	-0.217	-0.205	-0.154
0.00456	0.8855	+0.0627	-0.0068	-0.291	-0.305	-0.282
0.00228	0.7059	+0.203	+0.07	-0.254	-0.176	-0.312
0.00114	0.4717	+0.331	+0.164	-0.0885	-0.025	-0.0741
0.000570	0.4051	+0.188	+0.182	-0.0257	-0.0104	-0.0223
0.000285	0.4517	+0.108	+0.0502	-0.0832	-0.107	-0.113
0.000143	0.4927	+0.0621	+0.0543	-0.0201	-0.133	-0.21

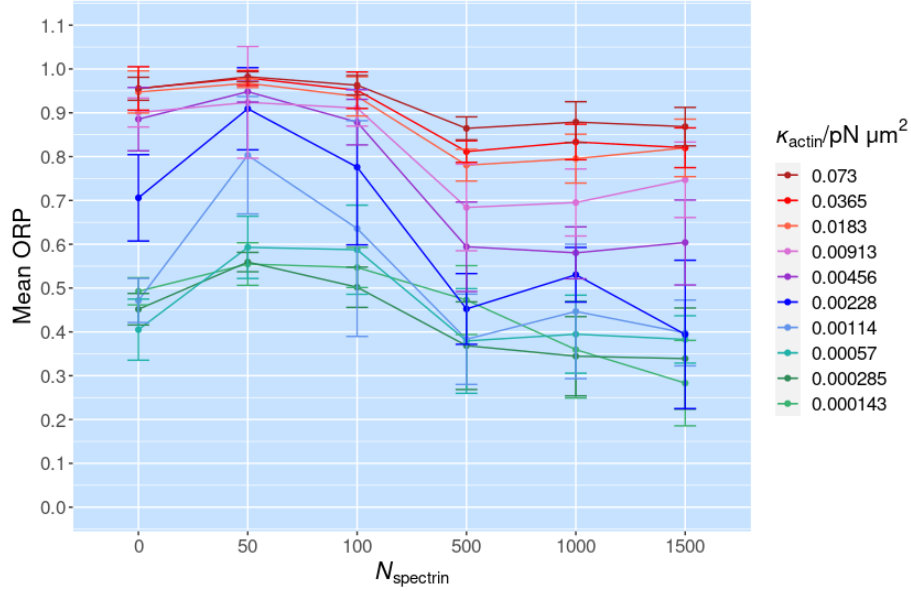


Figure 3.8: Mean ORP with Actin Stiffness for Varying Spectrin Densities. Here we show the variation in mean ORP with the number of spectrin, N_{spectrin} , for a range of actin stiffnesses when interacting with membrane-bound spectrin tetramers. We note a reduction in mean ORP, particularly at high spectrin numbers, mainly affecting actin filaments of mid-range stiffness.

While all values of N_{spectrin} show a similar trend across the actin stiffness range, it is clear that interactions with spectrin have an effect on the ORP measurement of each actin filament.

Interestingly, the mean ORP measurement shows an increase where levels of spectrin are low. In Figure 3.7 we note that results for N_{spectrin} of 50 and 100 sit above the red line denoting $N_{\text{spectrin}} = 0$ across the full range of actin stiffnesses. Table 3.2 gives a more in depth view of these changes; where $N_{\text{spectrin}} = 50$, ORP increases for each of the 10 stiffnesses, while for $N_{\text{spectrin}} = 100$, 7 of the 10 actin stiffnesses show an increase. The change is most pronounced for stiffnesses in the range $\kappa_{\text{actin}} \in [0.000570, 0.00228]$ pN μm^2 , as illustrated in Figure 3.8 where we observe a large jump for these stiffnesses.

At higher numbers of spectrin, a favourable effect on mean ORP can be observed across all actin stiffnesses, with Table 3.2 showing decreases for $N_{\text{spectrin}} = 500$ and above. As illustrated in Figure 3.8, it appears that mid-range stiffnesses are the most susceptible to spectrin interaction related changes in configuration, with κ_{actin} of 0.00228 and 0.00456 pN μm^2 appearing to show the greatest changes. This is confirmed in Table 3.2 where these 2 stiffnesses show decreases in mean ORP of up to ~ 0.3 relative to their original configuration.

Table 3.3: Spectrin Tetramers: ORP Results Below Threshold. *Information is given for each parameter set where one or more repeat simulations gave an ORP measurement below the threshold. We detail the mean, standard deviation, and minimum ORP value of the parameter set, and the number of simulations, N , with an ORP result below 0.3, from a maximum of $N = 10$.*

N_{spectrin}	$\kappa_{\text{actin}}/\text{pN}$ μm^2	Mean ORP	Standard Deviation	Minimum ORP	$N < 0.3$
0	0.000570	0.4051	0.0697	0.2771	1
100	0.00114	0.6358	0.2461	0.1018	1
500	0.000143	0.4726	0.0786	0.2931	1
	0.000285	0.3685	0.1000	0.2238	3
	0.000570	0.3794	0.1195	0.2330	3
	0.00114	0.3832	0.1030	0.2303	2
1000	0.000143	0.3595	0.1104	0.2096	4
	0.000285	0.3445	0.0904	0.1483	2
	0.000570	0.3947	0.0890	0.2143	1
	0.00114	0.4467	0.1534	0.1873	2
1500	0.000143	0.2831	0.0975	0.1270	5
	0.000285	0.3390	0.1154	0.1445	4
	0.000570	0.3828	0.0540	0.2923	1
	0.00114	0.3976	0.0750	0.2793	1
	0.00228	0.3942	0.1693	0.1638	3

Table 3.3 lists those parameter sets which generated at least one result below the 0.3 ORP threshold. While some single simulations met the threshold for low levels of spectrin, higher spectrin levels were associated with more regular occurrence of ring-like configurations, extending over a wider stiffness range. In all cases, ring formation was possible only with low to mid range stiffnesses in the range $\kappa_{\text{actin}} \in [0.000143, 0.00228]$ pN μm^2 . In addition, ring formation occurred in a maximum of 50% of the 10 repeat simulations carried out for each parameter set, with many parameters yielding just 1 sub-threshold result. This is indicative of a high level of variability between sets even when parameters are identical.

In Figure 3.9 we display a set of images from the simulation that yielded the minimum ORP value of 0.1018. The simulation parameters were $N_{\text{spectrin}} = 100$ and $\kappa_{\text{actin}} = 0.00114$ pN μm^2 . The majority of spectrin tetramers (shown in purple) are attached to the actin filament, with the binding protein shown in yellow. The actin filament forms a ring with spectrin tetramers attached on both sides, aligned in parallel. At the ends of the filament there is a small region of overlap, and here there is a deviation from the ring shape, with spectrin tetramers bridging the 2 ends, creating a small spiral effect. While this actin configuration is very close to an ideal ring shape, it was the only result from the parameter set with a value below the 0.3 threshold, and the mean of this parameter set is relatively high at 0.6358.

Overall, these results show that actin filaments are able to form ring-like configurations when interacting with membrane-bound spectrin, however this appears to be likely only for actin filaments with reduced stiffness, and requires an abundance of spectrin. Rings are not formed reliably, and the configurations can differ substantially between repeats carried out with identical parameters. This variability makes it difficult to establish the conditions required for ring formation to occur.

3.6 Ordered Membrane Binding

In Sections 3.4 and 3.5, links to the membrane were positioned randomly. We now consider a case where actin binding proteins are placed at a specific axial location. Such an ordered region of membrane linking proteins may be possible in the following hypothetical scenarios:

- Spectrin tetramers are able to align with one another by stacking in parallel or linking at specific domains.
- Proteins such as the IQGAP 'curly' domain are in effect (Palani et al. (2020)).
- There are guidance cues from adjacent cells (Hauser et al. (2018)).

Initially, we place 20 actin membrane linking proteins at regular intervals around the membrane at the $x = 0$ position. Properties of these linkers are

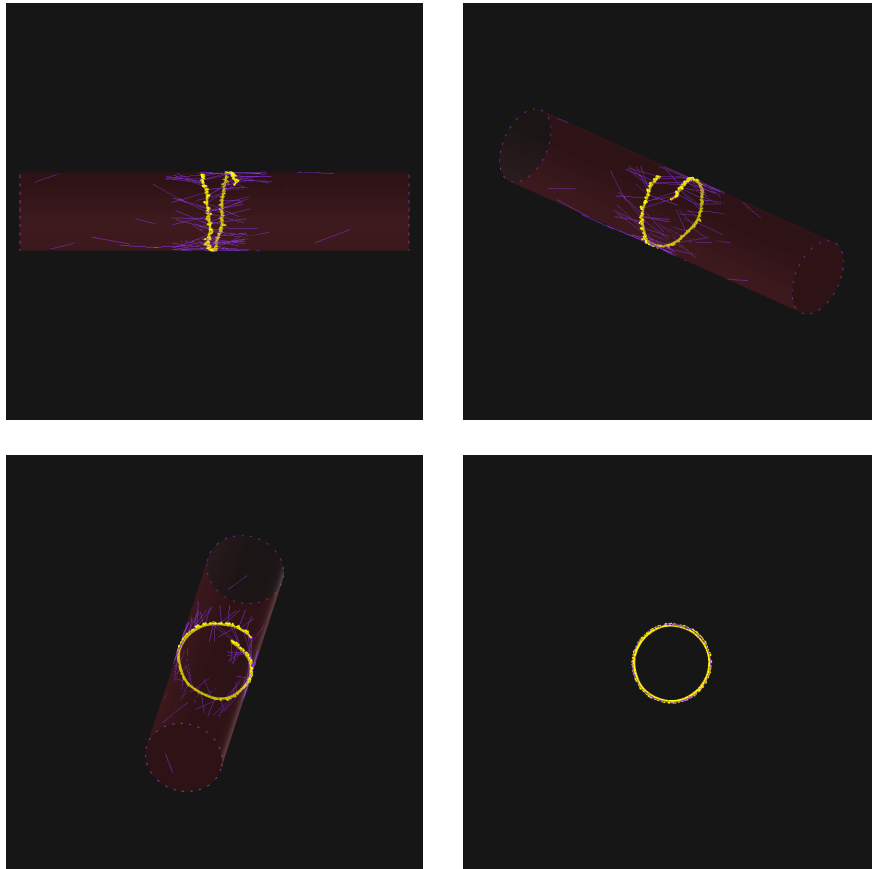


Figure 3.9: Simulation Images with $N_{\text{spectrin}} = 100$ and $\kappa_{\text{actin}} = 0.00114 \text{ pN } \mu\text{m}^2$. Spectrin tetramers are shown in purple, confined to the membrane surface. The single actin filament is shown decorated with yellow actin-spectrin linking proteins. The range of views shows a circular arrangement, with spectrin tetramers bundling densely at either side. The ORP value for this simulation was 0.1018.

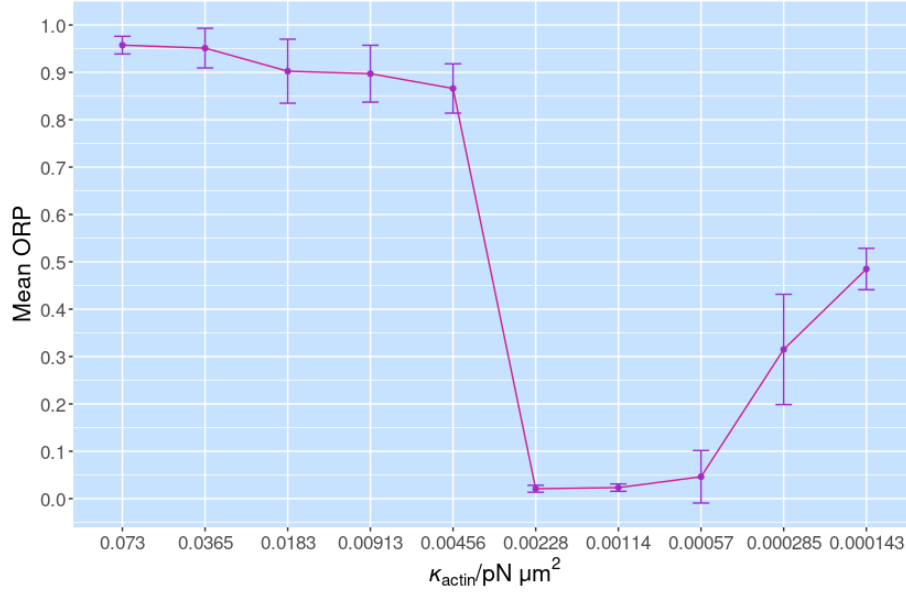


Figure 3.10: Aligned Actin Membrane Binding. Where actin membrane binding proteins are placed in a circular arrangement, actin of $0.00456 > \kappa_{\text{actin}} \geq 0.000570 \text{ pN } \mu\text{m}^2$ are able to form ideal ring-like configurations as shown by the minimal ORP values across this range.

as in Section 3.4. As before, we allow actin filaments of varying stiffness to diffuse throughout the cell, and measure the ORP after 800 seconds of simulation time. The results are shown in Figure 3.10, with further details in Table 3.4 for parameter sets with at least one result below the 0.3 threshold. We note that for $\kappa_{\text{actin}} \in \{0.000570, 0.00114, 0.00228\} \text{ pN } \mu\text{m}^2$ mean ORP is close to zero with very little variation. Interestingly, the 3 actin stiffnesses which formed rings most reliably from this parameter set were those with persistence lengths on the order of $10^{-1} \mu\text{m}$ in length, and roughly equal to the cell radius of $R_{\text{axon}} = 0.2 \mu\text{m}$.

Figure 3.11 shows example results for several actin stiffnesses; the actin filament binds to each of the membrane-binding proteins, forming a circle at $x = 0$. Results for actin of stiffness above this range are broadly in line with those with random membrane binding and as shown in Figure 3.11 (Upper left), they extend mainly along the longitudinal axis of the cylinder, binding to a single site and remaining out of reach of the remaining links. For $\kappa_{\text{actin}} = 0.000285 \text{ pN } \mu\text{m}^2$, mean ORP was lower than in the random case, with larger error bars. Figure 3.11 (Upper right) shows alignment with roughly half of the membrane binding proteins, however the filament was flexible enough to miss several in sequence, looping back to connect with them.

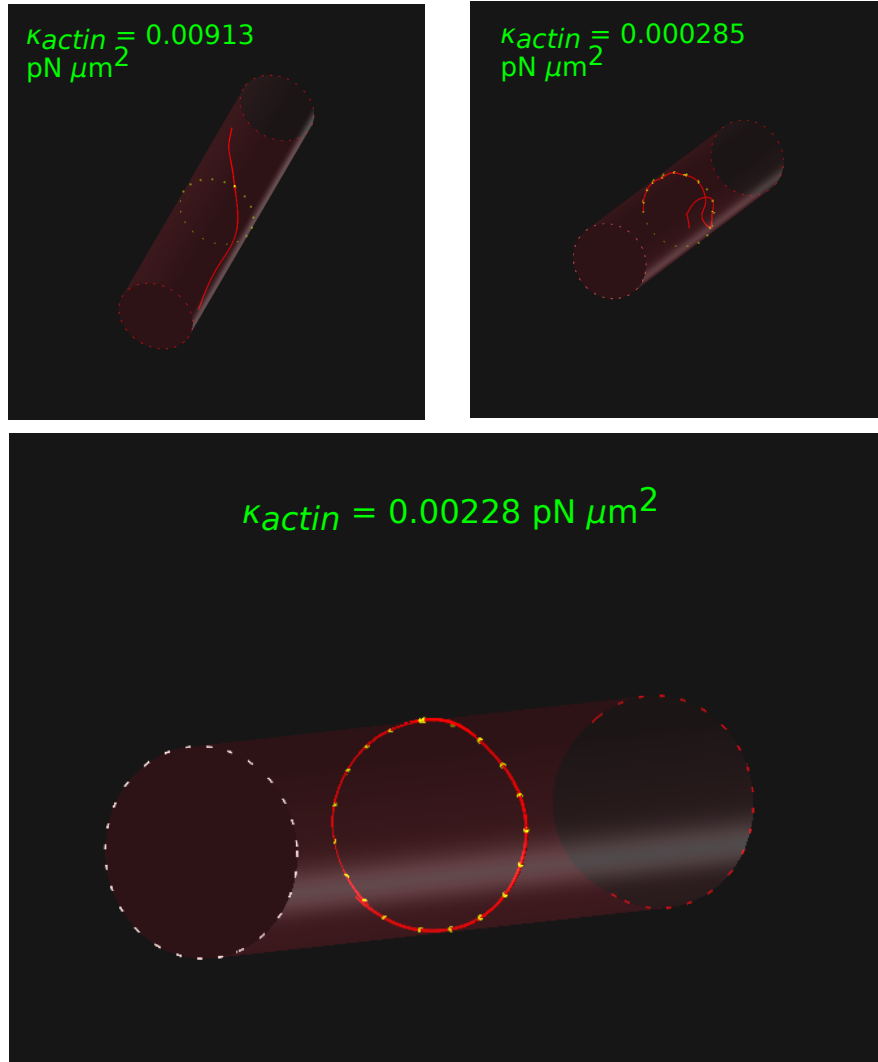


Figure 3.11: Aligned Actin Membrane Binding Example Configurations. An actin filament with κ_{actin} approximately equal to the stiffness of cofilactin is shown in upper left pane, while a low value of κ_{actin} is shown in the upper right. The lower pane shows an example configuration from $\kappa_{actin} = 0.00228 \text{ pN } \mu\text{m}^2$ - a set in which all filaments were able to form rings.

Table 3.4: Aligned Actin Membrane Binding: ORP Results Below Threshold. Details of mean, standard deviation, and minimum ORP are given here for parameter sets yielding one or more ORP results below the 0.3 threshold, along with the number of repeat simulations of the set, N , with ORP below threshold, from a maximum of $N = 10$.

$\kappa_{\text{actin}}/\text{pN}$ μm^2	Mean ORP	Standard Deviation	Minimum ORP	$N < 0.3$
0.000285	0.3150	0.1164	0.0420	3
0.000570	0.0462	0.0554	0.0188	10
0.00114	0.0233	0.0078	0.0135	10
0.00228	0.0209	0.0073	0.0100	10

While we have shown that organised membrane linking proteins are able to create actin rings for specific actin stiffnesses, it is useful to investigate whether these rings are able to remain intact if these membrane tethers are removed. If actin filaments are able to retain such a configuration, this could suggest that multiple rings may be generated at a single site, with ring creation and periodic spacing being distinct processes. To investigate the stability of these rings of actin, we carried out an additional simulation for $\kappa_{\text{actin}} = 0.00228 \text{ pN } \mu\text{m}^2$, removing the membrane binding proteins from the simulation after 800 seconds of simulation time and observing the filament for a short time after detachment.

Figure 3.12 shows the ORP measurement plotted at 0.5 second intervals for 10 seconds commencing at the 800 second point at which the membrane binding proteins were detached. The ORP measurement at 800 seconds was 0.01015, which is within the range expected for this stiffness based on Figure 3.10. We see an immediate and rapid increase in ORP after detachment of membrane binding proteins, reaching a value of 0.2151 at 0.5 seconds, and 0.5050 at 3.5 seconds. The value continues to increase, exceeding 0.6 by 6.5 seconds and 0.7 by 8 seconds, and despite some substantial fluctuations there appears to be an upward trend towards the value of around 0.7 expected for actin of this stiffness

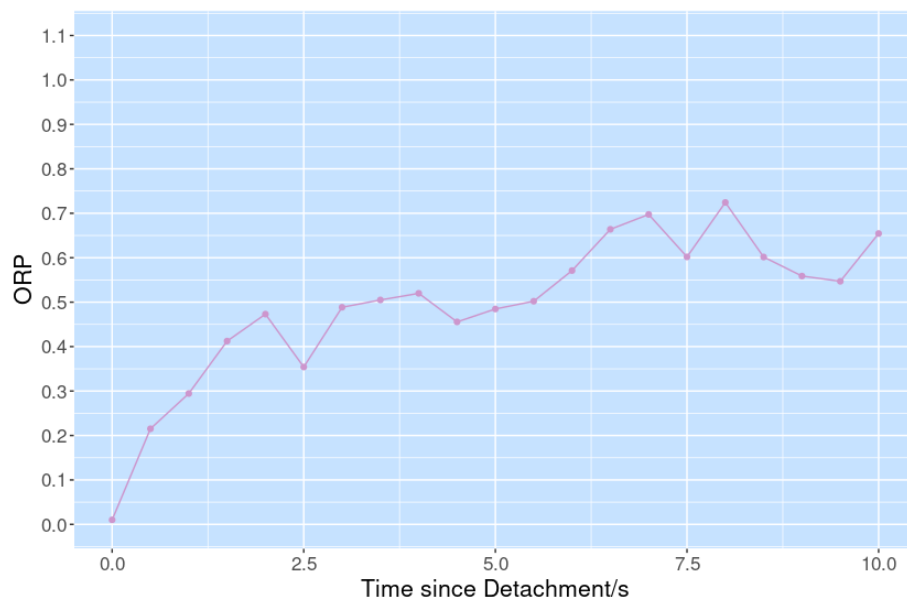


Figure 3.12: ORP Measurement after Detachment of Membrane Binding Proteins. An actin filament of $\kappa_{\text{actin}} = 0.00228 \text{ pN } \mu\text{m}^2$ is simulated for 800 seconds interacting with ordered membrane binding proteins. These proteins are detached and removed from the simulation at this point, and the filament is simulated for a further 10 seconds. Here we show how the ORP measurement evolves from the point of detachment. The ORP measurement begins close to zero, however this rises to above 0.2 within 0.5 seconds of detachment, continuing to increase to values of 0.55 and above within around 6 seconds.

when placed in a cell without any additional interactions as shown in Figure 3.5.

Figure 3.13 shows a series of images from the simulation, illustrating the configurational changes occurring. At $t = 0$ s since detachment, we see an ideal ring configuration, however within 0.2 seconds the ring begins to unravel, with its ends moving in opposite directions. We see further separation of the ends of the filament after 1.2 seconds, and a tilting of the remaining ring shape which causes it to move out of alignment with the circular plane of the cell and turn towards the cylindrical axis. At $t = 10$ s, the ring shape is no longer observable, and the filament aligns with the cylindrical axis in an elongated and slightly curved configuration. These results show that actin rings are not stable unless in continuous connection with the membrane, with detachment resulting in a rapid return to the configuration expected for their stiffness.

While the results of Figure 3.13 show that the ring shape is lost on detachment of actin membrane binding proteins, it is possible that actin may be secured into rings by proteins such as adducin which have an actin bundling function (Mische et al. (1987)). Could such associations secure the actin filaments within actin rings, helping to reinforce and stabilise the structure and allowing stable rings to be formed without a requirement to remain linked to the membrane?

To investigate this, we extend the previous model to include an actin crosslinking protein. The crosslinking protein had a binding range of $r_{\text{bind}} = 0.02\mu\text{m}$, binding rate of $r_{\text{bind}} = 10\text{ s}^{-1}$, and unbinding at a rate of 0.001 s^{-1} and force of 3 pN . The stiffness of the crosslinker was $k_{\text{link}} = 25\text{ pN }\mu\text{m}$. We introduced 100 actin crosslinkers for the final 300 seconds of the 800 second simulation time, then detach the actin membrane binding proteins as previously. Figure 3.14 shows the crosslinked actin filament at the timepoints captured previously. Despite the ends of the filaments remaining secure, the ring shape deviates from its original alignment quickly, beginning to tilt into the axial plane by $t = 1.2\text{ s}$. At $t = 10\text{ s}$, the ring is no longer oriented around the membrane, instead appearing slightly elongated and aligned mainly with the cylindrical axis.

3.7 In-Cell Actin Polymerisation

In Sections 3.3 - 3.6 our actin filaments were of fixed length, however it is highly likely that the actin which forms the MPS is nucleated and polymerised within the axon environment, and studies have demonstrated a connection between the final configuration of actin and the shape of the environment in which it is polymerised (Miyazaki et al. (2015)). It is therefore useful to explore whether in-cell polymerisation significantly alters our results, and we now revisit the model used in Section 3.5 in which we placed actin filaments into an axon-like cell containing membrane-bound spectrin with which it can interact. We investigate a range of actin stiffnesses while varying the rate of polymerisation, r_{growth} , in cases with and without spectrin present.

Actin incorporated into the MPS is expected to be nucleated by formins;

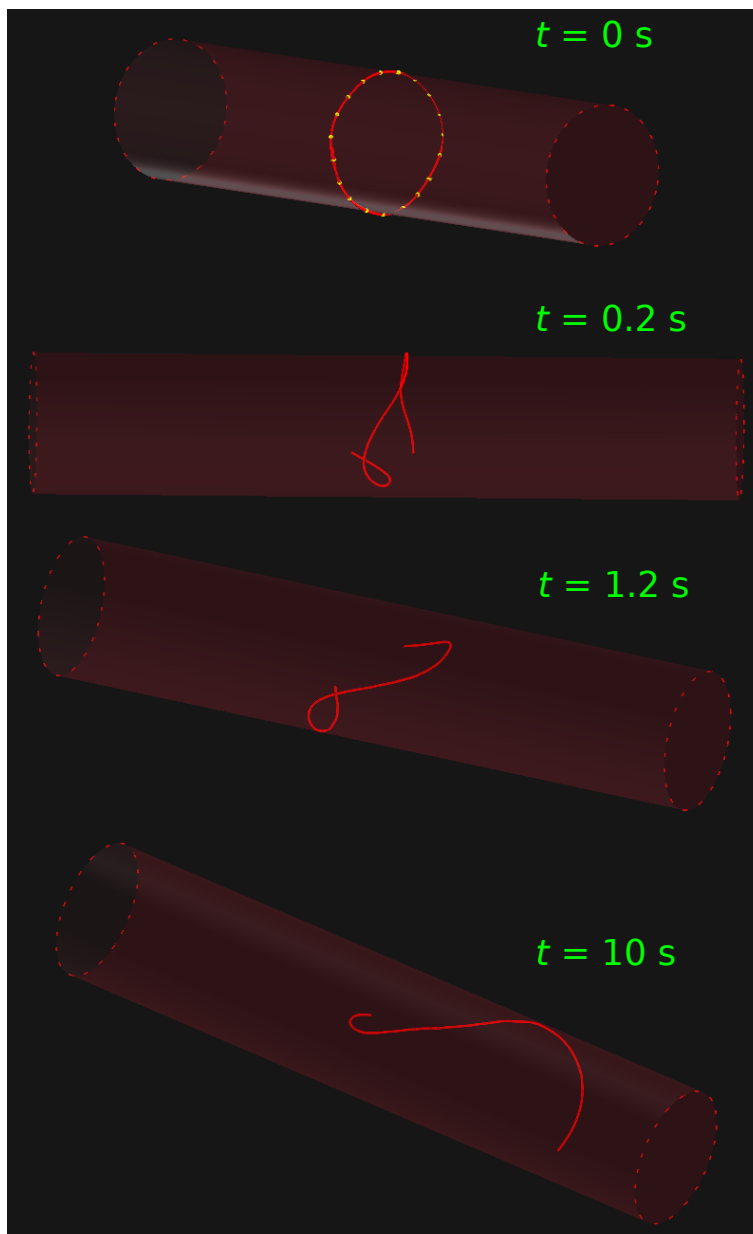


Figure 3.13: Filament Configuration after Detachment of Membrane Binding Proteins. An actin filament of $\kappa_{\text{actin}} = 0.00228 \text{ pN } \mu\text{m}^2$ initially forms an ideal ring when bound to the ordered membrane binding proteins. These proteins are detached and removed from the simulation, causing rapid configurational changes to the filament.

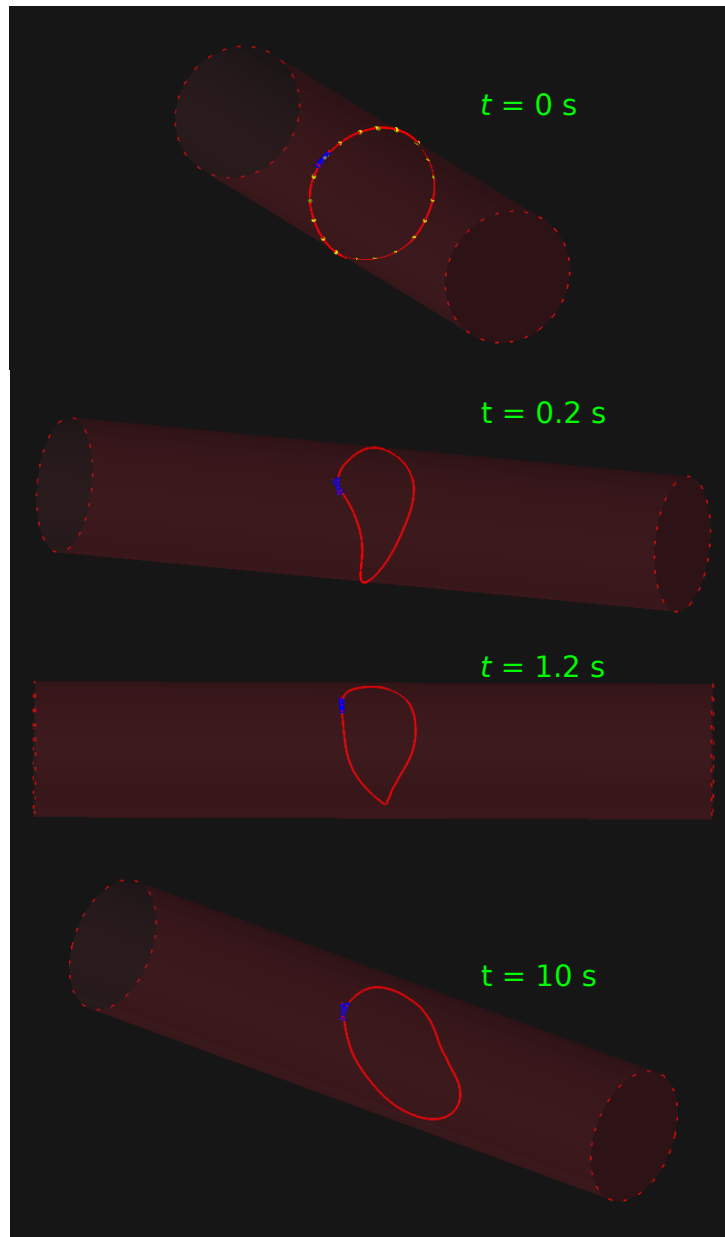


Figure 3.14: Crosslinked Filament Configuration after Detachment of Membrane Binding Proteins. *The actin crosslinking proteins are shown in blue securing the ends of the filament which forms an ideal ring at $t = 0 \text{ s}$. Once detached, the ring quickly tilts, losing its original orientation.*

proteins which grow unbranched actin filaments, remaining attached to the end of the filament (Pruyne et al. (2002)). We therefore model an actin nucleating protein which nucleates a single filament actin at a rate of $r_{\text{nuc}} = 0.5 \text{ s}^{-1}$ and does not unbind, remaining at the end of the filament throughout the simulation.

On nucleation, a filament of $0.01 \mu\text{m}$ is created, and proceeds to polymerise at a specified rate which we varied. Formin-nucleated actin filaments in yeast have been shown to polymerise at a rate of 12 subunits per second (Courtemanche et al. (2013)), and with an actin subunit rise of 2.76 nm (Dominguez and Holmes (2011)), this corresponds to a polymerisation rate of $r_{\text{growth}} = 0.033 \mu\text{m s}^{-1}$. This rate is dynamic however, with linear dependence on the available concentration of ATP-bound actin monomers as shown across a range of 0.05 to 280 subunits per second (Pollard (1986)) (corresponding to $0.000138 - 0.77 \mu\text{m s}^{-1}$). A range of additional factors can influence polymerisation rate; formin-nucleated actin has been found to polymerise at an elevated rate in the presence of profilin, while slowing dramatically in response to forces (Courtemanche et al. (2013)). Dematin is also able to slow polymerisation of actin (Siegel and Branton (1985)). To explore the impact of polymerisation rate we chose to use the observed rate in yeast (Courtemanche et al. (2013)), and values a factor of 10 larger and smaller, giving a parameter set of $r_{\text{growth}} \in \{0.33, 0.033, 0.0033\} \mu\text{m s}^{-1}$.

We initially simulated actin only, carrying out 10 repeat simulations per parameter set and calculating the mean and standard deviation of these 10 results. Figure 3.15 shows the variation of mean ORP across the actin stiffness range of $\kappa_{\text{actin}} \in [0.000143, 0.0730] \text{ pN } \mu\text{m}^2$ for the 3 actin polymerisation rates. Equivalent results for non-polymerised, fixed length actin are shown on this Figure in red for comparison. In this Figure, we see that the majority of results across all polymerisation rates mirror those of non-polymerised actin. There appear to be some small differences at the mid-range stiffnesses of $\kappa_{\text{actin}} \in [0.000570, 0.00456] \text{ pN } \mu\text{m}^2$. In Figure 3.16 we plot mean ORP with r_{growth} and these differences can be seen more clearly, with a dip in mean ORP for $\kappa_{\text{actin}} = 0.00228 \text{ pN } \mu\text{m}^2$ at $r_{\text{growth}} = 0.033 \mu\text{m s}^{-1}$, and another for $\kappa_{\text{actin}} = 0.00114 \text{ pN } \mu\text{m}^2$ at $r_{\text{growth}} = 0.0033 \mu\text{m s}^{-1}$.

In Table 3.5 we show the magnitude of these changes, detailing the change in mean ORP for each polymerisation speed, relative to the mean ORP result for non-polymerised actin of the same stiffness. We see that in many cases, there is an increase in mean ORP, with 9 out of 10 actin stiffnesses showing an increase at the most rapid polymerisation rate of $r_{\text{growth}} = 0.33 \mu\text{m s}^{-1}$, and 6 of the 10 results increasing for the slower rates, $r_{\text{growth}} \in \{0.033, 0.0033\} \mu\text{m s}^{-1}$. These increases are, however, very small in magnitude, reaching a maximum of 0.0269. In the table we note that for the 2 parameter sets which showed decreases in Figures 3.15 - 3.16, $\kappa_{\text{actin}} = 0.00228 \text{ pN } \mu\text{m}^2$ at $r_{\text{growth}} = 0.033 \mu\text{m s}^{-1}$, and $\kappa_{\text{actin}} = 0.00114 \text{ pN } \mu\text{m}^2$ at $r_{\text{growth}} = 0.0033 \mu\text{m s}^{-1}$, changes in mean ORP are of ~ 0.1 in magnitude, while other decreases detailed in the table are on the order of 10^{-2} or below.

Overall, polymerisation within the cell appears to make very little difference where no spectrin is present, with variations being very small in magnitude and

Table 3.5: In-Cell Polymerisation without Spectrin: Mean ORP Variation Relative to Non-Polymerised Result. *The change in mean ORP is shown to 3 significant figures relative to non-polymerised actin of equal stiffness for 3 values of the polymerisation rate, r_{growth} .*

$\kappa_{\text{actin}}/\text{pN } \mu\text{m}^2$	Mean ORP for Non-Polymerised Actin	Δ Mean ORP for $r_{\text{growth}}/\mu\text{m s}^{-1}$		
		0.33	0.033	0.0033
0.0730	0.9344	+0.0269	+0.0243	+0.0249
0.0365	0.9491	+0.00120	-0.0106	+0.00470
0.0183	0.9219	+0.0174	+0.00870	+0.00450
0.00913	0.9005	+0.00720	-0.00750	+0.0217
0.00456	0.8809	+0.0154	-0.0216	-0.0475
0.00228	0.7145	+0.00750	-0.1188	+0.0195
0.00114	0.5217	-0.0607	+0.00560	-0.106
0.000570	0.4430	+0.0123	+0.0123	-0.0249
0.000285	0.4604	+0.0111	+0.00670	-0.0222
0.000143	0.4778	+0.00120	+0.00490	+0.0119

no clear pattern of changes detectable.

Next we investigated whether this result changed if spectrin tetramers were present while actin was polymerising within the cell. We introduced 500 spectrin tetramers which we confine to the membrane, along with actin-spectrin linking proteins with properties as defined in Sections 3.2.8 and 3.5, and repeated the simulation sets.

Figure 3.17 shows the variation of mean ORP for actin stiffness in the range of $\kappa_{\text{actin}} \in [0.000143, 0.0730]$ pN μm^2 for the 3 actin polymerisation rates, when polymerised with 500 spectrin tetramers present on the membrane. As previously, we show equivalent results for non-polymerised actin interacting with 500 spectrin tetramers in red on this Figure. These sets of results are strikingly different when compared with those polymerised in the absence of spectrin; for the most rapid polymerisation rate of $r_{\text{growth}} = 0.33 \mu\text{m s}^{-1}$, mean ORP increases across the range of actin stiffnesses, displaying very large error bars particularly at the mid range stiffnesses. Mean ORP then decreases at $r_{\text{growth}} = 0.033 \mu\text{m s}^{-1}$, reducing further for $r_{\text{growth}} = 0.0033 \mu\text{m s}^{-1}$.

In Figure 3.18 we plot mean ORP against r_{growth} for each actin stiffness. We see mean ORP increasing initially, rising from the non-polymerised result to reach a peak at $r_{\text{growth}} = 0.33 \mu\text{m s}^{-1}$, followed by a reduction as the polymeri-

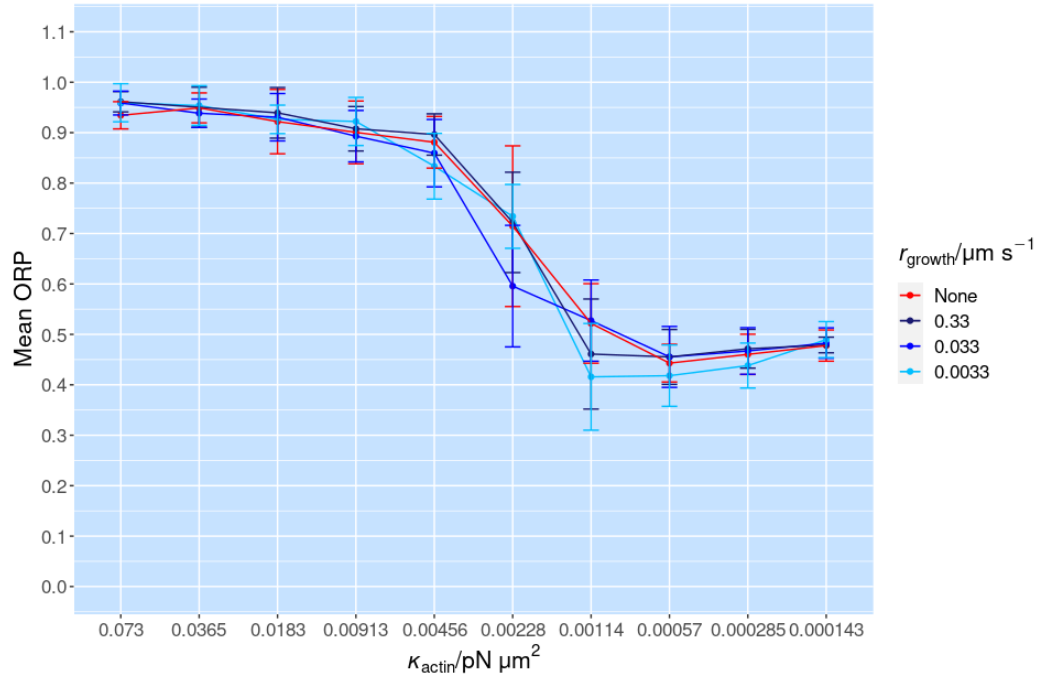


Figure 3.15: Actin Only: Mean ORP with Actin Stiffness for Varying Polymerisation Rates. We show mean ORP results gathered over 10 repeat simulations for actin filaments polymerised at $r_{\text{growth}} \in \{0.33, 0.033, 0.0033\}$, across the range of 10 actin stiffnesses. Results for fixed length, non-polymerised actin are shown in red for comparison. The graph shows high levels of agreement between polymerised and non-polymerised actin for the majority of actin stiffnesses, with small decreases at $\kappa_{\text{actin}} \in \{0.00228, 0.00114\}$ for r_{growth} of 0.033 and 0.0033 $\mu\text{m s}^{-1}$ respectively.

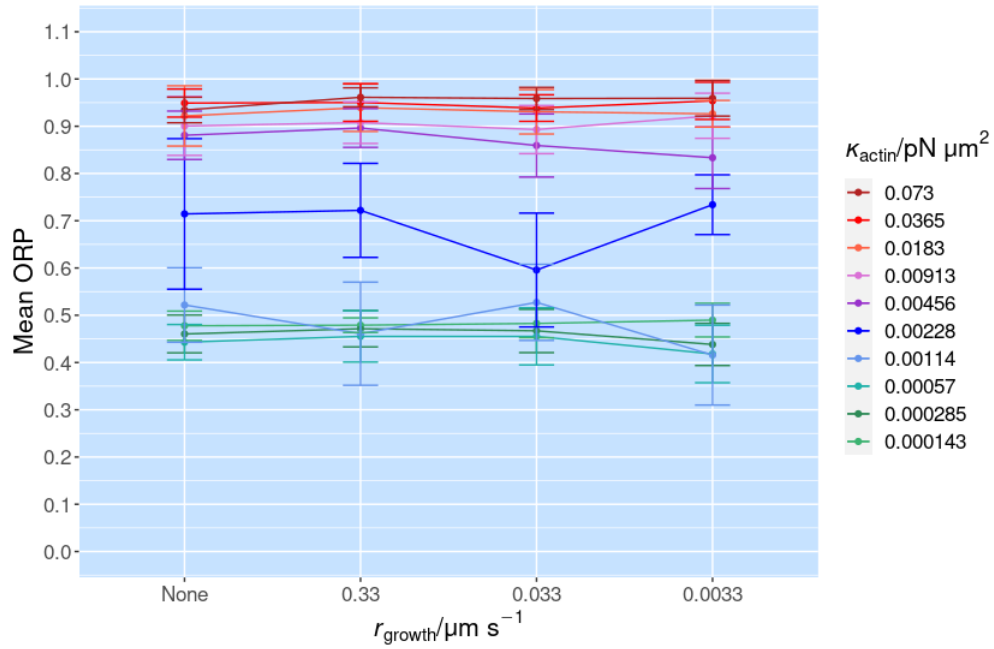


Figure 3.16: Actin Only: Mean ORP with Actin Polymerisation Rate for Varying Actin Stiffness. Mean ORP is displayed for 3 values of polymerisation rate, r_{growth} as well as non-polymerised actin which is shown at the first point on the x axis. For the highest and lowest actin stiffnesses there is very little change with polymerisation rate and results stay in line with those of non-polymerised actin, however at $\kappa_{\text{actin}} = 0.00228 \text{ pN } \mu\text{m}^2$ with $r_{\text{growth}} = 0.033 \mu\text{m s}^{-1}$, and $\kappa_{\text{actin}} = 0.00114 \text{ pN } \mu\text{m}^2$ with $r_{\text{growth}} = 0.0033 \mu\text{m s}^{-1}$, mean ORP decreases by around 0.1.

sation rate slows. These changes appear most pronounced for κ_{actin} of 0.00228 and 0.00456 pN μm^2 .

Table 3.6 details the magnitudes of these changes in mean ORP relative to the results of a non-polymerised actin filament under the same conditions. We note that in all cases, mean ORP increases for the most rapid polymerisation rate, $r_{\text{growth}} = 0.33 \mu\text{m s}^{-1}$, and the magnitude of this increase varies with actin stiffnesses, being on the order of 10^{-2} for $\kappa_{\text{actin}} \geq 0.00913 \text{ pN } \mu\text{m}^2$ and $\kappa_{\text{actin}} \leq 0.000570 \text{ pN } \mu\text{m}^2$, and 10^{-1} for $\kappa_{\text{actin}} \in [0.00114, 0.00456] \text{ pN } \mu\text{m}^2$.

At a polymerisation rate of $r_{\text{growth}} = 0.033 \mu\text{m s}^{-1}$, 9 of the 10 parameter sets showed decreases in mean ORP; all sets of $\kappa_{\text{actin}} \leq 0.00456 \text{ pN } \mu\text{m}^2$ showed decreases of > 0.1 in magnitude, while $\kappa_{\text{actin}} \geq 0.00913 \text{ pN } \mu\text{m}^2$ showed smaller fluctuations of order $\leq 10^{-2}$. The greatest change occurred for $\kappa_{\text{actin}} = 0.00456 \text{ pN } \mu\text{m}^2$ with mean ORP decreasing by 0.328 relative to the non-polymerised results for actin of this stiffness.

At the slowest polymerisation rate of $r_{\text{growth}} = 0.0033 \mu\text{m s}^{-1}$, all parameter sets showed decreases in mean ORP. This decrease was on order of magnitude of 10^{-1} for all sets of $\kappa_{\text{actin}} \leq 0.0183 \text{ pN } \mu\text{m}^2$, and smaller at 10^{-2} for $\kappa_{\text{actin}} \geq 0.0365 \text{ pN } \mu\text{m}^2$. The decrease in mean ORP reached a maximum of 0.385 for $\kappa_{\text{actin}} = 0.00456 \text{ pN } \mu\text{m}^2$ and was > 0.2 for all stiffnesses below $\kappa_{\text{actin}} = 0.00913 \text{ pN } \mu\text{m}^2$.

Figures 3.17 - 3.18 and Table 3.6 clearly demonstrate that mean ORP changes in response to actin polymerisation rate when spectrin tetramers are present on the membrane, but how does this translate to levels of ring creation?

In Figure 3.19 we look at the filaments more closely, quantifying how ring-like they are based on a set of ORP classifications which are detailed in the legend in Subfigure 3.19e. We present images for each of our polymerisation conditions, analysing data from non-polymerised actin in Subfigure 3.19a, and our 3 polymerisation rates in Subfigures 3.19b - 3.19d. The stacked bars in these images show the distribution of ORP classifications for each sample of 10 repeat simulations associated with an actin stiffness.

In Subfigure 3.19a bars are green for $\kappa_{\text{actin}} \geq 0.00228 \text{ pN } \mu\text{m}^2$ indicating ORP values of ≥ 0.3 , while stiffnesses below this value show small numbers of filaments in the yellow range with $0.2 \leq \text{ORP} < 0.3$. For the most rapid growth rate, $r_{\text{growth}} = 0.33 \mu\text{m s}^{-1}$, as shown in Subfigure 3.19b, most bars are green, with small numbers in the yellow range and orange range of $0.1 \leq \text{ORP} < 0.2$ for actin stiffnesses $\kappa_{\text{actin}} \in [0.000285, 0.00228] \text{ pN } \mu\text{m}^2$. At $r_{\text{growth}} = 0.033 \mu\text{m s}^{-1}$, as shown in Subfigure 3.19c there are high proportions of filaments in the regions of interest for $\kappa_{\text{actin}} \leq 0.00913 \text{ pN } \mu\text{m}^2$, with some filaments appearing in the red zone with $0.1 \leq \text{ORP}$, demonstrating high levels of agreement with an ideal ring configuration. Finally at the slowest polymerisation rate, $r_{\text{growth}} = 0.0033 \mu\text{m s}^{-1}$, shown in Subfigure 3.19d, all parameter sets at $\kappa_{\text{actin}} \leq 0.00913 \text{ pN } \mu\text{m}^2$ show high levels of ring formation, with $\kappa_{\text{actin}} = 0.000570 \text{ pN } \mu\text{m}^2$ appearing to give the most favourable results, with all filaments showing $\text{ORP} \leq 0.2$ and 7 of the 10 filaments having $\text{ORP} < 0.1$.

Overall, the results of this Section show that actin rings can form when actin is polymerised within the cell, provided spectrin tetramers are present

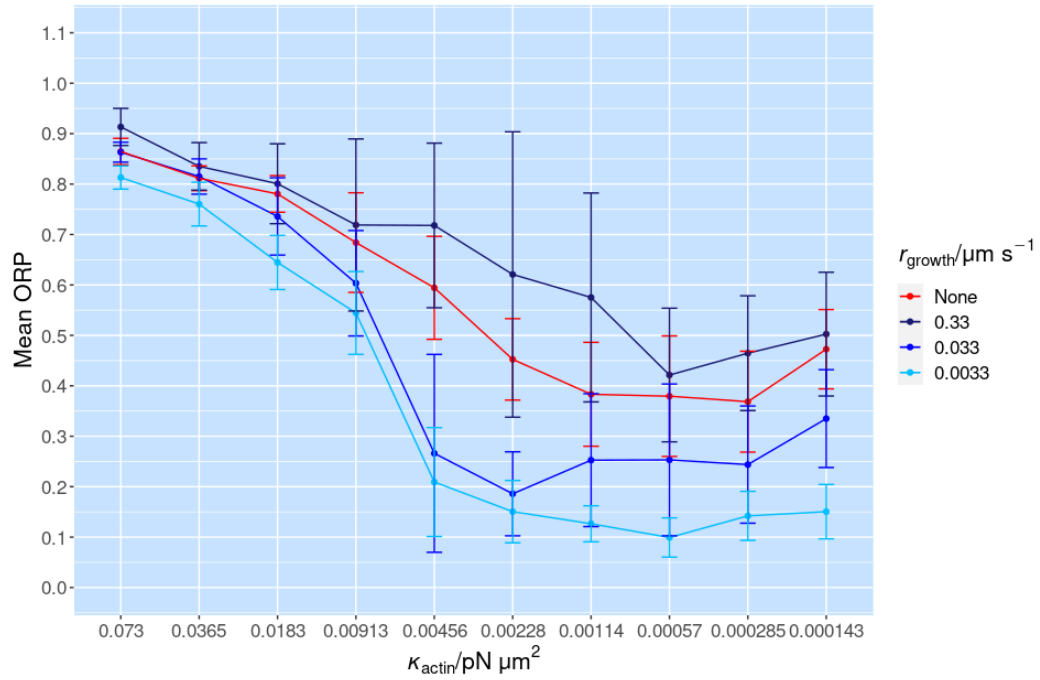


Figure 3.17: Mean ORP with Actin Stiffness for Varying Polymerisation Rates in Presence of Spectrin Tetramers. Mean ORP results are shown for actin filaments polymerised in the presence of 500 spectrin tetramers at $r_{\text{growth}} \in \{0.33, 0.033, 0.0033\}$, across the range of 10 actin stiffnesses. Results for fixed length, non-polymerised actin interacting with this quantity of spectrin are shown in red for comparison. We see a clear impact of in-cell polymerisation; mean ORP increases across all actin stiffnesses when polymerised at the most rapid speed of $r_{\text{growth}} = 0.33 \mu\text{m s}^{-1}$, followed by large decreases as the polymerisation rate slows.

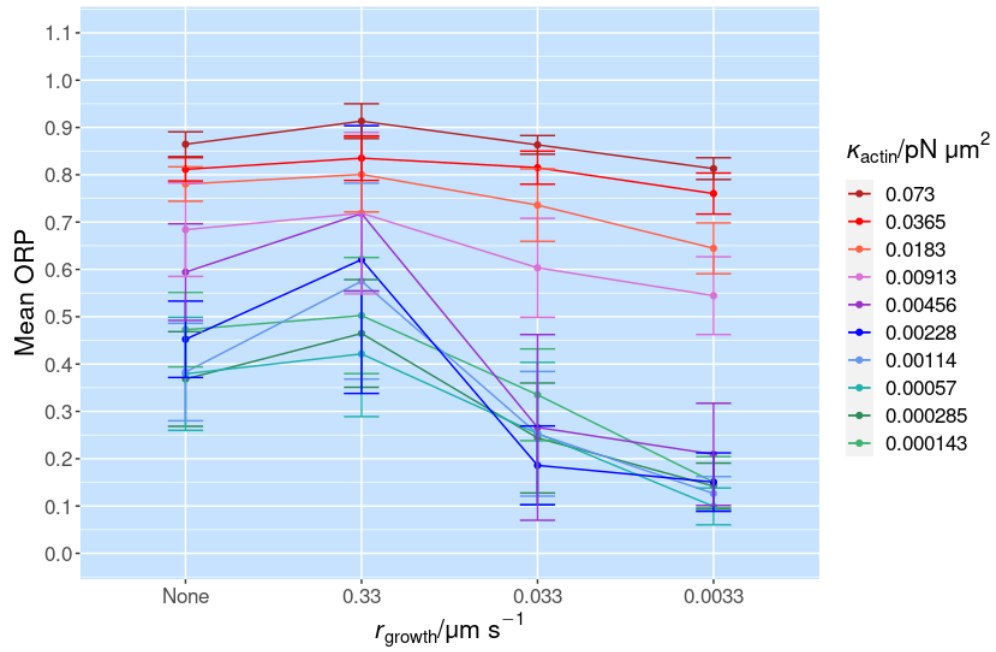


Figure 3.18: Mean ORP with Spectrin Density for varying Actin Stiffnesses in Presence of Spectrin Tetramers. *Mean ORP is shown for 3 values of polymerisation rate, r_{growth} as well as non-polymerised actin. Mean ORP increases at $r_{\text{growth}} = 0.33 \mu\text{m s}^{-1}$, then begins to reduce as polymerisation speed is slowed. These changes appear most pronounced at mid-range stiffnesses of $\kappa_{\text{actin}} \in [0.00228, 0.00456] \text{ pN } \mu\text{m}^2$.*

Table 3.6: In-Cell Polymerisation with $N_{\text{spectrin}} = 500$: Mean ORP Variation Relative to Non-Polymerised Result. *The change in mean ORP is shown to 3 significant figures relative to non-polymerised actin of equal stiffness for 3 values of the polymerisation rate, r_{growth} .*

$\kappa_{\text{actin}}/\text{pN}$ μm^2	Mean ORP for Non- Polymerised Actin	Δ Mean ORP for $r_{\text{growth}}/\mu\text{m s}^{-1}$		
		0.33	0.033	0.0033
0.0730	0.8645	+0.0488	-0.00130	-0.0515
0.0365	0.8115	+0.0236	+0.00350	-0.0512
0.0183	0.7805	+0.0202	-0.0446	-0.136
0.00913	0.6840	+0.0349	-0.0806	-0.140
0.00456	0.5943	+0.124	-0.328	-0.385
0.00228	0.4524	+0.168	-0.267	-0.302
0.00114	0.3832	+0.192	-0.131	-0.257
0.000570	0.3794	+0.0420	-0.126	-0.280
0.000285	0.3685	+0.0962	-0.125	-0.226
0.000143	0.4726	+0.0299	-0.138	-0.322

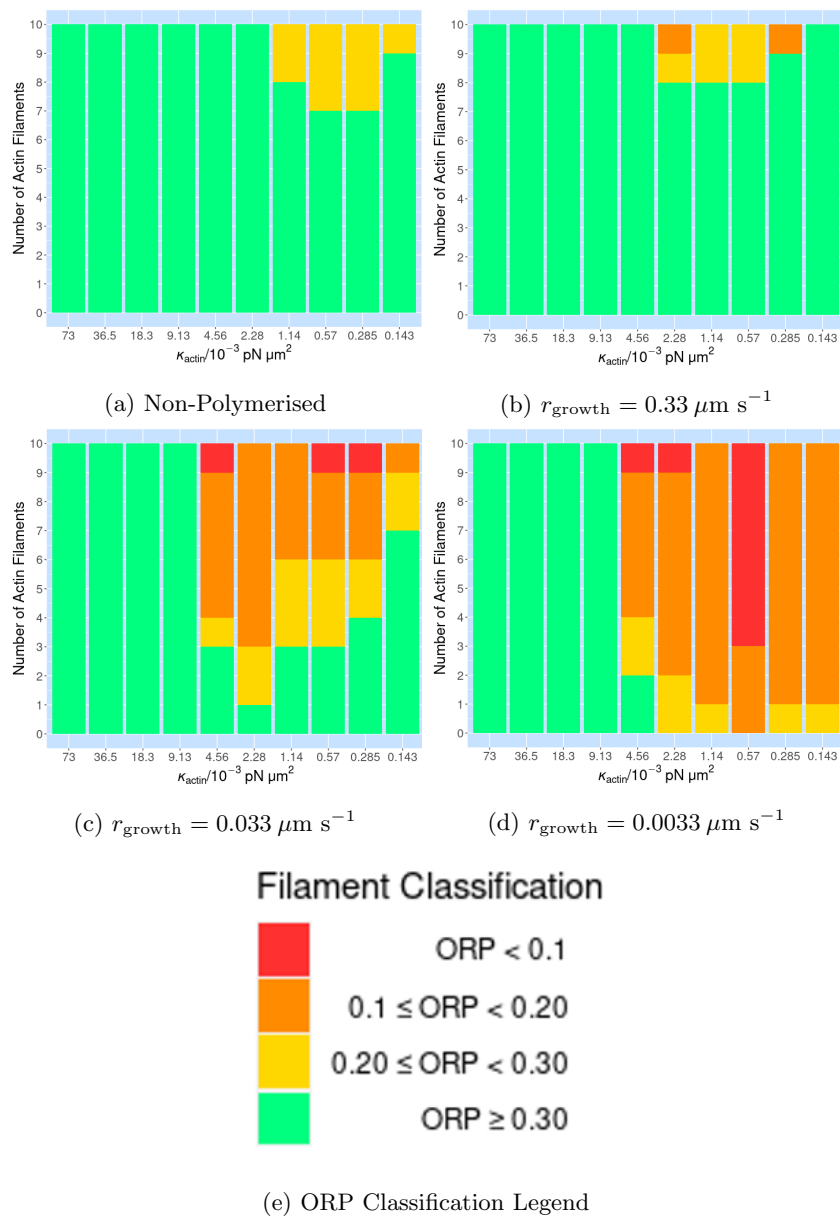


Figure 3.19: Ring Formation for In-Cell Actin Polymerisation with 500 Spectrin Tetramers. Bars display the classification of actin filaments from 10 repeat simulations according to the legend in Subfigure e. Subfigure a shows results for actin which is non-dynamic in length, while Subfigures b-d show results at decreasing rates of polymerisation. Ring formation appears uncommon for non-polymerising or rapidly polymerising actin but occurs more frequently at slow polymerisation rates and low actin stiffnesses.

with which it can interact. Ring formation required a low actin stiffness of $\kappa_{\text{actin}} \leq 0.00456 \text{ pN } \mu\text{m}^2$. The rate of polymerisation was also important; ring formation was observed for rates of $r_{\text{growth}} \leq 0.033 \mu\text{m s}^{-1}$ only. Rings were created fairly reliably for parameter sets falling within these value ranges despite variations between repeats due to the stochastic processes involved.

Qualitatively, it appeared that the short, flexible actin filaments present shortly after nucleation were more likely to orient around the circumference of the axon if quickly linked to spectrin tetramers present on the membrane. Spectrin was then recruited to both sides of the filament, stacking in parallel, further reinforcing growth around the membrane circumference which facilitates ring formation. As the spectrin levels in these simulations were fairly low, motion of spectrin was substantial particularly along the length of the cylindrical cell, and in some cases spectrin tetramer motion caused the actin filament to deviate from its original direction of growth, instead spiralling outwards. It would be instructive to look more closely at the impact of increasing numbers of spectrin tetramers to determine whether rings are created more reliably when motion of spectrin is limited by increased density.

3.8 Discussion

In Section 3.3 we found that actin filaments did not form rings when placed within our axon-like cell, nor did they form rings when interacting with randomly placed proteins which linked them to the membrane as shown in Section 3.4.

We discovered in Section 3.5 that our results improved when spectrin tetramers were introduced on the cell membrane. We observed reductions in mean ORP for $n_{\text{spectrin}} \geq 500$, affecting mainly actin in the stiffness range $\kappa_{\text{actin}} \in [0.00228, 0.00456] \text{ pN } \mu\text{m}^2$. As well as a reduction in mean ORP, many of these parameter sets yielded results with ORP values of < 0.3 which we consider to be ring-like to some degree.

When membrane binding proteins were placed in a ring in Section 3.6, we were able to reliably create actin rings for stiffnesses in the range $\kappa_{\text{actin}} \in [0.000570, 0.00228] \text{ pN } \mu\text{m}^2$, however these rings were unstable, unravelling and reorienting rapidly if detached from their membrane adhesions, and losing orientation even when their ends were secured to maintain a ring-like shape.

Finally in Section 3.7 we discovered that in-cell polymerisation of actin had a substantial impact on ORP results provided that spectrin tetramers were present on the membrane as the actin filament was polymerising. As for our previous results on actin-spectrin interactions, the actin stiffnesses of 0.00228 and 0.00456 $\text{pN } \mu\text{m}^2$ gave the most favourable results. We noted a dependence on the rate of polymerisation, observing reductions in mean ORP with decreasing rate as well as the appearance of more rings with precise degrees of alignment to our ideal configuration.

In our next Chapter, we build on these findings, working with systems of multiple filaments in a larger cell. Can our single filament results be applied to

these larger systems, causing multiple rings to self-assemble into a connected, MPS-like structure?

Chapter 4

Multiple Filament Self-Assembly

4.1 Introduction

In Chapter 3, we found that it is possible for an actin filament to form a ring within a narrow axon-like geometry, however this was unlikely to occur for actin of standard stiffness, even when able to interact with ideally placed membrane binding proteins. We discovered that to form rings, actin had to be of a low stiffness of $\kappa_{\text{actin}} \leq 0.00456 \text{ pN } \mu\text{m}^2$. In addition, ring formation occurred mainly when actin was polymerised within the cell, and a slow rate of polymerisation, $r_{\text{growth}} = 0.0033 \mu\text{m s}^{-1}$, gave the best results in terms of a reduced mean value of the Orientational Order Parameter (ORP) - a value corresponding to the level of alignment of an actin filament with a filament of equal length, aligned in a ring around the cell membrane, as defined in Section 3.2.2. These parameters also gave the highest numbers of ORP results below the threshold of 0.3 which we use to detect ring-like structures. Ring formation was also greatly facilitated by interactions with membrane-bound spectrin tetramers.

In this Chapter, we extend our investigations to consider multiple actin filaments. We work in a larger space representing a section of a typical axon, investigating whether co-operative effects occur when spectrin tetramers are able to interact with large numbers of actin filaments. In this Chapter, we focus on both self-assembly of actin rings, and the spatial organisation of these filaments within the axon.

In Section 4.2 we detail the methods used in this Chapter. In Section 4.3 we begin our investigations with a preliminary analysis, establishing suitable parameters for our simulations by assessing the effects of spectrin tetramer stiffness, along with the impact of different cell lengths and boundary types. In Section 4.4, we repeat the simulations of Section 3.5, surveying the effects

of varying densities of spectrin tetramers with multiple actin filaments within our larger cell space, while also comparing repeat simulations with identical parameters to determine the level of variability in our results.

In Section 4.5 we revisit actin polymerisation, extending the results of Section 3.7 to the case of multiple actin filaments. Section 4.5.1 provides an initial investigation focusing on 3 parameter sets of interest, and we follow with a sweep of a broader range of actin stiffnesses and polymerisation rates in Section 4.5.2. Section 4.6 examines the properties of the actin-spectrin linking protein, aiming to determine whether the connection should be stable or more transient in nature for best results, and assessing the influence of the availability of linking proteins on the final results. In Section 4.7 we perform a further analysis of spectrin density while adopting the optimum values for other parameters as determined in the previous sections.

In Section 4.8 we carry out a sweep of parameter combinations, aiming to determine the range of actin stiffnesses and polymerisation rates for which actin rings are possible when using those parameters which have generated the best results in previous sections, comparing and contrasting to the results of Section 4.5.2. Finally, in Section 4.9, we alter the cell morphology by increasing the radius, and observe the effect this has on our results. We end the Chapter with a short discussion in Section 4.10.

4.2 Methods

We continue to use Cytosim software as detailed in Section 3.2.1, and adopt the fibre properties as described in Sections 3.2.7 and 3.2.8. We adapt the cell dimensions and boundary conditions to allow for a larger section of axonal space to be modelled, as detailed in Section 4.3.2. Simulation properties were as described in Section 3.2.6, however as large-scale simulations can be time-consuming to run, we kept the number of repeats for each parameter set to a minimum where we deemed it reasonable to do so. The number of repeats used are stated and justified in each results section. We acknowledge that there can be substantial variability between simulations, even with identical parameters, and this should be taken into consideration when interpreting results.

The ORP data analysis calculation was used to quantify 'ring-like' properties for individual actin filaments, as described in Section 3.2.2.

To identify any periodic patterning within our simulations, we carry out Autocorrelation and Power Spectrum analyses, using methods as described in Section 2.4.4. For the results in this Chapter we did not calculate these measures for all simulations as in Chapter 2.6, instead plotting individual results that were deemed of interest.

4.3 Initial Investigations

In preparation for larger scale simulations, some initial exploratory simulations were carried out. Given that the stiffness of spectrin is unknown, we first vary this parameter across a range of stiffnesses, observing the influence of these changes on results and selecting a suitable value. Next we consider effects of cell size and boundary type on the simulation results, and make appropriate choices for these properties. The results of these simulations informed our choices of key simulation parameters and constants in the sections that follow.

For the simulations in this section, the length and stiffness of actin filaments were held constant, with $L_{\text{actin}} = 1.32 \mu\text{m}$ and $\kappa_{\text{actin}} = 0.00910 \text{ pN } \mu\text{m}^2$, approximating cofilactin (McCullough et al. (2008)). Filaments were placed at random at the first timestep, and simulations ran for 820 seconds as in Chapter 3, with the initial 20 seconds of simulation time including spectrin and actin-spectrin linking proteins only.

4.3.1 Spectrin Stiffness

As discussed in Section 3.2.8, the stiffness of brain spectrin is currently unknown, and in our investigations in Chapter 3, we assumed a value of $\kappa_{\text{spectrin}} = 0.07 \text{ pN } \mu\text{m}^2$ - a factor of 10^3 stiffer than the value found experimentally for erythrocyte spectrin, $\kappa_{\text{spectrin}} = 7.02 \times 10^{-5} \text{ pN } \mu\text{m}^2$ (Stokke et al. (1985)). As spectrin tetramers in simulations with multiple actin filaments are able to bridge pairs of filaments, the stiffness of spectrin may play a greater role in results than in the case of single actin filaments, and so we modelled a small $2 \mu\text{m}$ section of axon with periodic boundaries containing 500 spectrin tetramers confined to the membrane as in Section 3.2.8, and introduced 20 actin filaments. Spectrin stiffness was varied for $\kappa_{\text{spectrin}} \in \{7 \times 10^{-5}, 7 \times 10^{-4}, 7 \times 10^{-3}, 7 \times 10^{-2}, 7 \times 10^{-1}\} \text{ pN } \mu\text{m}^2$. Actin-spectrin linker proteins were included at $N_{\text{linker}} = 2.5N_{\text{spectrin}}$. 3 simulations were run for each parameter set initially, and as results varied very little between sets, no further simulations were carried out.

Figure 4.1 shows the mean ORP and standard deviation error bars for the 5 κ_{spectrin} values. The mean is taken over 60 actin filaments for each parameter set (20 actin filaments per repeat simulation) The mean is close to 1 and is consistent across the range of spectrin stiffnesses. This suggests that the stiffness of spectrin has no noticeable effect on the configuration of actin in our model.

A limitation of our model is that vertices of spectrin tetramers each experience a restoring force directed towards the membrane, and this influences the configurations that can be adopted towards those within the plane of the membrane. It is possible that spectrin stiffness would have a more noticeable effect if spectrin were anchored from select points only, however incorporating such a feature would require adaptations to the software. It is likely that MPS-based spectrin would experience connections to the membrane at several locations along its length, being tethered via Ankyrin-B at its centrepoint, with the possibility of other connections (Zhang et al. (2019)), but also being attached to actin at each end, through which further membrane connections could be made

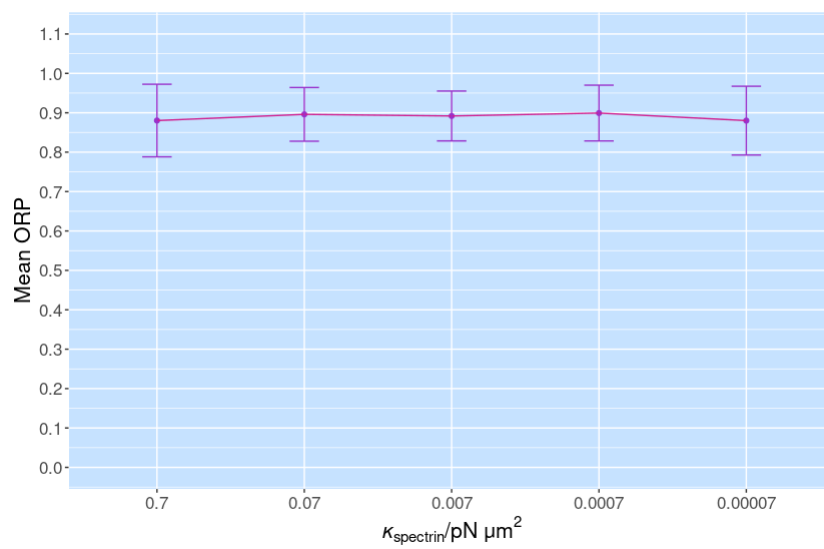


Figure 4.1: Mean ORP for Different Spectrin Stiffnesses. *This plot shows the mean ORP result for a total of 60 actin filaments of $\kappa_{\text{actin}} = 0.00910 \text{ pN } \mu\text{m}^2$ per spectrin stiffness value. 500 spectrin tetramers were used in these simulations. All results appear approximately equal.*

via linking proteins such as IQGAP proteins (Palani et al. (2020)), and Dematin (Siegel and Branton (1985)). We also expect that spectrin would be recruited to the membrane rapidly due to the high concentrations of Ankyrin-B present in early development (Galiano et al. (2012)). Modelling the spectrin tetramer with membrane confinement in this manner allowed us to simplify various membrane tethering processes, removing the need to model several additional and poorly understood spectrin and actin membrane-binding proteins or processes.

Considering the results of this Section, along with the above justification of our membrane tethering approach, we therefore choose a fixed value of spectrin stiffness, $\kappa_{\text{spectrin}} = 0.07 \text{ pN } \mu\text{m}^2$, and use this value in all further simulations.

4.3.2 Cell Size and Boundaries

In Chapter 3, we focussed on a small, $2 \mu\text{m}$ section of an infinite periodic axonal space, however the finite size of the axon and presence of intra-axonal boundaries is of relevance when considering self-assembly and periodic organisation of multiple actin filaments.

A typical axon has length of between 0.1 mm and 3 m (Kandel et al. (2000), Chapter 2), with an AIS of around $20\text{-}60 \mu\text{m}$ proximal to the soma (Leterrier et al. (2017)). Many axons are punctuated by Nodes of Ranvier, occurring at $1\text{-}2 \text{ mm}$ intervals, with each node occupying around $2 \mu\text{m}$ of axonal length (Kandel et al. (2000), Chapter 8). Even if we assume the minimum axon length and maximum region occupied by the AIS, the length of a section of axon between intra-axonal boundaries is $\sim 40 \mu\text{m}$. Simulating such a large space would require the inclusion of large numbers of cytoskeletal filaments and lies far beyond the capabilities our computational resources. We must therefore compromise between realistic biological lengthscales and computation time.

Given that the MPS appears to assemble proximal to the soma initially (Zhong et al. (2014)), it is highly desirable to include a boundary with which our filaments can interact, ruling out the use of periodic boundary conditions. In addition, while we wish to minimise the length of axon in our model, we do not wish to impose unrealistic levels of confinement. We therefore carry out simulations across a range of lengthscales, comparing results from a periodic space with those from a fixed boundary environment. Our aim is to find a balanced level of confinement, where the majority of actin filaments show an ORP value similar to those observed in the periodic case.

Simulations were carried out with axon-like environments of radius, $R_{\text{axon}} = 0.2 \mu\text{m}$, and length $L_{\text{axon}} \in \{2, 4, 6\} \mu\text{m}$. Periodic boundaries were used initially, followed by a fixed boundary capsule shaped space. A capsule shape was used as opposed to a cylinder; when a cylindrical cell was tested, we found that spectrin had a tendency to cluster on the circular endcaps. This was undesirable as it created artificially dense populations of spectrin in these regions. A capsule shape mitigates this as the curvature of the hemispherical caps prevents build-up of spectrin. Where a capsule-shaped cell was used, the length accounts for the cylindrical region, excluding the hemispherical caps at each end. Membrane-

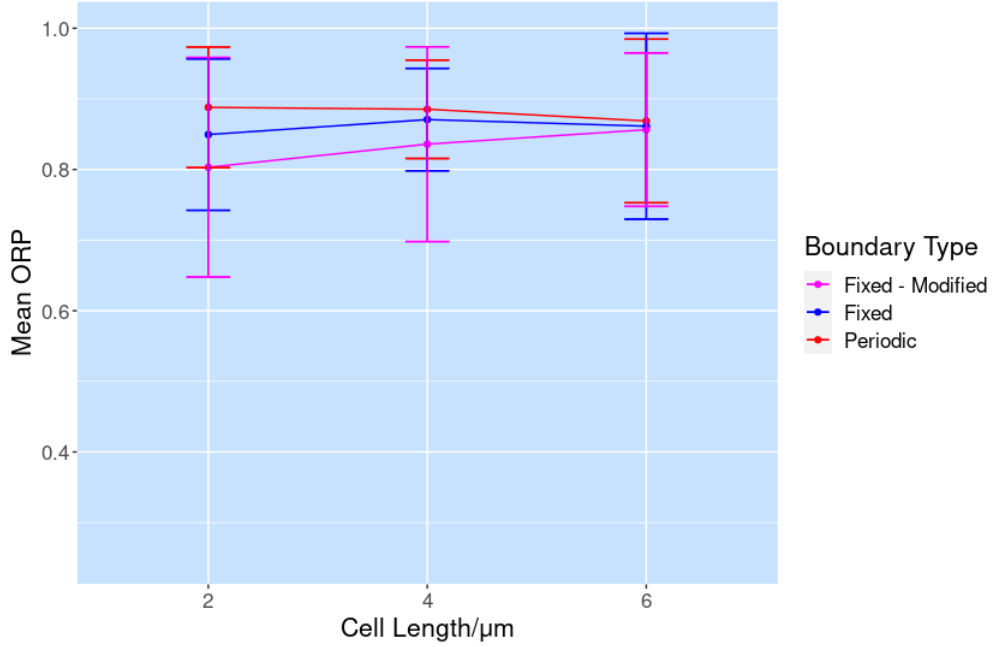


Figure 4.2: Effect of Boundaries and Cell Size. *This plot shows the ORP averaged over 3 simulations per parameter set, each containing 20 actin filaments. We investigate cell lengths of $L_{\text{axon}} \in \{2, 4, 6\} \mu\text{m}$, simulating periodic and fixed boundaries in each case, along with the customised fixed boundary described in 4.3.2. While some differences can be seen at shorter cell lengths, when our cell length reaches $L_{\text{axon}} = 6 \mu\text{m}$, results for each boundary type appear equivalent.*

bound spectrin was present with properties as detailed in Section 3.2.8, with 500 spectrin tetramers for each $2 \mu\text{m}$ of axonal length, and linker proteins with properties as detailed in Section 3.5 present at levels of $N_{\text{linker}} = 2.5N_{\text{spectrin}}$. 20 actin filaments were used in each case.

Due to the capsule shape of the fixed boundary cell, we noted that the density of spectrin tetramers was very high close to the boundary. This was due to the curvature of the hemispherical ends of the cell, which caused any spectrin tetramers placed there to migrate onto the cylindrical regions where curvature is reduced. To allow for a more homogeneous spectrin distribution, we created a third geometry in which we placed spectrin tetramers on the cylindrical region of the cell only. We define a second cylindrical space of length L_{axon} within the capsule shaped cell and restrict actin filaments to this region to avoid these filaments becoming trapped in the hemispherical end caps, which could artificially reduce the ORP measure. This modified fixed boundary geometry was compared with the periodic and fixed boundary cases.

Results are shown in Figure 4.2. We carried out 3 simulations for each parameter set and deemed this to be sufficient as results between sets differed only slightly. The results for each boundary type appear to be similar, however we note a small reduction in mean ORP for the 2 fixed boundary sets when compared to the case of periodic boundaries. As cell size increases this difference diminishes, and for a 6 μm cell, all 3 results are very closely matched.

Based on these results, and for the reasons stated above, we chose to use a 6 μm cell, adopting the modified fixed boundary geometry, with actin restricted to a cylindrical region centered on the capsule cell shape, with length $L_{\text{axon}} = 6\mu\text{m}$, and radius $R_{\text{axon}} = 0.2\mu\text{m}$.

4.4 Membrane-Bound Spectrin

To begin our investigations with multiple filaments, we repeat the simulations of Section 3.5, varying both actin stiffness and the density of spectrin tetramers, in a set of simulations using non-polymerised actin of fixed length, $L_{\text{actin}} = 1.32\mu\text{m}$.

We adopt the axonal cell environment and spectrin stiffness which we identified as most suitable in Section 4.3. Actin stiffness is varied across a subset of those values which we used in Section 3.5; we neglect the lowest 2 stiffnesses which formed tight coils and are therefore not deemed to be of interest, while also neglecting the stiff, stabilised form of actin which appeared too rigid to form rings within our narrow cell. This gives an actin stiffness range of $\kappa_{\text{actin}} = [0.000570, 0.0365]$ pN μm^2 . We varied the number of spectrin tetramers present over $N_{\text{spectrin}} \in \{0, 150, 300, 1500, 3000, 4500\}$ to maintain the same number per μm of axonal length that were used in Section 3.5. In each simulation, 60 actin filaments were present, allowing 10 per μm of axonal length. This was chosen based on the assumption that 2 filaments form each ring (Vasilopoulos et al. (2019)), and is an amount sufficient to create 30 actin rings at the expected 180-200 nm spacing within our 6 μm length cell. We carried out 3 simulations per parameter set initially, comparing results with identical parameters to ensure this sample size was sufficient.

In Figure 4.3, we show the variation in mean ORP as actin stiffness is reduced, for varying numbers of spectrin tetramers. We show equivalent results for $N_{\text{spectrin}} = 0$ on this plot in red. It is clear that the presence of spectrin tetramers alters the configuration of actin; we see lower mean ORP values for stiffnesses of around $\kappa_{\text{actin}} = 0.00228$ pN μm^2 and above, with higher numbers of spectrin tetramers corresponding with lower ORP values. For stiffnesses of $\kappa_{\text{actin}} \leq 0.00114$ pN μm^2 this trend is reversed, and higher numbers of spectrin cause an increase in mean ORP relative to the case of $N_{\text{spectrin}} = 0$. In all cases, error bars increase in size when spectrin is present.

These changes are further illustrated in Figure 4.4, which shows variation with the number of spectrin, for each of the actin stiffnesses tested. We see mean ORP levels reducing with increased spectrin for $\kappa_{\text{actin}} \geq 0.00456$ pN μm^2 . At 0.000570 and 0.00114 pN μm^2 , mean ORP increases, while for $\kappa_{\text{actin}} = 0.00228$

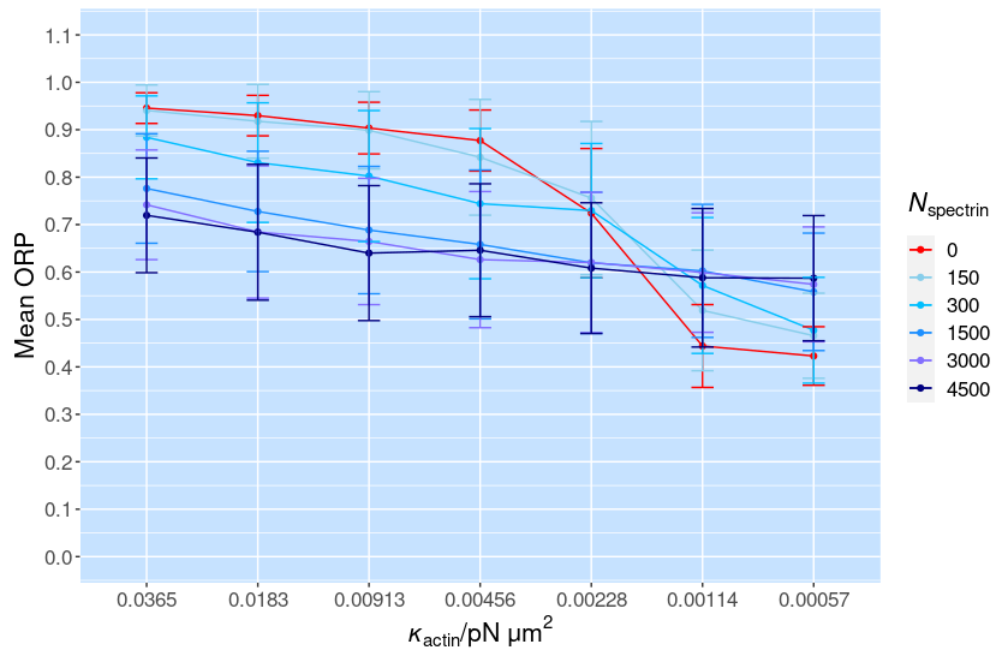


Figure 4.3: Mean ORP with Actin Stiffness for Varying N_{spectrin} . The mean ORP is shown based on 3 repeat simulations each containing 60 actin filaments. The $N_{\text{spectrin}} = 0$ result is shown in red for reference. ORP appears reduced where spectrin numbers are high, however at stiffnesses below $\kappa_{\text{actin}} = 0.00228 \text{ pN } \mu\text{m}^2$, we do not see the large reduction in ORP observed in the case of $N_{\text{spectrin}} = 0$, and the mean ORP value remains fairly stable as stiffness is reduced.

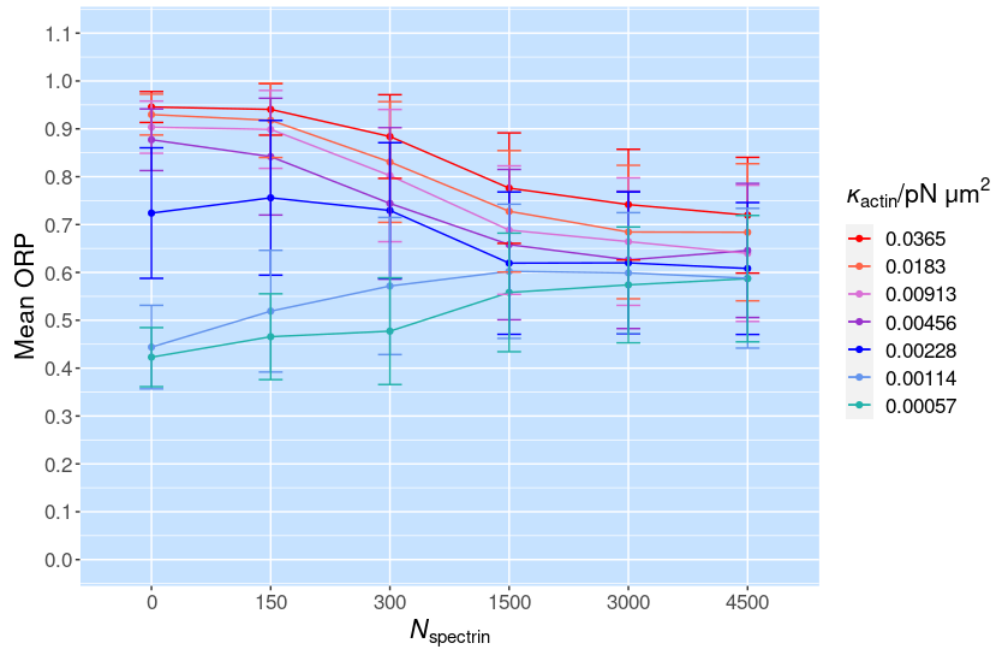


Figure 4.4: Mean ORP with N_{spectrin} for varying Actin Stiffnesses. We see the expected trend with mean ORP taking lower values as actin stiffness reduces. For actin stiffnesses of $\kappa_{\text{actin}} = 0.00228 \text{ pN } \mu\text{m}^2$ and above, mean ORP reduces as spectrin numbers increase, however this trend is not observed for stiffnesses of $\kappa_{\text{actin}} \leq 0.00114 \text{ pN } \mu\text{m}^2$. Mean ORP increases with the number of spectrin for these low stiffnesses.

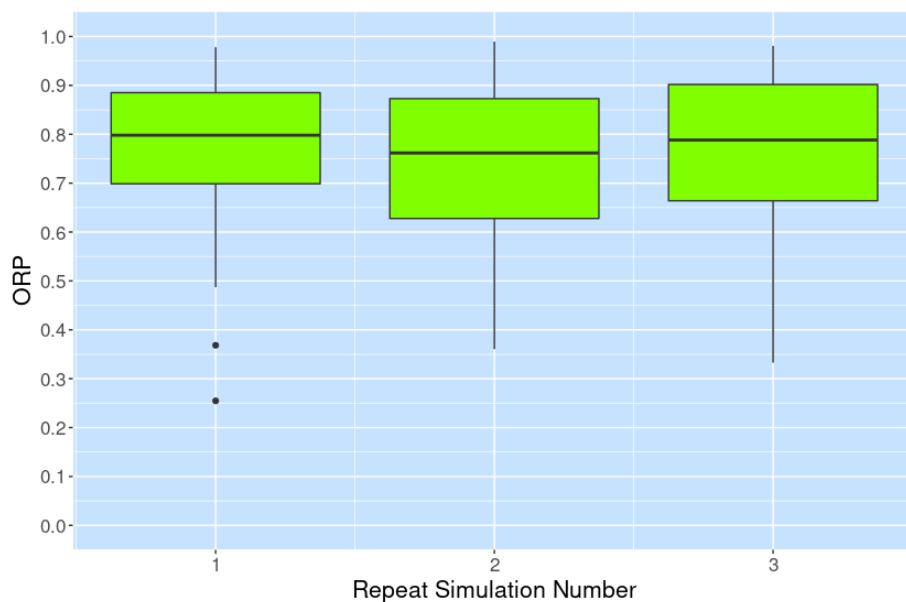


Figure 4.5: Membrane-Bound Spectrin: Set Comparison. *We plot ORP data from 3 repeat simulations, each containing 60 actin filaments, for the parameter set with $N_{\text{spectrin}} = 150$ and $\kappa_{\text{actin}} = 0.00228 \text{ pN } \mu\text{m}^2$. Variations are small between sets and the data appear similar.*

$\text{pN } \mu\text{m}^2$ an initial increase is seen as N_{spectrin} increases from 0 to 150, however levels fall once spectrin numbers are increased further.

Table 4.1 displays the magnitude of changes in mean ORP, relative to the case without spectrin, which is shown in column 2. Reductions in mean ORP of 0.20 and above in magnitude are common where N_{spectrin} is 1500 and above.

After carrying out 3 repeat simulations per parameter set, we compared the data from each set for the parameter combination $N_{\text{spectrin}} = 150$ and $\kappa_{\text{actin}} = 0.00228 \text{ pN } \mu\text{m}^2$. These parameter values were selected as the data showed the largest standard deviation in this case. To determine the level of variation between repeat sets we use boxplots to compare the data from each of the 3 repeat simulations, with 60 actin filaments included in each set. Figure 4.5 compares these datasets. There are some variations in range between sets, however the median values are very similar, being within the ORP range of 0.75 to 0.80, and they show a similar interquartile range. As the variation between sets was small, we did not carry out any further repeats.

When comparing our results to those of Section 3.5, in which we simulated a single actin filament in a small, periodic cell, we see a slightly different pattern of changes. For stiffer actin filaments of $\kappa_{\text{actin}} > 0.00456 \text{ pN } \mu\text{m}^2$ the reduction in mean ORP at higher spectrin numbers of 1500-4500 shown in Table 4.1 is of

Table 4.1: Spectrin Tetramers: Mean ORP Variation Relative to $N_{\text{spectrin}} = 0$. We show the change in mean ORP to 3 significant figures for each value of N_{spectrin} , relative to the mean ORP value for $N_{\text{spectrin}} = 0$ given in column 2. Increases and decreases are shown in red and blue text respectively.

$\kappa_{\text{actin}}/\text{pN}$ μm^2	Mean ORP for $N_{\text{spectrin}} = 0$	Δ Mean ORP for N_{spectrin}				
		150	300	1500	3000	4500
0.0365	0.9456	-0.005	-0.0617	-0.170	-0.204	-0.226
0.0183	0.9298	-0.012	-0.0991	-0.202	0.245	-0.246
0.00913	0.9035	-0.0047	-0.101	-0.215	-0.239	-0.264
0.00456	0.8772	-0.0353	-0.133	-0.219	-0.251	-0.231
0.00228	0.7240	+0.0319	+0.0055	-0.105	-0.104	-0.116
0.00114	0.4440	+0.0751	+0.128	+0.158	+0.155	+0.144
0.000570	0.4230	+0.0427	+0.0543	+0.135	+0.151	+0.164

slightly greater magnitude than the single actin results for equivalent numbers of spectrin of 500-1500 shown in Table 3.2. This begins to change at $\kappa_{\text{actin}} \leq 0.00456 \text{ pN } \mu\text{m}^2$, with reductions in ORP being of reduced magnitude initially, then switching to an increase when actin stiffness reaches $0.00114 \text{ pN } \mu\text{m}^2$ and below.

The different trends shown in Figure 3.5 are interesting; for stiffer actin filaments, the lower levels of mean ORP at higher spectrin densities relative to the single filament case are likely due to cooperativity, with patterns of circumferential alignments tending to propagate as ring-formation at one location re-organises spectrin locally, influencing the orientation of nearby actin filaments. Similarly, for filaments with stiffness of $\kappa_{\text{actin}} \leq 0.00456 \text{ pN } \mu\text{m}^2$, this cooperativity is the likely cause of the increase in mean ORP, as actin of low stiffness is more likely to misalign, causing a propagating pattern of misalignments throughout the cell.

Rings were not generally formed within these sets, with all 60 actin filaments taking ORP values of 0.3 and above in the vast majority of cases. There were a maximum of 4 actin filaments per set below the 0.3 threshold, with no ORP values of < 0.1 .

4.5 In-Cell Actin Polymerisation

We previously found in-cell polymerisation of actin to have a beneficial influence on ring formation; in Section 3.7 we nucleated short actin filaments probabilistically, allowing them to polymerise at various rates up to a maximum length. We found that the mean ORP of these filaments was substantially reduced compared to fixed length, non-polymerising actin. This reduction occurred at polymerisation rates of $r_{\text{growth}} \leq 0.033 \mu\text{m s}^{-1}$, and required the presence of spectrin tetramers.

We now investigate whether a similar effect occurs when multiple actin filaments are nucleated and polymerised together within a larger cell. We begin with initial observations of 3 actin stiffnesses polymerised at different rates in Section 4.5.1, followed by a more in-depth survey across a range of stiffnesses and polymerisation rates in Section 4.5.2.

4.5.1 Initial Investigation

To begin our investigations, we simulate actin filaments of stiffness $\kappa_{\text{actin}} \in \{0.0365, 0.00913, 0.00228\}$ pN μm^2 . As in Section 3.7, we nucleate actin at a rate of $r_{\text{nuc}} = 0.5 \text{ s}^{-1}$ with an initial length of $0.01 \mu\text{m}$. We then polymerise at rates $r_{\text{growth}} \in \{0.33, 0.033, 0.0033\} \mu\text{m s}^{-1}$ up to a maximum length of $L_{\text{actin}} = 1.32 \mu\text{m}$. To maintain consistency with Section 3.7, we use the same density of spectrin tetramers, with 500 per $2 \mu\text{m}$ of axial length of our cell environment, giving a total of $N_{\text{spectrin}} = 1500$ for our $6 \mu\text{m}$ cell. We carry out 3 repeat simulations per parameter set.

Figure 4.6 shows the mean ORP and standard deviation error bars calculated from results combined from each set of 3 repeat simulations, giving a total of 180 values per parameter set. The magnitudes of the change in mean ORP is shown in Table 4.2, relative to non-polymerised actin of fixed length $L_{\text{actin}} = 1.32 \mu\text{m}$ which is shown in Column 2, and appears in red on Figure 4.6.

Results for polymerised actin appear very similar to those of non-polymerised actin for the stiffest filaments of $\kappa_{\text{actin}} = 0.0365$ pN μm^2 , with Table 4.2 showing changes in mean ORP of 10^{-2} magnitude and below for this actin stiffness at each of the 3 polymerisation rates. For the lower stiffnesses, it appears that rapid polymerisation of $r_{\text{growth}} = 0.33 \mu\text{m s}^{-1}$ gives slightly higher ORP values than non-polymerised actin. Polymerisation at $r_{\text{growth}} = 0.033 \mu\text{m s}^{-1}$ slightly reduces ORP for $\kappa_{\text{actin}} = 0.00913$ pN μm^2 , with a change of 0.0205. A larger reduction of 0.196 is observed for $\kappa_{\text{actin}} = 0.00228$ pN μm^2 at this polymerisation rate. The slowest polymerisation rate of $r_{\text{growth}} = 0.0033 \mu\text{m s}^{-1}$ caused large reductions in ORP for κ_{actin} of 0.00913 and 0.00228 pN μm^2 , with mean ORP dropping by > 0.2 in these cases.

In Figures 4.7 - 4.9 we show snapshots taken from the final timestep of one simulation from each parameter set investigated. We show fixed length, non-polymerised actin in the upper image, followed by actin polymerised at descending rates in the images below.

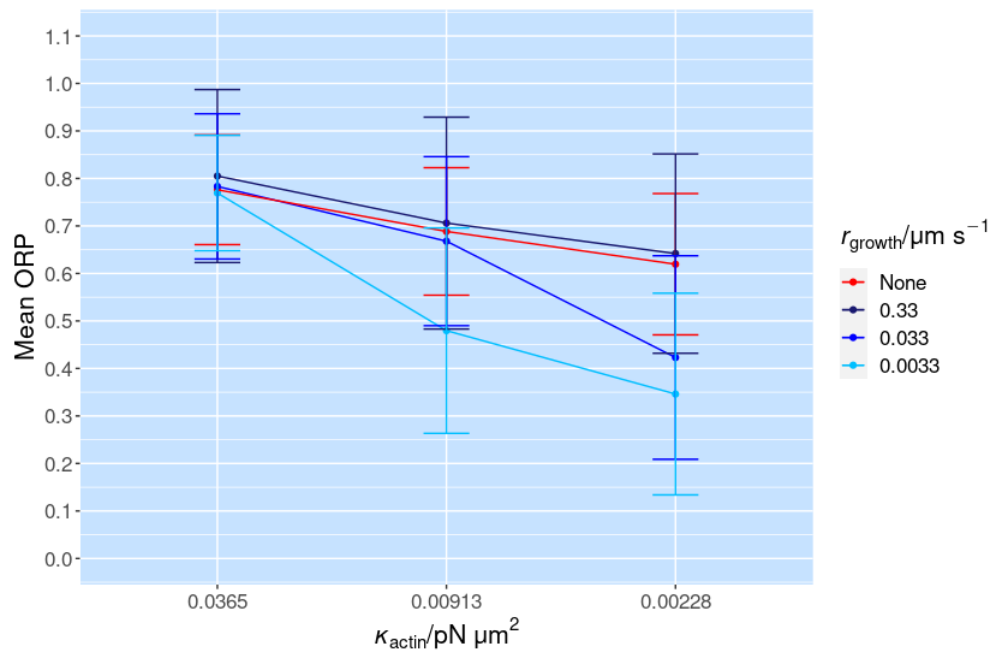


Figure 4.6: Multiple Filaments - Variation of ORP with Actin Stiffness and Growth Rate. *The mean ORP result remains in line with the non-polymerised result, shown in red, for all growth rates when actin of a standard stiffness, $\kappa_{\text{actin}} = 0.0365 \text{ pN } \mu\text{m}^2$, is considered, however at reduced stiffnesses, mean ORP reduces as growth rate slows.*

Table 4.2: In-Cell Polymerisation with 1500 spectrin: Mean ORP Variation Relative to Non-Polymerised Result

$\kappa_{\text{actin}}/\text{pN } \mu\text{m}^2$	Mean ORP for Non-Polymerised Actin	Δ Mean ORP for $r_{\text{growth}}/\mu\text{m s}^{-1}$		
		0.33	0.033	0.0033
0.0365	0.7761	+0.0289	+0.00710	-0.00680
0.00913	0.6884	+0.0176	-0.0205	-0.209
0.00228	0.6194	+0.0224	-0.196	-0.273

In Figure 4.7, actin filaments of $\kappa_{\text{actin}} = 0.0365 \text{ pN } \mu\text{m}^2$ line the membrane, forming gentle curves and loose spirals. As the polymerisation rate decreases, it appears that these curves become slightly steeper, spiralling around the cylindrical membrane at a shorter pitch than in the upper images. The mean ORP value remains high however, and no rings can be seen in these images.

Figure 4.8 shows results for $\kappa_{\text{actin}} = 0.00913 \text{ pN } \mu\text{m}^2$. Again, the upper 2 images show actin in an elongated form, with ORP values > 0.6 . In the third image, with $r_{\text{growth}} = 0.033 \mu\text{m s}^{-1}$, mean ORP remains relatively high at 0.6283, however small numbers of actin rings are visible, mainly occurring in short sections of 2-3 parallel filaments, connected laterally by dense spectrin tetramers. At the slowest polymerisation rate of $r_{\text{growth}} = 0.0033 \mu\text{m s}^{-1}$, there are many regions of at least partial ring-like organisation. Some regions appear highly organised, with rings oriented at 90° to the longitudinal axis, while other rings appear tilted, and in some areas actin becomes disorganised in patches, possibly due to depletion of spectrin tetramers locally.

Finally, in Figure 4.9 we see results for $\kappa_{\text{actin}} = 0.00228 \text{ pN } \mu\text{m}^2$. ORP values are around 0.6 for the upper 2 images, and actin filaments appear highly curved and disorganised, adopting a wide variety of configurations on the membrane. Many rings appear in the third image, where $r_{\text{growth}} = 0.033 \mu\text{m s}^{-1}$, and mean ORP decreases to 0.4. At $r_{\text{growth}} = 0.0033 \mu\text{m s}^{-1}$, actin rings form long continuous sections of organisation, with gaps between sections where spectrin is depleted due to incorporation into the actin-spectrin structure. Mean ORP in this case is slightly above the 0.3 threshold, indicating a high level of ring formation.

4.5.2 Varying Actin Stiffness and Growth Rate

We found in Section 4.5.1 that reduced actin stiffness and slow polymerisation rates appeared to give the lowest mean ORP results. To investigate the dependency on these factors further, we sweep a range of low actin stiffnesses with

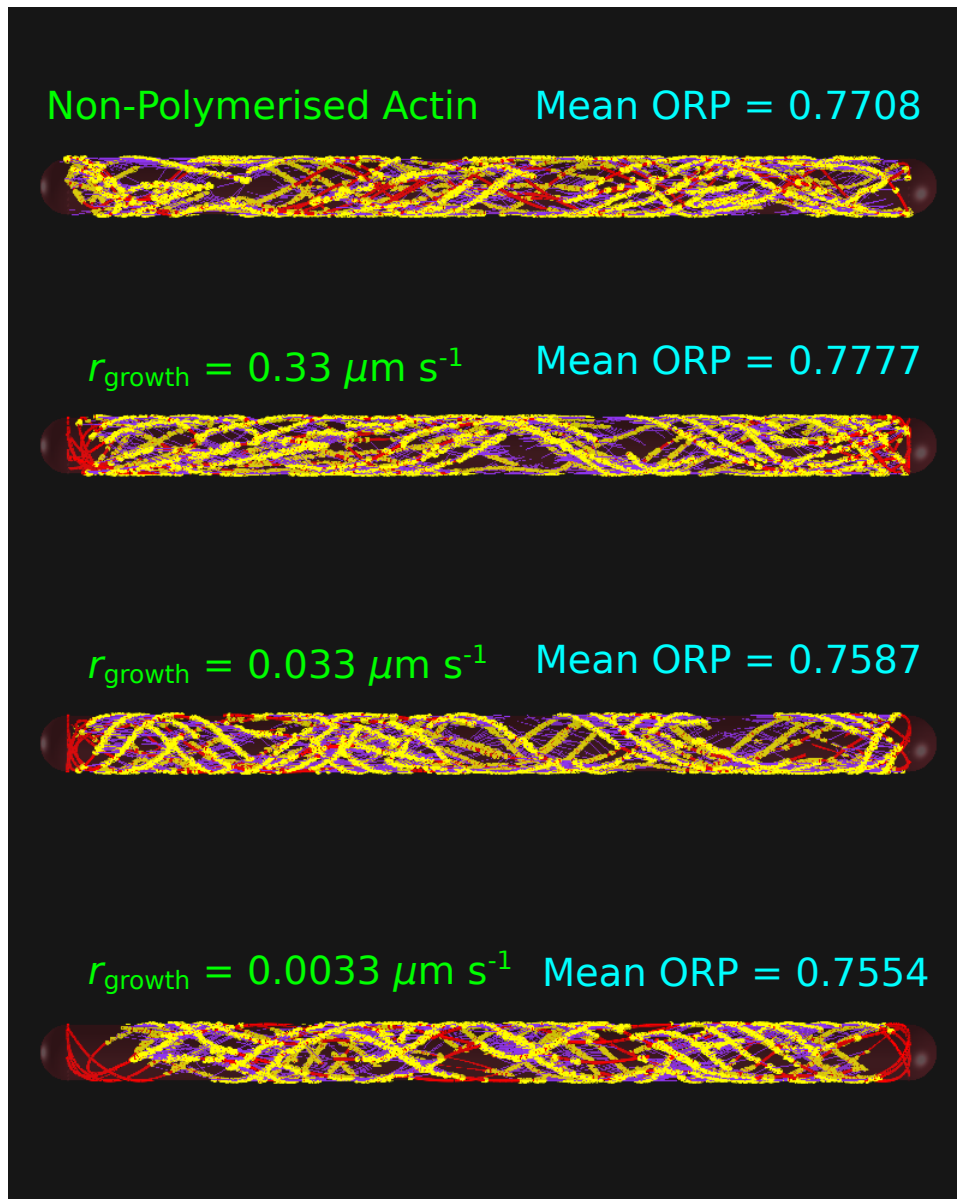


Figure 4.7: In-Cell Actin Polymerisation Examples: $\kappa_{\text{actin}} = 0.0365 \text{ pN } \mu\text{m}^2$. Example results are shown at the final timestep in the simulation for actin polymerised at several rates, compared to non-polymerised actin (upper image). We display actin filaments in red, connecting to spectrin tetramers, shown in purple. The connecting proteins are displayed in yellow. We see smooth curves and spirals in each of the 4 images, with ORP values > 0.7 for each polymerisation condition.

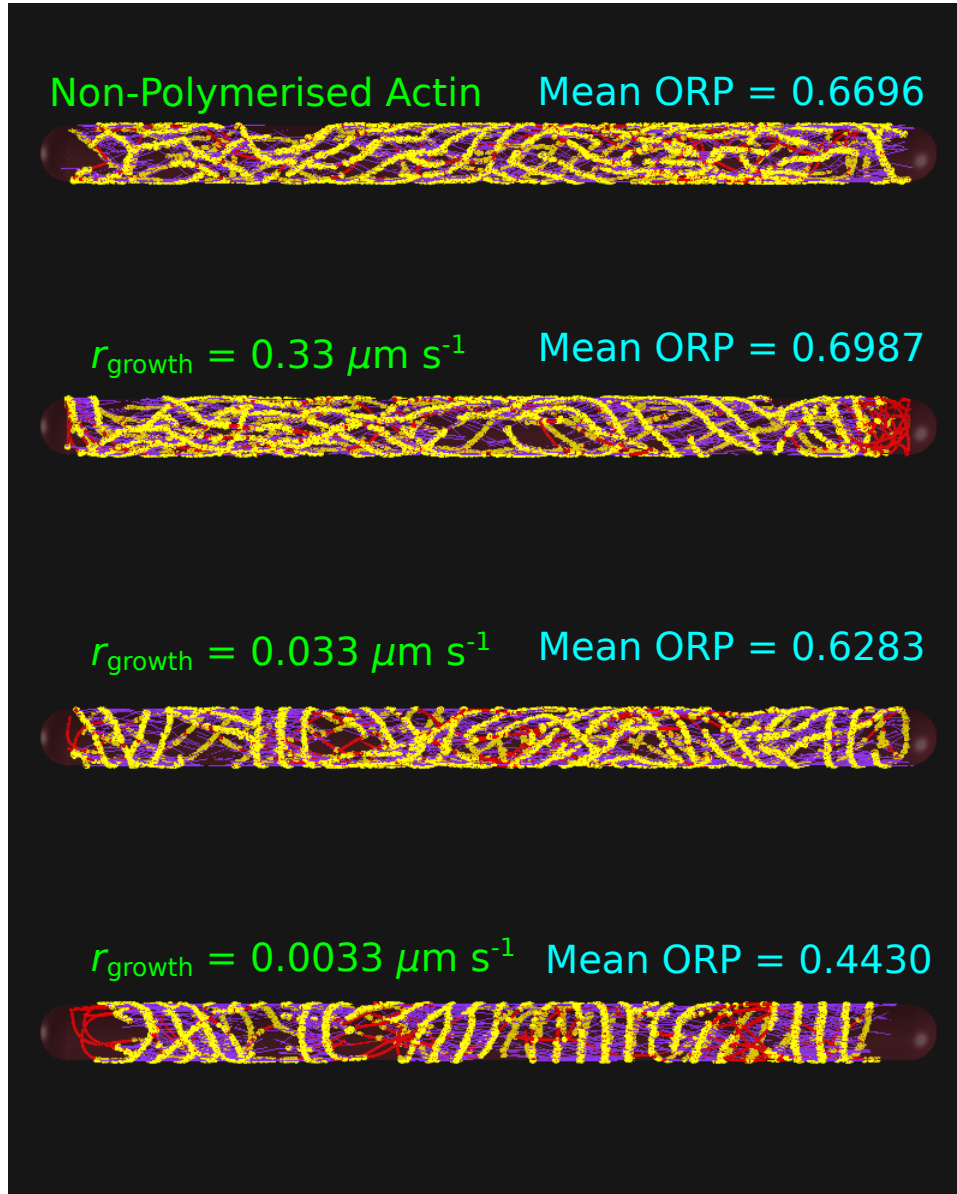


Figure 4.8: In-Cell Actin Polymerisation Examples: $\kappa_{\text{actin}} = 0.00913 \text{ pN } \mu\text{m}^2$. We see some actin rings begin to appear at $r_{\text{growth}} = 0.033 \mu\text{m s}^{-1}$, becoming more organised and regular at $r_{\text{growth}} = 0.0033 \mu\text{m s}^{-1}$ with mean ORP of 0.44.

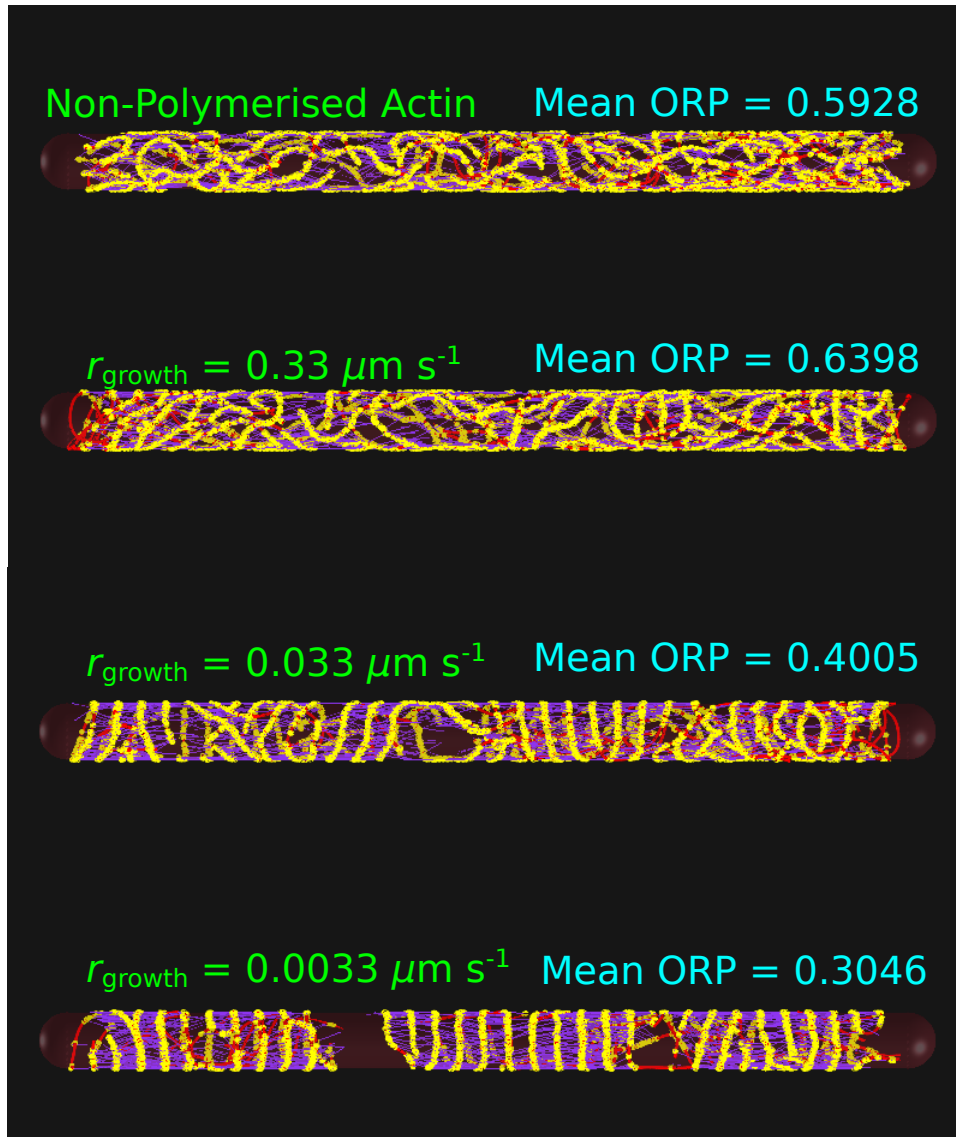


Figure 4.9: In-Cell Actin Polymerisation Examples: $\kappa_{\text{actin}} = 0.00228 \text{ pN } \mu\text{m}^2$. Actin filaments appear disorganised for non-polymerised actin and rapid polymerisation rates, as shown in the 2 upper images. At slower polymerisation rates, rings begin to form, and high levels of organisation are seen at $r_{\text{growth}} = 0.0033 \mu\text{m s}^{-1}$ (lower image), with mean ORP of 0.30.

$\kappa_{\text{actin}} \in [0.001, 0.01]$ pN μm^2 while simultaneously varying the polymerisation rate across $r_{\text{growth}} \in [0.001, 0.01]$ $\mu\text{m s}^{-1}$. In each case we vary the parameters in increments of 0.001 in magnitude. Due to the large number of parameter combinations this involves, we performed a single simulation of 60 actin filaments per parameter set.

Figure 4.10 shows mean ORP across these parameter ranges, with yellow indicating the highest values, and blue for the lowest ORP values. The pattern in this data is not clear, however it appears that lower polymerisation rates give slightly better results to a larger range of actin stiffnesses. In Figure 4.11 we display the number of actin filaments out of 60 which give sub-threshold results. Red indicates a high number, greater than half of the total actin filaments, while green indicates few to none in this range. Again there is some variation in results with no clear pattern, but we can see that the best results are achieved using the slowest polymerisation speeds. In general, results appear to improve as actin stiffness is reduced.

As the results based on single simulations shown in Figures 4.10 - 4.11 did not show a clear pattern, we carry out a further analysis on one actin stiffness, varying polymerisation rate, with 10 repeat simulations per parameter set. We used an actin stiffness of $\kappa_{\text{actin}} = 0.005$ pN μm^2 and varied the polymerisation rate across the range used previously.

In Figure 4.12 we show these results. We combine the set of 60 ORP values from each of the 10 repeat simulations into a single dataset to create these box-plots with each box representing 600 ORP values. The median values indicated by the black bar appear in line with one another across the full range, with only a very slight dip at 0.001. The minimum and maximum values extend across almost the entire available range of ORP values, while the interquartile ranges appear similarly sized for every polymerisation rate, extending from roughly around 0.2 to 0.5.

Next, we focus on ring formation; Figure 4.13 shows bars representing the classification of the 600 actin filaments analysed for each value of r_{growth} , with results of 0.3 and over shown in green, and those below the 0.3 threshold, showing some degree of ring-like organisation, are in yellow, orange, and red, as indicated by the legend. In each case, more than half of the filaments had ORP values above the threshold. There is no clear pattern to the proportions of sub-threshold results, with each bar appearing fairly similar, however the slowest polymerisation rate, $r_{\text{growth}} = 0.001$ $\mu\text{m s}^{-1}$, appeared to have more actin filaments in the red category.

To observe any differences between repeat sets, we compare each repeat for parameter values of $\kappa_{\text{actin}} = 0.005$ pN μm^2 with polymerisation rate $r_{\text{growth}} = 0.001$ $\mu\text{m s}^{-1}$, as shown in Figure 4.14. A wide range of ORP values is present within each of the 10 repeat simulations, with whiskers covering the vast majority of the possible ORP range in most cases, and a fairly wide interquartile range. Median values range from around 0.25 to 0.4, however all median values fall within the large interquartile ranges of the remaining boxes, and differences do not appear significant.

Figure 4.15 shows a series of timepoints from the parameter set that yielded

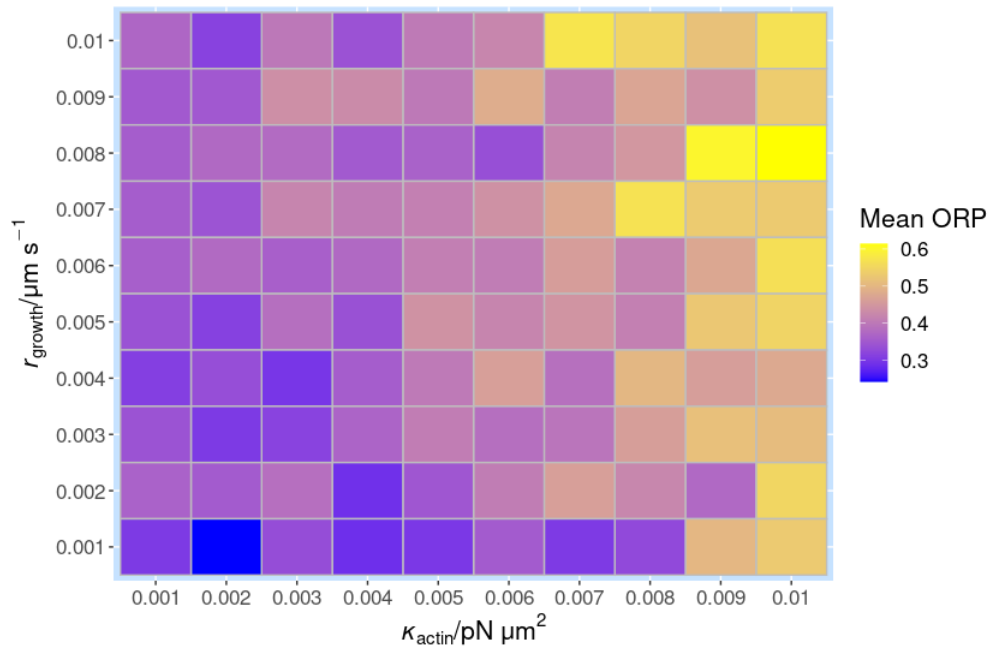


Figure 4.10: In-Cell Polymerisation: Mean ORP with Actin Stiffness and Polymerisation Rate. We measure the mean ORP value for 60 actin filaments from a single simulation per parameter combination, sweeping $\kappa_{\text{actin}} \in [0.001, 0.1] \text{ pN } \mu\text{m}^2$ and polymerisation rates, $r_{\text{growth}} \in [0.001, 0.01] \mu\text{m s}^{-1}$. 1500 spectrin tetramers were included. ORP values above 0.5 appear in yellow and are restricted to the stiffest actin filaments. The lowest mean ORP results occur for low stiffness and the slowest polymerisation rate, as indicated in blue.

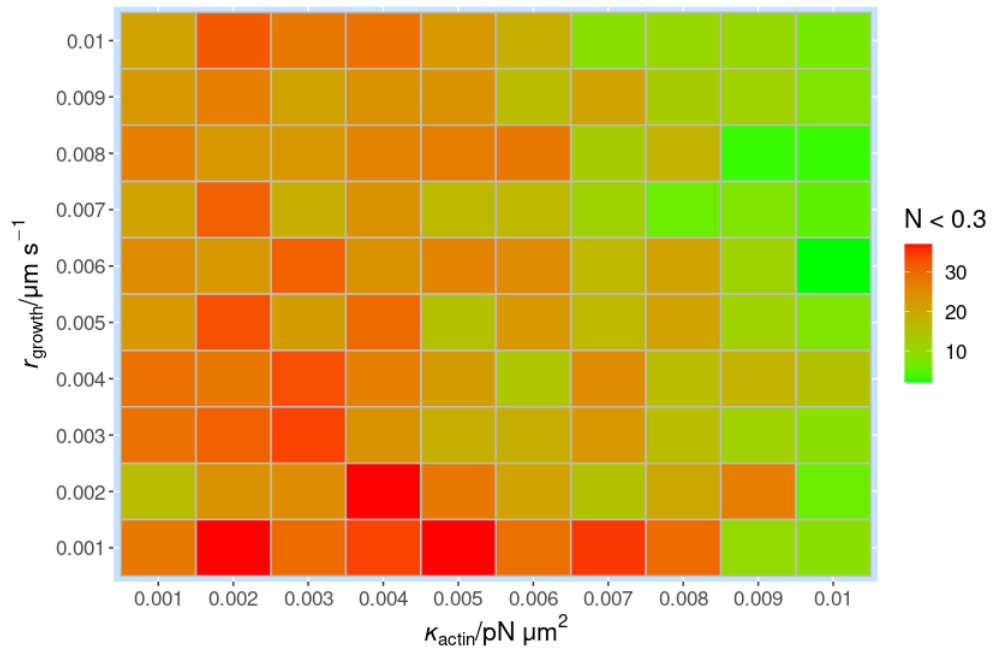


Figure 4.11: In-Cell Polymerisation: ORP Classification with Actin Stiffness and Polymerisation Rate. *The number of actin filaments with ORP values below the 0.3 threshold are represented on a scale from green to red as indicated by the legend. Results in green with low numbers of ring-like filaments occur mainly at higher stiffnesses, while low stiffnesses and slow polymerisation rates yield the most results with high numbers of below threshold results, as shown in red.*

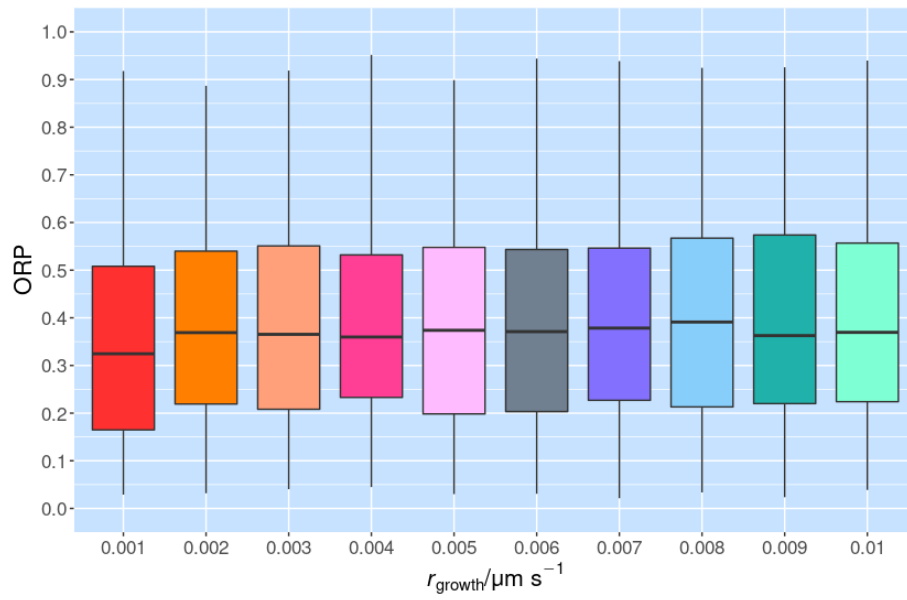


Figure 4.12: ORP with Polymerisation Rate for $\kappa_{\text{actin}} = 0.005 \text{ pN } \mu\text{m}^2$. We combine ORP values for each of the 60 actin filaments, for 10 repeat simulations per parameter set, giving 600 values per box. Results appear very similar across the range of polymerisation rates, $r_{\text{growth}} \in [0.001, 0.01] \mu\text{m s}^{-1}$, and no dependence on rate is discernible for this range of parameter values.

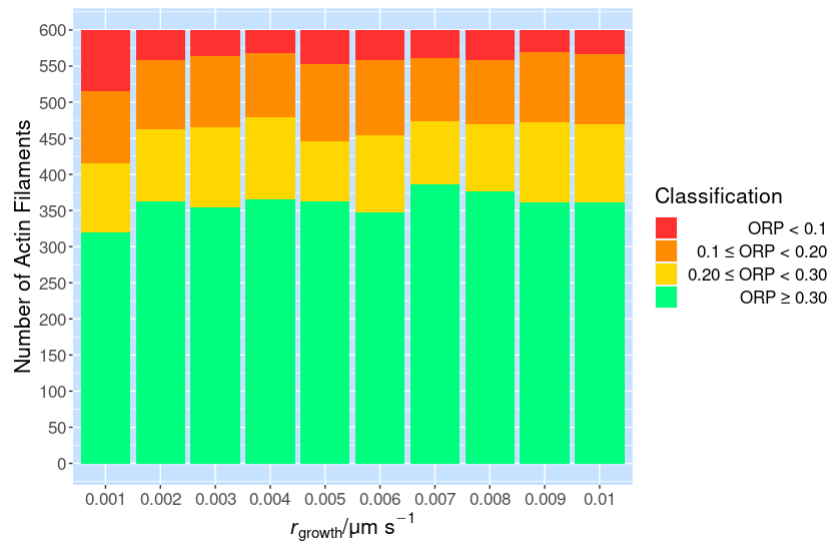


Figure 4.13: ORP Classification with Polymerisation Rate for $\kappa_{\text{actin}} = 0.005 \text{ pN } \mu\text{m}^2$. Data from 10 repeat simulations, each containing 60 actin filaments, is presented in a bar which is coloured according to the numbers of actin filaments with ORP values within 4 ranges as indicated by the legend. In each case, the majority of filaments have ORP values of 0.3 and above, shown in green, with small numbers of the most ring-like filaments, as shown in red.

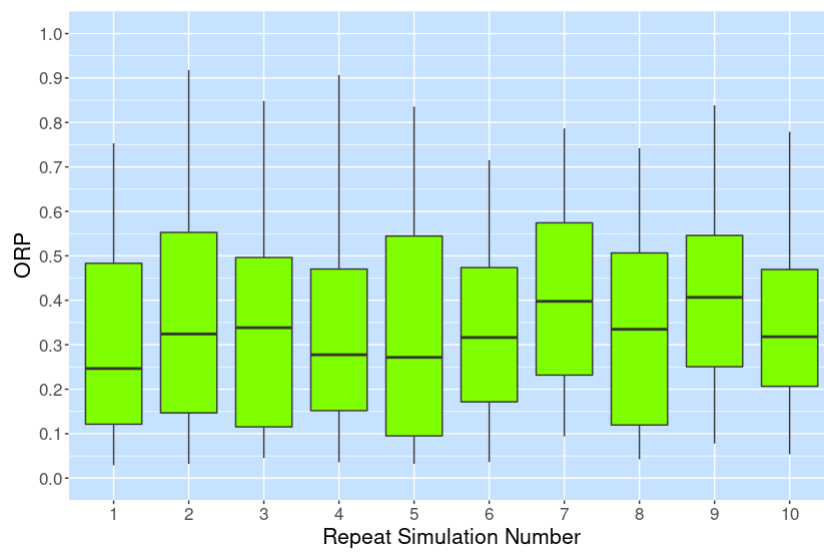


Figure 4.14: Actin Polymerisation: Set Comparison. *We compare the 10 repeat simulations for parameters $\kappa_{\text{actin}} = 0.005 \text{ pN } \mu\text{m}^2$ with $r_{\text{growth}} = 0.001 \mu\text{m s}^{-1}$. Some variation is visible between repeat simulations, however the large ranges of values present in each set suggests that these variations are unlikely to be significant.*

the most favourable results; this had actin stiffness of $\kappa_{\text{actin}} = 0.002 \text{ pN } \mu\text{m}^2$ and $r_{\text{growth}} = 0.001 \mu\text{m s}^{-1}$. The mean ORP of this set was 0.2425, with a minimum of 0.0367. 13 of the 60 actin filaments had ORP values of below 0.1 showing high levels of agreement with our ideal ring configuration, while 18 filaments had values of 0.1 or greater, but under 0.2. 6 filaments had ORP value of 0.2 or greater, but less than 0.3, and 23 had ORP of 0.3 or above.

We see initially short filaments in Figure 4.15a, elongating around the membrane circumference. Neighbouring filaments joining together with dense spectrin tetramers aligned in parallel with one another, and perpendicular to the actin filaments. It appears from these images that distinct regions begin to form as early as 100 seconds into the simulation (Figure 4.15b), with patches devoid of spectrin beginning to develop, becoming clearly visible in Figure 4.15e at 495 seconds. In the final simulation step, at 2140 seconds, we see 2 spatially separated regions of 12-13 actin rings each, as shown in Figure 4.15f. There is some tilting of these rings, and some disorganised sections of actin can be seen in red, while some of the rings do not span the full circumference of the membrane.

As spectrin is depleted in regions of the cell, it may be that an insufficiency of spectrin allows growing filaments to become disorganised, deviating from their initial ring-like trajectory. Rings that are well formed are seen to be connected by very dense, highly aligned spectrin tetramers. With this in mind, it's possible that increasing the amount of spectrin available could improve results.

While spectrin density was varied in Section 4.4, this was done with non-polymerising actin. Given the strongly increased likelihood of ring formation in actin polymerised within the cell, it is useful to revisit spectrin density to accurately assess its impact on growing actin filaments. We investigate this in Section 4.7, but first, we review the properties of our actin-spectrin linking protein.

4.6 Actin-Spectrin Crosslinking

Prior to looking at spectrin density in more detail, it is useful to assess the impact of turnover of the linking protein which joins spectrin to actin. In our previous simulations we have used a relatively high rate of binding at $r_{\text{bind}} = 10 \text{ s}^{-1}$, with a slow unbinding rate of $r_{\text{unbind}} = 0.001 \text{ s}^{-1}$, with $f_{\text{unbind}} = 3 \text{ pN}$. This was done to ensure the connections in which we were interested occurred fairly rapidly and with low turnover. Given that the precise nature and dynamics of this connection in the MPS are unknown, we chose to explore a range of binding and unbinding rates. In doing so we wish to understand whether the actin-spectrin connected must occur rapidly, or more gradually. We also wish to determine the effect of highly dynamic connections with rapid turnover, compared with more stable connections.

We use parameters which we found to be suitable for ring formation to occur in Section 4.5.1, with $\kappa_{\text{actin}} = 0.00228 \text{ pN } \mu\text{m}^2$ and $r_{\text{growth}} = 0.0033 \mu\text{m s}^{-1}$. We used 1500 spectrin tetramers, with the number of actin-spectrin linking proteins being set at $N_{\text{link}} = 5N_{\text{spectrin}}$ initially.

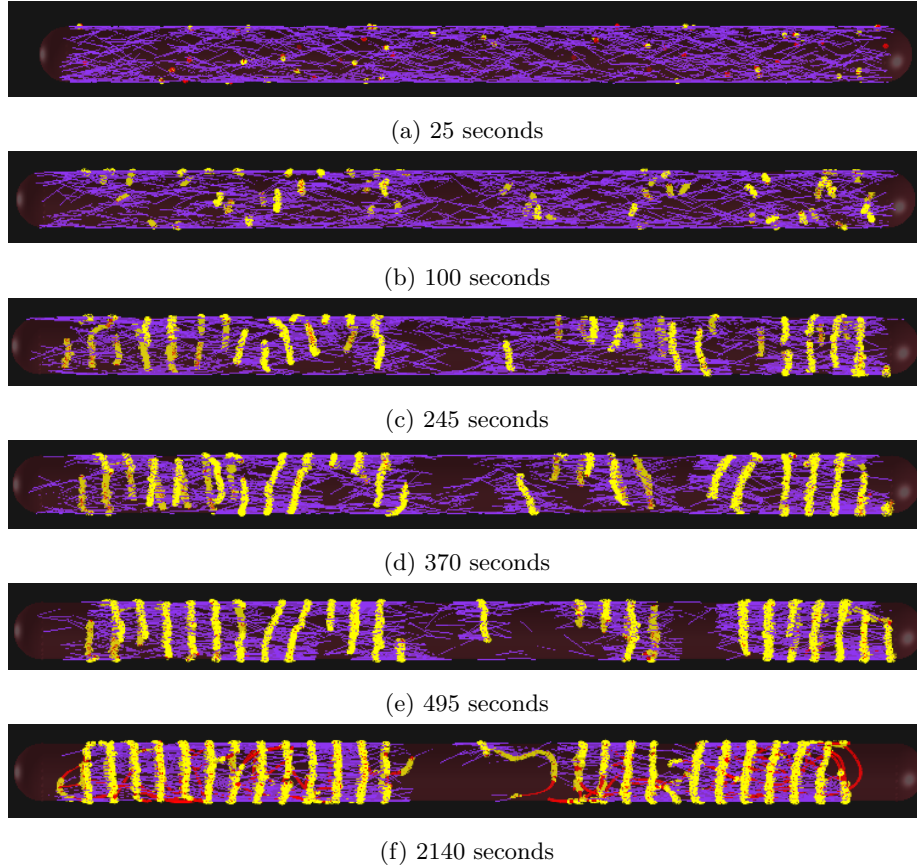


Figure 4.15: Simulation Timelapse Images for $\kappa_{\text{actin}} = 0.002 \text{ pN } \mu\text{m}^2$ and $r_{\text{growth}} = 0.001 \mu\text{m s}^{-1}$. We show simulation results at 6 timepoints; at 25 seconds, short actin filaments (in red) are nucleated and begin to polymerise slowly, connecting with spectrin tetramers (purple) via a linking protein shown in yellow. The filaments elongate at 100 seconds, and by 245 seconds longer filaments are beginning to align in parallel around the membrane. At 370 seconds and 495 seconds, patches of local organisation appear, with spectrin being depleted in some areas as it is incorporated into the ring pattern. Image 4.15f shows the final simulation step, with 2 large regions of organised actin rings separated by a large gap, with an isolated filament occupying this region.

The actin-spectrin linking protein possesses 2 'hands', with one hand linking to actin only, and the other to spectrin. We chose to keep the properties of the spectrin binding hand constant while varying those of the actin binding hand. We vary both r_{bind} and r_{unbind} for the actin binding hand of the actin-spectrin linker across the range of $[10, 1, 0.1, 0.01, 0.001] \text{ s}^{-1}$. The unbinding force was maintained at 3 pN.

We run a single simulation containing 60 actin filaments for each parameter combination. As we were able to observe clear patterns from these samples of 60 filaments, we did not run any further simulations.

Figure 4.16 shows how different ratios of r_{bind} and r_{unbind} affect the mean ORP measurement; the graph shows a high mean ORP value of around 0.8 - 0.9 in the cases where $\left(\frac{r_{\text{bind}}}{r_{\text{unbind}}}\right) \leq 1$. This is as expected, as this transient connection is unlikely to be sufficient to create such a stable structure. Mean ORP values were at their lowest where the binding rate was high, with r_{bind} of 1 and 10 s^{-1} giving results below 0.5. At these binding rates, $r_{\text{unbind}} = 0.1 \text{ s}^{-1}$ had the lowest mean ORP at between 0.20-0.25, while $r_{\text{unbind}} = 0.01 \text{ s}^{-1}$ also showed substantial reduction at around 0.3.

We look more closely at these results in Figure 4.17, in which we show results across a range of r_{unbind} values for a fixed binding rate, $r_{\text{bind}} = 1 \text{ s}^{-1}$. As there is a large increase in ORP values within the range $r_{\text{unbind}} \in [0.1, 1] \text{ s}^{-1}$, we carried out additional simulations at the intermediate rates, $r_{\text{unbind}} = 0.25 \text{ s}^{-1}$ and 0.50 s^{-1} . ORP values remain high at high unbinding rates of $r_{\text{unbind}} = 0.5 \text{ s}^{-1}$ and above, with median values of 0.8 - 0.9, although several outliers are shown for these values. Between 0.5 and 0.1 s^{-1} there is a large decrease, with median values falling to 0.2, followed by small increases as the rate slow further, reaching a median of around 0.45 at $r_{\text{unbind}} = 0 \text{ s}^{-1}$.

We continue to use this dataset, next examining the degree of ring formation at each unbinding rate. As shown in Figure 4.18, ring formation is also increased for parameters with decreased mean and median ORP values. $r_{\text{unbind}} = 0.1 \text{ s}^{-1}$ showed the highest numbers of actin filaments with ORP values below the 0.3 threshold, with around 3 quarters of the values showing some level of ring-like arrangement.

Figure 4.18 shows a pattern of increasing ring-formation as r_{unbind} increases from $0 - 0.1 \text{ s}^{-1}$, however this trend is reversed as r_{unbind} increases beyond this range, with ring-formation becoming negligible or absent from $r_{\text{unbind}} = 0.5 \text{ s}^{-1}$ and above. From the values of r_{unbind} tested here, the optimum value is therefore $r_{\text{unbind}} = 0.1 \text{ s}^{-1}$ - one tenth of the rate of r_{bind} .

The results of our investigations on unbinding rate suggest that formation of rings requires stable actin-spectrin connections with relatively slow turnover. This is likely to be related to both the slow rate of actin polymerisation, and the cooperative effects occurring in our simulations; links to spectrin are required for actin to polymerise and orient in the desired circumferential direction, and these links must remain stable for a sufficient time to allow the filament to grow and make further connections. This is particularly important as alignment of an actin filament further influences spectrin alignment and therefore the likelihood

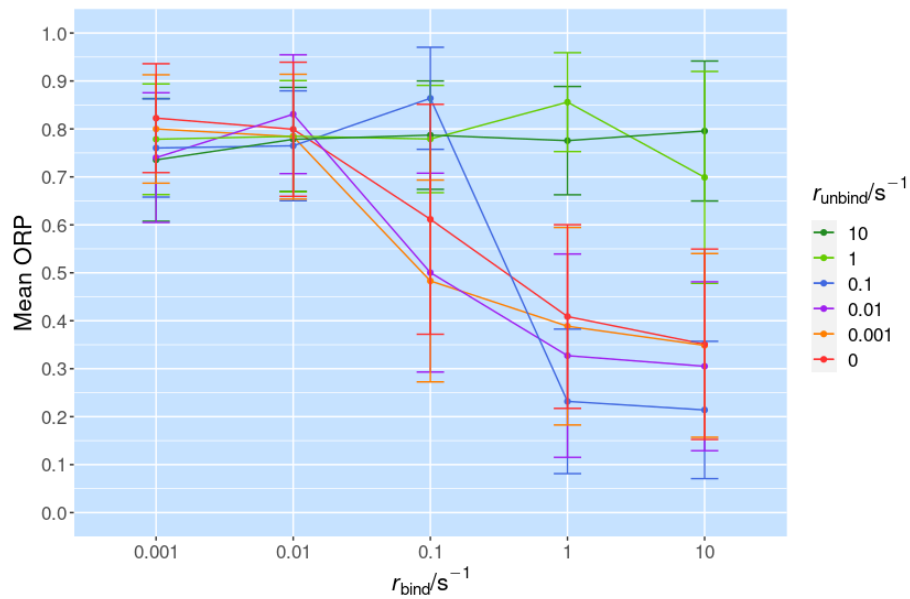


Figure 4.16: Actin-Spectrin Crosslink Turnover. We use actin of properties $\kappa_{\text{actin}} = 0.00228 \text{ pN } \mu\text{m}^2$ and $r_{\text{growth}} = 0.0033 \mu\text{m } s^{-1}$, which interacts with 1500 spectrin tetramers. We vary r_{bind} for a range of r_{unbind} values. The results show that the most rapid rates of binding with $r_{\text{bind}} \geq 1 \text{ s}^{-1}$ give the lowest ORP values on average, when combined with r_{unbind} rates of between 0 and 0.1.

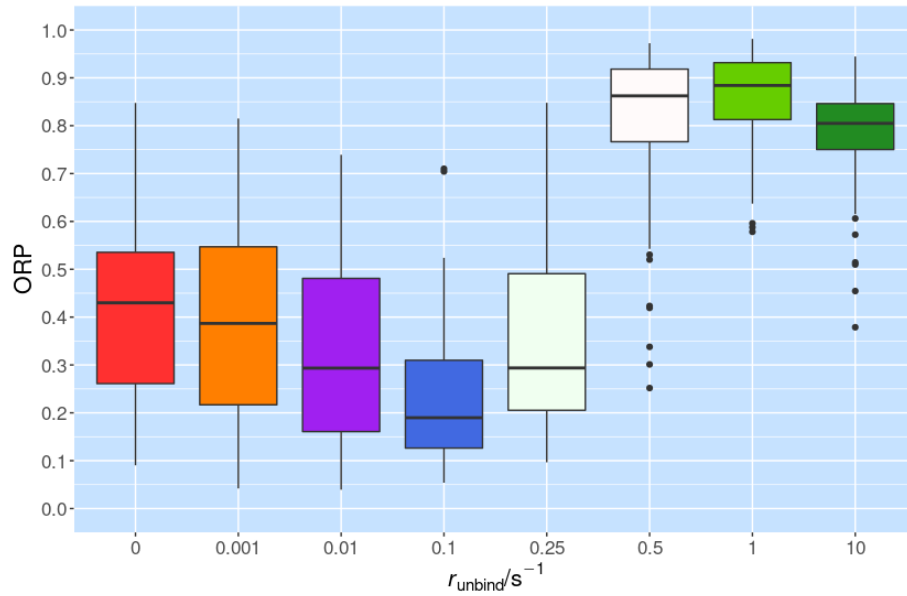


Figure 4.17: Actin-Spectrin Crosslinking: ORP for $r_{\text{bind}} = 1 \text{ s}^{-1}$ with Varying r_{unbind} . We show results for a range of unbinding rates, $r_{\text{unbind}} \in \{10, 1, 0.5, 0.25, 0.1, 0.01, 0.001, 0\} \text{ s}^{-1}$ with r_{bind} constant at 1 s^{-1} . Each box represents a single simulation of 60 actin filaments, each with $\kappa_{\text{actin}} = 0.00228 \text{ pN } \mu\text{m}^2$ and $r_{\text{growth}} = 0.0033 \text{ } \mu\text{m } \text{s}^{-1}$, interacting with 1500 spectrin tetramers and 7500 actin-spectrin crosslinking proteins. Where $r_{\text{unbind}} \geq r_{\text{bind}}$, median ORP is high, at 0.8 and above. At $r_{\text{unbind}} \leq r_{\text{bind}}$, ORP values decrease dramatically, with the ratio, $\left(\frac{r_{\text{unbind}}}{r_{\text{bind}}}\right) = 0.1$ displaying the lowest median value of slightly below 0.2.

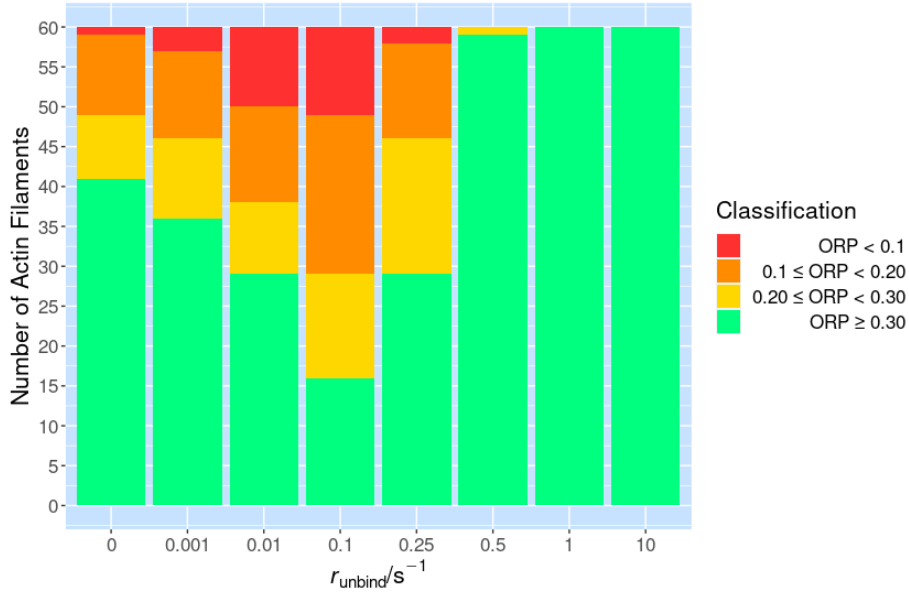


Figure 4.18: Actin-Spectrin Crosslinking: ORP Classification for $r_{\text{bind}} = 1 \text{ s}^{-1}$ with Varying r_{unbind} . We show results for a range of unbinding rates, $r_{\text{unbind}} \in \{10, 1, 0.5, 0.25, 0.1, 0.01, 0.001, 0\} \text{ s}^{-1}$ with r_{bind} constant at 1 s^{-1} . Each bar represents a single simulation of 60 actin filaments, each with $\kappa_{\text{actin}} = 0.00228 \text{ pN } \mu\text{m}^2$ and $r_{\text{growth}} = 0.0033 \text{ } \mu\text{m} \text{ s}^{-1}$, interacting with 1500 spectrin tetramers and 7500 actin-spectrin crosslinking proteins. No rings are formed for $r_{\text{unbind}} \geq r_{\text{bind}}$. At $r_{\text{unbind}} \leq r_{\text{bind}}$, ring formation is possible and the proportion of rings within the sample increases with increased r_{unbind} .

of another actin ring assembling at the opposite terminal of connected spectrin tetramers. Given this cooperative aligning effect, it is beneficial for some detachment to occur, as this gives an opportunity for any misaligned actin filaments to be corrected as the structure assembles. This explains the reduced ring-formation at unbinding rates below $r_{\text{unbind}} = 0.1 \text{ s}^{-1}$.

In our previous simulations, we have set the number of actin-spectrin linking proteins at $N_{\text{linker}} = 5N_{\text{spectrin}}$. This was done to ensure high availability, encouraging connections to be formed rapidly and abundantly. Before continuing, we briefly revisit this value to determine what effect this number has on our simulation results. We use actin of $\kappa_{\text{actin}} = 0.00228 \text{ pN } \mu\text{m}^2$ and $r_{\text{growth}} = 0.0033 \text{ } \mu\text{m} \text{ s}^{-1}$, interacting with 1500 spectrin tetramers. We adopt properties for the actin-spectrin linker protein of $r_{\text{bind}} = 1 \text{ s}^{-1}$ and $r_{\text{unbind}} = 0.1 \text{ s}^{-1}$ as these values were most favourable to our results earlier in this Section. We then simulate the range $N_{\text{linker}} \in \{1, 2, 3, 4, 5, 6, 7, 8, 9, 10\}N_{\text{spectrin}}$.

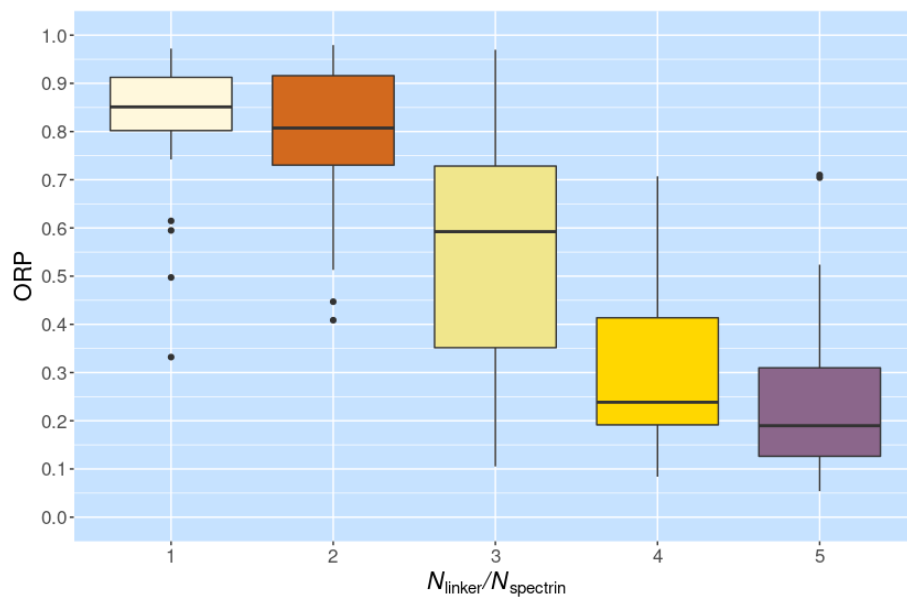


Figure 4.19: ORP with Number of Actin-Spectrin Linking Proteins. We use actin filaments with properties $\kappa_{\text{actin}} = 0.00228 \text{ pN } \mu\text{m}^2$ and $r_{\text{growth}} = 0.0033 \mu\text{m s}^{-1}$, interacting with 1500 spectrin tetramers. We vary the number of actin-spectrin linking proteins available from 1 to 5 times N_{spectrin} .

In Figure 4.19 we show the results. Median ORP values are 0.8 and over when $\left(\frac{N_{\text{linker}}}{N_{\text{spectrin}}}\right) \leq 2$. ORP values decrease with increased N_{linker} , and the lowest median value and range were associated with $N_{\text{linker}} = 5N_{\text{spectrin}}$, with a median around 0.2. It is possible that increasing the number of linking proteins further may be beneficial, however we chose to limit our range of exploration as $N_{\text{linker}} = 2N_{\text{spectrin}}$ is a sufficient level to saturate spectrin binding sites, and it may be biologically unrealistic to simulate very high concentrations of these proteins. In addition, simulation of large numbers of proteins increases computation time. We therefore continue our investigations maintaining the availability of linking proteins at $N_{\text{linker}} = 5N_{\text{spectrin}}$. The precise nature of connection between actin and spectrin within the MPS is currently poorly understood, with multiple possible candidate proteins as detailed in Section 1.3.6, therefore biological data on the concentration of connecting proteins is currently unavailable.

4.7 Spectrin Density

In our previous simulations we have used a fixed number of 1500 spectrin tetramers. This value was chosen to maintain equivalence with the single actin filament simulations of Chapter 3, in which 500 spectrin tetramers were placed in a $2 \mu\text{m}$ cell. In Section 4.4 we found that an increase in the number of spectrin tetramers influenced the configuration of actin filaments, with the stiffer filaments within our range showing an ORP reduction.

While rings were not formed in general in these simulations of non-polymerised actin, the effect of increased spectrin levels may differ when actin is polymerised within the cell. In particular, as polymerised actin filaments exist at short lengths for a time which is dependent on their polymerisation rate, r_{growth} , a high density of spectrin may be more beneficial, as the stacking in parallel of many tetramers may cause connected actin filaments to orient within the circular plane of the cell, polymerising around the membrane circumference.

To investigate this, we select a parameter combination that has shown a tendency to form rings in our other simulations; here we use $\kappa_{\text{actin}} = 0.00228 \text{ pN } \mu\text{m}^2$ and $r_{\text{growth}} = 0.0033 \mu\text{m s}^{-1}$. We alter the binding properties of our actin-spectrin connecting protein to the values which we found to be most favourable to ring formation in Section 4.6, using $r_{\text{bind}} = 1 \text{ s}^{-1}$ and $r_{\text{unbind}} = 0.1 \text{ s}^{-1}$. We maintain the binding and unbinding rates of the spectrin linking hand at the previous levels, with $r_{\text{bind}} = 10 \text{ s}^{-1}$ and $r_{\text{unbind}} = 0.001 \text{ s}^{-1}$. We use $f_{\text{unbind}} = 3 \text{ pN}$ for both hands of the actin-spectrin linking protein.

We carry out 1 simulation of 60 filaments per parameter set, varying the number of spectrin tetramers from 0 to 4500 in increments of 500, adjusting the number of actin-spectrin linking proteins each time to maintain $N_{\text{linker}} = 5N_{\text{spectrin}}$.

In Figure 4.20 we show boxplots of ORP values at each spectrin density. Median ORP is between 0.7 and 0.8 where $N_{\text{spectrin}} \leq 500$, dropping to around

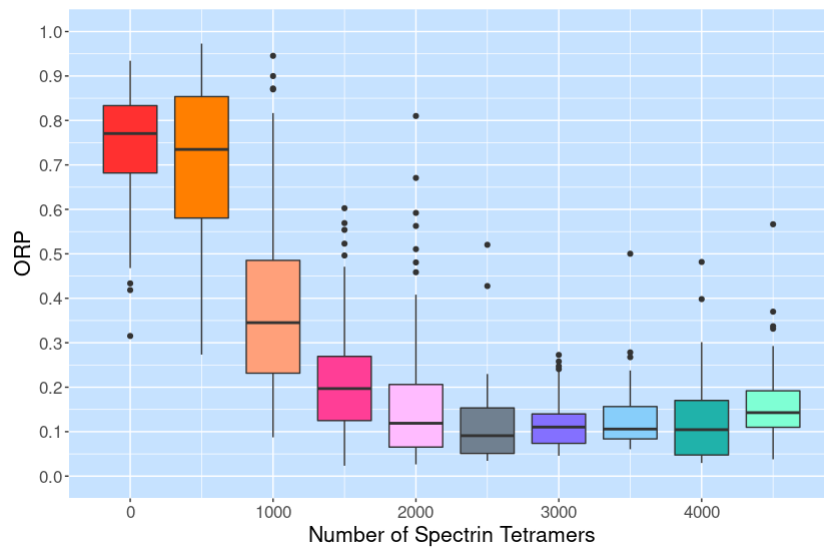


Figure 4.20: ORP with Spectrin Density. *We vary the number of spectrin tetramers from 0 to 4500 in intervals of 500, carrying out a single simulation containing 60 actin filaments for each value. The boxplots show a substantial reduction in mean ORP when spectrin numbers are increased above 1000. At 2500 and above, there is smaller drop in mean, with the interquartile range also becoming smaller. There are many outliers, particularly at higher numbers of spectrin.*

0.35 at 1000, and 0.2 at 1500 spectrin tetramers. From $N_{\text{spectrin}} = 2000$, median ORP reaches a minimum, remaining between 0.1 and 0.15 for each number of spectrin tetramers from 2000 to 4500. Outliers are present in 9 of the 10 parameter sets, however these outliers remain below 0.6 where $N_{\text{spectrin}} \geq 2500$, and the interquartile ranges of these sets were small.

Figure 4.20 shows that dense spectrin is beneficial in reducing ORP values, however that this effect saturates at around 2000 tetramers, with no further improvement as density is increased beyond this point. The reason for this saturation is unclear, however it may be due to the requirement for a degree of plasticity; in Section 4.6 we showed that it is beneficial for misaligned filaments to have an opportunity to move and realign with influence from local tetramers and connected actin filaments. Therefore, while increased density is beneficial in creating the preferred alignment of spectrin with the cell axis, it additionally results in spectrin tetramers becoming locked in position, unable to exhibit any plasticity in their arrangement. As spectrin is introduced to the cell prior to actin polymerisation, this drawback may counter the benefits of increased alignment for high spectrin densities.

Outliers are common in Figure 4.20 and this appears to be largely associated with partial incorporation of actin; as all actin nucleators are introduced simultaneously it is common for actin filaments to compete locally for attachment to spectrin. This results in many rings having a second or third actin filament partially incorporated into the spectrin scaffold in the local region, leaving a 'tail' which hangs off the membrane, and an increased ORP measure. Outliers may also occur due to misalignment in regions of spectrin depletion. These outliers may be avoided by introducing actin and spectrin to local regions gradually, allowing sequential assembly to occur.

Levels of ring formation are shown in Figure 4.21; at 1000 spectrin tetramers, just under half of the actin filaments have ORP values below the 0.3 threshold. This continues to increase with each set. At $N_{\text{spectrin}} = 2500$, more than half of the 60 actin filaments had ORP values of 0.1 or less, with a large number in the orange region. The sample at $N_{\text{spectrin}} = 3000$ did not contain any ORP values of 0.3 or above, with every actin filament within the sample appearing ring-like to some degree. Spectrin numbers of 3500-4500 also showed high levels of ring formation, however these results did not surpass those of 2500-3000 tetramers. This would suggest that while increasing spectrin numbers can influence ring formation, the effect appears to reach a maximum at this point.

So far we have focused on ring formation with our ORP measure, however, we are also interested in the patterns formed by filaments along the axon. To look into these arrangements, we calculate and plot the autocorrelation and power spectrum values for selected simulations. We use the methods as described in Section 2.4.4 and plot results for $N_{\text{spectrin}} \in \{0, 1500, 3000, 4500\}$.

Figure 4.22 shows results where no spectrin tetramers were present. In Figure 4.22a, no periodicity is evident, with a gradual decline to a single peak slightly above 0.2 in magnitude at a wavelength of 340 nm. In Figure 4.22b we note low power values, with a small magnitude peak of 0.0198 at a wavelength of 3003 nm - roughly half of the system size.

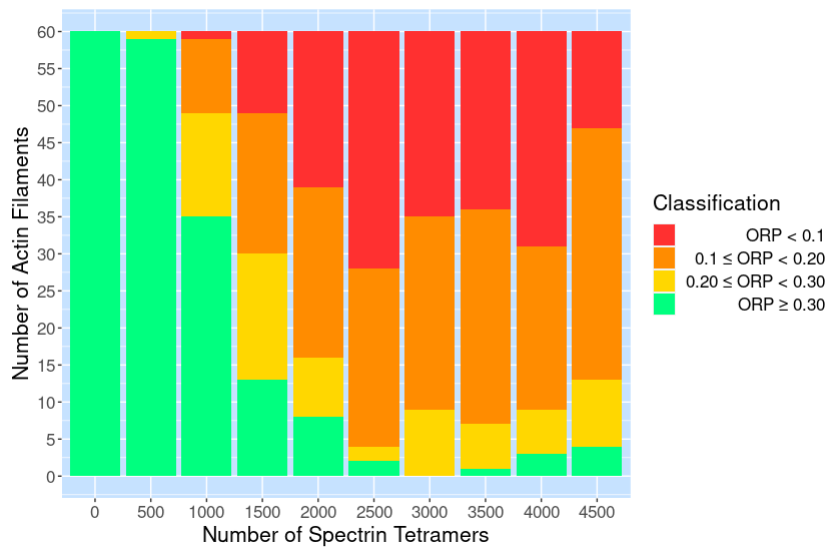
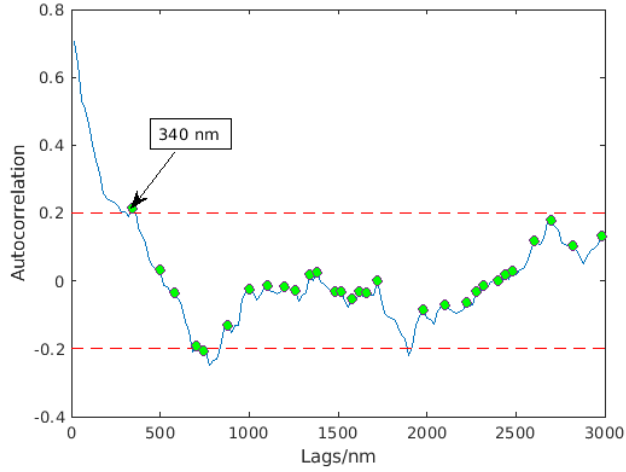
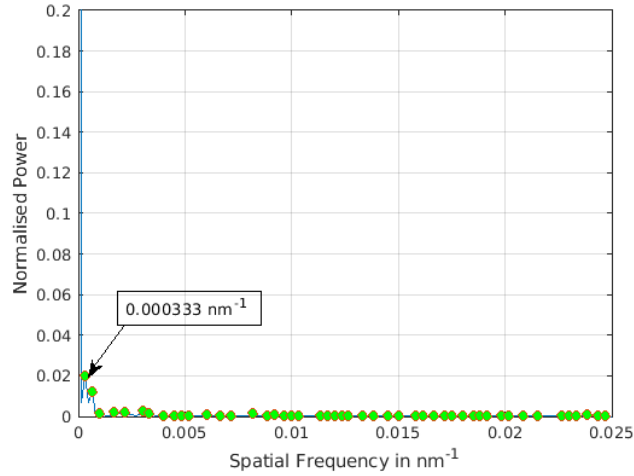


Figure 4.21: ORP Classification with Spectrin Density. We plot stacked bars representing the ORP classifications for a single simulation containing 60 actin filaments per parameter set. As shown in the legend, red, orange, and yellow portions of the bar account for filaments with ORP values below 0.3. There is a clear increase in this portion when increasing N_{spectrin} to 1500 tetramers, while 2500 and 4000 spectrin tetramers show the most filaments in red, with ORP below 0.1.

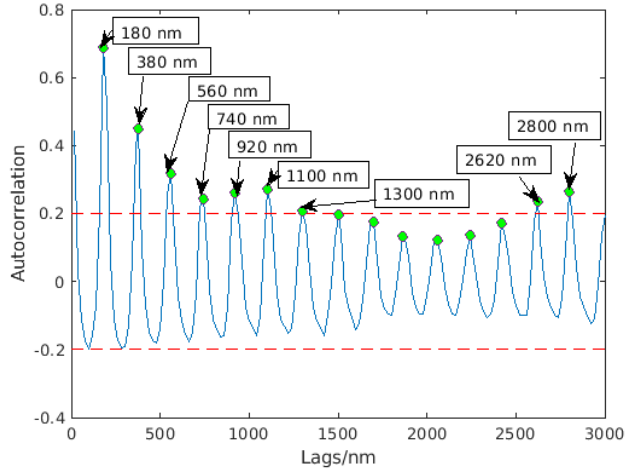


(a) Autocorrelation. *Autocorrelation is shown for lags up to 3000 nm. Green points indicate local maxima. A peak of 0.216 is shown at 340 nm.*

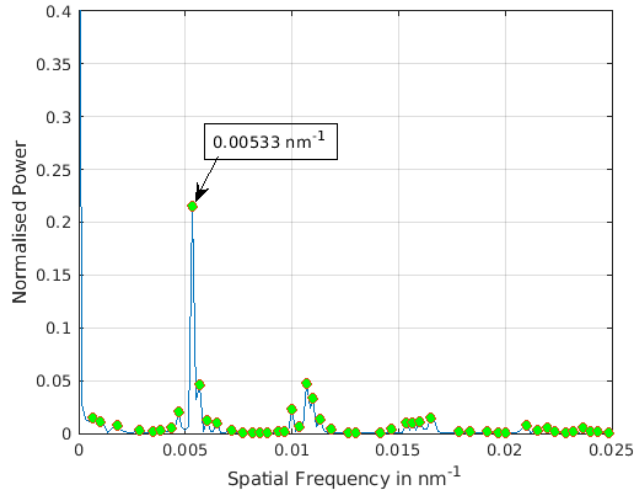


(b) Power with Spatial Frequency. *A small peak in normalised power of 0.0198 is shown at low frequencies, corresponding to wavelength of 3003 nm.*

Figure 4.22: Periodicity of Actin Filaments Without Spectrin. *We show results for autocorrelation and power for a simulation with 60 actin filaments of stiffness $\kappa_{\text{actin}} = 0.00228 \text{ pN } \mu\text{m}^2$, polymerised at $r_{\text{growth}} = 0.0033 \text{ } \mu\text{m s}^{-1}$, in a cell without spectrin tetramers present.*



(a) Autocorrelation. Autocorrelation is shown for lags up to 3000 nm. Green points indicate local maxima.



(b) Power with Spatial Frequency. A peak of 0.215 magnitude is shown at 0.00533 nm^{-1} , corresponding to a wavelength of 188 nm.

Figure 4.23: Periodicity of Actin Filaments With 1500 Spectrin. We show results for autocorrelation and power for a simulation with 60 actin filaments of stiffness $\kappa_{\text{actin}} = 0.00228 \text{ pN } \mu\text{m}^2$, polymerised at $r_{\text{growth}} = 0.0033 \text{ } \mu\text{m s}^{-1}$, in a cell with 1500 spectrin tetramers present.

Figure 4.23 shows results where 1500 spectrin tetramers were present; in contrast to the results without spectrin tetramers, long-range periodicity is evident in these figures. In Figure 4.23a we display autocorrelation up to lags of 3000 nm, finding a series of well-defined, consecutive peaks. There are 7 peaks of over 0.2 in magnitude at lags of 1500 nm or less; the first peak is at 180 nm, with an interval of 200 nm to the second peak at 380 nm. This is followed by 4 consecutive peaks at 180 nm intervals, and a 7th peak at a 200 nm interval. While the magnitude of peaks dips below 0.2 above this point, the function remains periodic, gradually increasing and exceeding 0.2 at 2620 nm, with a further peak at 2800 nm. Overall, this data shows high levels of long-range periodicity at a wavelength of 180 - 200 nm, consistent with the observed spacing of MPS components in imaging studies (Xu et al. (2013), Lukinavičius et al. (2014), Zhong et al. (2014), D’Este et al. (2015), D’Este et al. (2016), Leite et al. (2016), Han et al. (2017), Qu et al. (2017), Krieg et al. (2017), Unsain et al. (2018a)). In Figure 4.23b we see a peak of 0.215 in magnitude, corresponding to a wavelength of 188 nm.

In Figures 4.24 and 4.25 we show results for $N_{\text{spectrin}} = 3000$ and $N_{\text{spectrin}} = 4500$ respectively. Autocorrelation results continue to show large magnitude peaks, with consecutive peaks at intervals of 180 - 200 nm to one another, consistent with actin being spaced periodically by spectrin tetramers. In Figure 4.24b we find a peak at 182 nm wavelengths at 0.249 magnitude, while in Figure 4.25b the peak has shifted to 188 nm, and increased to 0.279 in magnitude.

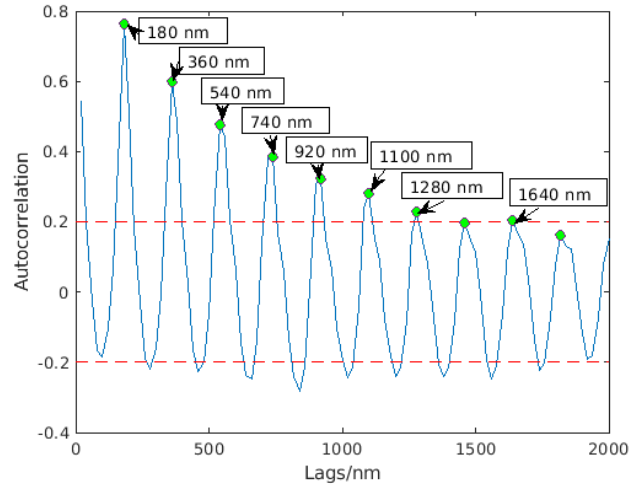
Taken together, these results show that the density of spectrin tetramers present is highly influential on ring formation when actin is polymerised within the cell, with periodic organisation evident at 1500 tetramers, and densities of around 2000 tetramers and above showing high degrees of ring formation, with up to half of the sample exhibiting an ORP value less than one, in addition to long-range periodic organisation.

4.8 Actin Stiffness and Polymerisation Rate

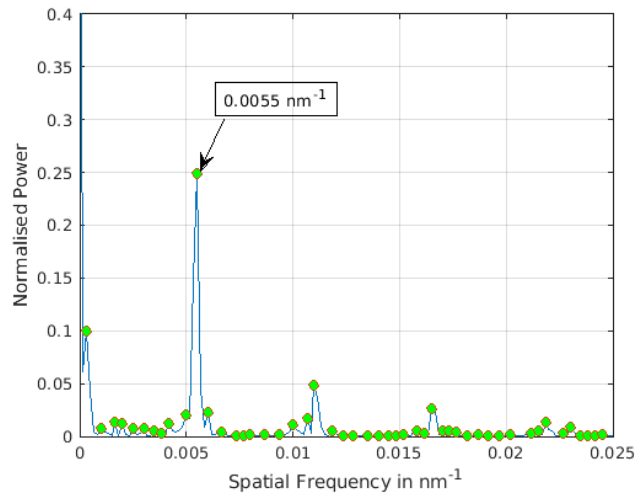
In Section 4.5, we explored the effects on in-cell polymerisation, with a range of actin stiffnesses and polymerisation rates. While our initial results in Section 4.5.1 suggested that reduced polymerisation rates resulted in enhanced levels of ring formation, we were unable to determine optimum values for κ_{actin} and r_{growth} in this case, with the ORP values for $\kappa_{\text{actin}} = 0.05$ pN μm^2 at a range of polymerisation rates from 0.001 to 0.01 $\mu\text{m s}^{-1}$ appearing similar in Section 4.5.2.

In the Sections that followed, we established values for r_{bind} , r_{unbind} , and N_{spectrin} which enhanced levels of ring formation. We now use these improved parameters, returning to the exploration of actin stiffness and polymerisation rate, aiming to determine the range of these parameter combinations for which rings are likely to be created.

We explore the range of actin stiffnesses, $\kappa_{\text{actin}} \in [0.004, 0.04]$ pN μm^2 , with polymerisation rates, $r_{\text{growth}} \in [0.001, 0.1]$ $\mu\text{m s}^{-1}$. We use $N_{\text{spectrin}} = 2500$,

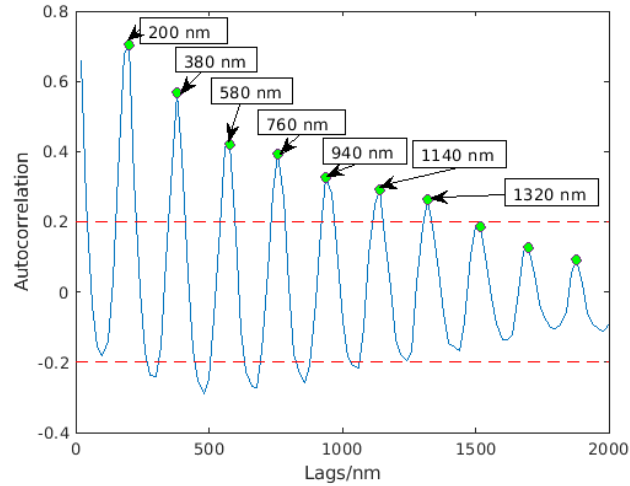


(a) Autocorrelation. Autocorrelation is shown for lags up to 2000 nm. Green points indicate local maxima.

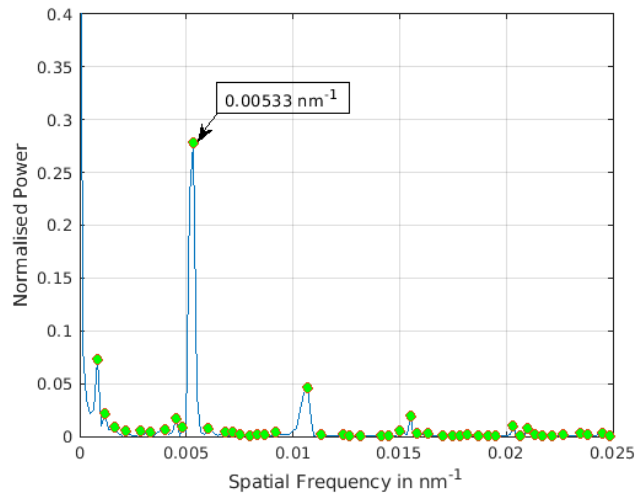


(b) Power with Spatial Frequency. A peak of 0.249 magnitude is shown at 0.0055 nm^{-1} , corresponding to a wavelength of 182 nm.

Figure 4.24: Periodicity of Actin Filaments With 3000 Spectrin. We show results for autocorrelation and power for a simulation with 60 actin filaments of stiffness $\kappa_{\text{actin}} = 0.00228 \text{ pN } \mu\text{m}^2$, polymerised at $r_{\text{growth}} = 0.0033 \text{ } \mu\text{m s}^{-1}$, in a cell with 3000 spectrin tetramers present.



(a) Autocorrelation. Autocorrelation is shown for lags up to 3000 nm. Green points indicate local maxima.



(b) Power with Spatial Frequency. A peak of 0.279 magnitude is shown at 0.00533 nm^{-1} , corresponding to a wavelength of 188 nm.

Figure 4.25: Periodicity of Actin Filaments With 4500 Spectrin. We show results for autocorrelation and power for a simulation with 60 actin filaments of stiffness $\kappa_{\text{actin}} = 0.00228 \text{ pN } \mu\text{m}^2$, polymerised at $r_{\text{growth}} = 0.0033 \text{ } \mu\text{m s}^{-1}$, in a cell with 4500 spectrin tetramers present.

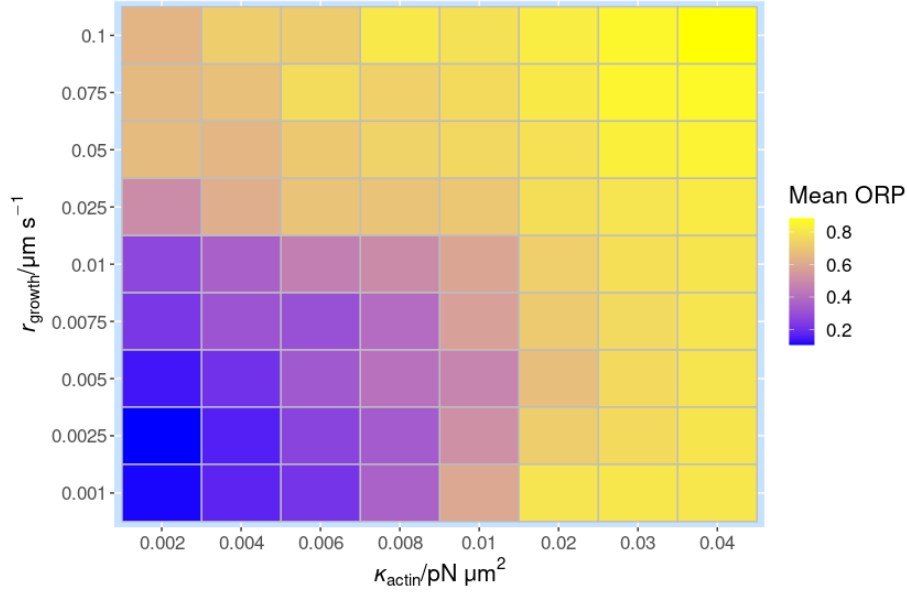


Figure 4.26: Mean ORP with Polymerisation Rate and Actin Stiffness. *60 actin filaments of stiffness $\kappa_{\text{actin}} \in [0.002, 0.04]$ pN μm^2 , polymerised at rates of $r_{\text{growth}} \in [0.001, 0.1]$ $\mu\text{m s}^{-1}$, in a cell with 2500 spectrin tetramers..*

with $N_{\text{linker}} = 5N_{\text{spectrin}}$. For the actin binding hand of our actin-spectrin linker, we use a binding rate of $r_{\text{bind}} = 1 \text{ s}^{-1}$ and unbinding at $r_{\text{unbind}} = 0.1 \text{ s}^{-1}$

We initially carried out a single simulation per parameter combination. As the results appeared to follow a clear pattern, we did not perform any additional simulations.

In Figure 4.26 we show the mean ORP value as we vary κ_{actin} and r_{growth} . Results with high ORP values are shown in yellow, with purple representing mid-range values, and blue indicating a low value of around 0.2. We see that blue tiles are restricted to the lowest actin stiffness, $\kappa_{\text{actin}} = 0.00228 \text{ pN } \mu\text{m}^2$, in combination with the slowest polymerisation rates, $r_{\text{growth}} \in [0.001, 0.005] \mu\text{m s}^{-1}$. Purple tiles occur for actin stiffnesses up to around $\kappa_{\text{actin}} = 0.01 \text{ pN } \mu\text{m}^2$ combined with polymerisation rates of up to $0.01 \mu\text{m s}^{-1}$. At stiffnesses of $\kappa_{\text{actin}} = 0.02 \text{ pN } \mu\text{m}^2$ and above, the majority of tiles appear yellow.

Figure 4.27 shows the number of rings for each parameter set with ORP of less than 0.3. The greatest numbers of rings occur for low stiffnesses of up to $\kappa_{\text{actin}} = 0.008 \text{ pN } \mu\text{m}^2$ in combination with slow polymerisation rates of $0.01 \mu\text{m s}^{-1}$ and below, with the lowest polymerisation rates and stiffnesses giving the highest numbers of results below this threshold.

Having explored and optimised several of our parameter values in Sections 4.6 - 4.7, we have now improved on the results of Section 4.5.2 and gained a

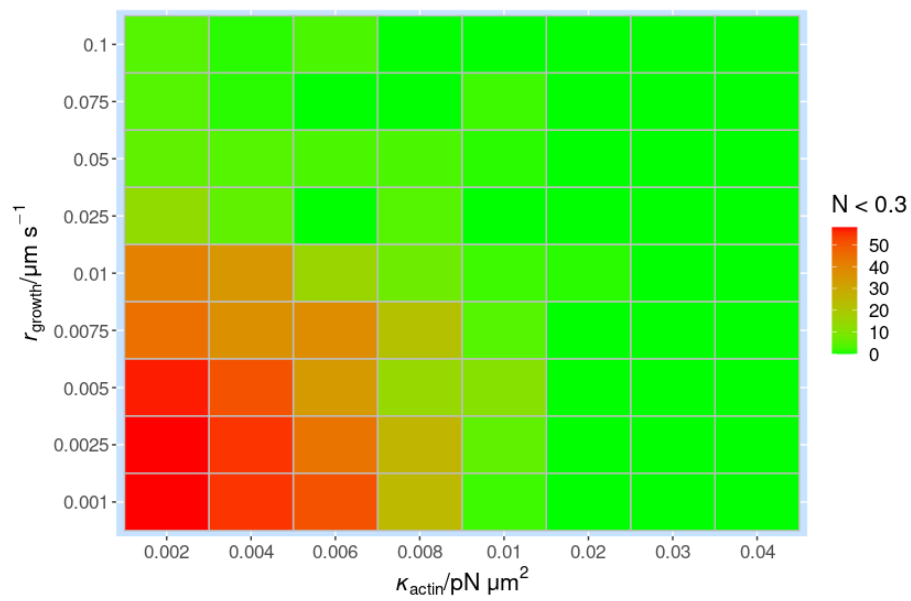


Figure 4.27: Number of Rings with Actin Polymerisation Rate and Stiffness. 60 actin filaments of stiffness $\kappa_{\text{actin}} \in [0.002, 0.04] \text{ pN } \mu\text{m}^2$, polymerised at rates of $r_{\text{growth}} \in [0.001, 0.1] \mu\text{m s}^{-1}$, in a cell with 2500 spectrin tetramers.

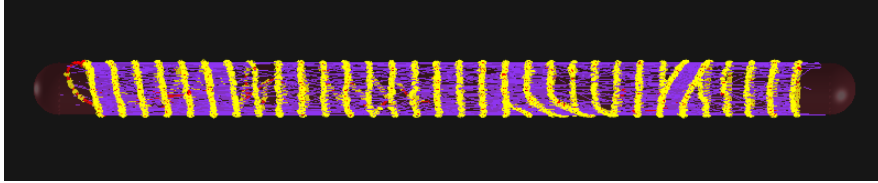


Figure 4.28: Example Simulation Image with a Combination of Low Actin Stiffness and Slow Polymerisation Rate. 60 actin filaments of stiffness $\kappa_{\text{actin}} 0.00228$ pN μm^2 are polymerised at rates of $r_{\text{growth}} = 0.001 \mu\text{m s}^{-1}$, in a cell containing 2500 spectrin tetramers.

clearer picture of how reduced actin stiffness and slow in-cell polymerisation lead to enhanced levels of ring formation. Figure 4.28 shows results achieved with a combination of low actin stiffness and a slow polymerisation rate.

4.9 Effect of Cell radius

In the previous Section, we found that ring formation required a reduced actin stiffness, with unmodified actin of the stiffness measured experimentally, $\kappa_{\text{actin}} = 0.036$ pN μm^2 (Isambert et al. (1995)), being highly unlikely to form rings within our axon-like environment.

Axon diameters typically range from $0.1 - 10 \mu\text{m}$ (Perge et al. (2012)), and therefore in simulating a model axon of $R_{\text{axon}} = 0.2 \mu\text{m}$, we have chosen to explore the smaller end of this range. How would our results differ in a model axon of increased radius? As rings in a wider axon would possess a reduced degree of curvature, ring-formation may become possible for stiffer forms of actin. Alternatively, the resulting decrease in membrane curvature could alter the patterns adopted by interacting actin and spectrin, preventing ring formation entirely.

To explore the effect of an increased cell radius, we simulate axons of $R_{\text{axon}} \in \{0.2, 0.4, 0.6\} \mu\text{m}$. We maintain a constant density of spectrin per μm^2 on the cell membrane; at $R_{\text{axon}} = 0.2 \mu\text{m}$ we include 2500 spectrin tetramers, increasing to 5000 at $R_{\text{axon}} = 0.4 \mu\text{m}$, and 7500 at $R_{\text{axon}} = 0.6 \mu\text{m}$. For each cell radius, we simulate 3 stiffnesses of actin, using $\kappa_{\text{actin}} \in \{0.00228, 0.0091, 0.036\}$ pN μm^2 . These stiffnesses correspond to persistence lengths of $L_p \in \{0.533, 2.13, 8.41\} \mu\text{m}$.

We previously used an actin filament length of $L_{\text{actin}} = 1.32 \mu\text{m}$ within a cell of radius, $R_{\text{axon}} = 0.2 \mu\text{m}$. To calculate this we found the number of whole actin monomers contained within the cell circumference measurement, and added 12 monomers to allow a small region of overlap, ensuring that the result was divisible by 4 to allow compatibility with the segmentation size of $0.022 \mu\text{m}$. The length of $L_{\text{actin}} = 1.32 \mu\text{m}$ contains 240 monomers, each contributing 5.5 nm (Kandel et al. (2000), Chapter 4) to the filament length. We apply this formula to the actin filaments used in simulations of increased radius to ensure

that single-filament actin rings could be formed, rounding to the nearest set of 4 monomers where necessary. For $R_{\text{axon}} = 0.4 \mu\text{m}$ this formula gives a length of $L_{\text{actin}} = 2.574 \mu\text{m}$ (468 monomers), while for $R_{\text{axon}} = 0.6 \mu\text{m}$ we arrive at $L_{\text{actin}} = 3.828 \mu\text{m}$ (696 monomers). We increase the time allocated in the simulation for polymerisation to occur, to take account of this increased length, using a polymerisation rate of $r_{\text{growth}} = 0.0033 \text{ s}^{-1}$.

We run 2 simulations per parameter set, combining results from these simulations. We display results in Figure 4.29; each of the 3 graphs represents a different actin stiffness, while boxes show results at different cell radii. Each box represents ORP results for 120 actin filaments. In Figure 4.29a, we see low median ORP values of around ~ 0.1 across all 3 cell radii, with several outliers in each case. Below, in Figure 4.29b, there is a reduction in median ORP from slightly above 0.3 at the smallest radius of $R_{\text{axon}} = 0.2 \mu\text{m}$, to around ~ 0.1 at the 2 larger radii. Interestingly, a large reduction in ORP is shown for the stiffest form of actin with $\kappa_{\text{actin}} = 0.036 \text{ pN } \mu\text{m}^2$ and $L_p = 8.41 \mu\text{m}$; in Figure 4.29c median ORP at $R_{\text{axon}} = 0.2 \mu\text{m}$ is close to 0.8, dropping to 0.45 at $R_{\text{axon}} = 0.4 \mu\text{m}$, and slightly above 0.2 at $R_{\text{axon}} = 0.6 \mu\text{m}$.

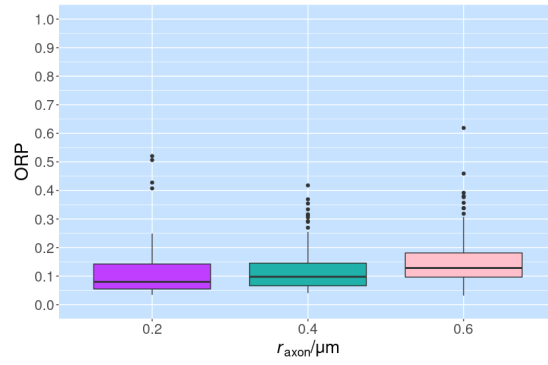
These results show that, within the ranges tested, an increase in axon radius has a beneficial effect on the formation of actin rings for stiffer actin filaments. Rings were able to form reliably even with actin of standard stiffness when the cell radius was increased to $R_{\text{axon}} = 0.6 \mu\text{m}$.

We show example images taken from the final simulation timestep for actin of $\kappa_{\text{actin}} = 0.036 \text{ pN } \mu\text{m}^2$ in Figure 4.30. In the upper image, we see that in a narrow axon with $R_{\text{axon}} = 0.2 \mu\text{m}$ actin appears as elongated, spiralling filaments. When the axon radius increases to $R_{\text{axon}} = 0.4 \mu\text{m}$, spirals are still visible however they appear more upright. Finally at the largest radius of $R_{\text{axon}} = 0.6 \mu\text{m}$, many of these spirals have oriented at close to 90° relative to the longitudinal axis of the cylinder, forming rings at each end of the cell, connected by a central region containing mainly spiralling actin. We note that within this larger cell space, a number of spectrin tetramers now occupy the hemispherical endcaps of the cell - areas which were unoccupied at low radii due to their high curvature. This results in a small decrease in the density of spectrin on the remainder of the membrane, however this is unlikely to affect results significantly.

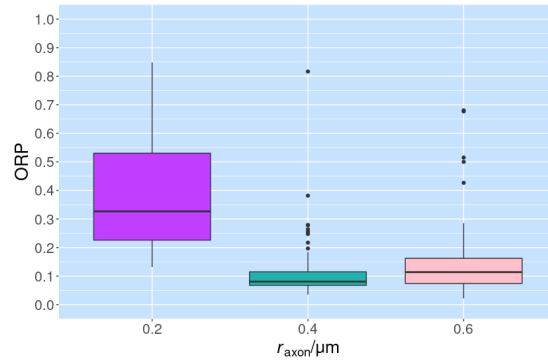
It would be highly illuminating to continue to increase the radius; given the differences in the arrangement of the actin-spectrin network in different regions of the neuron, such as the soma, there may be a threshold radius at which parallel ring formation transitions to a polygonal network. Unfortunately, as simulation duration increases rapidly with increased spectrin numbers, it was not feasible to increase the radius further in this study.

4.10 Discussion

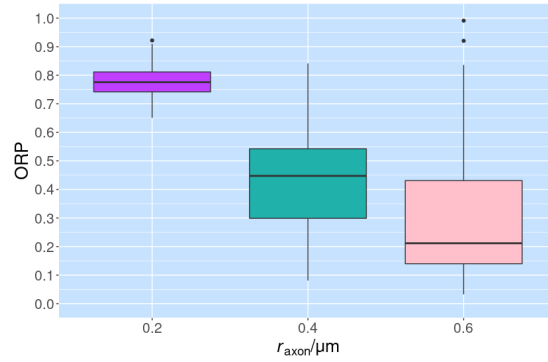
In Section 4.4 we found that an increased density of spectrin tetramers reduced the ORP measure for non-polymerised actin with $\kappa_{\text{actin}} \geq 0.00228 \text{ pN } \mu\text{m}^2$. We then investigated in-cell polymerisation of actin in Section 4.5, finding that



(a) $\kappa_{\text{actin}} = 0.00228 \text{ pN } \mu\text{m}^2$, $L_p = 0.533 \text{ } \mu\text{m}$.



(b) $\kappa_{\text{actin}} = 0.0091 \text{ pN } \mu\text{m}^2$, $L_p = 2.13 \text{ } \mu\text{m}$.



(c) $\kappa_{\text{actin}} = 0.036 \text{ pN } \mu\text{m}^2$, $L_p = 8.41 \text{ } \mu\text{m}$.

Figure 4.29: Effect of Increasing Axon Radius on Actin of 3 Different Stiffnesses. We show results at axon radii of $R_{\text{axon}} \in \{0.2, 0.4, 0.6\} \text{ } \mu\text{m}$, with each boxplot corresponding to a different actin stiffness and corresponding persistence length. Results for the stiffer actin filaments shown in the centre and lower images show reduced ORP values at larger radii.

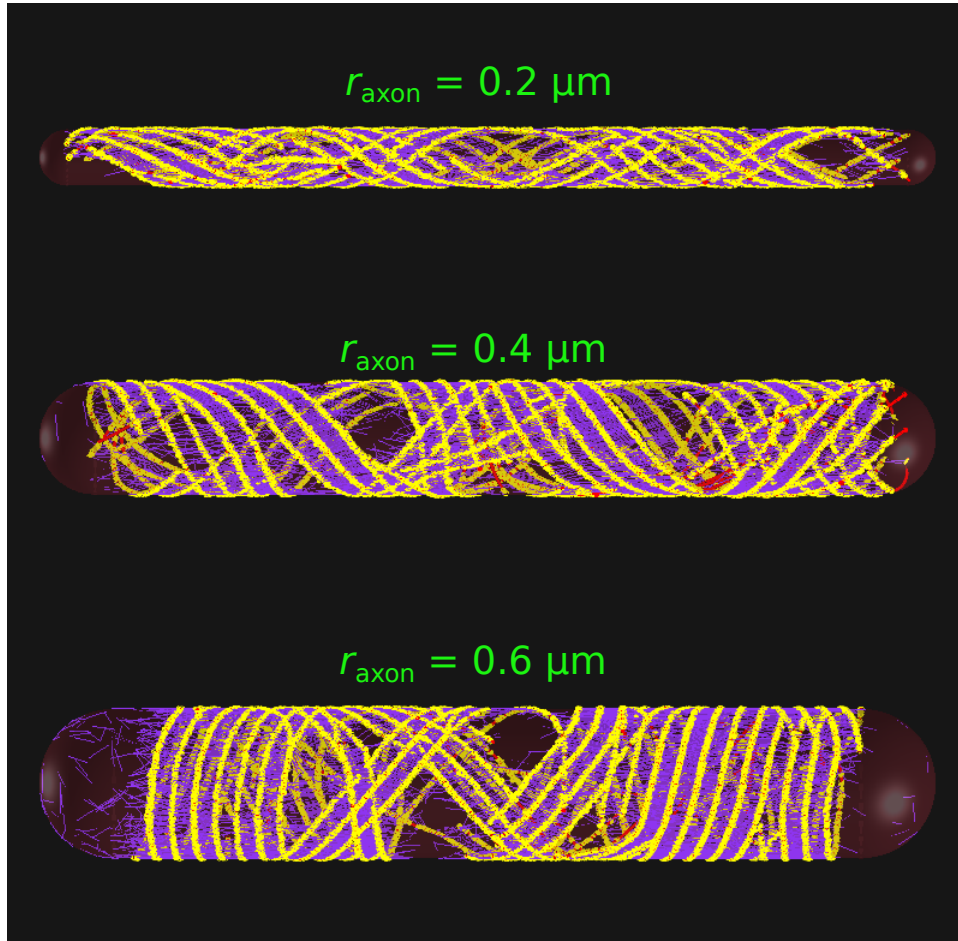


Figure 4.30: Effect of Increasing Axon Radius for Actin of $\kappa_{\text{actin}} = 0.036 \text{ pN } \mu\text{m}^2$, corresponding to a persistence length of $L_p = 8.41 \mu\text{m}$. We show the arrangement of actin and spectrin at the final timestep of simulations with $R_{\text{axon}} \in \{0.2, 0.4, 0.6\} \mu\text{m}$. At the smallest radius (upper image) actin forms elongated spirals, which become more upright as radius increases (centre image). At the largest radius (lower image), we observe several consecutive actin ring-like structures at each end of the cell, connected by regions containing spiralling actin.

a slow rate of polymerisation of $r_{\text{growth}} = 0.033 \mu\text{m s}^{-1}$ and below facilitated ring formation for $\kappa_{\text{actin}} \leq 0.00913 \text{ pN } \mu\text{m}^2$, but finding no significant difference between rates from $0.001 - 0.01 \text{ s}^{-1}$.

Actin-spectrin linking proteins worked best at creating rings when binding rates were high at r_{bind} of $1 - 10 \text{ s}^{-1}$, while an unbinding rate of $r_{\text{unbind}} = 0.1 \text{ s}^{-1}$ resulted in the lowest ORP measurement and highest numbers of rings formed. We found that an abundance of actin-spectrin linking proteins greater than the level required for binding site saturation was also beneficial to ring formation.

The level of spectrin had a substantial effect on ring formation when actin was polymerised within the cell; we found in Section 4.7 that ORP dropped rapidly where the number of spectrin tetramers present increased from 0 to 2000, remaining low as we increased numbers further up to 4500. In this Section we also confirmed periodic organisation of actin, observable when spectrin levels were at 1500 and above.

In Section 4.8 we used the best parameter values determined in previous Sections, reviewing a range of actin stiffnesses and polymerisation rates. We found that low mean ORP values and high numbers of rings resulted reliably from polymerisation rates under $0.01 \mu\text{m s}^{-1}$, and actin stiffnesses of $0.01 \text{ pN } \mu\text{m}^2$ or less. Finally in Section 1.4.1, we found that an increased cell radius led to dramatic reductions in ORP values for stiffer actin filaments.

Through these results we have demonstrated that it is possible to simulate self-assembly of the periodic actin rings and alternating spectrin tetramers of the MPS. The key factors which influenced self-assembly were in-cell polymerisation of actin at a reduced rate, and the presence of large numbers of membrane-bound spectrin tetramers to which actin could rapidly bind via a large population of actin-spectrin linking proteins.

The essential role of spectrin has already been established by experiment; as discussed in Section 1.3.5, knockdown (Zhong et al. (2014)) or use of mutants with very low levels (Lorenzo et al. (2019)) of βII spectrin has been found to destroy or greatly reduce abundance of the periodic actin-spectrin pattern in rodents. Similarly, studies have shown that overexpression of βII spectrin has a beneficial effect, resulting in MPS that is more abundant and widespread (Zhong et al. (2014)). These observations appear to support our results, demonstrating a need for a spectrin, and a pattern forming effect which is optimised when spectrin is abundant. In our simulation results we identified minimum levels of spectrin required for pattern formation, a range over which pattern formation increased with increased numbers of spectrin, and an approximate threshold beyond which increased spectrin levels provided no additional benefit. It is difficult to explore a full range of spectrin levels experimentally due to lethality of βII spectrin knockout in mammalian cells (Leterrier (2019)), however experiments in which spectrin is up or down regulated and MPS abundance and regularity measured could give experimental confirmation of the existence of such thresholds. Further manipulations could be targeted towards any of the range of proteins which are believed to facilitate actin-spectrin binding.

Our results on the role of actin polymerisation rate have not yet been investigated experimentally. From our simulation results, we predict that poly-

merisation at a reduced rate, ideally below around $0.005 \mu\text{m s}^{-1}$, is likely to occur for actin filaments incorporated into the MPS during early developmental stages. While the polymerisation rate of MPS-related actin has not yet been investigated, the proteins dematin and coronin2b have been shown to slow actin polymerisation (Siegel and Branton (1985), Chen et al. (2020)) and interestingly were both recently found to be associated with the MPS (Zhou et al. (2020)). Experimental work is needed to explore the roles of these proteins in the MPS. Our simulation results are predictive of a degree of correlation between levels of these polymerisation slowing proteins, and MPS abundance and regularity. Imaging studies in which levels of these proteins are manipulated and MPS abundance is measured would be insightful in confirming the role of polymerisation rate and the involvement of these proteins.

Overall our results suggest a number of avenues of experimental study, and we discuss and develop these ideas further in the Conclusion.

Chapter 5

Conclusions

In this study, our aim was to reproduce self-assembly of the axonal MPS in a model system. We wished to understand how the main cytoskeletal filaments and proteins of the MPS would position and orient spatially when placed within a cylindrical cell, representative of an axonal section. Observing the configurations adopted gives insight into possible self-assembly mechanisms, helping us to establish whether the MPS arrangement of periodically spaced actin rings separated by spectrin tetramers is simply caused by component proteins interacting within the bounds of a tubular cell, or whether specific biological processes, interactions, and modifications, are required to drive this self-assembly.

In Chapter 2, we used a greatly simplified model, approximating actin and spectrin as rigid rods which interact via passive crosslinks and hardcore repulsion only, and simulating motion via a random walk in a $2\ \mu\text{m}$ axonal section with fixed boundaries and an impenetrable central microtubule array. A Monte Carlo method was used to sample configurational information on large numbers of random walks. We were not able to recreate self-assembly using this method, noting that actin filaments were most likely to orient with the longitudinal axis of the cell, and occupy central regions, maximising distance from boundaries. In addition, analysis of periodicity failed to detect any significant patterning. These results suggest that cell morphology and simple actin and spectrin linking interactions are insufficient to drive self-assembly.

In Chapters 3 and 4, we continued our investigations, using a more complex model in which we introduced a number of biologically realistic properties. Using the Cytosim software package (Nedelec and Foethke (2007)), we modelled actin and spectrin as flexible fibres, simulating their motion with Langevin dynamics. We extended our model through introduction of membrane confinement or adhesion, actin-spectrin crosslinks, and actin polymerisation, simulating protein events through a modified Gillespie algorithm. We were able to observe self-assembly of an MPS-like structure, containing rings of actin, spaced periodically along the longitudinal axis of the cell. The assembly of this structure required abundant spectrin, confined to the membrane, interacting with actin,

which must be polymerised within the cell. The connections between actin and spectrin were key to self-assembly, and results required a rapid connection and relatively slow turnover, with high availability of connecting proteins being beneficial. We found that actin of reduced stiffness, polymerised at a slow rate, was most likely to adopt an MPS-like configuration, however this was possible for actin of standard stiffness when the cell radius was increased.

In Section 5.1, we discuss our key findings and conclusions that can be drawn, as well as the limitations of our study. In Section 5.2 we suggest several areas in which our results could be extended or improved upon. We conclude the research in Section 5.3 with some final comments.

5.1 Discussion and Evaluation

As the full range of processes involved in MPS self-assembly are not currently understood, and experimental values for properties of some key components are unavailable, we cannot draw precise conclusions relating to the conditions of self-assembly. We can, however, make observations on some general principles which resulted in self-assembly within our model. We discuss our findings here, relating our model results to biological components or processes through which our work could be validated with experimental evidence.

We found self-assembly of an MPS-like structure to be driven by interactions between actin and membrane-bound spectrin; spectrin tetramers have a tendency to align with the longitudinal axis of our narrow cylindrical cell, bundling in parallel as observed *in vitro* (Hauser et al. (2018)). The results of Chapters 2 and 3 demonstrated that actin filaments of $\kappa_{\text{actin}} \geq 0.00456 \text{ pN } \mu\text{m}^2$ also tend to align this way, even when existing at scales on the order of 10 nm. This creates a tug-of-war between interacting actin and spectrin, with the outcome dependent on the stiffnesses and lengths of the interacting proteins, the level of connectivity, and any constraints related to bundling and so on. We observed that if actin was recruited to the membrane at a short length, then it was common to see the filament being oriented around the circular membrane plane, perpendicular to spectrin which aligned with the longitudinal axis. As actin polymerised, it could remain in this orientation, creating a ring, or deviate from this course, forming spirals with various pitch. Alternatively, it could become disorganised, with this outcome often being observed where spectrin was depleted locally.

Dense bundled spectrin on the membrane tended to increase the likelihood of actin remaining on course; in our simulations we required a density of around 332 spectrin tetramers per μm^2 of membrane surface or above to reliably create the structure. We also required actin-spectrin interactions to proceed rapidly, ensuring incorporation onto the membrane at an early stage of polymerisation when the actin filament is short. While the mode of connection between actin and spectrin within the MPS is currently poorly understood, we suggest that the protein, dematin, recently found to be associated with the MPS (Zhou et al. (2020)), could play a role in facilitating a rapid and favourable connection, in

light of evidence of its ability to enhance actin-spectrin interaction (Koshino et al. (2012)).

Where polymerisation proceeded at a reduced rate, spectrin had sufficient time to move into binding range which facilitated parallel stacking and alignment of spectrin, provided actin remained perpendicular to the longitudinal axis. Binding of spectrin occurred at both sides of the growing actin filament, and this further reinforced the direction of polymerisation. We suggest that the proteins, dematin, and coronin2b, found to be associated with the MPS (Zhou et al. (2020)) may assist in this process, as both have been observed to slow actin polymerisation (Siegel and Branton (1985), Chen et al. (2020)). Through experimental studies, the rate of polymerisation, and the action of these proteins, could be confirmed.

A reduced stiffness of actin was beneficial in our narrow cell, and although the impact of stiffness was reduced when cell radius was increased, it's possible that ring formation is facilitated by a reduction of stiffness, either through modifications such as association of cofilin (McCullough et al. (2008)), or through the action of IQGAP proteins, which could cause bending directly (Palani et al. (2020)). We require experimental validation of the presence of these proteins. The length of actin within the MPS also requires experimental confirmation; in Chapters 3 and 4 we used actin filaments of lengths on the μm scale as observed by Vassilopoulos et al. (2019). Shorter filaments may lead to a different outcome, however the process of crosslinking short actin filaments may be relatively similar to the polymerisation of longer filaments in this context. Nevertheless, further experimental evidence on the length of MPS-based actin would be valuable to inform future modelling studies.

While observing our simulation results, we found that pattern formation at one location causes an alignment of spectrin tetramer terminals on either side of the actin ring, with this spectrin alignment creating ideal conditions for additional rings to form. Through this process, the periodic pattern of rings is reinforced across local areas, resulting in several adjacent rings. Through this mechanism, the creation of a single actin ring by any mechanism could allow a series of consecutive rings to be created. Alternatively, alignment of spectrin tetramers could result in a similar process. We are lacking experimental information about the properties of brain spectrin, and it would be highly informative to discover whether spectrin possesses an ability to align with other tetramers, perhaps through interactions at the C-termini of the β monomer, located centrally within the tetramer.

In our simulations, all spectrin tetramers were present at the beginning of the simulation, with actin filaments or nucleators being introduced a short time later. It's likely, however, that a gradual introduction of actin and spectrin in local regions would produce improved results, allowing individual rings to form consecutively. This could be achieved in practice through the microtubule-based trafficking of spectrin to MPS generation hotspots as observed by Glomb et al. (2022).

5.2 Future Work

The MPS remains a topic of active research, with much to be discovered about its assembly processes and properties, as well as its purpose and benefits to the cell. In this Section we discuss some of the remaining questions, suggesting several areas in which our results could be developed further.

5.2.1 Parameter Optimisation

In this study we focused on identifying parameters of interest, making observations on the impact of changing these parameters. We found that the system displayed high levels of sensitivity to small changes in certain parameters. This may suggest that a highly specified biological process is involved in MPS self-assembly, with signalling pathways creating ideal conditions. While we have identified several parameters of interest, it is likely that further parameters are involved, with an ideal parameter combination existing to reliably create this structure. Ongoing biological studies may uncover details of these processes in future, however, *in silico* studies can play an important supportive role. A machine learning based approach may be a useful addition to our study, using an intelligent and automated method to vary multiple parameters and identify the optimum set of values.

5.2.2 Exploration of Different Morphologies

In Section 4.9 we found that an increase in axon radius enabled ring generation using actin of increased stiffness. It is unclear at this stage whether actin within the MPS is of standard stiffness or a reduced stiffness related to cofilin modification or similar. It is also yet to be established whether IQGAP proteins play a role in shaping actin into rings in the MPS (Palani et al. (2020)). While experimental results are needed to determine the properties of MPS-based actin, our study could be extended to explore different morphologies. It would be illuminating to observe how the arrangement of MPS components evolves in a morphology of increasing radius, or in cells of a different shape.

We show in Figure 5.1 some preliminary explorations, using our components in a spherical cell. In this cell of radius $R_{\text{cell}} = 0.6 \mu\text{m}$ we include 1500 membrane-bound spectrin tetramers, maintaining the density of 331.57 spectrin per μm^2 as used previously, with $N_{\text{linker}} = 5N_{\text{spectrin}}$. We simulate 20 actin filaments of $L_{\text{actin}} = 1.32 \mu\text{m}$ initially as shown in the upper image, followed by a simulation with 60 filaments at $L_{\text{actin}} = 0.44 \mu\text{m}$, with results shown in the lower image. Interestingly, we see that actin is still able to form an MPS-like pattern on a spherical cell, with up to 5-6 actin filaments appearing in parallel, and adjacent filaments connecting via spectrin tetramers. For shorter filaments, there is slightly more diversity in the orientation of these patches of alignment, resulting in a meshwork appearance as sections of local order encounter neighbouring sections at an angle to one another. It would be interesting to investigate this

further, observing the shift in alignment and orientation as membrane curvature reduces. This would help us to understand why the MPS is most commonly found in tubular morphologies, while a hexagonal arrangement is preferred on the soma and some dendrites (Han et al. (2017)).

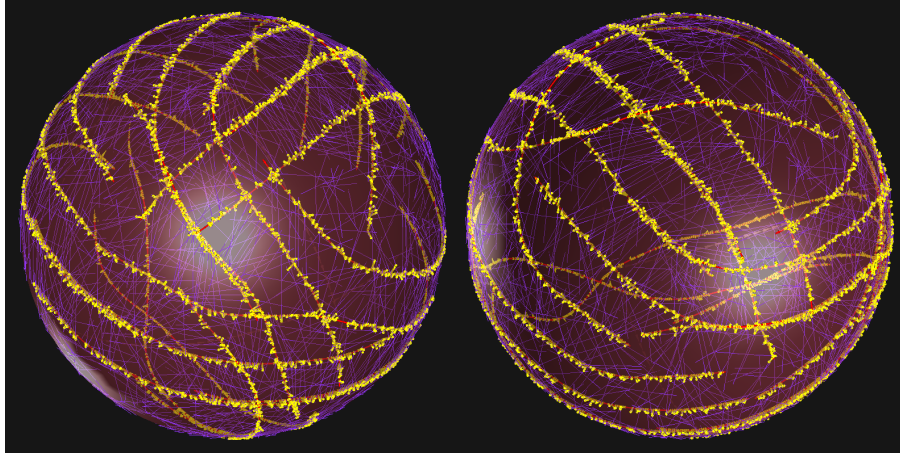
5.2.3 Microtubule Interactions

Experimental studies have found that stabilisation of microtubules leads to more robust development of the MPS (Dubey et al. (2020)), while disruption of either actin (Qu et al. (2017)) or microtubules (Zhong et al. (2014)) disrupts the MPS. These observations indicate a level of dependency, however the mechanism of connection between the MPS and microtubule arrays remains poorly understood. Results in this study were produced without inclusion of microtubules, however it would be useful to adapt the model to include a microtubule array, myosin motor proteins, and a deformable boundary. This would allow an exploration of the balance of tension between these components.

5.3 Concluding Remarks

Research into the MPS structure has the potential to impact our understanding of neuronal development, disease, and injury. An understanding of the conditions under which the MPS assembles could give us valuable information on the reasons behind the limited regeneration capacity of neurons, potentially leading to the development of new treatments for neurodegenerative conditions. Through this study we have gained an understanding of several factors which can influence self-assembly of the MPS. This remains an exciting and fast-moving field, and we await future developments with interest.

$L_{\text{actin}} = 1.32 \mu\text{m}$



$L_{\text{actin}} = 0.44 \mu\text{m}$

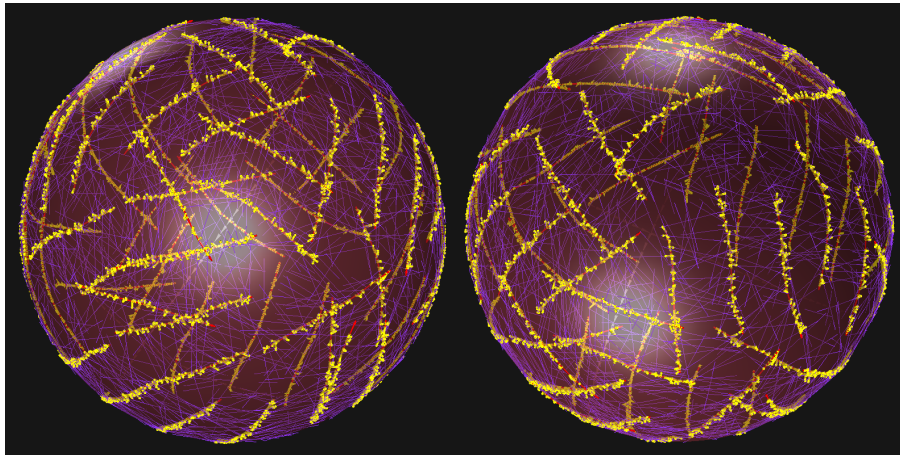


Figure 5.1: Effect of Altering Cell Morphology - Spherical Cell. *Here we simulate actin of $\kappa_{\text{actin}} = 0.0091 \text{ pN } \mu\text{m}^2$, approximating cofilactin. Actin polymerises at a rate of $r_{\text{growth}} = 0.0033 \mu\text{m s}^{-1}$ within a spherical cell of radius $R_{\text{cell}} = 0.6 \mu\text{m}$, interacting with 1500 membrane-bound spectrin tetramers, and actin-spectrin linking proteins at $N_{\text{linker}} = 5N_{\text{spectrin}}$. Results are shown for $L_{\text{actin}} = 1.32 \mu\text{m}$ (upper image), as well as a shorter filament of $L_{\text{actin}} = 0.44 \mu\text{m}$ (lower image).*

Appendix A

Timestep Dependency

While timesteps of below 1 ms are commonly used in simulation of proteins, Cytosim is able to perform simulations with larger timesteps, which allows us to simulate for long durations or complete complex simulations in much shorter timeframes than what could traditionally be achieved. While a timestep that is too large will cause the code to become unstable and generate errors or erratic results, on average, results from a suitably small range of timesteps should appear indistinguishable, with no dependence on timestep used.

In order to test the timestep for our system, we created a system representative of the more advanced simulations carried out in Chapter 4, with nucleated actin, membrane-bound spectrin, and actin crosslinkers, within a capsule shaped environment of 6 μm in length. Simulations were carried out using steps of 1, 2, 4, 8, 16, 32, 64, 128, 256, and 512 ms, and each simulation was repeated 5 times. The number of steps was calculated to allow for 1 hour of simulation time, however some simulations were aborted before this time had elapsed due to excessive computation time.

The bending energy of actin filaments was monitored at various time points throughout each simulation. This was chosen as this is closely related to the ORP measure used to evaluate our simulations, however has the benefit of being obtainable direct from the simulation results with no further analysis required.

Time steps greater than 32 ms were discounted due to lack of stability, showing large changes in bending energy throughout the simulation time. The results for timesteps from 1-16 ms are shown in Figure A.1. It is evident from this plot that the mean bending energy is dependent upon the timestep used, reducing as the step size increases. A number of similar tests were carried out on systems with different properties and parameter values, and we found to be the case in every scenario tested. We communicated our findings to the developers of Cytosim however this issue could not be rectified within the course of our research.

In order to estimate the magnitude of this difference in bending energy, we examine data obtained at times when the energy appears to have reached a

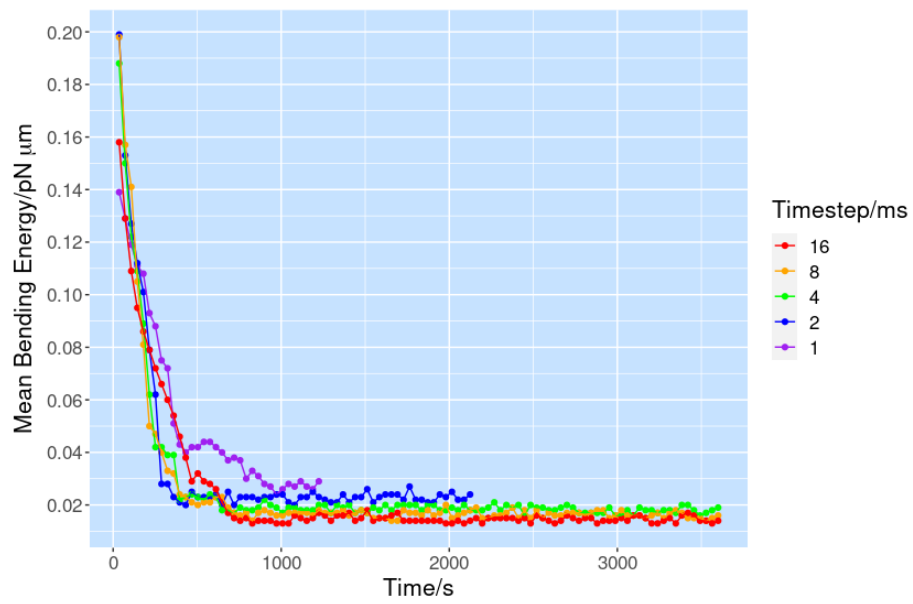


Figure A.1: Mean Bending Energy with Timestep. *These results show that mean bending energy is at its highest for the smallest timestep of 1 ms, and reduces systematically as timestep increases.*

plateau in all cases. As there are small fluctuations throughout the simulations due to their stochastic nature, we analyse bending energy results from a series of timepoints, $t \in \{864, 900, 936, 972, 1008, 1044, 1080, 1116, 1152, 1188, 1225\}$ s. For each timestep, we combine the data from these 11 timepoints and calculate the mean of these values, as shown in Table A.1. This value represents an average plateau bending energy for the timestep. Overall, the largest timestep of 16 ms corresponded to a mean bending energy of $0.0131 \text{ pN } \mu\text{m}$ less than the smallest timestep of 1 ms.

Table A.1: Plateau Mean Bending Energy. *Bending energy is shown for each timestep to 3 significant figures. The mean is obtained by averaging over values obtained at 11 timepoints beginning at $t = 864$ s. Magnitude of bending energy decreases as timestep increases, with a total difference of $0.0131 \text{ pN } \mu\text{m}$ between the highest and lowest timesteps included here.*

Timestep/ms	Mean Bending Energy/ $\text{pN } \mu\text{m}$
1	0.0275
2	0.0228
4	0.0190
8	0.0169
16	0.0144

Next we look at the distribution of these values using boxplots as shown in Figure A.2. This figure further illustrates the decrease in energy with timestep, with the interquartile range of each timestep occupying a distinct set of values, without overlapping the ranges of other timesteps.

These results show a clear dependence of bending energy with the timestep used, however the effect of this dependency is small and is unlikely to cause undue influence to our results. Nevertheless, we felt it was important to be cautious given that bending energy is key to interpretation of our results, and in order to mitigate any favourable effect of this dependency we chose to use a timestep of 16 ms - a value which showed the lowest levels of mean bending energy.

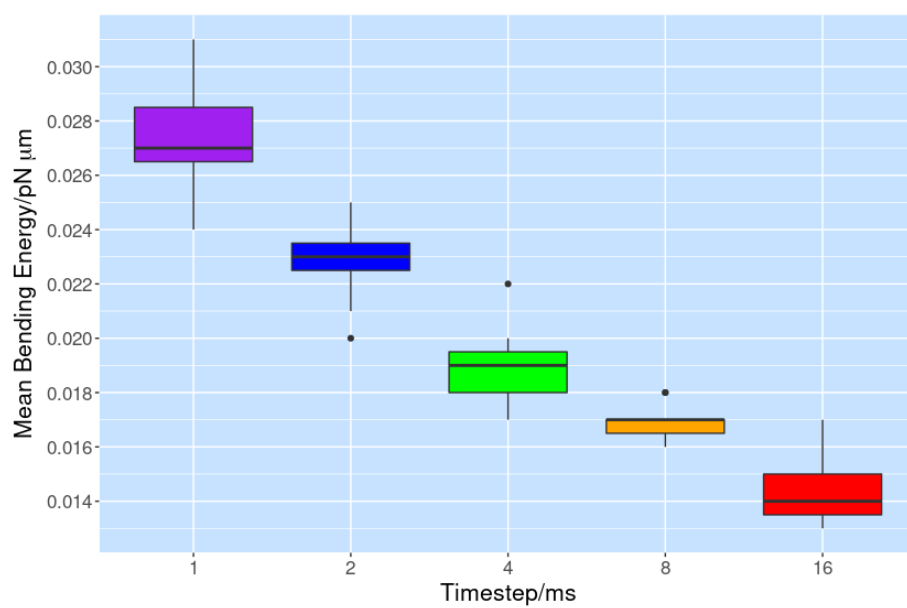


Figure A.2: Plateau Bending Energy with Timestep. Each box represents a set of bending energy measurements gathered across 11 time points. These results show that plateau bending energy values are at their highest at a timestep of 1 ms, decreasing with each increase in step duration.

Bibliography

- Abouelezz, A., Stefen, H., Segerstråle, M., Micinski, D., Minkeviciene, R., Lahti, L., Hardeman, E. C., Gunning, P. W., Hoogenraad, C. C., Taira, T., Fath, T., and Hotulainen, P. (2020). Tropomyosin Tpm3.1 is required to maintain the structure and function of the Axon Initial Segment. *iScience*, 23(5).
- Adalbert, R. and Coleman, M. P. (2013). Review: Axon pathology in age-related neurodegenerative disorders. *Neuropathol. Appl. Neurobiol.*, 39(2):90–108.
- Ahmad, F. J., Hughey, J., Wittmann, T., Hyman, A., Greaser, M., and Baas, P. W. (2000). Motor proteins regulate force interactions between microtubules and microfilaments in the axon. *Nat. Cell Biol.*, 2(5):276–280.
- Ahmadzadeh, H., Smith, D. H., and Shenoy, V. B. (2015). Mechanical effects of dynamic binding between Tau proteins on microtubules during axonal injury. *Biophys. J.*, 109(11):2328–2337.
- Alberts, B., Johnson, A., Lewis, J., Raff, M., Roberts, K., and Walter, P. (2002). *Molecular Biology of the Cell*. Garland Science, fourth edition.
- Amor, V., Zhang, C., Vainshtein, A., Zhang, A., Zollinger, D. R., Eshed-Eisenbach, Y., Brophy, P. J., Rasband, M. N., and Peles, E. (2017). The paranodal cytoskeleton clusters Na⁺ channels at nodes of Ranvier. *Elife*, 6:1–15.
- Baines, A. J. (2014). Link up and fold up - Templating the formation of spectrin tetramers. *J. Mol. Biol.*, 426(1):7–10.
- Banerjee, N. and Park, J. (2015). Modeling and simulation of biopolymer networks: Classification of the cytoskeleton models according to multiple scales. *Korean J. Chem. Eng.*, 32(7):1207–1217.
- Bär, J., Kobler, O., Van Bommel, B., and Mikhaylova, M. (2016). Periodic F-actin structures shape the neck of dendritic spines. *Sci. Rep.*, 6(November):1–9.
- Bar-Ziv, R. and Moses, E. (1994). Instability and "pearling" states produced in tubular membranes by competition of curvature and tension. *Phys. Rev. Lett.*, 73(10):1392–1395.

- Barabas, F. M., Masullo, L. A., Bordenave, M. D., Giusti, S. A., Unsain, N., Refojo, D., Cáceres, A., and Stefani, F. D. (2017). Automated quantification of protein periodic nanostructures in fluorescence nanoscopy images: Abundance and regularity of neuronal spectrin membrane-associated skeleton. *Sci. Rep.*, 7(1):1–10.
- Behnel, S., Bradshaw, R., Citro, C., Dalcin, L., Seljebotn, D. S., and Smith, K. (2011). Cython: The best of both worlds. *Comput. Sci. Eng.*, 13(2):31–39.
- Berger, S. L., Leo-Macias, A., Yuen, S., Khatri, L., Pfennig, S., Zhang, Y., Agullo-Pascual, E., Caillol, G., Zhu, M. S., Rothenberg, E., Melendez-Vasquez, C. V., Delmar, M., Letierrier, C., and Salzer, J. L. (2018). Localized myosin II activity regulates assembly and plasticity of the axon initial segment. *Neuron*, 97(3):555–570.e6.
- Bernal, R., Pullarkat, P. A., and Melo, F. (2007). Mechanical properties of axons. *Phys. Rev. Lett.*, 99(1):6–9.
- Berthoumieux, H., Maître, J. L., Heisenberg, C. P., Paluch, E. K., Jülicher, F., and Salbreux, G. (2014). Active elastic thin shell theory for cellular deformations. *New J. Phys.*, 16.
- Bloch, R. J. and Pumphlin, D. W. (1992). A model of spectrin as a concertina in the erythrocyte membrane skeleton. *Trends Cell Biol.*, 2(7):186–189.
- Brito, C. and Sousa, S. (2020). Non-muscle myosin 2A (NM2A): Structure, regulation and function. *Cells*, 9(7):12–16.
- Brown, J. W., Bullitt, E., Sriswasdi, S., Harper, S., Speicher, D. W., and McKnight, C. J. (2015). The physiological molecular shape of spectrin: A compact supercoil resembling a Chinese finger trap. *PLoS Comput. Biol.*, 11(6):1–20.
- Chen, Y., Xu, J., Zhang, Y., Ma, S., Yi, W., Liu, S., Yu, X., Wang, J., and Chen, Y. (2020). Coronin 2B regulates dendrite outgrowth by modulating actin dynamics. *FEBS Lett.*, 594(18):2975–2987.
- Coles, C. H. and Bradke, F. (2015). Coordinating neuronal actin-microtubule dynamics. *Curr. Biol.*, 25(15):R677–R691.
- Costa, A. R., Pinto-Costa, R., Sousa, S. C., and Sousa, M. M. (2018). The regulation of axon diameter: from axonal circumferential contractility to activity-dependent axon swelling. *Front. Mol. Neurosci.*, 11(September):1–7.
- Costa, A. R., Sousa, S. C., Pinto-Costa, R., Mateus, J. C., Lopes, C. D., Costa, A. C., Rosa, D., Machado, D., Pajuelo, L., Wang, X., Zhou, F. Q., Pereira, A. J., Sampaio, P., Rubinstein, B. Y., Pinto, I. M., Lampe, M., Aguiar, P., and Sousa, M. M. (2020). The membrane periodic skeleton is an actomyosin network that regulates axonal diameter and conduction. *Elife*, 9:1–21.

- Costa, M., Draper, B. W., and Priess, J. R. (1997). The role of actin filaments in patterning the *Caenorhabditis elegans* cuticle. *Dev. Biol.*, 184(2):373–384.
- Courtemanche, N., Lee, J. Y., Pollard, T. D., and Greene, E. C. (2013). Tension modulates actin filament polymerization mediated by formin and profilin. *Proc. Natl. Acad. Sci. U. S. A.*, 110(24):9752–9757.
- Dasbiswas, K., Hu, S., Schnorrer, F., Safran, S. A., and Bershadsky, A. D. (2018). Ordering of myosin ii filaments driven by mechanical forces: Experiments and theory. *Philos. Trans. R. Soc. B Biol. Sci.*, 373(1747).
- Datar, A., Ameeramja, J., Bhat, A., Srivastava, R., Mishra, A., Bernal, R., Prost, J., Callan-Jones, A., and Pullarkat, P. A. (2019). The roles of microtubules and membrane tension in axonal beading, retraction, and atrophy. *Biophys. J.*, 117(5):880–891.
- Deng, H., Wang, W., Yu, J., Zheng, Y., Qing, Y., and Pan, D. (2015). Spectrin regulates Hippo signaling by modulating cortical actomyosin activity. *Elife*, 2015(4):1–18.
- D’Este, E., Kamin, D., Göttfert, F., El-Hady, A., and Hell, S. W. (2015). STED nanoscopy reveals the ubiquity of subcortical cytoskeleton periodicity in living neurons. *Cell Rep.*, 10(8):1246–1251.
- D’Este, E., Kamin, D., Velte, C., Göttfert, F., Simons, M., and Hell, S. W. (2016). Subcortical cytoskeleton periodicity throughout the nervous system. *Sci. Rep.*, 6:1–8.
- Dominguez, R. and Holmes, K. C. (2011). Actin structure and function. *Annu. Rev. Biophys.*, 40(1):169–186.
- Dubey, S., Bhembre, N., Bodas, S., Veer, S., Ghose, A., Callan-Jones, A., Pullarkat, P., and Sens, P. (2020). The axonal actin-spectrin lattice acts as a tension buffering shock absorber. *Elife*, 9:1–22.
- Eira, J., Silva, C. S., Sousa, M. M., and Liz, M. A. (2016). The cytoskeleton as a novel therapeutic target for old neurodegenerative disorders. *Prog. Neurobiol.*, 141:61–82.
- Elshenawy, M. M., Canty, J. T., Oster, L., Ferro, L. S., Zhou, Z., Blanchard, S. C., and Yildiz, A. (2019). Cargo adaptors regulate stepping and force generation of mammalian dynein–dynactin. *Nat. Chem. Biol.*, 15(11):1093–1101.
- Fan, A., Joy, M. S. H., and Saif, T. (2019). A connected cytoskeleton network generates axonal tension in embryonic: *Drosophila*. *Lab Chip*, 19(18):3133–3139.
- Fan, A., Tofangchi, A., Kandel, M., Popescu, G., and Saif, T. (2017). Coupled circumferential and axial tension driven by actin and myosin influences in vivo axon diameter. *Sci. Rep.*, 7(1):1–12.

- Fath, T., Fischer, R. S., Dehmelt, L., Halpain, S., and Fowler, V. M. (2011). Tropomodulins are negative regulators of neurite outgrowth. *Eur. J. Cell Biol.*, 90(4):291–300.
- Faty, M., Fink, M., and Barral, Y. (2002). Septins: A ring to part mother and daughter. *Curr. Genet.*, 41(3):123–131.
- Frenkel, D. and Smit, B. (2002). *Understanding molecular simulation - from algorithms to applications*. Academic Press, second edition.
- Galiano, M. R., Jha, S., Ho, T. S. Y., Zhang, C., Ogawa, Y., Chang, K. J., Stankewich, M. C., Mohler, P. J., and Rasband, M. N. (2012). A distal axonal cytoskeleton forms an intra-axonal boundary that controls axon initial segment assembly. *Cell*, 149(5):1125–1139.
- Gallo, G. (2013). More than one ring to bind them all: Recent insights into the structure of the axon. *Dev. Neurobiol.*, 73(11):799–805.
- Gartner, T. E. and Jayaraman, A. (2019). Modeling and simulations of polymers: A roadmap. *Macromolecules*, 52(3):755–786.
- Gateva, G., Kremneva, E., Reindl, T., Kotila, T., Kogan, K., Gressin, L., Gunning, P. W., Manstein, D. J., Michelot, A., and Lappalainen, P. (2017). Tropomyosin isoforms specify functionally distinct actin filament populations in vitro. *Curr. Biol.*, 27(5):705–713.
- Gittes, F., Mickey, B., Nettleton, J., and Howard, J. (1993). Flexural rigidity of microtubules and actin filaments measured from thermal fluctuations in shape. *J. Cell Biol.*, 120(4):923–934.
- Glomb, A. O., Swaim, G., and Llancao, P. M. (2022). Scaled-expansion of the membrane associated cytoskeleton requires conserved kinesin adaptors.
- Godena, V. K., Brookes-Hocking, N., Moller, A., Shaw, G., Oswald, M., Sancho, R. M., Miller, C. C., Whitworth, A. J., and De Vos, K. J. (2014). Increasing microtubule acetylation rescues axonal transport and locomotor deficits caused by LRRK2 Roc-COR domain mutations. *Nat. Commun.*, 5:1–11.
- Gordon-Weeks, P. R. and Fournier, A. E. (2014). Neuronal cytoskeleton in synaptic plasticity and regeneration. *J. Neurochem.*, 129(2):206–212.
- Gregory, S. L., Ebrahimi, S., Milverton, J., Jones, W. M., Bejsovec, A., and Saint, R. (2008). Cell division requires a direct link between microtubule-bound RacGAP and Anillin in the contractile ring. *Curr. Biol.*, 18(1):25–29.
- Hammarlund, M., Jorgensen, E. M., and Bastiani, M. J. (2007). Axons break in animals lacking β -spectrin. *J. Cell Biol.*, 176(3):269–275.
- Han, B., Zhou, R., Xia, C., and Zhuang, X. (2017). Structural organization of the actin-spectrin-based membrane skeleton in dendrites and soma of neurons. *Proc. Natl. Acad. Sci. U. S. A.*, 114(32):E6678–E6685.

- Hannezo, E., Dong, B., Recho, P., Joanny, J.-F., and Hayashi, S. (2015). Cortical instability drives periodic supracellular actin pattern formation in epithelial tubes. *Proc. Natl. Acad. Sci.*, 112(28):8620–8625.
- Harris, C. R., Millman, K. J., van der Walt, S. J., Gommers, R., Virtanen, P., Cournapeau, D., Wieser, E., Taylor, J., Berg, S., Smith, N. J., Kern, R., Picus, M., Hoyer, S., van Kerkwijk, M. H., Brett, M., Haldane, A., del Río, J. F., Wiebe, M., Peterson, P., Gérard-Marchant, P., Sheppard, K., Reddy, T., Weckesser, W., Abbasi, H., Gohlke, C., and Oliphant, T. E. (2020). Array programming with NumPy. *Nature*, 585(7825):357–362.
- Hauser, M., Yan, R., Li, W., Repina, N. A., Schaffer, D. V., and Xu, K. (2018). The spectrin-actin-based periodic cytoskeleton as a conserved nanoscale scaffold and ruler of the neural stem cell lineage. *Cell Rep.*, 24(6):1512–1522.
- He, J., Zhou, R., Wu, Z., Carrasco, M. A., Kurshan, P. T., Farley, J. E., Simon, D. J., Wang, G., Han, B., Hao, J., Heller, E., Freeman, M. R., Shen, K., Maniatis, T., Tessier-Lavigne, M., and Zhuang, X. (2016). Prevalent presence of periodic actin–spectrin-based membrane skeleton in a broad range of neuronal cell types and animal species. *Proc. Natl. Acad. Sci.*, 113(21):6029–6034.
- Hill, C. S., Coleman, M. P., and Menon, D. K. (2016). Traumatic Axonal Injury: Mechanisms and translational opportunities. *Trends Neurosci.*, 39(5):311–324.
- Huang, C. Y.-M., Zhang, C., Zollinger, D. R., Leterrier, C., and Rasband, M. N. (2017). An α II spectrin-based cytoskeleton protects large-diameter myelinated axons from degeneration. *J. Neurosci.*, 37(47):11323–11334.
- Hunter, J. D. (2007). Matplotlib: A 2D graphics environment. *Comput. Sci. Eng.*, 9(3):90–95.
- Isambert, H., Venier, P., Maggs, A. C., Fattoum, A., Kassab, R., Pantaloni, D., and Carlier, M. F. (1995). Flexibility of actin filaments derived from thermal fluctuations. Effect of bound nucleotide, phalloidin, and muscle regulatory proteins. *J. Biol. Chem.*, 270(19):11437–11444.
- J. Rajagopalan, A. Tofangchi, and Saif, M. T. A. (2010). Drosophila neurons actively regulate axonal tension in vivo. *Biophys. J.*, 99(10):3208–3215.
- Jia, R., Li, D., Li, M., Chai, Y., Liu, Y., Xie, Z., Shao, W., Xie, C., Li, L., Huang, X., Chen, L., Li, W., and Ou, G. (2019). Spectrin-based membrane skeleton supports ciliogenesis. *PLoS Biol.*, 17(7).
- Jülicher, F., Kruse, K., Prost, J., and Joanny, J. F. (2007). Active behavior of the cytoskeleton. *Phys. Rep.*, 449(1-3):3–28.
- Kahn, O. I. and Baas, P. W. (2016). Microtubules and growth cones: Motors drive the turn. *Trends Neurosci.*, 39(7):433–440.

- Kandel, E., Schwartz, J., and Jessell, T. (2000). *Principles of Neural Science*. McGraw-Hill, fourth edition.
- Kasas, S., Kis, A., Riederer, B. M., Forró, L., Dietler, G., and Catsicas, S. (2004). Mechanical properties of microtubules explored using the finite elements method. *ChemPhysChem*, 5(2):252–257.
- Kim, T., Hwang, W., and Kamm, R. D. (2009). Computational analysis of a cross-linked actin-like network. *Exp. Mech.*, 49(1):91–104.
- Kole, T. P., Tseng, Y., Huang, L., Katz, J. L., and Wirtz, D. (2004). Rho kinase regulates the intracellular micromechanical response of adherent cells to Rho activation. *Mol. Biol. Cell*, 15(7):3475–3484.
- Koshino, I., Mohandas, N., and Takakuwa, Y. (2012). Identification of a novel role for dematin in regulating red cell membrane function by modulating spectrin-actin interaction. *J. Biol. Chem.*, 287(42):35244–35250.
- Krieg, M., Dunn, A. R., and Goodman, M. B. (2014). Mechanical control of the sense of touch by β -spectrin. *Nat. Cell Biol.*, 16(3):224–233.
- Krieg, M., Stühmer, J., Cueva, J. G., Fetter, R., Spilker, K., Cremers, D., Shen, K., Dunn, A. R., and Goodman, M. B. (2017). Genetic defects in β -spectrin and tau sensitize *C. Elegans* axons to movement-induced damage via torque-tension coupling. *Elife*, 6(2010):1–35.
- Laporte, D., Ojic, N., Vavylonis, D., and Wu, J. Q. (2012). α -actinin and fimbrin cooperate with myosin II to organize actomyosin bundles during contractile-ring assembly. *Mol. Biol. Cell*, 23(16):3094–3110.
- Lavoie-Cardinal, F., Bilodeau, A., Lemieux, M., Gardner, M. A., Wiesner, T., Laramée, G., Gagné, C., and De Koninck, P. (2020). Neuronal activity remodels the F-actin based submembrane lattice in dendrites but not axons of hippocampal neurons. *Sci. Rep.*, 10(1):1–17.
- Lazarus, C., Soheilypour, M., and Mofrad, M. R. (2015). Torsional behavior of axonal microtubule bundles. *Biophys. J.*, 109(2):231–239.
- Leite, S. C., Sampaio, P., Sousa, V. F., Nogueira-Rodrigues, J., Pinto-Costa, R., Peters, L. L., Brites, P., and Sousa, M. M. (2016). The actin-binding protein α -Adducin is required for maintaining axon diameter. *Cell Rep.*, 15(3):490–498.
- Leite, S. C. and Sousa, M. M. (2016). The neuronal and actin commitment: Why do neurons need rings? *Cytoskeleton*, 73(9):424–434.
- Leterrier, C. (2019). A dual role for β II-spectrin in axons. *Proc. Natl. Acad. Sci. U. S. A.*, 116(31):15324–15326.
- Leterrier, C., Dubey, P., and Roy, S. (2017). The nano-architecture of the axonal cytoskeleton. *Nat. Rev. Neurosci.*, 18(12):713–726.

- Letort, G., Politi, A. Z., Ennomani, H., Théry, M., Nedelec, F., and Blanchoin, L. (2015). Geometrical and mechanical properties control actin filament organization. *PLoS Comput. Biol.*, 11(5):1–21.
- Li, J., Dao, M., Lim, C. T., and Suresh, S. (2005). Spectrin-level modeling of the cytoskeleton and optical tweezers stretching of the erythrocyte. *Biophys. J.*, 88(5):3707–3719.
- Li, X., Matsuoka, Y., and Bennett, V. (1998). Adducin preferentially recruits spectrin to the fast growing ends of actin filaments in a complex requiring the MARCKS-related domain and a newly defined oligomerization domain. *J. Biol. Chem.*, 273(30):19329–19338.
- Liu, C. H. and Rasband, M. N. (2019). Axonal spectrins: Nanoscale organization, functional domains and spectrinopathies. *Front. Cell. Neurosci.*, 13(May).
- Lorenzo, D. N., Badea, A., Davis, J., Hostettler, J., He, J., Zhong, G., Zhuang, X., and Bennett, V. (2014). A PIK3C3-Ankyrin-B-Dynactin pathway promotes axonal growth and multiorganelle transport. *J. Cell Biol.*, 207(6):735–752.
- Lorenzo, D. N., Badea, A., Zhou, R., Mohler, P. J., Zhuang, X., and Bennett, V. (2019). β I-spectrin promotes mouse brain connectivity through stabilizing axonal plasma membranes and enabling axonal organelle transport. *Proc. Natl. Acad. Sci. U. S. A.*, 116(31):15686–15695.
- Lowery, J., Kuczmarski, E. R., Herrmann, H., and Goldma, R. D. (2015). Intermediate filaments play a pivotal role in regulating cell architecture and function. *J. Biol. Chem.*, 290(28):17145–17153.
- Lukinavičius, G., Reymond, L., D’Este, E., Masharina, A., Göttfert, F., Ta, H., Güther, A., Fournier, M., Rizzo, S., Waldmann, H., Blaukopf, C., Sommer, C., Gerlich, D. W., Arndt, H. D., Hell, S. W., and Johnsson, K. (2014). Fluorogenic probes for live-cell imaging of the cytoskeleton. *Nat. Methods*, 11(7):731–733.
- Magee, J. C. (2000). Dendritic integration of excitatory synaptic input. *Nat. Rev. Neurosci.*, 1(3):181–90.
- McCullough, B. R., Blanchoin, L., Martiel, J. L., and De La Cruz, E. M. (2008). Cofilin increases the bending flexibility of actin filaments: Implications for severing and cell mechanics. *J. Mol. Biol.*, 381(3):550–558.
- Mehboob, S., Song, Y., Witek, M., Long, F., Santarsiero, B. D., Johnson, M. E., and Fung, L. W. (2010). Crystal structure of the nonerythroid α -spectrin tetramerization site reveals differences between erythroid and nonerythroid spectrin tetramer formation. *J. Biol. Chem.*, 285(19):14572–14584.

- Metropolis, N., Rosenbluth, A. W., Rosenbluth, M. N., Teller, A. H., and Teller, E. (1953). Equation of state calculations by fast computing machines. *J. Chem. Phys.*, 21(6):1087–1092.
- Mirijanian, D. T. and Voth, G. A. (2008). Unique elastic properties of the spectrin tetramer as revealed by multiscale coarse-grained modeling. *Proc. Natl. Acad. Sci.*, 105(4):1204–1208.
- Mische, S. M., Mooseker, M. S., and Morrow, J. S. (1987). Erythrocyte adducin: A calmodulin-regulated actin-bundling protein that stimulates spectrin-actin binding. *J. Cell Biol.*, 105(6 I):2837–2845.
- Miyazaki, M., Chiba, M., Eguchi, H., Ohki, T., and Ishiwata, S. (2015). Cell-sized spherical confinement induces the spontaneous formation of contractile actomyosin rings in vitro. *Nat. Cell Biol.*, 17(4):480–489.
- Mostowy, S. and Cossart, P. (2012). Septins: The fourth component of the cytoskeleton. *Nat. Rev. Mol. Cell Biol.*, 13(3):183–194.
- Moughamian, A. J. and Holzbaur, E. L. (2012). Dynactin is required for transport initiation from the distal axon. *Neuron*, 74(2):331–343.
- Mutalik, S. P., Joseph, J., Pullarkat, P. A., and Ghose, A. (2018). Cytoskeletal mechanisms of axonal contractility. *Biophys. J.*, 115(4):713–724.
- Nedelec, F. and Foethke, D. (2007). Collective Langevin dynamics of flexible cytoskeletal fibers. *New J. Phys.*, 9.
- Oda, T., Makino, K., Yamashita, I., Namba, K., and Maéda, Y. (1998). Effect of the length and effective diameter of F-actin on the filament orientation in liquid crystalline sols measured by X-ray fiber diffraction. *Biophys. J.*, 75(6):2672–2681.
- Palani, S., Balasubramanian, M., and Köster, D. (2020). Calponin-Homology Domain mediated bending of membrane associated actin filaments. 1:1–26.
- Paoletti, A. and Chang, F. (2000). Analysis of mid1p, a protein required for placement of the cell division site, reveals a link between the nucleus and the cell surface in fission yeast. *Mol. Biol. Cell*, 11(8):2757–2773.
- Papandréou, M. J. and Leterrier, C. (2018). The functional architecture of axonal actin. *Mol. Cell. Neurosci.*, 91(May):151–159.
- Paramore, S., Ayton, G. S., Mirijanian, D. T., and Voth, G. A. (2006). Extending a spectrin repeat unit. I: Linear force-extension response. *Biophys. J.*, 90(1):92–100.
- Pelham, R. J. and Chang, F. (2002). Actin dynamics in the contractile ring during cytokinesis in fission yeast. *Nature*, 419(6902):82–86.

- Perge, J. A., Niven, J. E., Mugnaini, E., Balasubramanian, V., and Sterling, P. (2012). Why do axons differ in caliber? *J. Neurosci.*, 32(2):626–638.
- Peterson, J. R. and Mitchison, T. J. (2002). Small molecules, big impact: A history of chemical inhibitors and the cytoskeleton. *Chem. Biol.*, 9(12):1275–1285.
- Pfister, B. J., Iwata, A., Meaney, D. F., and Smith, D. H. (2004). Extreme stretch growth of integrated axons. *J. Neurosci.*, 24(36):7978–7983.
- Pielage, J., Cheng, L., Fetter, R. D., Carlton, P. M., Sedat, J. W., and Davis, G. W. (2008). A presynaptic giant ankyrin stabilizes the NMJ through regulation of presynaptic microtubules and transsynaptic cell adhesion. *Neuron*, 58(2):195–209.
- Pollard, T. D. (1986). Rate constants for the reactions of ATP- and ADP-actin with the ends of actin filaments. *J. Cell Biol.*, 103(6):2747–2754.
- Prados, A., Brey, J. J., and Sánchez-Rey, B. (1997). A dynamical Monte Carlo algorithm for master equations with time-dependent transition rates. *J. Stat. Phys.*, 89(3-4):709–734.
- Prost, J., Jülicher, F., and Joanny, J. F. (2015). Active gel physics. *Nat. Phys.*, 11(2):111–117.
- Pruyne, D., Evangelista, M., Yang, C., Bi, E., Zigmond, S., Bretscher, A., and Boone, C. (2002). Role of formins in actin assembly: Nucleation and barbed-end association. *Science (80-.)*, 297(5581):612–615.
- Qu, Y., Hahn, I., Webb, S. E., Pearce, S. P., and Prokop, A. (2017). Periodic actin structures in neuronal axons are required to maintain microtubules. *Mol. Biol. Cell*, 28(2):296–308.
- Rafiq, N. M., Lyons, L. L., Gowrishankar, S., De Camilli, P., and Ferguson, S. M. (2022). JIP3 links lysosome transport to regulation of multiple components of the axonal cytoskeleton. *Commun. Biol.*, 5(1):1–10.
- Rasband, M. N. (2010). The axon initial segment and the maintenance of neuronal polarity. *Nat. Rev. Neurosci.*, 11(8):552–562.
- Schelski, M. and Bradke, F. (2017). Neuronal polarization: From spatiotemporal signaling to cytoskeletal dynamics. *Mol. Cell. Neurosci.*, 84:11–28.
- Schwayer, C., Sikora, M., Slovák, J., Kardos, R., and Heisenberg, C. P. (2016). Actin rings of power. *Dev. Cell*, 37(6):493–506.
- Shahinnejad, A., Haghpanahi, M., and Farmanzad, F. (2013). Finite element analysis of axonal microtubule bundle under tension and torsion. *Procedia Eng.*, 59:16–24.

- Shotton, D. M., Burke, B. E., and BRANTON, D. (1979). The molecular structure of human erythrocyte spectrin. Biophysical and electron microscopic studies. *J. Mol. Biol.*, 131(2):303–329.
- Sidenstein, S. C., D’Este, E., Böhm, M. J., Danzl, J. G., Belov, V. N., and Hell, S. W. (2016). Multicolour multilevel STED nanoscopy of actin/spectrin organization at synapses. *Sci. Rep.*, 6(March):1–8.
- Siegel, D. L. and Branton, D. (1985). Partial purification and characterization of an actin-bundling protein, band 4.9, from human erythrocytes. *J. Cell Biol.*, 100(3):775–785.
- Smith, A. S., Nowak, R. B., Zhou, S., Giannetto, M., Gokhin, D. S., Papoin, J., Ghiran, I. C., Blanc, L., Wan, J., and Fowler, V. M. (2018). Myosin IIA interacts with the spectrin-actin membrane skeleton to control red blood cell membrane curvature and deformability. *Proc. Natl. Acad. Sci.*, 115(19):E4377–E4385.
- Smith, D. H. (2009). Stretch growth of integrated axon tracts: Extremes and exploitations. *Prog. Neurobiol.*, 89(3):231–239.
- Smith, D. H., Wolf, J. A., Lusardi, T. A., Lee, V. M.-Y., and Meaney, D. F. (1999). High tolerance and delayed elastic response of cultured axons to dynamic stretch injury. *J. Neurosci.*, 19(11):4263–4269.
- Soheilypour, M., Peyro, M., Peter, S. J., and Mofrad, M. R. (2015). Buckling behavior of individual and bundled microtubules. *Biophys. J.*, 108(7):1718–1726.
- Sörensen, P. M., Iacob, R. E., Fritzsche, M., Engen, J. R., Briehner, W. M., Charras, G., and Eggert, U. S. (2012). The natural product cucurbitacin e inhibits depolymerization of actin filaments. *ACS Chem. Biol.*, 7(9):1502–1508.
- Stokke, B. T., Mikkelsen, A., and Elgsaeter, A. (1985). Human erythrocyte spectrin dimer intrinsic viscosity: Temperature dependence and implications for the molecular basis of the erythrocyte membrane free energy. *BBA - Biomembr.*, 816(1):102–110.
- Szikora, S., Földi, I., Tóth, K., Migh, E., Vig, A., Bugyi, B., Maléth, J., Hegyi, P., Kaltenecker, P., Sanchez-Soriano, N., and Mihaly, J. (2017). The formin DAAM is required for coordination of the actin and microtubule cytoskeleton in axonal growth cones. *J. Cell Sci.*, 130(15):2506–2519.
- Takahashi, H., Rico, F., Chipot, C., and Scheuring, S. (2018). α -helix unwinding as force buffer in spectrins. *ACS Nano*, 12(3):2719–2727.
- The Mathworks, I. (2020). Matlab.

- Tofangchi, A., Fan, A., and Saif, M. T. A. (2016). Mechanism of axonal contractility in embryonic *Drosophila* motor neurons in vivo. *Biophys. J.*, 111(7):1519–1527.
- Unsain, N., Bordenave, M. D., Martinez, G. F., Jalil, S., Von Bilderling, C., Barabas, F. M., Masullo, L. A., Johnstone, A. D., Barker, P. A., Bisbal, M., Stefani, F. D., and Cáceres, A. O. (2018a). Remodeling of the actin/spectrin membrane-associated periodic skeleton, growth cone collapse and F-Actin decrease during axonal degeneration. *Sci. Rep.*, 8(1):1–16.
- Unsain, N., Stefani, F. D., and Cáceres, A. (2018b). The actin/spectrin membrane-associated periodic skeleton in neurons. *Front. Synaptic Neurosci.*, 10(MAY):1–8.
- Uzoigwe, C. (2006). The human erythrocyte has developed the biconcave disc shape to optimise the flow properties of the blood in the large vessels. *Med. Hypotheses*, 67(5):1159–1163.
- Van Essen, D. C. (1997). A tension-based theory of morphogenesis and compact wiring in the central nervous system. *Nature*, 385(6614):313–318.
- Vassilopoulos, S., Gibaud, S., Jimenez, A., Caillol, G., and Letierrier, C. (2019). Ultrastructure of the axonal periodic scaffold reveals a braid-like organization of actin rings. *Nat. Commun.*, 10(1):1–13.
- Vavylonis, D., Wu, J. Q., Hao, S., O’Shaughnessy, B., and Pollard, T. D. (2008). Assembly mechanism of the contractile ring for cytokinesis by fission yeast. *Science (80-.)*, 319(5859):97–100.
- Wang, G., Simon, D. J., Wu, Z., Belsky, D. M., Heller, E., O’Rourke, M. K., Hertz, N. T., Molina, H., Zhong, G., Tessier-Lavigne, M., and Zhuang, X. (2019). Structural plasticity of actin-spectrin membrane skeleton and functional role of actin and spectrin in axon degeneration. *Elife*, 8:1–23.
- Wang, T., Li, W., Martin, S., Papadopoulos, A., Joensuu, M., Liu, C., Jiang, A., Shamsollahi, G., Amor, R., Lanoue, V., Padmanabhan, P., and Meunier, F. A. (2020). Radial contractility of actomyosin rings facilitates axonal trafficking and structural stability. *J. Cell Biol.*, 219(5).
- Whitfield, C. A. and Hawkins, R. J. (2016). Immersed boundary simulations of active fluid droplets. *PLoS One*, 11(9):1–30.
- Wickham, H. (2009). *ggplot2: elegant graphics for data analysis*. Springer, New York, London.
- Witte, H., Neukirchen, D., and Bradke, F. (2008). Microtubule stabilization specifies initial neuronal polarization. *J. Cell Biol.*, 180(3):619–632.
- Wolfram Research, I. (2019). Mathematica 12.0.

- Xu, K., Zhong, G., and Zhuang, X. (2013). Actin, spectrin, and associated proteins form a periodic cytoskeletal.pdf. *Science*, 339(January):452–6.
- Yamaoka, H., Matsushita, S., Shimada, Y., and Adachi, T. (2012). Multiscale modeling and mechanics of filamentous actin cytoskeleton. *Biomech. Model. Mechanobiol.*, 11(3-4):291–302.
- Yamashiro, S., Gokhin, D. S., Kimura, S., Nowak, R. B., and Fowler, V. M. (2012). Tropomodulins: Pointed-end capping proteins that regulate actin filament architecture in diverse cell types. *Cytoskeleton*, 69(6):337–370.
- Yogev, S., Cooper, R., Fetter, R., Horowitz, M., and Shen, K. (2016). Microtubule organization determines axonal transport dynamics. *Neuron*, 92(2):449–460.
- Zeiger, A. S. and Layton, B. E. (2008). Molecular modeling of the axial and circumferential elastic moduli of tubulin. *Biophys. J.*, 95(8):3606–3618.
- Zhang, Y., Abiraman, K., Li, H., Pierce, D. M., Tzingounis, A. V., and Lykotraftitis, G. (2017). Modeling of the axon membrane skeleton structure and implications for its mechanical properties. *PLoS Comput. Biol.*, 13(2):1–22.
- Zhang, Y., Tzingounisid, A. V., and Lykotraftitisid, G. (2019). Modeling of the axon plasma membrane structure and its effects on protein diffusion. *PLoS Comput. Biol.*, 15(5):1–26.
- Zhong, G., He, J., Zhou, R., Lorenzo, D., Babcock, H. P., Bennett, V., and Zhuang, X. (2014). Developmental mechanism of the periodic membrane skeleton in axons. *Elife*, 3.
- Zhou, A. R., Han, B., Nowak, R., Lu, Y., Heller, E., and Xia, C. (2020). Title : Proteomic and functional analyses of the periodic membrane skeleton in neurons.
- Zhou, R., Han, B., Xia, C., and Zhuang, X. (2019). Membrane-associated periodic skeleton is a signaling platform for RTK transactivation in neurons. *Science (80-.)*, 365(6456):929–934.